université de BORDEAUX

THÈSE PRÉSENTÉE

POUR OBTENIR LE GRADE DE

DOCTEUR DE

L'UNIVERSITÉ DE BORDEAUX

ÉCOLE DOCTORALE SCIENCES DE LA VIE ET DE LA SANTÉ

SPÉCIALITÉ BIOCHIMIE

Par Arunima BHATTACHARYA

Mécanismes d'inhibition du ribosome par des antibiotiques contexte-dépendants ciblant le centre de décodage du ribosome bactérien

Mechanisms of ribosome inhibition by context-dependent antibiotics targeting the decoding center of the bacterial ribosome

Sous la direction de : Dr C Axel INNIS

Soutenue le 14 octobre 2026

Membres du jury :

M. BOËL, Grégory	Directeur de recherche, IBPC, Université Paris Cité	Président du jury
Mme. PLISSON-CHASTANG, Célia	Directrice de recherche, CBI, Université de Toulouse	Rapportrice
M. GILLET, Reynald	Professeur des universités, IGDR, Université de Rennes	Rapporteur
M. ENNIFAR, Éric	Directeur de recherche, IBMC, Université de Strasbourg	Examinateur
M. INNIS, Axel	Directeur de recherche, Université de Bordeaux	Directeur de thèse

Résumé (en français)

Mécanismes d'inhibition du ribosome par des antibiotiques contexte-dépendants ciblant le centre de décodage du ribosome bactérien

Les antibiotiques sont essentiels en médecine moderne pour lutter contre les bactéries pathogènes, mais la résistance aux antibiotiques existants constitue une menace sérieuse pour les patients et la pérennité des systèmes de santé. Si l'innovation est nécessaire pour introduire de nouveaux traitements, il est tout aussi important de revisiter les médicaments existants afin de comprendre leurs mécanismes d'action complets et d'explorer des moyens de les améliorer pour combattre les pathogènes résistants. Les antibiotiques ciblant le ribosome, acteur central de la machinerie de synthèse des protéines bactériennes, représentent la majorité des médicaments cliniques utilisés. Les recherches de la dernière décennie ont révélé que, contrairement à l'idée longtemps admise selon laquelle ces drogues inhibent la synthèse de toutes les protéines avec la même efficacité, plusieurs antibiotiques sont sélectifs et inhibent la traduction de manière séquence-spécifique. L'étude du mécanisme d'action de tels antibiotiques contexte-dépendants est importante, car elle peut mener à de nouvelles stratégies pour combattre les pathogènes résistants de manière espèce-spécifique. Les drogues ciblant le ribosome peuvent inhiber la traduction en se liant à plusieurs sites fonctionnellement importants. Le centre de décodage, où le code génétique contenu dans l'ARNm est traduit en protéines, est une cible thérapeutique critique : des perturbations de cette fonction peuvent conduire à une mauvaise traduction et à la production de protéines aberrantes, compromettant in fine la viabilité cellulaire. Bien que plusieurs antibiotiques ciblant le centre de décodage soient utilisés en clinique, leur mode d'action contexte-dépendant reste peu exploré. Dans ce travail, j'étudie le mécanisme d'action séquence-dépendant de deux antibiotiques ciblant le centre de décodage du ribosome bactérien — les odilorhabdines, une classe relativement nouvelle d'antibiotiques peptidiques découverte au cours de la dernière décennie, et la tigécycline, une tétracycline de troisième génération utilisée en pratique clinique courante. Pour identifier les contextes de séquence dans lesquels ces drogues inhibent la traduction et induisent un blocage ribosomique en plus de leur capacité à perturber l'activité de décodage du ribosome, j'ai utilisé le toeprinting inverse couplé au séquençage haut débit (iTP-Seq), une technique de profilage *in vitro* permettant de localiser les ribosomes bloqués sur un ARNm avec une résolution au codon. Pour étudier le mécanisme d'action des odilorhabdines, j'ai également eu recours à la cryomicroscopie électronique et à l'analyse de particules individuelles, me permettant d'identifier les divers états conformationnels de ribosomes bloqués par l'antibiotique. Dans l'ensemble, cette thèse révèle le mode d'inhibition séquence-dépendant de deux antibiotiques ciblant le centre de décodage du ribosome, et décrit le mécanisme d'action d'une classe d'antibiotiques récemment découverte à l'échelle structurale, contribuant aux connaissances fondamentales nécessaires au développement rationnel d'antibiotiques ciblant le ribosome.

Mots-clés: **Antibiotiques, Ribosome, iTP-Seq, Cryo-EM**

Abstract (in English)

Mechanisms of ribosome inhibition by context-dependent antibiotics targeting the decoding center of the bacterial ribosome

Antibiotics are essential in modern medicine to combat bacteria pathogenic to humans, but resistance to existing antibiotics is a serious threat to patient lives and the sustainability of healthcare infrastructure. While innovation is necessary to introduce novel treatments, it is also important to revisit existing drugs in detail to understand their complete mechanisms of action and explore ways to improve them to combat resistant pathogens. Antibiotics targeting the ribosome, the main player in the bacterial protein synthesis machinery, account for the majority of clinical drugs in use. Research over the last decade has revealed that contrary to the long-held view that ribosome-targeting drugs inhibit the synthesis of all proteins with the same efficiency, many antibiotics are selective and inhibit translation in a sequence-specific manner. Probing into the mechanism of action of such context-dependent antibiotics is important since this can lead to novel methods of counteracting drug-resistant pathogens in a species-specific manner. Ribosome-targeting drugs can inhibit translation by binding to several functionally important sites on the ribosome, and the decoding center, where the genetic code encoded in the mRNA is translated into proteins, is a critical drug target, since perturbations in the decoding function can lead to mistranslation and production of aberrant proteins, ultimately compromising cell viability. While several decoding center-targeting antibiotics exist in clinical use, their context-dependent mode of action has remained underexplored. In this work, I study the sequence-dependent mechanism of action of two classes of antibiotics targeting the decoding center of the bacterial ribosome – odilorhabdins, a relatively new class of peptide antibiotics discovered in the last decade, and tigecycline, a third-generation tetracycline in regular clinical use. To identify the sequence contexts where these drugs induce ribosomal stalling in addition to their impact on decoding fidelity, I used inverse toeprinting coupled to high-throughput sequencing (iTP-Seq), an *in vitro* profiling technique that can locate ribosomes stalled on mRNA with codon resolution. Further, to investigate the mechanism of action of odilorhabdins, I used cryo-electron microscopy and single-particle analysis and studied multiple conformational states of drug-bound ribosomes stalled on a representative arrest motif. Overall, this thesis reveals the sequence-dependent mode of inhibition of two antibiotics targeting the decoding center of the ribosome, and elaborates the mechanism of action of a recently discovered class of antibiotics at the structural level, contributing to the foundational knowledge needed for structure-guided development of next-generation ribosome-targeting antibiotics.

Keywords: Antibiotics, Ribosome, iTP-Seq, Cryo-EM

ARNA INSERM U1212, CNRS UMR 5320

146 rue Léo Saignat, 33076 Bordeaux

To my grandparents and my parents

দাদান, দিদান, বাবা ও মা-কে

Acknowledgements

I would like to start by expressing my gratitude to my jury members, **Dr Célia Plisson-Chastang**, **Prof Reynald Gillet**, **Dr Éric Ennifar**, and **Dr Grégory Boël,** for taking the time to read and evaluate my work. My research was funded by the European Research Council (ERC) under the European Union's Horizon 2020 research and innovation programme (grant agreement No. 724040), the Agence Nationale de la Recherche, France (ANR-22-CE11-0012-01), and the Fondation pour la Recherche Médicale (Fin de thèse 4e année; FDT202504020196).

The journey of the last four years has been one of many firsts. Moving out of the comfort of home in Kolkata, India, for the first time, to start building a new life alone in Bordeaux while jumping on an adventure called the PhD had initially seemed like a daunting task. I believe I grew up quite a bit in these last years, amidst several lessons and discoveries, both scientific and personal, and when I look back, I realize that none of it would have been possible without the constant support of the wonderful people I am grateful to have found in this foreign land, which I have now started calling my second home.

First of all, I would like to thank my thesis supervisor, **Axel Innis**, for the opportunity to embark on this adventure. Thank you for your patience with my innumerable questions and for believing in me. I am very grateful to you for all the scientific conferences and courses I have had the opportunity to attend as a member of the lab – they have broadened my intellectual outlook enormously. I also want to thank you for the diverse memories we made at lab outings, for indulging in my (sometimes silly) ribosome humor, and for creating the song on the ribosome-antibiotic situationship (copyright AI and AI) – I hold these quite close to my heart. Thank you for all your advice – I hope one day this scientific offspring in the lab family tree can make you proud. :-)

I want to thank **Mélanie Gillard** for teaching me the basics in the lab and for her immense patience while I adjusted to the change in lab culture and environment across continents. Beyond the lab, thank you for your kind words during my lowest times and for helping me find realistic solutions to get back on track. I am grateful for the shared lunches, the ARNA retreat organizations, the conference in California, and, of course, your unique sense of humor, which has grown on me over the years. I will sorely miss the daily morning briefings in your office – it had become a favorite habit to start the day laughing, even if at ourselves. Thank you for everything :-)

I would like to thank **Fanny Boissier**, one of my first officemates and my go-to person during the initial months in Bordeaux. Thank you for all the cryo-EM data collections, the training and scientific discussions, for always cheering me up with your kind words, stories, and laughter during difficult times, and for all the shared memories in Grenoble. Merci pour tout :-)

I would then like to thank **Thibaud Renault** for his help with the iTP-Seq data analysis and for introducing me to so many unknown spheres in the analytical and computational world. Thank you for pushing me to play around with different packages and removing the fear of breaking the computer – even if I can barely 'vibe-code' now, I took my first steps in Python thanks to you. Thank you also for the shared laughter over niche scientific memes during the breaks of data analysis, for

the valuable scientific discussions interwoven amidst that laughter, and, finally, for not letting fMet stay a blank ;-)

I also want to thank **Anne Bourdoncle** for her support and kindness during the last four years.

I am immensely grateful to **Gaëlle Duflot** –the quiet woman who sat next to me during my first group meeting and became possibly the most important part of my life in Bordeaux. Thank you for being my most dependable rock through the last four years, both inside and outside the lab, even when the journeys were not smooth for both of us. Thank you for being my toeprint gel partner, playlist partner, Inkscape partner, lunch partner… Bref, no amount of thank you is enough (lab) bestie. Safe to say I got the best one.

I would next like to thank **Pauline Cossard** for being the 'elder PhD sister' in the lab when I arrived and for being there for me when I was often very scared in the beginning. I have missed you a lot over the last 2.5 years but thank you for staying connected virtually whenever I needed advice or a shoulder to lean on. The PhD alliance you founded is very much alive, passed on two more times after me and still the source of a lot of solidarity (sometimes unwantedly extreme). I am also grateful to the veteran PhDs of the lab, **Élodie Leroy** and **Alba Herrero del Valle,** for their virtual support and advice during various times of my journey.

I also want to thank **Michaela Novotná** – it has been a wonderful full-circle experience, beginning my PhD with you visiting the lab and ending it with you here as a postdoc. Thank you for all the scientific help, the shared conference memories, the friendship, and for your warm welcome in Prague.

Thank you, **Dorian Gayral,** for your scientific inputs and your 'trainings' for testing my resilience – I hope they are useful one day. I wish you all the best for your PhD and everything beyond.

Thank you, **Lélaud Esnault,** for the friendship, for always indulging in my shenanigans, and for my first Christmas dinner experience. I am very proud of your journey over the last two years and very grateful for the support during my not-so-great times. Good luck with the rest of your PhD and everything ahead! #Crousà11h30 forever ;-)

I want to thank our collaborators, **Alexander (Shura) Mankin**, **Nora Vázquez-Laslop**, **Yury Polikanov**, **Ingo Wohlgemuth**, **Marina Rodnina**, **Nils Gunnar von Heijne**, **Ane Metola**, **Justin Westerfield** and **Maxime Gualtieri** for insightful discussions throughout the multiple projects I was fortunate to be a part of. Thank you, **Shura** and **Grégory,** also for being a part of my thesis committee and advising me to ask the important questions. Thank you also to **Esther Marza**, my tutor – your advice and kindness have been instrumental in navigating some of the uphill paths of the last four years.

Many thanks to **Fabien Darfeuille**, **Anaïs Le Rhun**, **Denis Dupuy**, **Jeanne Leblond-Chain**, **Isabelle Iost** and **Andres Escalera-Maurer** for your encouragement and for the valuable conversations on my projects and career. I would also like to thank all the members of the **MicroR3 & BacRB** teams. Thank you, **Sébastien Fribourg**, for the scientific discussions over Crous lunches and the exclusive 'Namaste's

in the corridor, and **Stéphane Thore**, for the impromptu lunch-outs and for your honest advice during scientific and career conversations.

I am appreciative of **Delphine Dargère, Sandrine Chabas,** and **Stéphanie Durrieu** for their relentless efforts to ensure the lab is a safe place for everyone, and for our frequent chats about progress and life in general. I am also grateful to **Laetitia Cointement** and **Malika Vloeberghs** – you have been saviors before every conference – thank you for always finding a solution, no matter how last-minute my conference registration, poster-printing, or visa requirements were.

A huge shoutout for the office crew in the BBS who, over the years, have seen my most unfiltered self and embraced it with friendship, laughter, a few cocktails and always an extended hand for help – thank you, **Adriana**, **Maéva**, **Anne-Louise, Yoann, Mathilde, Marine, Dina, Juliette, Jazmin, Carlos (+ Mariana)**, **Florian** and **Sahil.** I am also grateful to our IECB neighbors, **Sramona**, **Jéssica**, **Mayara (+ Wanderson)** and **Rafael** for the many cherished memories. Thank you all for always boosting my spirits. <3

I also need to thank **Jessica Colombo** for being my mentor-turned-friend. I am grateful we met via Femmes et Sciences and that our conversations have continued since. Thank you for your availability and your advice, both professional and personal. You never cease to inspire me. Grazie mille!

While staying ~8000 km away from home meant I could not visit friends and family every other weekend, I am very grateful to everyone who stayed in touch from across the borders, often adjusting time zones (or sometimes outright choosing to shift to Europe). Thank you, **Samriddhi, Rajarshi, Rajdeep, Drishan, Subhamjyoti, Sombuddha, Annesha** di**, Tara** da and **Agniva** da for being a call or text away and for minimizing the inevitable feeling of isolation that comes with living in a country that does not speak your language. I also express my gratitude towards **Sayak** Sir, **Sohini** Ma'am, **Gaurab** da**, Sarmishta** di**, Souradip** da**, Rupsha** di and **Wrick** da for the regular check-ins and important advice. It has been a privilege to remain in touch long after my tenure in your lab.

I also owe a thank you to the things that kept me sane: the playlists and the non-academic books that reminded me there is a world beyond the lab, and ceramic painting, which I picked up in Bordeaux, and which taught me that not everything needs to be perfect — sometimes creating something on your own and letting it be is enough. Gratitude is also due to all the doctors and my physiotherapists who ensured I could get up on my feet and move, post September 2025.

And finally, thank you to my parents, **Swati Bhattacharya** and **Arindam Bhattacharya,** and my grandparents, **Susanta Sen Sharma** and the late **Bijali Sen Sharma**. Whatever I am today, I am because of you. Thank you for giving me the privilege and courage to dream big and for teaching me the discipline required to achieve them. আশীর্বাদ করো, যেন আরও এগিয়ে যেতে পারি।

To all those not mentioned but who supported me or contributed a passing 'Bonjour' and smile that made my day: thank you, merci beaucoup, ধন্যবাদ!

Table of Contents

Résumé (en français) ii

Abstract (in English) iii

Acknowledgements v

List of Abbreviations x

List of Tables xiii

List of Figures xiv

Preface 17

Chapter 1: Introduction 19

1.1. Antibiotic discovery: the Golden Age, the resistance crisis and the need for innovation 20

1.2. Protein synthesis in bacteria as a major antibiotic target 25

1.2.1. An overview of the bacterial translation machinery 25

1.2.2. Decoding and translocation as vulnerable antibiotic targeting steps 36

1.2.3. SSU-binding antibiotics that affect decoding, accommodation and translocation 58

1.3. Aims and Objectives 64

Chapter 2: Methodological Overview and Methods 66

2.1. Methodological Overview 67

2.1.1. Investigation of ribosomal stalling landscapes with classical and inverse toeprinting 67

2.1.2. Visualisation of stalled ribosomal complexes using cryo-EM 73

2.2. Methods 76

2.2.1. Inverse toeprinting coupled to next-generation sequencing (iTP-Seq) 76

2.2.2. Classical Toeprinting/Primer Extension Inhibition 82

2.2.3. Cryo-EM single particle reconstruction of NOSO-502-bound *E. coli* 70S ribosomes stalled on the mDDP motif 84

Chapter 3: Mechanism of inhibition of translation by the odilorhabdin class of peptide antibiotics 88

3.1. Introduction: Odilorhabdins - a Novel Class of Peptide Antibiotics 91

3.1.1. From the discovery of odilorhabdins to the optimisation of lead compounds 91
3.1.2. Odilorhabdins target the decoding center of the bacterial ribosome 97
3.1.3. Resistance to odilorhabdins 99
3.1.4. Towards further characterization of odilorhabdins 100
3.2. Results and Discussion 104
3.2.1. Determination of concentrations of odilorhabdins to be used in iTP-Seq experiments 104
3.2.2. Processing of next-generation sequencing reads and quality control 105
3.2.3. iTP-Seq reveals sequence- and concentration-dependent stalling of elongating ribosomes in the presence of NOSO-502 and NOSO-96624 109
3.2.4. Arrest motifs selected for structural analyses 125
3.2.5. Cryo-EM single particle reconstruction of NOSO-502-bound *E. coli* 70S ribosomes stalled on the mDDP motif 128
3.2.6. Conformational landscape of NOSO-502-bound *E. coli* 70S ribosomes stalled on the mDDP motif 132
3.2.7. Structural basis of proofreading impairment and translocation inhibition revealed by the conformational landscape of NOSO-502-bound stalled ribosomes 154
3.3. Conclusion and Perspectives 160
Chapter 4: Context-dependent inhibition of translation by tigecycline 162
4.1. Introduction: Tigecycline – a third-generation derivative of tetracycline 164
4.2. Results and Discussion 169
Tigecycline-induced context-dependent stalling of ribosomes during elongation 172
Tigecycline-induced stalling of ribosomes during initiation 179
4.3. Conclusion and Perspectives 180
Chapter 5: General Conclusion and Perspectives 182
Supplementary Figures and Tables 187
Appendix A: Presentations at conferences (2022-2026) 204
Appendix B: Review article 205
References 215

List of Abbreviations

- 2D: Two-dimensional
- 3D: Three-dimensional
- A-site: Aminoacyl-tRNA binding site
- A: Adenine
- aa-tRNA: Aminoacyl-tRNA
- aaRS: Aminoacyl-tRNA synthetase
- ADME-Tox: Absorption, Distribution, Metabolism, Excretion and Toxicity
- Ala/A: Alanine
- AMR: Antimicrobial resistance
- Arg/R: Arginine
- ASF: A-site finger
- ASL: Anticodon stem-loop
- Asn/N: Asparagine
- Asp/D: Aspartate or Aspartic acid
- bp: Base pair
- BPPL: Bacterial priority pathogens list
- C: Cytosine
- cDNA: Complementary DNA
- Cf: Final concentration
- Ci: Initial concentration
- cryo-EM: Cryo-electron microscopy
- CryoSPARC: Cryo-EM Single Particle Ab-Initio Reconstruction and Classification
- CTD: C-terminal domain
- Cys/C: Cysteine
- Dab(β-OH): α, γ-diamino-β-hydroxybutyric acid
- Dbt: α, δ -diaminobutane
- DC: Decoding center
- ddNTP: Dideoxynucleoside triphosphate
- DESeq2: Differential Expression analysis for RNA-Seq data version 2
- Dha: α, β-dehydroarginine
- Dhl: δ-hydroxylysine
- DNA: Deoxyribonucleic acid
- dNTP: Deoxynucleoside triphosphate
- E-site: Exit, deaminoacyl tRNA binding site
- EC: Elongation-competent complex
- EF-G: Elongation factor G
- EF-Tu: Elongation factor thermo-unstable
- FDA: Food and Drug Administration
- Fig.: Figure
- fMet-tRNA or tRNAi or fMet-tRNA$_f^{Met}$: formyl-methionyl-initiator tRNA

- fMet/m: N-formylmethionine
- G: Guanine
- GAC: GTPase activating center
- GDP: Guanosine diphosphate
- Gln/Q: Glutamine
- Glu/E: Glutamate or Glutamic acid
- Gly/G: Glycine
- GTP: Guanosine triphosphate
- GTPase: Guanosine triphosphatase
- GTPγS: Guanosine 5'-O-[gamma-thio]triphosphate
- HEPES: 4-(2-hydroxyethyl)-1- piperazineethanesulfonic acid
- His/H: Histidine
- IC: Initiation complex
- IC_{50}: Half-maximal inhibitory concentration
- IF - Initiation factor
- Ile/I: Isoleucine
- iTP-Seq: Inverse toeprinting coupled with next-generation sequencing
- Leu/L: Leucine
- LSU: Large subunit
- Lys/K: Lysine
- MDR: Multidrug-resistant
- Met/M: Methionine
- MIC: Minimal inhibitory concentration
- mRNA: Messenger RNA
- NGS: Next generation sequencing
- NPET: Nascent peptide exit tunnel
- nt: Nucleotide
- NTD: N-terminal domain
- NTP: Nucleoside triphosphate
- ODL: Odilorhabdin
- ORF: Open reading frame
- Orn: Ornithine
- P-site: Peptidyl-tRNA binding site
- PAGE: Polyacrylamide gel electrophoresis
- PCR: Polymerase chain reaction
- PDB: Protein Data Bank
- Phe/F: Phenylalanine
- PHENIX: Python-based Hierarchical ENvironment for Integrated Xtallography
- Pi: Inorganic phosphate
- PIC: Pre-initiation complex
- Pro/P: Proline
- PTC: Peptidyl transferase center

- PyDESeq2: Python Differential Expression analysis using DESeq2
- RBS: Ribosome binding site
- RF: Release factor
- RNA: Ribonucleic acid
- RNase: Ribonuclease
- RRF: Ribosome recycling factor
- rRNA: Ribosomal RNA
- S: Svedberg
- SD: Shine-Dalgarno
- Ser/S: Serine
- smFRET: Single-molecule Förster resonance energy transfer
- SPA: Single particle analysis
- SRL: Sarcin-ricin loop
- SSU: Small subunit
- T: Thymine
- TBE: Tris-borate-EDTA
- Thr/T: Threonine
- TIG: Tigecycline
- tRNA: Transfer RNA
- Trp/W: Tryptophan
- Tyr/Y: Tyrosine
- U: Uracil
- uORF: Upstream ORF
- UTR: Untranslated region
- Val/V: Valine
- Vf: Final volume
- WHO: World Health Organization
- Δ: Deletion

List of Tables

Table 1: WHO Bacterial Priority Pathogens List 2024 23
Table 2: Nomenclature of tRNAs based on ribosomal positions during translation 56
Table 3: Cryo-EM data collection and processing details 130
Table 4: Distribution of 27 ribosomal 3D classes into functional states by composition of tRNA and associated elongation factors 131
Table 5: Architecture of monitoring bases of the decoding center and corresponding 30S conformation in published time-resolved cryo-EM PRE-C structures (Loveland et al. 2020) 146
Table 6: Architecture of monitoring bases of the decoding center and corresponding 30S conformation in sub-states C1-C10 (this work) 146

Supplementary Tables:

Supplementary Table 7: List of oligonucleotides used for iTP-Seq and toeprinting 200
Supplementary Table 8: List of TruSeq index sequences used in iTP-Seq for each replicate 201

List of Figures

Figure 1: Overview of the discovery of antibiotics and their clinical introduction 21
Figure 2: Structural architecture of the bacterial ribosome 27
Figure 3: Overview of the steps of translation initiation leading to the formation of the 70S initiation complex 30
Figure 4: Models for proton transfer during peptide bond formation 33
Figure 5: Overview of the bacterial translation cycle 36
Figure 6: Overview of representative antibiotics targeting the bacterial ribosome 37
Figure 7: The genetic code 39
Figure 8: Secondary and tertiary structures of tRNA 41
Figure 9: Decoding center arrangements during initial selection 47
Figure 10: Overview of decoding 50
Figure 11: Overview of translocation 56
Figure 12: Principle of classical toeprinting 68
Figure 13: Comparison of toeprinting and ribosome profiling techniques 70
Figure 14: Overview of the experimental steps of iTP-Seq 72
Figure 15: Schematic overview of the cryo-EM workflow for NOSO-502-stalled *E. coli* 70S ribosomal complexes 75
Figure 16: Odilorhabdin production by entomopathogenic bacteria 92
Figure 17: Odilorhabdin biosynthetic gene cluster in *Xenorhabdus nematophila* 94
Figure 18: Chemical structures of odilorhabdin lead compounds 96
Figure 19: NOSO-95179 bound to the *T. thermophilus* 70S ribosome 99
Figure 20: Chemical structures of NOSO-502 and NOSO-96624 101
Figure 21: Half-maximal inhibitory concentrations (IC_{50}) of NOSO-502 and NOSO-96624 105
Figure 22: Distribution of obtained sequencing reads 107
Figure 23: Proportion of sequencing reads retained after data processing and quality control 108
Figure 24: Schematic illustration of the nomenclature applied to the different ribosome sites on an inverse toeprint 108
Figure 25: Heatmap grid representing the di-amino acid motifs enriched across -2, E, P and A-sites in the presence of 0.4µM of NOSO-502 111
Figure 26: Heatmap grid representing the di-amino acid motifs enriched across -2, E, P and A-sites in the presence of 0.3µM of NOSO-96624 112

Figure 27: Heatmap grid representing the di-amino acid motifs enriched across -2, E, P and A-sites in the presence of 40µM of NOSO-502 115
Figure 28: Heatmap grid representing the di-amino acid motifs enriched across -2, E, P and A-sites in the presence of 40µM of NOSO-96624 116
Figure 29: Combinatorial sequence preferences across -2, E, P and A-sites during odilorhabdin-induced translation arrest 118
Figure 30: Heatmaps representing per-position codon enrichment across -2, E, P and A-sites in the presence of NOSO-502 and NOSO-96624 at low and high concentrations 123
Figure 31: Stalling patterns of odilorhabdin-bound ribosomal complexes on selected arrest motifs 127
Figure 32: Cryo-EM data processing workflow using CryoSPARC for *E. coli* mDDP-70S-NOSO-502 40µM complexes 129
Figure 33: Bar plot showing the distribution of particles in each of the 27 ribosomal 3D classes 131
Figure 34: Conformational landscape of 9 functional states of the NOSO-502-bound 70S *E. coli* ribosome across the translation cycle 133
Figure 35: Analysis of density features for mRNA and tRNA sequence assignment 135
Figure 36: Analysis of peptide density on tRNAs in different sub-states 137
Figure 37: Structural and conformational features of functional state A 139
Figure 38: Structural and conformational features of functional state B 142
Figure 39: Structural and conformational features of functional state C, Part 1 145
Figure 40: Structural and conformational features of functional state C, Part 2 147
Figure 41: Structural and conformational features of functional states D and E 149
Figure 42: Structural and conformational features of functional state F 151
Figure 43: Structural and conformational features of functional states G, H and I 153
Figure 44: Conformational landscape and particle distribution of NOSO-502-bound stalled ribosomal complexes 159
Figure 45: Binding site, chemical structures and initiation-targeting mechanism of tigecycline 166
Figure 46: Distribution of obtained sequencing reads 170
Figure 47: Proportion of sequencing reads retained after data processing and quality control 171

Figure 48: Heatmap grid representing the di-amino acid motifs enriched across -2, E, P and A-sites in the presence of 5µM of tigecycline _____ 173
Figure 49: Heatmap grid representing the di-amino acid motifs enriched across -2, E, P and A-sites in the presence of 50µM of tigecycline _____ 174
Figure 50: Heatmap grid representing the di-amino acid motifs enriched across -2, E, P and A-sites in the presence of 500µM of tigecycline _____ 175
Figure 51: Combinatorial sequence preferences across ribosomal sites during tigecycline-induced translation arrest _____ 176
Figure 52: Heatmaps representing per-position codon enrichment across -2, E, P and A-sites in the presence of 5µM, 50µM, and 500µM tigecycline _____ 178
Figure 53: A. Heatmap representing amino acid enrichment in the A-site in ribosomes stalled during initiation with fMet in the P-site; B. Combinatorial nucleotide sequence preferences in the P and A-sites during tigecycline-induced translation arrest at initiation _____ 179

Supplementary Figures:

Supplementary Figure 54: A. Schematic of the DNA template library sequence used for iTP-Seq experiments; B. TBE-Urea-polyacrylamide gel (9%) of the (NNN)15 mRNA transcript; C. Dot blot for quality control of mRNA biotinylation. _____ 188
Supplementary Figure 55: Gel excision strategy for iTP-Seq library preparation for next-generation sequencing _____ 188
Supplementary Figure 56: Stalling patterns of odilorhabdin-bound ribosomal complexes on screened arrest motifs _____ 189
Supplementary Figure 57: Cryo-EM maps of the 27 reconstructed sub-states colored by local resolution _____ 190
Supplementary Figure 58: Fourier Shell Correlation (FSC) curves of the 27 reconstructed sub-states _____ 194
Supplementary Figure 59: Heatmap grid representing the di-amino acid motifs enriched across -2, E, P and A-sites in the presence of 0.05µM of tigecycline _____ 198
Supplementary Figure 60: Heatmap grid representing the di-amino acid motifs enriched across -2, E, P and A-sites in the presence of 0.5µM of tigecycline _____ 199
Supplementary Figure 61: Plasmid map of pIVEX2.3d-luc _____ 202

Preface

Antibiotics are a cornerstone of modern medicine; however, the accelerating emergence of antibiotic-resistant bacterial infections has become a critical global health threat. Antimicrobial resistance (AMR), which extends beyond antibiotic resistance but is often used synonymously, is projected to result in 39.1 million direct deaths and 169 million associated deaths worldwide between 2025 and 2050 (Naghavi et al. 2024). Although antibiotic stewardship, including the selection of the optimal drug regimen, dosing, duration of therapy and route of administration, is of central importance in mitigating the global burden of the "overlooked pandemic" of antibiotic resistance (Barlam et al. 2016; Laxminarayan 2022), the exploration and development of novel antibacterials, or improving existing ones to bypass resistance, is also essential. However, our ability to optimize these treatments is often limited by an incomplete understanding of their molecular mechanics. To effectively bypass resistance, it is important to re-examine the exact mechanisms of action of existing drugs.

In a bacterial cell, the major targets of the most commonly known antibiotics include one or more of the processes of DNA uncoiling, RNA synthesis, cell wall synthesis, cell membrane permeability maintenance, folate synthesis, or protein synthesis (reviewed in Davies and Davies 2010; Hutchings et al. 2019). Antibiotics that target the prokaryotic protein synthesis machinery, i.e., the bacterial ribosome and translation, constitute more than half of all antibiotics used in the treatment of infectious diseases (Wilson 2014). While the binding sites and mechanisms of action of several of these ribosomal antibiotics have been deciphered (reviewed in Lin et al. 2018), there was a long-standing assumption that these drugs inhibit translation with equal efficiency at every codon of a gene. However, this concept has been challenged in recent years, and the field of studying context-dependent ribosomal antibiotics has made rapid progress (reviewed in Vázquez-Laslop and Mankin 2018). Context-dependence is rooted in the shifting molecular landscape of the translating ribosome – as it moves along the mRNA, the specific combinations of codon sequences, tRNAs, and amino acids, each with varied physicochemical and kinetic properties, constantly redefine the local environment in which translation, and hence antibiotics, must function. Thus, when the bacterial proteome was discovered to be selectively remodeled by context-specific macrolide antibiotics (Kannan

et al. 2012), inhibiting only the translation of sequences with certain motifs and not others, this opened the door to a novel approach to drug design, based on programmed drug-induced translation arrest. Technological developments in sequencing technologies (e.g., ribosome profiling, inverse toeprinting) alongside high-resolution structures (crystallographic and cryo-EM reconstructions) of antibiotic-ribosome complexes have eventually shown that several classes of antibiotics inhibit translation in a context-specific way (e.g., chloramphenicol, oxazolidinones, ketolides, orthosomycins, kasugamycin, tetracenomycins etc.) (Choi et al. 2020; Tsai et al. 2022; Syroegin et al. 2022; Beckert et al. 2021; Mangano et al. 2022; Y. Zhang et al. 2022; Leroy et al. 2023). Several of the sequences causing drug-dependent ribosomal stalling are involved in the regulation of antibiotic resistance gene expression, underlining the importance of how studying context-specific antibiotic action can help to understand and target species-specific protein synthesis pathways in pathogenic, antibiotic-resistant strains (Vázquez-Laslop and Mankin 2018). At the onset of this work, most characterized context-specific drugs were known to bind at the nascent peptide exit tunnel (NPET) and inhibit peptide bond formation between specific amino acids. It was not sufficiently clear whether similar selectivity exists for drugs targeting other functional regions of the ribosome. To bridge this gap and expand our understanding of context-specific inhibition, I investigated two antibiotics that act at the decoding center on the 30S ribosomal subunit: odilorhabdins and tigecycline. Odilorhabdins represent a relatively novel class of peptide antibiotics with reported activity against several multidrug-resistant pathogens, while tigecycline is a third-generation glycylcycline derived from the tetracycline class. I used a combination of biochemical (high-throughput inverse toeprinting and classical toeprinting) and structural biology (single-particle cryo-EM analysis) techniques to study their sequence-dependent mechanisms of action. This thesis is organized into five chapters. Chapter 1 introduces the era of antibiotic resistance and the bacterial ribosome, focusing on the decoding center as a drug target to inhibit the decoding and translocation steps of translation elongation. Chapter 2 details the experimental protocols and techniques employed throughout this research. Chapters 3 and 4 present the results for odilorhabdins and tigecycline, respectively, detailing their sequence-specific modes of action. Finally, Chapter 5 summarizes the findings and discusses the future implications of this work for antimicrobial development.

Chapter 1

Introduction

1.1. Antibiotic discovery: the Golden Age, the resistance crisis and the need for innovation

The use of rudimentary antimicrobials to treat infectious diseases dates back to early human civilizations; for example, the Ebers Papyrus (c. 1550 BC) describes the use of moldy bread and medicinal soil as therapeutic agents (Haas 1999). However, the advent of modern antimicrobial chemotherapy is generally attributed to Paul Ehrlich, who introduced arsphenamine (Salvarsan) for the treatment of *Treponema pallidum* (Ehrlich 1913). The discovery of penicillin by Alexander Fleming (Fleming 1929) from cultures of the *Penicillium* mold marked a pivotal scientific breakthrough, although its widespread clinical use followed only in the subsequent decade. Salvarsan was superseded by sulfonamides (e.g., Prontosil), the first synthetic broad-spectrum antibacterials to be used clinically (Domagk 1935). Building on these advances, the late 1930s saw the emergence of systematic efforts to identify microorganisms as sources of antibacterial compounds. Pioneering work by Selman Waksman led to the discovery of several bioactive secondary metabolites from soil-dwelling *Actinomycetes*, such as neomycin and streptomycin, the latter representing the first active treatment against tuberculosis (Waksman and Woodruff 1940; Waksman and Woodruff 1941; Waksman and Schatz 1945). During this period, Waksman formally introduced the term 'antibiotic' - derived from the Greek words 'anti' (against) and 'biotikos' (concerning life) - into literature by naming a new species of soil bacteria, *Actinomyces antibioticus*, antagonistic to pathogenic and non-pathogenic bacteria (Waksman and Woodruff 1941). Phenotypic screening of soil microorganisms, including *Actinomycetes*, as well as other bacteria and fungi, enabled the identification of numerous natural products and marked the onset of the “Golden Age” of antibiotic discovery (1940s–1960s). This period was characterized by the rapid discovery and clinical introduction of a wide range of antibiotic classes, both natural and synthetic, many of which remain in use today (Davies and Davies 2010; Hutchings et al. 2019) (Fig. 1).

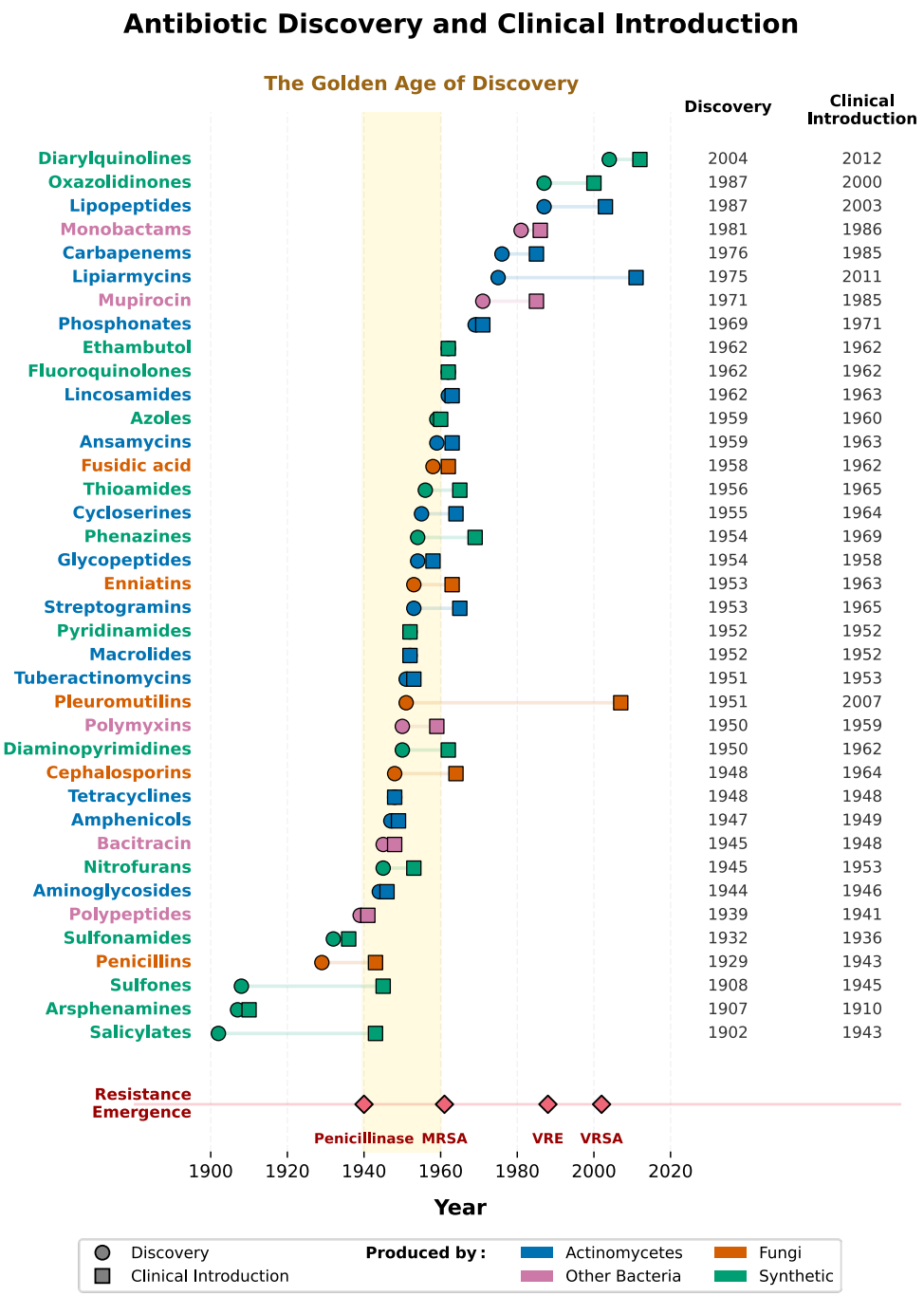

Figure 1: Overview of the discovery of antibiotics and their clinical introduction. The Golden Age of discovery of antibiotics (1940s-1960s) saw an exponential rise in the discovery and clinical introduction of the most common classes of antibiotics known today (Data from Hutchings et al. 2019). Also marked in red are the first reported years of emergence of resistance to penicillin (penicillinase enzyme, Abraham and Chain 1940), methicillin-resistant *Staphylococcus aureus* (MRSA, Jevons 1961), vancomycin-resistant *Enterococcus faecium* (VRE, Leclercq et al. 1988) and vancomycin-resistant *Staphylococcus aureus* (VRSA, Quirk 2002) – often considered key resistance emergence events to commonly used antibiotics.

The success of the Golden Age was however, accompanied by widespread and often excessive use, which quickly selected for resistant bacterial strains. For example, mutant strains of *Mycobacterium tuberculosis* resistant to therapeutic concentrations of streptomycin were reported as early as 1948 (Crofton and Mitchison 1948), merely four years after its introduction in 1944 for pulmonary tuberculosis, necessitating the shift to combination therapy. Similar patterns emerged across other bacterial species (reviewed in Davies and Davies 2010; Hutchings et al. 2019), and by the 1970s, there was a marked decline in the introduction of new antibiotics. This was driven by both the diminishing returns of soil-screening approaches, as most readily discoverable compounds had already been identified, alongside emerging economic disincentives, as the rapid onset of resistance undermined the commercial lifespan of new drugs even before they reached the market. This imbalance between sustainable antibiotic consumption and reduced innovation further intensified selective pressure for the emergence and spread of resistant bacterial strains.

Research on intrinsic mechanisms of antibiotic resistance identified that bacteria possess the ability to inactivate or degrade the drug, modify or mutate the drug target, impair influx and promote active efflux of the drug, and/or overproduce a target mimic, as has been extensively reviewed in literature (e.g., Cox and Wright 2013; Wilson 2014; Lin et al. 2018). While bacteria can have intrinsic resistance to certain antibiotics, they can also acquire antibiotic resistance genes via horizontal gene transfer from other resistant bacterial species, usually carried on mobile elements such as transposons, plasmids, or integrons (Lin et al. 2018). This benefits bacteria in the arms race against antibiotics, giving rise to strains that are resistant to multiple classes of antibiotics, termed multidrug-resistant (MDR) bacteria - a major challenge for effective treatment. Recognizing the urgency of this issue, the World Health Organization (WHO) published a bacterial priority pathogens list (BPPL) in 2017 identifying antibiotic-resistant pathogens that demand immediate attention for new drug development. The most recent version of the BPPL from 2024 categorizes pathogens into three tiers – critical, high and medium groups - based on how urgently we need new antibiotics to treat them, as listed in Table 1. Among the most clinically concerning among them are the ESKAPEE pathogens: *Enterococcus faecium, Staphylococcus aureus, Klebsiella pneumoniae, Acinetobacter baumannii, Pseudomonas aeruginosa, Enterobacter species, and Escherichia coli*. The

acronym “ESKAPEE” highlights their capacity to evade the effects of standard antibiotics, including broad-spectrum β-lactams, carbapenems, glycopeptides, fluoroquinolones, and aminoglycosides, rendering them primarily responsible for life-threatening infections in hospital settings (World Health Organization 2024).

Table 1: WHO Bacterial Priority Pathogens List 2024

Critical Group	High Group	Medium Group
• Carbapenem-resistant ***Acinetobacter baumannii*** • Third-generation cephalosporin-resistant **Enterobacterales** • Carbapenem-resistant **Enterobacterales** • Rifampicin-resistant ***Mycobacterium tuberculosis***	• Fluoroquinolone-resistant ***Salmonella typhi*** • Fluoroquinolone-resistant ***Shigella*** spp. • Vancomycin-resistant ***Enterococcus faecium*** • Carbapenem-resistant ***Pseudomonas aeruginosa*** • Fluoroquinolone-resistant non-typhoidal ***Salmonella*** • Third-generation cephalosporin and/or fluoroquinolone-resistant ***Neisseria gonorrhoeae*** • Methicillin-resistant ***Staphylococcus aureus***	• Macrolide-resistant Group A **Streptococci** • Macrolide-resistant ***Streptococcus pneumoniae*** • Ampicillin-resistant ***Haemophilus influenzae*** • Penicillin-resistant Group B **Streptococci**

Addressing the WHO priority pathogens requires a robust pipeline of new antibiotics; however, despite this urgent clinical need, the pharmaceutical industry has largely withdrawn investment from antibiotic research and development due to several economic reasons. For example, the rapid spread of AMR can significantly shorten the effective market life of a drug, even before it is commercially released. Additionally, any successful new antibiotic coming out of industrial R&D, with a unique mode of action against MDR pathogens, is often restricted as a treatment of last resort to preserve its efficacy and delay resistance, meaning that the most clinically valuable drugs are intentionally kept at low sales volumes, making the traditional revenue model linking profit to the drug sales economically unviable. This has shifted the burden of discovery primarily to academic laboratories and small-to-medium enterprises (SMEs) (Årdal et al. 2018; Hutchings et al. 2019; Årdal et al. 2020; Bertagnolio et al. 2024; Naghavi et al. 2024). While alternative therapeutic modalities such as phage therapy, antimicrobial peptides, and targeted antisense oligonucleotides (reviewed, e.g., in MacNair et al. 2024; Yarahmadi et al. 2025) offer promising avenues for combating resistant pathogens, most remain in preclinical or early-phase clinical development and face significant hurdles related to delivery, manufacturing scalability, regulatory approval, and cost-effectiveness. This reality underscores the continued reliance on existing antibiotic scaffolds. Ribosome-targeting antibiotics, which account for nearly half of all antibiotics in current therapeutic use (Lin et al. 2018), represent a particularly valuable class for such optimization. Indeed, between July 2017 and February 2025, among the 16 market-authorized traditional antibacterials, ribosome-targeting antibiotics inhibiting protein synthesis form the biggest class, underlining their continued clinical importance (World Health Organization 2025).

The ribosome translates genetic information from mRNA into protein with high fidelity, ensuring accurate codon recognition at its decoding center. Antibiotics that bind this region and disrupt decoding fidelity represent a promising avenue for combating resistant pathogens, as perturbations in this function can result in lethal mistranslation or stalling. My thesis investigates two such antibiotics—odilorhabdins and tigecycline—both of which target the decoding center but differ in their mechanisms and clinical profiles. Odilorhabdins are a recently discovered peptide antibiotic class (Pantel et al. 2018) whose molecular mechanism is not entirely understood. Tigecycline, a broad-spectrum glycylcycline in clinical use, is

suspected to inhibit translation in a sequence-dependent manner, though this context-dependency has not been characterized. Before diving into the findings on these drugs, I will first provide a contextual overview of ribosome architecture and the translation cycle in the next section, with emphasis on the decoding and translocation steps.

1.2. Protein synthesis in bacteria as a major antibiotic target

1.2.1. An overview of the bacterial translation machinery

The Bacterial Ribosome

The ribosome is a macromolecular ribonucleoprotein complex that serves as a molecular factory of the cell, translating genetic information encoded in messenger RNA (mRNA) into proteins. Initially described in the early 1950s as 'a small particulate component of the cytoplasm' in eukaryotic cells (Palade 1955), the ribosome received its official name in the latter half of the decade (Biophysical Society. and Roberts 1958). Bacterial ribosomes were first isolated and characterized in the late 1950s (Tissières and Watson 1958; Kurland 1960), laying the foundation for over half a century of research in 'ribosomology'.

The bacterial 70S ribosome, a 2.5-megadalton ribonucleoprotein complex, consists of two distinct subunits: the 30S small subunit (SSU) and the 50S large subunit (LSU) (Tissières and Watson 1958; Tissières et al. 1959).

The SSU comprises the 16S rRNA (1542 nucleotides in *E. coli*) and 21 ribosomal proteins (or 22 in thermophilic bacteria, which have an additional bTHX protein) (Brosius et al. 1978; Ban et al. 2014). The distinct structural landmarks of the SSU are called its head, beak, shoulder, platform, body, and spur (Fig. 2). Its interface with the LSU houses the mRNA-binding tunnel and the three tRNA-binding sites – the A or aminoacyl site (which binds the incoming aminoacyl-tRNA), the P or peptidyl site (which binds the peptidyl-tRNA), and the E or exit site (where the deacylated tRNA moves to, after peptide bond formation in the P-site). The main functional site of the SSU is the decoding center of the ribosome, which is involved in maintaining the fidelity of translation – it monitors base pairing between the codon on the mRNA and the anticodon of the incoming aminoacyl-tRNA (aa-tRNA) (Kaji and Kaji 1964;

Thompson and Stone 1977; Carter et al. 2000). The role of the decoding center has been elaborated in Section 1.2.2.

The LSU consists of the 5S rRNA (120 nucleotides in *E. coli*), 23S rRNA (2904 nucleotides in *E. coli*) and 33 ribosomal proteins (Brosius et al. 1980; Ban et al. 2014). It has an overall crown-like shape with key landmarks including the central protuberance, the L1-stalk and the mobile L7/L12-stalk. One of the major functional sites of the LSU is the peptidyl transferase center (PTC), which plays a central role in peptide bond formation between the nascent peptide on the P-site tRNA and the amino acid on the A-site tRNA (Traut and Monro 1964; Monro 1967; Maden et al. 1968). This site contains highly conserved rRNA bases which form base-pairing interactions with the universally conserved 3'-CCA ends of the acceptor stems of tRNA substrates and is notably an all-RNA catalytic site devoid of nearby ribosomal proteins, underscoring the function of the ribosome as a ribozyme (Noller et al. 1992; Samaha et al. 1995; Khaitovich et al. 1999; Ban et al. 2000; Nissen et al. 2000). The LSU further houses the GTPase activating center (GAC) which serves as the docking and activation site for translational GTPases (e.g., EF-Tu, EF-G among others), in coordination with the L7/L12 stalk and the sarcin-ricin loop (SRL) of the 23S rRNA (Sander et al. 1972; Hausner et al. 1987; Moazed et al. 1988). Its concerted mechanism of action during translation elongation is elaborated in Section 1.2.2.

The nascent peptide exit tunnel (NPET), a ~100 Å tunnel that guides the nascent polypeptides emerging from the PTC to the cytosol, and traverses the LSU, is also an important site (Bernabeu and Lake 1982). Its tunnel walls are formed primarily by conserved 23S rRNA residues and the loops of proteins uL4, uL22, uL23, and uL24 (Ban et al. 2000; Nissen et al. 2000). The NPET serves as a dynamic sensory environment – specific nascent peptide motifs, often in conjunction with small-molecule ligands or antibiotics, can interact with the tunnel residues to induce translational stalling. This capacity for peptide-mediated arrest underscores the role of the ribosome as a metabolic sensor that can modulate gene expression in response to the cellular environment (reviewed in Ito and Chiba 2013; Seip and Innis 2016; Bhattacharya et al. 2024).

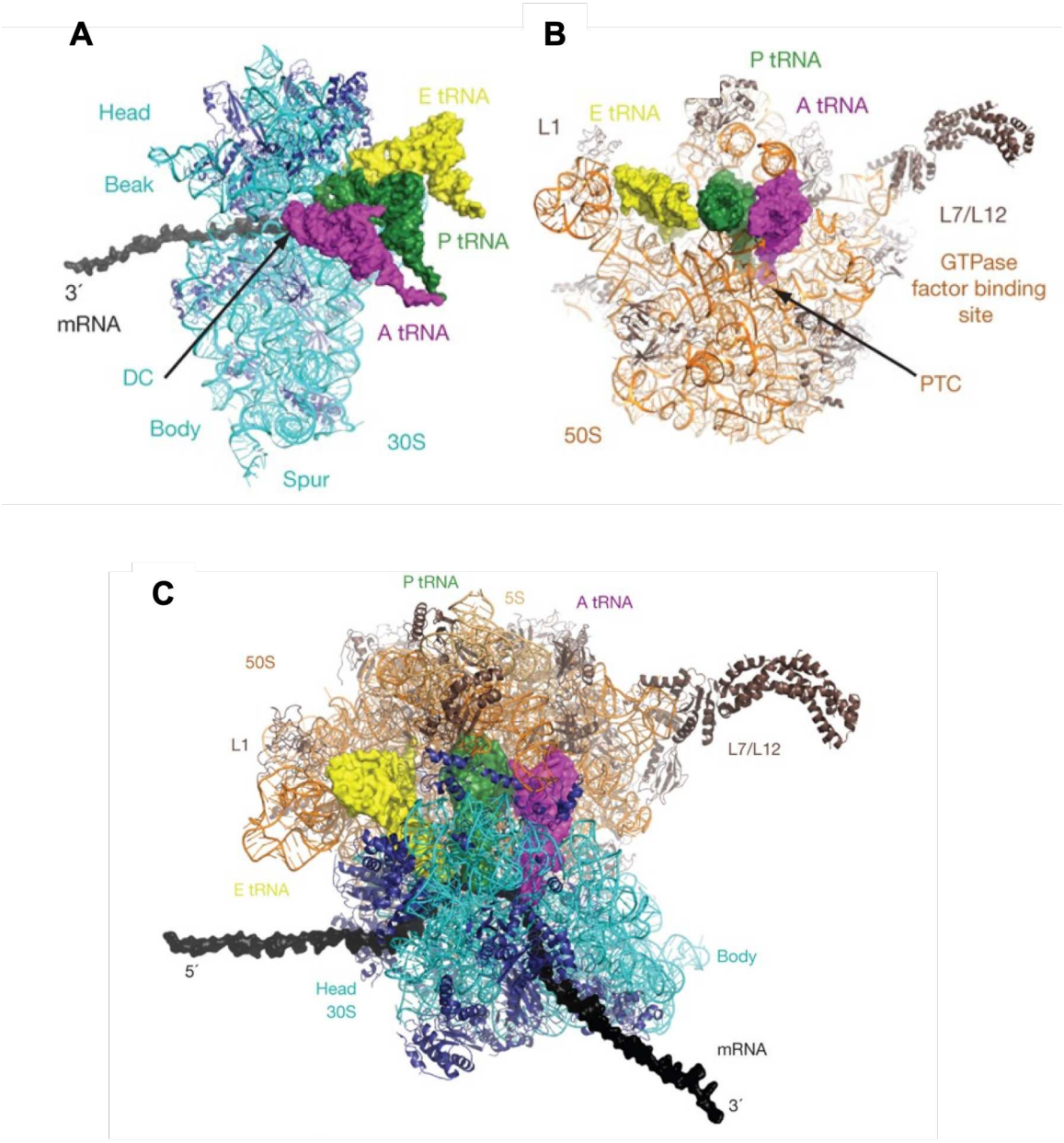

Figure 2: Structural architecture of the bacterial ribosome. (A) The architecture of the small 30S subunit with its head, beak, body and spur domains are shown, along with the mRNA and tRNA binding regions and the location of the decoding center (DC), the major functional site of the small subunit. The platform and shoulder domains of the 30S subunit, in this view, are hidden behind the tRNA. (B) The architecture of the large 50S subunit is shown with the key landmarks – central protuberance (CP), L1 and L7/L12 stalks. The location of the peptidyl transferase center (PTC) and the GTPase factor binding site are also shown, along with the tRNA binding sites. (C) The 50S and 30S subunits join to form the 70S ribosome. Adapted from Schmeing and Ramakrishnan 2009, with permission from Springer Nature (License No. 6323271481792).

The Bacterial Translation Cycle

Translation proceeds through four major stages: initiation, elongation, termination, and ribosome recycling, each of which is briefly described as follows.

Translation Initiation

The first step of translation, which is also the rate-limiting step, is initiation, where the ribosome recruits an mRNA and selects the start codon of the open reading frame (ORF). In prokaryotes, the translation start codon canonically corresponds to the methionine codon AUG, while infrequent initiation from GUG, UUG, and CUG can also occur (O'Connor et al. 2001; Ma et al. 2002). Initiation requires a specialized initiator tRNA (tRNAi), which is structurally distinct from elongator Met-tRNAs. In bacteria, this tRNA is specifically modified to carry a formyl-methionine group; hence, it is also referred to as fMet-tRNAi (Marcker and Sanger 1964; Clark and Marcker 1966; Leder and Nau 1967). Although the formyl group from the tRNAi is enzymatically removed co-translationally (Adams 1968; Sherman et al. 1985), it is absent in elongator Met-tRNAs – this selectivity of formylation is due to unique sequence features of the tRNAi in its anticodon, acceptor, and dihydrouridine stem-loops. This formylation also allows tRNAi to be recognised by the initiation factor IF2 (and not the elongation factor EF-Tu), targeting it to the ribosomal P-site (and not the A-site where elongator aminoacyl tRNAs are usually targeted) (Varshney and RajBhandary 1992; Varshney et al. 1993; Wu and RajBhandary 1997; Schmitt et al. 1998; Mayer et al. 2001; Barraud et al. 2008).

The SSU, initiation factors IF1, IF2, IF3 and the tRNAi form a labile 30S preinitiation complex (30S PIC) (Fig. 3) – while the factors can bind to the SSU independently of each other, the kinetically preferred sequence of factor association is IF3, IF2, then IF1 (Milón et al. 2012). The N-terminal and C-terminal domains (NTD and CTD, respectively) of IF3 align with the E- and P-sites of the SSU, respectively, along the mRNA path (Grunberg-Manago et al. 1975; Grigoriadou et al. 2007), while the GTPase IF2 and IF1 bind the SSU A-site where IF1 bridges IF2 and IF3 (Carter et al. 2000; Antoun et al. 2006a, 2006b; Simonetti et al. 2008; Julián et al. 2011). To initiate translation, the SSU must be accurately positioned on the mRNA. This is

facilitated by the Shine-Dalgarno (SD) sequence, an AG-rich ribosome binding site (RBS) located 6-7 nucleotides upstream of the initiation codon, which base-pairs with the CU-rich anti-SD sequence located at the 3' tail of the 16S rRNA of the SSU, forming a stable, non-covalent complex that facilitates the annealing of the 30S subunit (Shine and Dalgarno 1974; Steitz and Jakes 1975; Steven Ringquist et al. 1992). Here, IF3 plays a central role in initiation fidelity by discriminating against elongator tRNAs. Initially, the 30S PIC is in an unlocked or open intermediate where codon-anticodon base pairing has not yet occurred – in the absence of fMet-tRNAi, the CTD of IF3 shields the AUG codon in the P-site and interacts with IF1, which blocks the A-site. Three G–C pairs in the anticodon stem of fMet-tRNAi are important for selecting and stabilizing the tRNA via interactions with G1338 and A1339 at the head of the 30S subunit (Lancaster and Noller 2005; Korostelev et al. 2006; Hussain et al. 2016). Cognate recognition of the AUG codon induces a "latching" of the 30S head toward the body by a ∼10Å head tilt (at G1338), and shifts the tRNA, moving the CCA-fMet end by ∼25Å toward the 30S body, facilitating contact with IF2. This stabilizes the fMet-tRNAi in the P-site, forming the locked or closed 30S initiation complex (30S IC), and is accompanied by the dissociation of the IF3 CTD from the AUG codon and from IF1 (Antoun et al. 2006a, 2006b; Julián et al. 2011; Goyal et al. 2015; Hussain et al. 2016; López-Alonso et al. 2016). IF2 then coordinates the binding of the 50S subunit to form the 70S initiation complex (70S IC). GTP hydrolysis then allows dissociation of IF2 and formation of the elongation-competent 70S complex (70S EC), in which the fMet moiety is in the PTC, and the mRNA exposes the first elongation codon in the A-site (Nomura et al. 1967; Fabbretti et al. 2007; Marshall et al. 2009; Julián et al. 2011; B. Chen et al. 2015; Goyal et al. 2015; Liu and Fredrick 2015; MacDougall and Gonzalez 2015; Goyal et al. 2017). Subunit joining with IF2 to form the 70S IC involves partial head swivel and partial subunit rotation (∼4°), and upon IF2 dissociation, the ribosome adopts a non-rotated 70S EC conformation ready to bind the first elongator tRNA (Ling and Ermolenko 2015; Kaledhonkar et al. 2019).

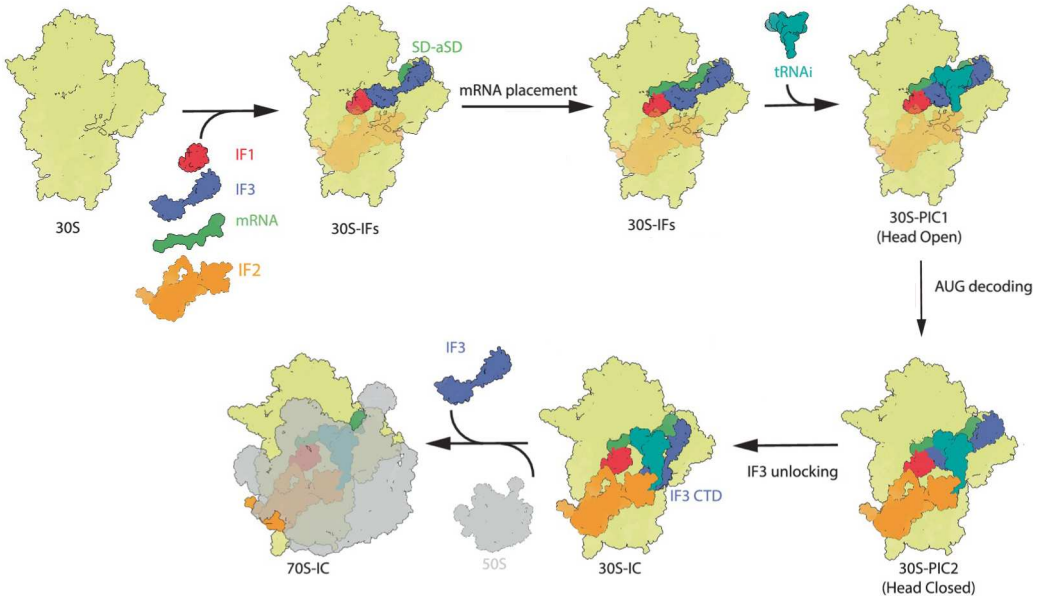

Figure 3: Overview of the steps of translation initiation leading to the formation of the 70S initiation complex. As described in the text, translation initiation involves the joining of the 30S subunit with the mRNA and initiation factors (IFs) 1, 2 and 3. Upon recognition of the Shine-Dalgarno (SD) sequence of the mRNA by the anti-Shine-Dalgarno (aSD) sequence of the 16S rRNA of the 30S subunit and subsequent mRNA placement, the initiator fMet-tRNA (tRNAi) is recruited, achieving the pre-initiation complex (PIC) with the 30S head in an open conformation. Upon successful codon-anticodon interaction between the start codon and the tRNAi, the 30S head adopts a closed conformation. This leads to the dissociation of the C-terminal domain of the IF3 (IF3-CTD) from the P-site, forming the 30S initiation complex (30S-IC). Subsequently, the 50S subunit joins the 30S-IC, leading to the formation of the 70S initiation complex (70S-IC), which is then ready to be matured into a 70S elongation-competent complex (70S-EC). Adapted from (Safdari et al. 2025). Licensed under CC BY 4.0 (https://creativecommons.org/licenses/by/4.0/).

Among fully sequenced prokaryotic genomes, the number of Shine-Dalgarno-led genes varies from ~12% to 90%, suggesting a significant number of non-SD-led mRNAs (Chang et al. 2006). For translation initiation, they rely on their 5' UTR, which is usually unfolded, and the AUG start codon resides in a single-stranded mRNA region close to the 5' end of the mRNA; hence, the local absence of secondary structure permits translation of mRNAs (Krishnan et al. 2010; Scharff et al. 2011). Another group of non-SD-led mRNAs comprises leaderless mRNAs that lack a 5' UTR (Grill et al. 2000; Vesper et al. 2011). Translation initiation in such cases is facilitated by direct binding to 70S ribosomes through an AUG start codon positioned at the 5' end of the mRNA, a process assisted by initiation factors IF2 and IF3 (Grill et al. 2000;

Krishnan et al. 2010; Yamamoto et al. 2016). The efficiency of translation initiation is governed by the specific initiation codon used, the mRNA secondary structure, and the presence of A/U-rich elements. A critical player in this process is the ribosomal protein bS1, which acts as a dynamic RNA-binding agent that unfolds structured mRNAs and helps position transcripts that lack strong SD sequences, ensuring they are correctly aligned for protein synthesis (Ringquist et al. 1995; Duval et al. 2013, 2015; Byrgazov et al. 2015).

Translation Elongation

Translation elongation is the central step of protein synthesis, involving a periodic repetition of three steps, as the ribosome moves along amino acid-encoding codons on the mRNA, until it reaches a stop codon. Elongation proceeds with an average of 12–21 amino acids incorporated into the nascent peptide per second in *E. coli* (Young and Bremer 1976; Bremer and Dennis 2008). The incorporation of one amino acid into the nascent protein can be described as an independent cycle, involving the following three steps:

- **Decoding:** This is the step where the ribosome recognizes an aminoacyl-tRNA (aa-tRNA) cognate to the A-site codon and rejects noncognate aa-tRNAs. Briefly, elongation factor thermounstable (EF-Tu) forms a ternary complex with GTP and a cognate aa-tRNA, delivering it to the A-site in a deformed high-energy A/T state. During the process of decoding, the ribosome monitors the base-pairing interaction between the mRNA codon and the tRNA anticodon in the A-site, ensuring that only tRNAs bearing the correct amino acid are accommodated. Cognate codon recognition then leads to a rapid hydrolysis of the GTP on EF-Tu, leading to its subsequent removal as EF-Tu-GDP (Rodnina et al. 1996; Valle et al. 2003). This relaxes the distorted conformation of the aa-tRNA, accommodating its 3’ end or acceptor arm into the A-site of the ribosome, in the A/A state (Moazed and Noller 1989; Agirrezabala et al. 2008). Another elongation factor EF-Ts (thermostable), then regenerates EF-Tu-GTP for subsequent elongation cycles by exchanging the GDP for GTP (Weissbach et al. 1970; Wieden et al. 2002). This step is crucial in maintaining translation fidelity and is a major antibiotic target. Section 1.2.2 provides a more detailed overview of this step.

- **Peptide bond formation:** Once the incoming cognate aa-tRNA is accommodated in the A-site, the ribosome catalyses the formation of a peptide bond between the A-site aa-tRNA and the P-site tRNA. This reaction either involves the initiator tRNAi (for the first peptide bond), or a peptidyl tRNA (during subsequent elongation cycles), resulting in a peptidyl-tRNA in the A-site and deacylated tRNA in the P-site. This step is catalyzed at the PTC of the 50S subunit, an environment composed primarily of RNA. The proximal ribosomal protein, bL27, approaches only within 8–10 Å of the reaction site, underscoring the role of the ribosome as a ribozyme with RNA being the major contributor to catalysis (Nissen et al. 2000; Voorhees et al. 2009).

  The chemistry of peptide bond formation is initiated by a nucleophilic attack of the α-amino group of the A-site aa-tRNA on the carbonyl carbon of the ester bond in the P-site peptidyl-tRNA. Compared to model substrates in solution, the ribosomal environment accelerates this reaction by about 10^7-fold. This catalysis is largely entropic, as the ribosome facilitates the reaction by precisely positioning tRNA residues, ordering water molecules, and providing electrostatic shielding (Sievers et al. 2004; P. K. Sharma et al. 2005; Wallin and Åqvist 2010). A critical aspect of this reaction is the movement of at least two protons within the PTC. Currently, two primary models account for this proton transfer. The first model, referred to as the "eight-membered proton shuttle", suggests that the attack of the α-amine group on the ester carbonyl carbon results in an eight-membered transition state. A proton from the α-amine group is received by the 2'-OH of A76 of the peptidyl-tRNA, which simultaneously donates its own proton to the carbonyl oxygen via an adjacent water molecule (Wallin and Åqvist 2010; Kuhlenkoetter et al. 2011; Zaher et al. 2011) (Fig. 4). Initially, this was considered a six-membered proton shuttle without considering the contribution of the water molecule (Schmeing et al. 2005). The second model, referred to as the "proton wire" model (Polikanov et al. 2014) is based on structural evidence of three trapped water molecules within the PTC, and also shows the involvement of the 2'-OH of A2451 of the 23S rRNA (Erlacher et al. 2005, 2006; Lang et al. 2008). According to this model, hydrogen bonding between the 2'OH of A76 of the P-site tRNA and the 2'OH of A2451 can allow the transfer of three protons through three water molecules. One of the water molecules (W1 in Fig. 4) residing in the PTC is proposed to be

partially negatively charged, coordinated by the N-terminus α-amino group of bL27, the 2'OH of A2451, the base of the 23S rRNA residue A2602, and the 5'-phosphate oxygen of A76 of the A-site tRNA. The proton liberated from the attacking amino group of the aminoacyl tRNA can thus be transferred through the hydrogen bond network until it reaches the water molecule W1 (Polikanov et al. 2014). Both models face ongoing scrutiny. While the proton wire model accounts for the hydration in the PTC, studies showing that the deletion of bL27 does not abolish peptide bond formation suggest that the role of the protein may not be strictly catalytic (Maracci et al. 2015). Conversely, the proton shuttle model is based on 50S subunit structures, not mimicking a biologically relevant complex. It has thus been criticized for suboptimal stereochemistry and for neglecting the role of the conserved A2451 residue (Polikanov et al. 2014).

Following peptide bond formation, the ribosome carries a deacylated tRNA in the P-site and a newly formed peptidyl-tRNA in the A-site. To empty the A-site for the next incoming aminoacyl-tRNA, the complex proceeds to the third step of elongation – translocation.

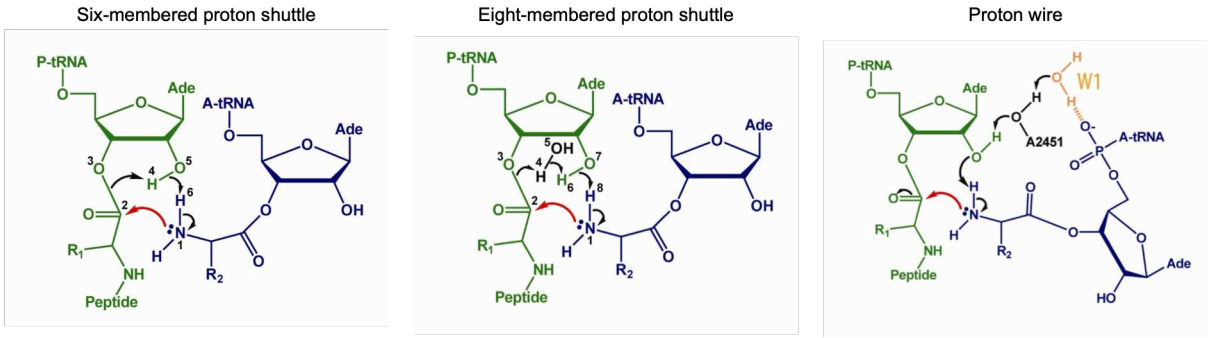

Figure 4: Models for proton transfer during peptide bond formation. Reaction mechanisms are shown for the six-membered and eight-membered proton shuttle and proton wire models. The nucleophilic attack is depicted by red arrows. Adapted from (Polikanov et al. 2014), with permission from Springer Nature (License No. 6323280118726).

- **tRNA-mRNA translocation:** In this final step of elongation, the A-site peptidyl tRNA and P-site deacylated tRNA translocate, by the length of exactly three nucleotides or one codon, through the ribosome, to the P- and E-sites, respectively, maintaining the reading frame of translation (Moazed and Noller 1989; Wen et al. 2008). This step is facilitated by the elongation factor EF-G, and entails different hybrid and chimeric states of the tRNAs,

characterised by the location of their anticodon stem loops and 3' acceptor ends in the ribosome (Moazed and Noller 1989). Translocation also involves a characteristic "ratchet-like" inter-subunit rotation of the ribosome, which goes back to the non-rotated state once translocation is over (Frank and Agrawal 2000; Frank et al. 2007; Horan and Noller 2007). In the context of the drugs I studied during my thesis, understanding the stepwise details of translocation is important, and hence I have elaborated it further in Section 1.2.2.

Translation Termination

Translation terminates when one of the three stop codons—UAG, UAA, and UGA—arrives at the A-site. These codons, also respectively known as amber, ochre, and opal, were first identified as nonsense codons that interrupt translation (Brenner et al. 1965, 1967). Unlike sense codons, which are recognized by tRNAs, stop codons are recognized by specialized protein enzymes known as release factors (RFs) (Capecchi 1967). Bacteria have two classes of RFs – class I (RF1 and 2) and class II (RF3). The class I RFs bind at the A-site in the non-rotated state of the ribosome and span the decoding center and the peptidyl-transferase center (Rawat et al. 2003; Rawat et al. 2006; Korostelev et al. 2008; Weixlbaumer et al. 2008; Korostelev et al. 2010). They recognize the stop codons by virtue of conserved tripeptide recognition motifs, e.g., RF1 recognizes the termination codons UAA and UAG via a Pro-Ala/Val-Thr motif in RF1 domain 2, while RF2 recognizes UAA and UGA via a Ser-Pro-Phe motif in RF2 domain 2 (Scolnick et al. 1968; K. Ito et al. 2000). Once the stop codon is recognized, nucleobases G530, A1492 and A1493 of the 16S rRNA and A1913 of the 23S rRNA in the decoding center move to allow the docking of a conserved GGQ motif of the RF into the PTC where specific interactions between the two catalyze the hydrolysis of the peptidyl-tRNA ester linkage, releasing the nascent peptide (Trobro and Åqvist 2009; Jin et al. 2010; Korostelev et al. 2010; Svidritskiy et al. 2019; Fu et al. 2019). After hydrolysis of the ester linkage of the peptidyl-tRNA, the Class I RF must dissociate from the A-site to allow ribosomal subunit and deacyl-tRNA dissociation and recycling. At this stage, class I RF-bound ribosomes sample large-scale 30S rearrangements, adopting intermediate rotational states, and the tRNA acceptor arm fluctuates between the P- and E-sites of the 50S subunit (Adio et al. 2018). While RF2 can

then dissociate spontaneously, the non-essential class II GTPase RF3 facilitates the dissociation of RF1 (Mikuni et al. 1994; Grentzmann et al. 1995; Freistroffer et al. 1997; Adio et al. 2018). RF3 stabilises a rotated state of the ribosome, characterised by inter-subunit rotation and a 30S head swivel (approximately 3° to 7°) with hybrid P/E tRNA (Ermolenko, Majumdar, et al. 2007; Gao et al. 2007; Fu et al. 2016). Subsequently, RF3 hydrolyzes GTP and dissociates from the ribosome (Zavialov et al. 2001; Zavialov et al. 2002; Pallesen et al. 2013; Koutmou et al. 2014; Peske et al. 2014).

Disassembly and Recycling of Ribosomes

Efficient ribosome recycling is essential for maintaining cellular protein synthesis – following translation termination, the ribosomes still contain mRNA and tRNA, which need to be released to allow the reuse of the ribosomal subunits in the next round of initiation. Dissociation of subunits is catalysed by the ribosome recycling factor (RRF) and EF-G (Hirashima and Kaji 1970, 1972, 1973; Ogawa and Kaji 1975; Janosi 1998; Gao et al. 2005). RRF binds to the A-site of the ribosome and stabilizes the post-termination rotated state, with the deacylated tRNA in the hybrid P/E binding state (Gao et al. 2005; Dunkle et al. 2011). EF-G•GTP is next recruited to the post-termination complex, and GTP hydrolysis causes the RRF to push against the ribosomal inter-subunit bridge, thereby promoting subunit splitting. Binding of IF3 to the released SSU then removes the tRNA, disrupting the reading frame and destabilizing the SSU-mRNA complex that can spontaneously disassemble, freeing the components of the ribosomal complex for subsequent rounds of translation (Karimi et al. 1999; Seo et al. 2004; Peske et al. 2005; Savelsbergh et al. 2009; Borg et al. 2016; Fu et al. 2016; Prabhakar et al. 2017).

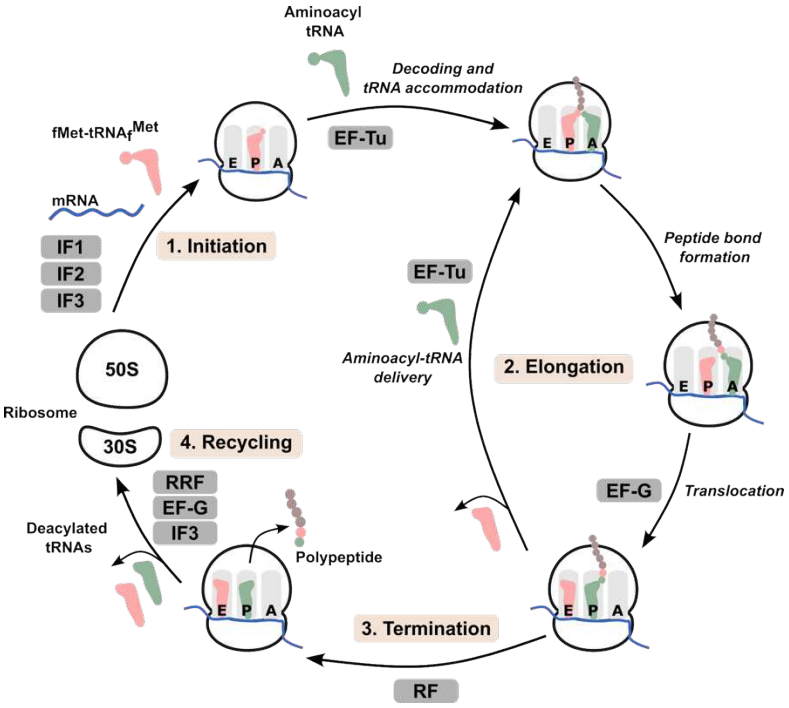

Figure 5: Overview of the bacterial translation cycle. Schematic showing the four steps of translation in bacteria – initiation, elongation, termination and recycling, along with the translation factors involved in each step.

1.2.2. Decoding and translocation as vulnerable antibiotic targeting steps

Translation elongation proceeds by the cyclic coordination of three sequential events: decoding, peptide bond formation, and translocation. Once an aminoacyl-tRNA is accurately accommodated into the A-site, the chemical catalysis of peptide bond formation within the PTC is almost instantaneous, with intrinsic rates estimated to be >100 s^{-1} under physiological conditions. The overall elongation cycle velocity is, however, restricted by significantly slower physical rearrangements, specifically tRNA accommodation (~8–10 s^{-1}) and translocation, the latter involving complex physical rearrangements such as inter-subunit rotation and 30S head swiveling (Pape et al. 1998; Rodnina and Wintermeyer 2001). Consequently, the speed and fidelity of the translation elongation cycle are predominantly governed by its two complex conformational checkpoints: decoding and translocation (Rodnina and Wintermeyer 2001; reviewed in Johansson et al. 2008; Wohlgemuth et al. 2011).

The kinetic and structural organization of elongation establishes distinct functional targets for antimicrobial intervention. Ribosome-targeting antibiotics can be broadly classified according

to their sites of binding and action, as depicted in Fig. 6. Each class of antibiotic targeting translation elongation usually exploits one or more of the following distinct mechanistic vulnerabilities: PTC inhibitors block the peptidyl transfer reaction, NPET binders prevent productive substrate positioning and peptide release, decoding center inhibitors compromise the fidelity and kinetics of A-site tRNA selection, and translocation inhibitors arrest the mechanical progression of tRNAs and mRNA through the ribosome (comprehensively reviewed in Wilson 2014; Lin et al. 2018).

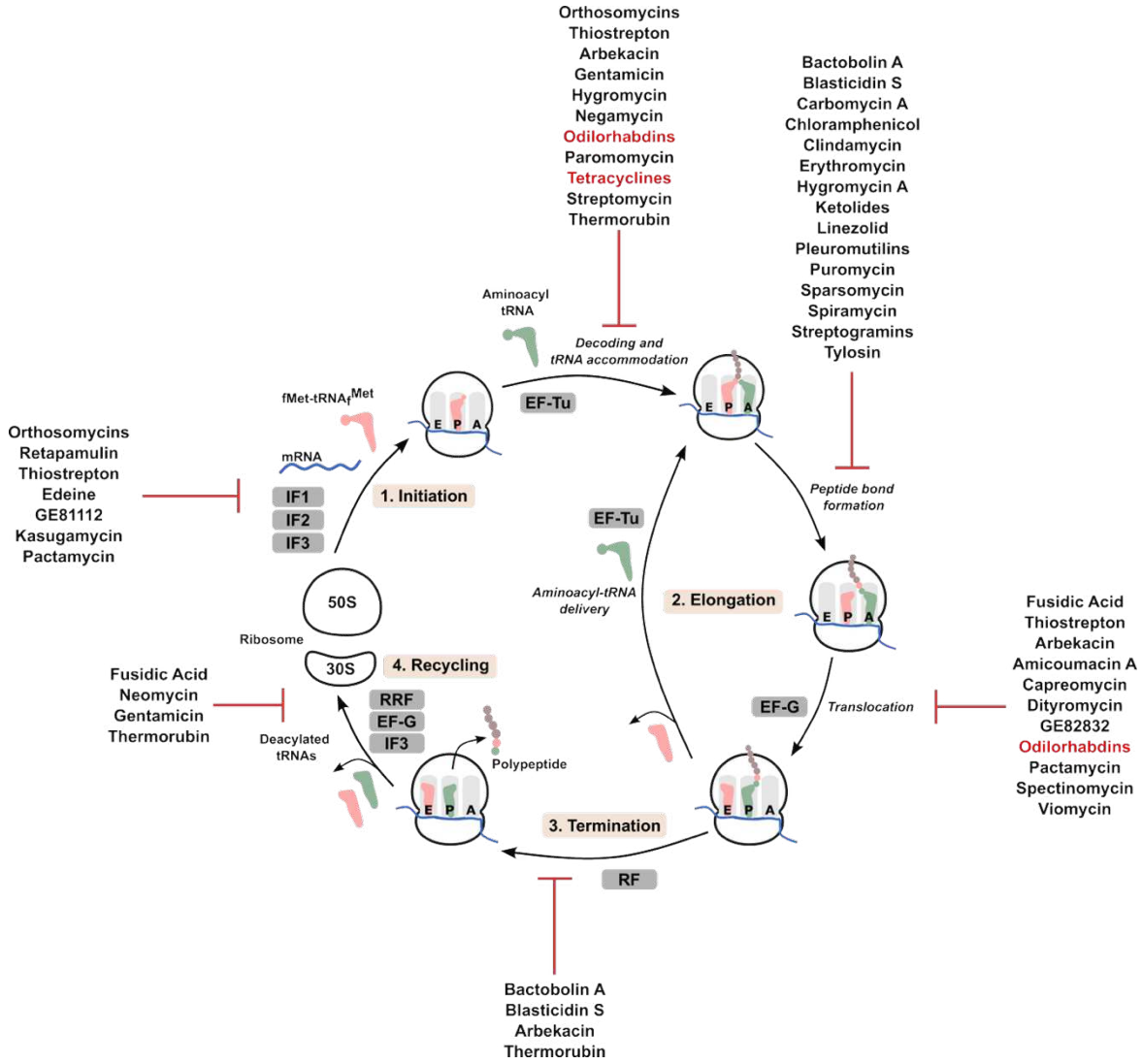

Figure 6: Overview of representative antibiotics targeting the bacterial ribosome. Schematic showing representative examples of widely used antibiotics that target the bacterial ribosome at different stages of translation. The two antibiotics discussed in this thesis - odilorhabdins and tigecycline (which belongs to the tetracycline family) are indicated in red. (Data from Wilson 2014; Lin et al. 2018.)

The antibiotics investigated in this work - odilorhabdins and tigecycline - exert their inhibitory effects by targeting the structural dynamics and fidelity of the decoding/accommodation and translocation checkpoints (Jenner et al. 2013; Schedlbauer et al. 2015; Pantel et al. 2018). Therefore, to establish the necessary wild-type structural and kinetic background for interpreting the drug-bound ribosomal states and context-dependent behaviour characterized in Chapters 3 and 4, the following subsections provide a detailed mechanistic overview of decoding and translocation.

The genetic code is decoded by tRNAs

The ribosome deciphers genetic information stored in mRNA as three-base triplet codons. In bacteria, 64 such codons map to 22 proteinogenic amino acids and three distinct stop signals (also called “nonsense codons”) that lead to translation termination. The establishment of this 64-codon map demonstrated that the genetic code is highly degenerate, where most amino acids are specified by multiple synonymous codons, although each individual codon specifies only a single amino acid (Crick et al. 1961; Nirenberg et al. 1963). While this genetic blueprint was long thought to be absolute across all life, the discovery of alternative codon assignments in mitochondrial genomes demonstrated that it is more accurately described as an "almost universal" code (Barrell et al. 1979). While 61 codons canonically code for the 20 standard proteinogenic amino acids, programmed genetic recoding mechanisms expand the repertoire to 22 (Ambrogelly et al. 2007) (Fig. 7). This expansion is achieved by reassigning traditional nonsense codons to direct the co-translational insertion of non-canonical amino acids – selenocysteine (Sec) (Cone et al. 1976; Zinoni et al. 1986) and pyrrolysine (Pyl) (Hao et al. 2002; Srinivasan et al. 2002).

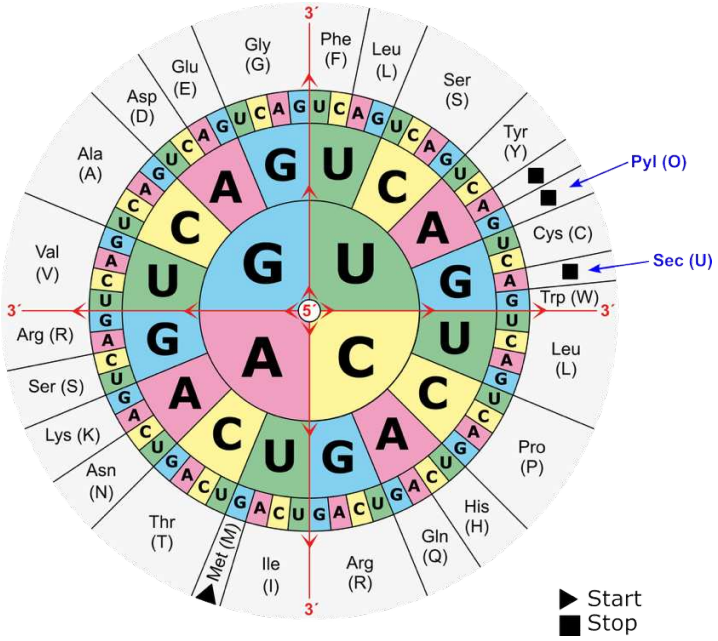

Figure 7: The genetic code. The 64 canonical codons and the encoded 20 amino acids are shown in black, along with the start and stop codons. The stop codons that can be reassigned to code for Pyl and Sec are also indicated.

The translation of nucleic acid sequences into functional polypeptide chains requires a physical bridge capable of reconciling two different chemical languages. This role is filled by transfer RNAs (tRNAs), which function as the macromolecular adaptors that bridge the information-encoding sequence of mRNA with the chemical identity of the 22 amino acids, thereby enabling the ribosome to translate nucleotide triplets into polypeptide sequences (Hoagland et al. 1958; Crick 1958). The secondary structure of tRNAs is a “cloverleaf” where the different regions of the nucleotide sequence base-pair with each other to form stem-loops (Holley et al. 1965) (Fig. 8). The five key regions include:

- **The Acceptor Stem:** Comprising the base-paired 5' and 3' extremities of the transcript, this region also contains the flexible, single-stranded 3'-CCA sequence. Its primary function is to serve as the highly specific metabolic site for aminoacylation, where it is recognized by its cognate aminoacyl-tRNA synthetase (aaRS) to covalently anchor the corresponding amino acid via an ester linkage to the 2'- or 3'-hydroxyl group of the terminal adenosine residue (Schimmel and Söll 1979; Rould et al. 1989; Giege et al. 1998; Ibba and Söll 2000). Further, its specific sequence features act as essential structural checkpoints for

recognition by elongation factor Tu (EF-Tu) in bacteria (Asahara et al. 1993; Sanderson and Uhlenbeck 2007).

- **The Dihydrouracil (D) Loop:** Characterized by the concentration of dihydrouracil residues, this loop acts as a critical folding and stability module. Biochemically, tertiary base-pairing interactions between highly conserved residues in the D-loop and the neighboring TΨC-loop hold the entire tRNA together, driving the molecule to fold from its loose secondary cloverleaf layout into its functional, rigid L-shaped tertiary architecture. Additionally, specific structural elements in the D-loop function as major identity determinants required for correct recognition by specific aminoacyl-tRNA synthetases (Kim et al. 1974; Robertus et al. 1974; Rould et al. 1989).
- **The Anticodon Loop:** This loop structurally presents the three-nucleotide anticodon sequence responsible for deciphering the genetic code. It functions by entering the decoding center of the SSU to form Watson-Crick base pairs at the first two positions of the mRNA codon, alongside permissible non-canonical pairings at the third Wobble position (Crick 1966; Kim et al. 1974; Ogle et al. 2001).
- **The TΨC-loop or the T-loop:** Named for its signature invariant pseudouridine (Ψ**)** and ribothymidine (T) residues, this loop forms the outer "elbow" region of the tertiary L-shape by interlacing with the D-loop (Kim et al. 1973, 1974). Beyond this structural scaffolding role, the T-loop interacts directly with the conserved binding pockets of EF-Tu during ternary complex delivery and establishes stabilizing contacts with the A-site finger (Helix 38) of the 23S rRNA within the large ribosomal subunit during accommodation (Nissen et al. 2000; Schmeing et al. 2009).
- **The Variable Loop:** Positioned between the anticodon loop and the TΨC-loop, this region displays significant variations in length across different tRNA species, ranging from short 4- or 5-nucleotide loops to longer 13-nucleotide hairpins. It serves as an identifying element to allow aminoacyl-tRNA synthetases to differentiate between different tRNAs (Biou et al. 1994; Cusack et al. 2000).

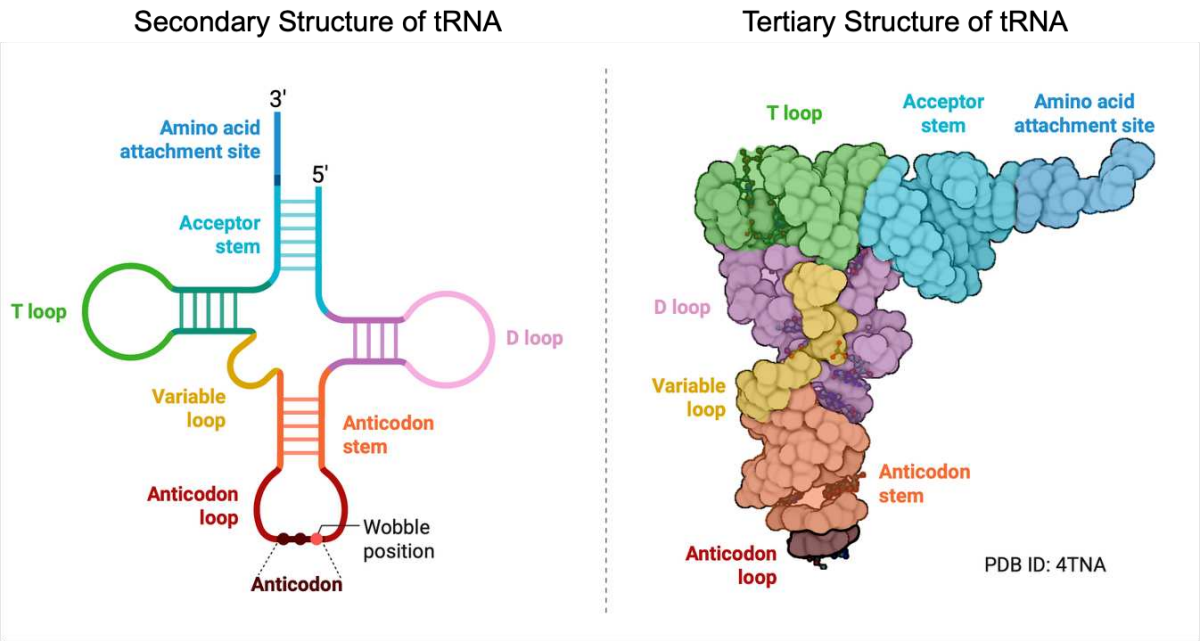

Figure 8: Secondary and tertiary structures of tRNA. The different regions of a tRNA are shown in the secondary and tertiary structures, indicated in distinct colors. Created with BioRender.com

In bacteria, the degeneracy of the genetic code is maintained through:

- **Iso-accepting tRNA species:** Distinct tRNA molecules that are aminoacylated with the identical amino acid but possess different anticodons to recognize distinct codons (Doctor et al. 1961; Yang and Novelli 1968).
- **The Wobble Hypothesis**: A mechanism wherein the third base of an mRNA codon can form non-canonical, non-Watson-Crick base pairs with the first position (the Wobble position) of the tRNA anticodon, enabling a single aminoacyl-tRNA species to pair with more than one codon variant (Crick 1966). The four common Wobble base pairs are guanine–uracil (G–U), hypoxanthine–uracil (I–U), hypoxanthine–adenine (I–A), and hypoxanthine–cytosine (I–C).

tRNAs also undergo extensive post-transcriptional processing, ranging from methylations (e.g., N6-methyladenosine) to more complex, multi-step hyper-modifications (e.g., N6-methyl-N6-threonylcarbamoyladenosine), catalyzed by dedicated sets of epitranscriptomic enzymes (Söll 1971; reviewed in Björk et al. 1987; databases at Dunin-Horkawicz 2006; Sordyl et al. 2026). While chemical modifications are distributed throughout the structural core of the tRNA to optimize overall folding, thermal stability, and rigidity (Giege et al. 1998), they

are concentrated within the anticodon loop, specifically at the Wobble position itself (usually nucleotide 34) and the position immediately adjacent to its 3' side (usually nucleotide 37) - only 7 of the 61 sense codons in *E. coli* are read exclusively by a tRNA without modifications at these two positions (Agris 2004). While position 34 directly monitors the mRNA base, modifications at position 37 are responsible for stabilizing the architecture of the entire loop and preventing the tRNA from slipping along the mRNA strand. In mutants lacking these modifications, the translation machinery suffers from frame-shifting during decoding, demonstrating that these modifications are critical for maintaining the reading frame of the ribosome (Urbonavicius et al. 2001; Murphy et al. 2004). Consequently, these chemical modifications also dictate the precise structural and thermodynamic landscape of the tRNA adapter before it encounters the active site of the ribosome. Furthermore, these chemical marks play a critical upstream role in controlling charging specificity by aminoacyl-tRNA synthetases, serving as primary identity elements that ensure a tRNA is paired with its correct cognate amino acid (Sylvers et al. 1993; Giege et al. 1998). During the decoding step of translation elongation, these aminoacyl-tRNA complexes are delivered to the ribosome by EF-Tu, where they are proofread to maintain translation fidelity.

The wide range and possible combinations of post-transcriptional modifications, variable Wobble pairing, and structural variations between iso-accepting tRNAs can generate kinetic and conformational heterogeneity within the decoding center. Context-dependent antibiotics can target this diversity, selectively inhibiting translation only in the presence of specific mRNA codons or distinct aminoacyl-tRNA species.

Mechanism of cognate aa-tRNA selection and accommodation during translation elongation

Translation is a highly accurate process with misincorporation rates ranging from 10^{-7} to 10^{-5}, with a few hotspots of 10^{-4} to 10^{-3}, depending on the type of mismatches in the codon – anticodon complex (Garofalo et al. 2019; Mordret et al. 2019; Rodnina 2023). This accuracy could not be explained historically by simple equilibrium thermodynamics, since early calculations based on the free-energy differences between canonical Watson-Crick pairings and near-cognate mismatches predicted a baseline error rate of approximately 10^{-2} (Loftfield

1963; Loftfield and Vanderjagt 1972). To address this discrepancy, it was postulated that the translation accuracy of the ribozyme could be exponentially enhanced by filtering the substrates through a series of irreversible steps driven by energy consumption – the concept of kinetic proofreading (Hopfield 1974; Ninio 1975). As such, the ribosome was considered a passive framework with no role in proofreading. The responsibility for maintaining translation fidelity was attributed solely to an intrinsic GTPase timer within EF-Tu that cleaves GTP at an invariant rate, regardless of the codon-anticodon match. This model was supported by early biochemical work demonstrating that EF-Tu directly mediates an energy-consuming proofreading step, where multiple GTP molecules are hydrolyzed in futile cycles for incorrect amino acid incorporation, compared to one cycle for correct ones (Hopfield et al. 1976; Thompson and Stone 1977). Following the irreversible GTP cleavage step, the slow structural transition of EF-Tu from its GTP-bound to its GDP-bound conformation was proposed to create a conformational delay intermediate (Ninio 1975) which acted as a kinetic buffer, providing a near-cognate tRNA with a temporal window to dissociate from the A-site due to its weaker hydrogen-bonding stability, before EF-Tu releases the aminoacyl tail of the tRNA, and retaining only the correct tRNAs (Hopfield 1974).

However, pioneering biochemical and kinetic work using pre-steady-state stopped-flow experiments in the late 1990s shifted this paradigm by demonstrating that the ribosome has an active role in driving precision through consecutive steps of initial selection (induced fit model) and proofreading (kinetic partitioning model) (Rodnina et al. 1995; Rodnina et al. 1996; Pape et al. 1999; Rodnina and Wintermeyer 2001; Blanchard, Gonzalez, et al. 2004; Johansson et al. 2012). By actively accelerating forward chemical steps for correct substrates while delaying those for incorrect ones, the ribosome was proposed to orchestrate these two distinct kinetic selection filters separated by an irreversible chemical step of GTP hydrolysis by EF-Tu, which formed the foundation for our current understanding of decoding and cognate tRNA accommodation.

The decoding center is the principal physical site of the ribosome responsible for monitoring the fidelity of codon-anticodon matching. It resides within a highly conserved asymmetric pocket in the SSU, consisting of regions of the 16S rRNA helices h44 and h18, and the

ribosomal protein uS12 (Noller and Chaires 1972; Moazed and Noller 1990; Carter et al. 2000; Ogle et al. 2001; Schmeing et al. 2009).

Broadly, in our current understanding, decoding proceeds through the following four checkpoints:

- **Initial selection (Induced Fit model)**

During initial selection, a ternary complex composed of EF-Tu, GTP, and an aminoacyl-tRNA (aa-tRNA) delivers the tRNA to the ribosome. Initial binding occurs in a codon-independent manner, positioning EF-Tu in contact with the ribosomal protein uL12 of the LSU (Kothe et al. 2004; Diaconu et al. 2005; Rodnina 2012). From this landing pad, the aa-tRNA samples the codon displayed in the A-site at the decoding center of the 30S subunit. Because the anticodon stem-loop (ASL) remains dynamically anchored at the decoding center to attempt base-pairing with the mRNA, while EF-Tu remains bound at the LSU, the tRNA molecule is forced to undergo a structural distortion. In this transient A/T state (more on tRNA states nomenclature in Table 2), the tRNA acts as a molecular spring. Single-molecule FRET (smFRET) studies have directly quantified these structural fluctuations, observing an untwisting and widening of the groove in the anticodon stem alongside a pronounced accommodation movement of the D-loop, acceptor stem, and elbow (Blanchard, Kim, et al. 2004; Munro et al. 2007; Geggier et al. 2010). Upon successful formation of Watson-Crick base pairs at the first and second codon positions, a cascade of long-range domain rearrangements is triggered within the SSU. This correct geometry is actively sensed by the conserved 16S rRNA residues A1492 and A1493 in h44, which interact with the 2'-hydroxyl groups at anticodon positions 35 and 36, respectively.

In a non-cognate scenario or in the absence of an A-site tRNA, these monitoring bases remain stacked inside the internal h44 platform (the "flipped-in" conformation) (Fig. 9). However, upon cognate tRNA recognition, the sensing of correct Watson-Crick geometry drives these bases to rotate dynamically out of the h44 helix, inserting directly into the minor groove of the newly formed anticodon–codon mini-helix (the "flipped-out" conformation) (Ogle et al. 2001, 2002, 2003; Agris 2004). In contrast to the stringent geometry required at the first two positions, the third (Wobble) position of the codon is monitored with greater structural flexibility. This position is coordinated by the ribosomal proteins uS12 and the 16S rRNA nucleotide G530 of h18 at the 30S shoulder. During a successful decoding event, the glycosidic

bond of G530 rotates from a syn conformation to an anti conformation, interacts indirectly through an Mg^{2+} ion with C518 and protein uS12, while C1054 interacts with nucleotide 34 of the tRNA. Simultaneously, flanking loops of the ribosomal protein uS12, featuring a conserved Pro45-Lys46 motif, interact with h44 to stabilize this highly ordered conformation of the decoding center. This triggers an induced-fit closure or "clamping" of the 30S subunit head and shoulder relative to the body (Powers and Noller 1994; Carter et al. 2000; Ogle et al. 2001, 2002, 2003).

This concerted decoding mechanism was established through experiments using miscoding aminoglycoside antibiotics and two classes of ribosomal mutations — error-prone ribosomal ambiguity (*ram*) mutations and error-restrictive mutations. Aminoglycosides bind h44 of 16S rRNA and directly contact A1492 and A1493, trapping these nucleotides in their “flipped-out” conformation (Ogle et al. 2001). By stabilizing this conformation, these drugs eliminate the free-energy barrier normally required for domain closure. As a result, the decoding center can no longer discriminate between canonical Watson–Crick base pairs and near-cognate mismatches, leading to elevated miscoding rates (Karimi and Ehrenberg 1994; Powers and Noller 1994; Ogle et al. 2002, 2003). Error-restrictive and *ram* mutations act in opposite directions on the same conformational equilibrium. Restrictive mutations hyperstabilize the “flipped-in” state, raising the activation energy for induced fit and allowing the ribosome to reject near-cognate tRNAs more stringently, at the cost of a reduced translation rate. Conversely, *ram* mutations (e.g., in 16S rRNA, uS4, uS5, and uS12) destabilize the “flipped-in” conformation of A1492 and A1493. Hence, by favoring premature domain closure, *ram* mutations allow catalytic forward acceleration, permitting accommodation of near-cognate tRNAs. While error-restrictive mutations in uS12 confer streptomycin resistance because they counteract the drug-induced forced closure, the *ram* mutation phenotypes are similar to aminoglycoside treatment, and indeed mutations at uS4 and uS12 were originally identified through their effects on streptomycin sensitivity, establishing a direct genetic link between the *ram* phenotypes and aminoglycoside action (Gorini et al. 1966; Rosset and Gorini 1969; Piepersberg et al. 1975; Van Acken 1975; Bohman et al. 1984; Karimi and Ehrenberg 1994; Maisnier-Patin et al. 2002; Sharma et al. 2007; Nikolay et al. 2015). Together, these three lines of experiments converge on the conclusion that the free-energy cost of 30S domain closure is

a major determinant of decoding accuracy, and its modulation in either direction alters the ability of the ribosome to discriminate cognate from near-cognate tRNA.

The local 30S rearrangement is also coupled to the 50S subunit via conserved residues at the tip of Helix 69 (H69) of the 23S rRNA, specifically A1913. A1913 is part of the intersubunit bridge B2a and directly probes the structural integrity of the A-site tRNA by packing against the phosphate-ribose backbone of the ASL while stacking closely with the flipped-out A1493. This intricate, tRNA-mediated base-stacking network ensures that only a canonical, rigid Watson-Crick match can successfully lock bridge B2a into its active configuration. In contrast, near-cognate mismatches cause a localized structural distortion that breaks the allosteric communication pathway between the subunits (Selmer et al. 2006; Ortiz-Meoz and Green 2010; Demeshkina et al. 2012; Loveland et al. 2017). Ultimately, the successful locking of bridge B2a and the accompanying SSU domain closure act as a mechanical lever, guiding the accommodation movement of the A/T-state tRNA and driving the precise docking of EF-Tu onto the sarcin-ricin loop (SRL; nucleotides 2653–2667 of the 23S rRNA) of the large subunit, assembling the GTPase-activating center, relocating its catalytic His84 in the GTP-binding pocket (Daviter et al. 2003; Voorhees et al. 2010; Adamczyk and Warshel 2011; Mittelstaet et al. 2011). These events trigger rapid GTP hydrolysis by EF-Tu, accelerating this forward chemical step by up to 10^5-fold for a correct decoding event, compared to a mismatch. Near-cognate tRNAs cannot satisfy these geometric constraints, and hence the active site remains unformed, the 30S subunit shoulder fails to clamp down, remaining in the "open" conformation, resulting in reduced GTPase activation and higher rejection probability from the A-site before GTP hydrolysis (Pape et al. 1998, 1999; Rodnina and Wintermeyer 2001; Ogle et al. 2002).

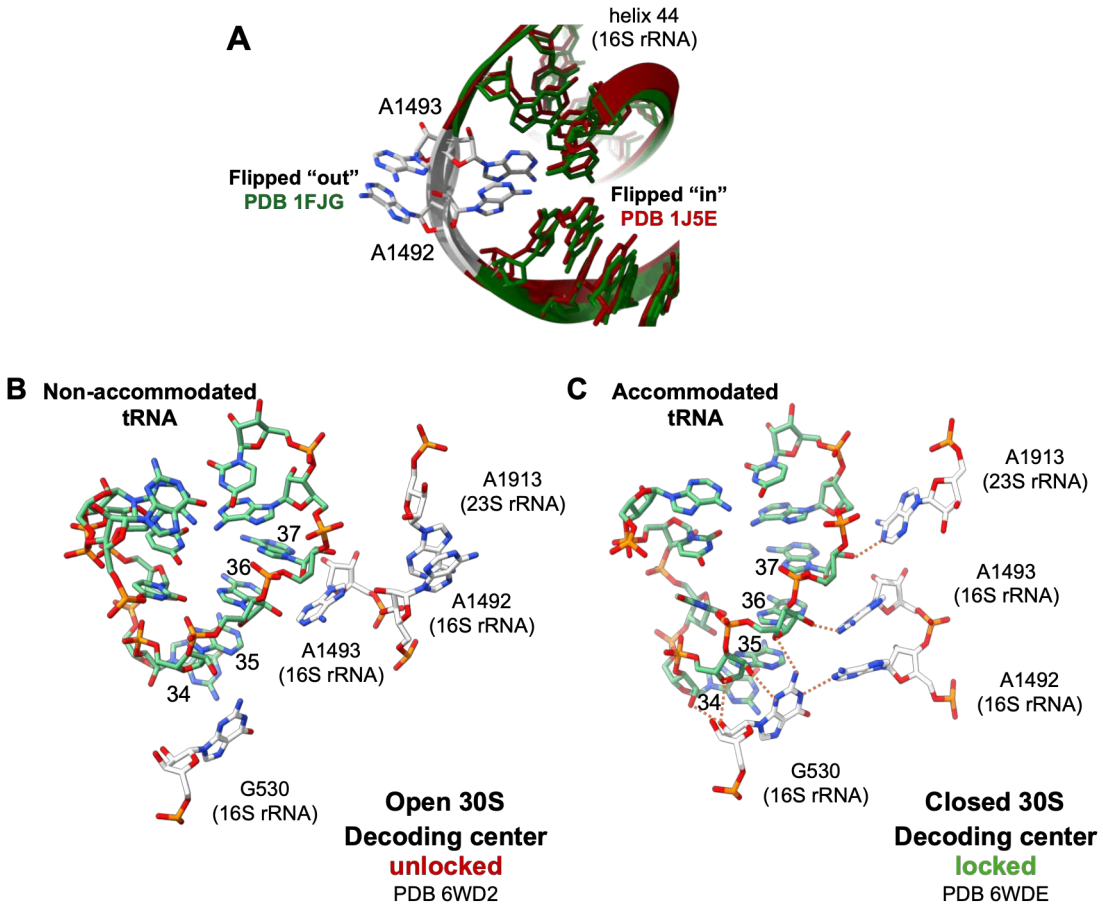

Figure 9: Decoding center arrangements during initial selection. A. The flipped "in" and flipped "out" conformations of the A1492 and A1493 bases of helix 44 (in maroon in PDB 1J5E (Wimberly et al. 2000) and in dark green in PDB 1FJG (Carter et al. 2000), respectively) of 16S rRNA as described in text. These structures represent the isolated 30S subunit. **B-C.** Conformations of the monitoring bases of the decoding center – G530, A1492, A1493 of 16S rRNA and A1913 of the 23S rRNA – before and after accommodation of cognate tRNA in the A-site, in open and closed 30S conformations, represented using PDB 6WD2 and 6WDE (Loveland et al. 2020), respectively. These structures represent the 70S subunit, where the tRNA is attached to EF-Tu (PDB 6WD2) or accommodated in the A-site (PDB 6WDE). The interactions between the monitoring bases and residues 34-37 of the tRNA are shown in orange dashed lines.

- **EF-Tu-dependent proofreading**

Following GTP hydrolysis, aa-tRNA remains EF-Tu-bound temporarily due to delayed inorganic phosphate (Pi) release (Kothe and Rodnina 2006). The ribosome continues fluctuating between open and closed conformations – the closed conformation favours the stable accommodation of a cognate tRNA while the open conformation allows near-cognate

substrates to spontaneously leave before peptide bond formation occurs (Geggier et al. 2010; Loveland et al. 2017, 2020). Historically, it was suggested that tRNA accommodation into the PTC occurs faster than, or concurrent with, the dissociation of EF-Tu-GDP, implying that EF-Tu might remain bound during accommodation (reviewed in Rodnina et al. 2005). Advanced smFRET investigations (Morse et al. 2020) and high-resolution ensemble and time-resolved cryo-EM studies (Loveland et al. 2017, 2020) recently showed that following inorganic phosphate release, the switch I and switch II regions of EF-Tu undergo a conformational collapse, shifting the factor into its low-affinity GDP-bound state. This structural collapse de-protects the tRNA acceptor stem, and the continuous fluctuation between ribosomal open and closed states mechanically assists in destabilizing the lingering EF-Tu molecule from the sarcin-ricin loop (SRL) on the 50S subunit. EF-Tu must completely release its grasp on the tRNA body and dissociate from the ribosome to physically clear the accommodation corridor, which can then allow the aa-tRNA acceptor stem to pivot freely up into the PTC (Loveland et al. 2020; Morse et al. 2020). EF-Ts subsequently reactivates the dissociated EF-Tu-GDP to EF-Tu-GTP for further cycles of aa-tRNA delivery to the ribosome (Wieden et al. 2002).

If a tRNA fails to accommodate quickly enough after EF-Tu leaves, which is often the case for near-cognate substrates due to the open-state fluctuations of the 30S subunit, the tRNA can remain transiently trapped in a proofreading intermediate state. Under these conditions, a free EF-Tu-GTP molecule from the cellular solution can re-engage the ribosome-bound tRNA, performing a futile cycle of secondary GTP hydrolysis in an attempt to pull the tRNA back out or retry selection (Morse et al. 2020).

- **EF-Tu-independent proofreading (Kinetic Partitioning model)**

Once EF-Tu dissociates from the ribosome, proofreading shifts from monitoring active catalytic assembly (induced fit) to a kinetic race between the forward rate of accommodation into the PTC and the backward rate of thermal dissociation (Pape et al. 1999; Rodnina and Wintermeyer 2001; Schmeing et al. 2009). Accommodation of aa-tRNA involves traversing the narrow intersubunit space, moving the tRNA acceptor stem and elbow approximately 80 Å from its EF-Tu binding site to the A-site in the PTC while the ASL remains bound to the decoding center. Thus, the tRNA changes conformation from the A/T to the A/A state. Accommodation also entails a ~2.5° rotation of the SSU relative to the LSU, repositioning both

the A-site finger (ASF, nucleotides 863–915 of Helix 38 in 23S rRNA) and Helix 89 to allow the tRNA to bypass structural obstacles and properly position its CCA end in the PTC of the LSU (Rodnina 2012; Loveland et al. 2017, 2020).

A cognate tRNA forms a highly stable base-pairing network within the decoding center – this tight thermodynamic anchor holds the anticodon stem-loop firmly in place, providing the structural leverage required for the tRNA body to swing into the PTC smoothly. The rate of accommodation thus outpaces the rate of spontaneous rejection, leading to swift peptide bond synthesis. A near-cognate tRNA, however, presents a mismatched codon-anticodon helix that is thermodynamically unstable, which increases the rejection rate by several orders of magnitude. The physical fluctuations of the unanchored tRNA body thus pull the adaptor entirely out of the active site before its distant acceptor stem can accommodate into the PTC, achieving high-fidelity sorting through kinetic means (Pape et al. 1998, 1999; Ogle et al. 2001; Rodnina and Wintermeyer 2001; Schmeing et al. 2009).

- **Additional proofreading at the PTC**

Even if a near-cognate tRNA accommodates its aminoacyl-CCA tail into the large subunit, it faces a final proofreading checkpoint within the peptidyl transferase center (PTC). High-resolution structures of the intact 70S ribosome have shown that the PTC requires precise positioning of the aminoacyl ester of the incoming aa-tRNA relative to the P-site peptidyl-tRNA, achieved through an induced-fit compaction of the active site upon CCA binding (Schmeing et al. 2005; Beringer and Rodnina 2007; Voorhees et al. 2009). Indeed, the geometric status of the distant decoding center is allosterically coupled to the PTC – molecular simulations indicate that a near-cognate tRNA, whose anticodon-stem loop retains the structural distortion of a mismatched codon–anticodon pair, follows a divergent accommodation trajectory that misaligns the CCA end relative to the catalytic core of the PTC (Girodat et al. 2023). This misalignment suppresses the forward rate of peptidyl transfer, providing an additional window for rejection before covalent bond formation.

Should a miscoded amino acid be nonetheless incorporated, and the ribosome continues to translocate, the resulting P-site mismatch triggers a downstream quality control response, leading to abortive termination where RF2 recognizes and hydrolyses the miscoded peptidyl

tRNA to rescue the ribosome (Zaher and Green 2009a, 2009b). Furthermore, smFRET studies have shown that base-pair mismatches between the peptidyl tRNA anticodon and the mRNA codon in the pre-translocation complex prolong late stages of EF-G-catalyzed translocation, and can also cause a “drop-off” or dissociation of the accommodated peptidyl-tRNA from the mRNA, preventing translation from continuing with the misincorporated amino acid (Alejo and Blanchard 2017).

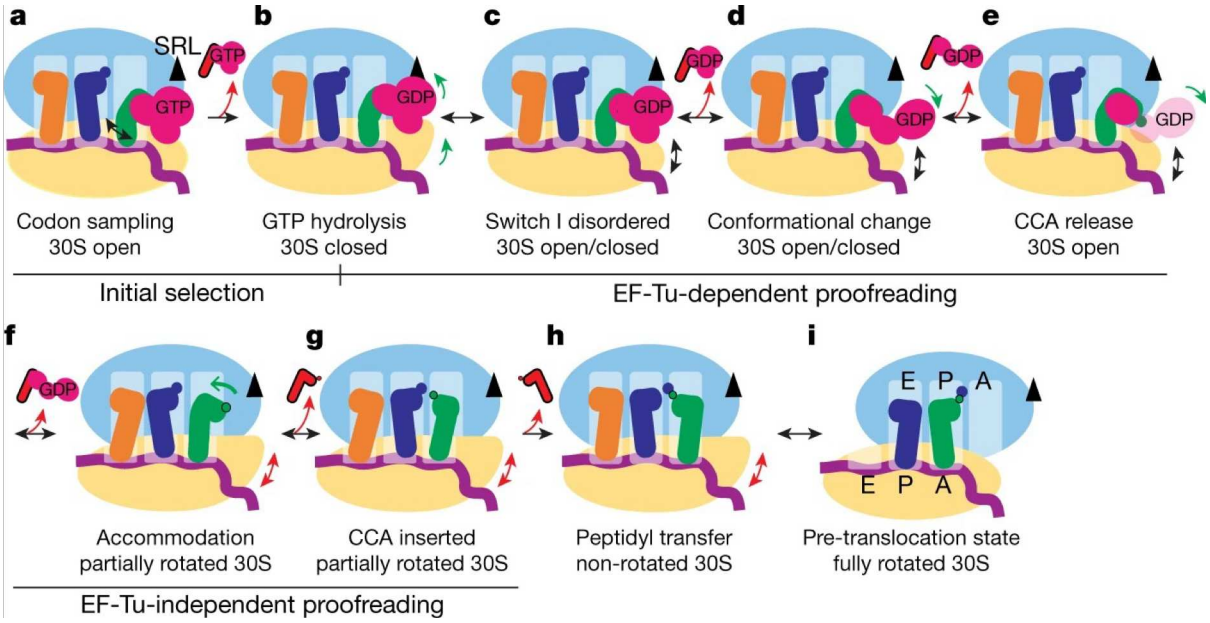

Figure 10: Overview of decoding. The sequential steps of decoding, as described in the text, are shown schematically – initial selection (a, b), EF-Tu-dependent proofreading (c-e) and EF-Tu-independent proofreading (f, g) – followed by peptidyl transfer and the pre-translocation state. EF-Tu is colored in magenta, cognate A-site tRNA is shown in green while near-cognate tRNA is shown in red. Black arrows indicate conformational changes such as EF-Tu rearrangements, 30S domain closure, dissociation of tRNA or EF-Tu. Green and red arrows indicate events predominant for cognate and near-cognate complexes, respectively. Adapted and modified from Loveland et al. 2020 with permission from Springer Nature (License No. 6323221235963).

These kinetic checkpoints and conformational equilibria indicate that the energy landscape of initial selection and tRNA accommodation can vary depending on the specific codon-anticodon pair. Context-dependent antibiotics may selectively target these localized thermodynamic variations, thereby increasing the likelihood of misreading of the genetic code or selective perturbation of tRNA accommodation.

Mechanism of translocation during translation elongation

Once peptide bond formation occurs, the ribosome enters the final stage of elongation – translocation. Translocation involves the precise coupling of the movement of the tRNAs together with the bound mRNA (the $tRNA_2$•mRNA module) so that the ribosome moves forward along the mRNA by exactly one codon. This coupling ensures that the anticodon loop does not slip onto an adjacent codon, causing a frameshift and mistranslation of all downstream sequences.

Our current understanding of translation elongation can be described in two broad steps – before and after the engagement of the highly conserved five-domain (D1–D5) EF-G GTPase, the elongation factor that accelerates translocation.

- **Translocation before EF-G association: fluctuation between PRE-C and PRE-H states**

After peptide bond formation, at the starting point of translocation, the ribosome assumes a highly dynamic pre-translocation (PRE) state containing a peptidyl-tRNA in the A-site and a deacylated tRNA in the P-site. At this stage, the tRNAs fluctuate between their classical (C) and hybrid (H) states, forming the PRE-C and PRE-H ribosomal complexes, respectively. This fluctuation is spontaneous and reversible, and has a rate of about 1–10 s^{-1} (Pestka 1969; Gavrilova and Spirin 1971; Spirin et al. 1976; Blanchard, Kim, et al. 2004; Munro et al. 2007; Cornish et al. 2008; Adio et al. 2015). However, smFRET studies have shown that this equilibrium between the PRE-C and PRE-H complexes is sensitive to the presence, identity, and acylation status of the P and A-site tRNAs (Blanchard, Kim, et al. 2004; Munro et al. 2007; Fei et al. 2008; Marshall et al. 2008) and misreading at the decoding center can perturb this equilibrium (Feldman et al. 2010; Wasserman et al. 2016). In the C state, the acceptor stems and ASLs of the tRNAs are located in the A and P-sites on both subunits, denoted as A/A and P/P for the peptidyl-tRNA and deacylated tRNA, respectively. In the H state, the acceptor stems and the tRNA elbow regions move towards the P and E-sites on the LSU, whereas the ASLs remain in the A and P-sites on the SSU. The deacylated tRNA adopts a single hybrid conformation (P/E), while the peptidyl-tRNA can fluctuate between two distinct hybrid conformations denoted as A/P and A/P*, where the elbow of the tRNA shifts ~20 Å towards the P-site relative to the A/P state (Table 2). The relative arrangement of the SSU and LSU in

the PRE-C state is called a non-rotated state of the ribosome, whereas the PRE-H conformations involve increased SSU body-rotation (~8° counterclockwise relative to the LSU) and SSU head-swivel (~6° in the direction of tRNA movement across the SSU head-body axis), denoted as the rotated state of the ribosome (Moazed and Noller 1989; Frank and Agrawal 2000; Blanchard, Kim, et al. 2004; Munro et al. 2007; Agirrezabala et al. 2008; Ratje et al. 2010; Dunkle et al. 2011; Belardinelli et al. 2016; Carbone et al. 2021; Petrychenko et al. 2021; Rundlet et al. 2021). Concomitant with the formation of the PRE-H states, the L1 stalk—a mobile protuberance of the LSU composed of ribosomal protein L1 and helices 76–78 of 23S rRNA—transitions from an open conformation in the PRE-C state to a closed conformation in the PRE-H state, in which it makes direct contact with the elbow of the P/E hybrid tRNA. This allows the L1 stalk to guide the deacylated tRNA toward the E-site as translocation proceeds (Fei et al. 2008, 2009; Cornish et al. 2009; Bock et al. 2013; Mohan and Noller 2017).

At this stage, translocation of the tRNA anticodons on the SSU is inefficient since the ribosome remains in a locked global conformation. Rapid translocation requires ribosome "unlocking", referring to the coordinated global conformational changes in the ribosome that allow both tRNAs to move simultaneously in the direction of translocation. Unlocking is initiated by EF-G domain 4 (D4), whose loop II wedges between the universally conserved monitoring bases A1492 and A1493 of helix 44 and the codon–anticodon duplex, physically displacing the peptidyl-tRNA–mRNA pair out of the decoding center and disrupting the contacts that clamp the A-site tRNA in a fixed conformation. EF-G is hence necessary to accelerate translocation to physiologically relevant rates (2–20 s^{-1}) at the cost of GTP hydrolysis (Kurland 1992; Fischer et al. 2010; Munro et al. 2010; Bock et al. 2013; Holtkamp et al. 2014; Carbone et al. 2021; Rundlet et al. 2021).

- **Translocation upon recruitment of EF-G**

EF-G•GTP binds preferentially to the rotated, PRE-H conformation of the ribosome rather than to the non-rotated PRE-C state. This selectivity arises because intersubunit rotation repositions the ribosomal GTPase activating center (GAC) — composed of the L10-L12 stalk, the L11 region, and the SRL — into a conformation that is complementary to the G-domain of EF-G (Diaconu et al. 2005; Voorhees et al. 2010). The initial recruitment of GTP-bound-EF-G domain 1 (D1) to the ribosome occurs through interactions with the L12 stalk, and upon

binding to the ribosome, EF-G adopts an elongated form spanning the interface between the SSU and LSU with its G-domain (D1) bound to the sarcin-ricin loop (SRL, helix H95), domains 2 (D2) and 3 (D3) contacting the SSU body and D4 pointing towards the codon-anticodon complex in the A-site of the SSU (Stark et al. 2000; Diaconu et al. 2005; Brilot et al. 2013; Salsi et al. 2014, 2015; Lin et al. 2015). The binding of EF-G•GTP engages PRE-H complexes to initiate "unlocking" of the peptidyl-tRNA from the decoding center, and this early translocation intermediate is called Intermediate 1 (INT1). It represents a rapidly transited conformation defined by a clockwise-rotated SSU, a partially swiveled SSU head domain, and complete translocation of the deacylated tRNA and partial translocation of the peptidyl tRNA relative to the LSU. The INT1 state is markedly slowed by the non-hydrolysable GTP analogue GTPγS and can be stalled by spectinomycin (SPC) (Carbone et al. 2021; Rundlet et al. 2021). The orientation of EF-G in the INT1 state acts as a pawl that stabilizes the rotated and swiveled state of the SSU, the hybrid states (A/P*, P/E) of tRNAs, the closed state of the L1 stalk, and positions the catalytic His91 of EF-G in an active orientation, leading to GTP hydrolysis (Fei et al. 2008; Cunha et al. 2013; Munro et al. 2010; Maracci and Rodnina 2016; Carbone et al. 2021; Petrychenko et al. 2021). The release of the reaction product Pi (inorganic phosphate) is, however, kinetically delayed (Rodnina et al. 1997). This delay is functionally significant: in the GDP•Pi state, the switch 1 (sw1) region of EF-G adopts a compact fold stabilized by interactions with Pi, switch 2 (sw2), the SRL, and helix 14 of 16S rRNA, thereby maintaining ribosomal subunits in the rotated conformation and holding EF-G tightly bound to the ribosome. The EF-G•GDP•Pi intermediate thus functions as a high-affinity anchor that keeps EF-G engaged with the PRE complex long enough to complete the tRNA–mRNA movement before EF-G dissociates, thereby preventing back-translocation and ensuring the reaction is productive (Holtkamp et al. 2014; Petrychenko et al. 2021; Carbone et al. 2021). The release of Pi induces significant conformational rearrangements in both EF-G and the ribosome. The sw1 region remodels from its compact, SRL-contacting fold to an extended conformation stabilized by contacts with D2, disrupting sw1–sw2–SRL interactions and returning the SRL to its ground-state conformation. The resulting refolding of the GTPase switch regions drives a large-scale rigid-body rotation of EF-G pivoting around the SRL, pushing D4 deeper into the decoding center, where it contacts the RNA backbone of the translocating codon–anticodon

duplex through conserved residues His583 and Gln507, ensuring reading frame maintenance and preventing frameshifting (Ramrath et al. 2013; Zhou et al. 2014; Niblett et al. 2021). Simultaneously, the SSU undergoes a scissor-like conformational change where the body rotates backwards relative to the LSU, while the SSU head swivels forward by ~18–21° (Ratje et al. 2010; Zhou et al. 2013, 2014). D2 of EF-G rolls over the SSU shoulder, stabilizing the back-rotated SSU body conformation, while D3 adjusts its SSU contacts to accommodate these changes (Belardinelli et al. 2016; Petrychenko et al. 2021; Rundlet et al. 2021; Carbone et al. 2021). This Intermediate 2 (INT2) reflects the post-hydrolysis conformation, which is typically stalled by fusidic acid. Pi release also promotes further tRNA movement – the tRNAs transition from hybrid (H) to chimeric (CHI) states, in which their ASLs shift with the mRNA relative to the SSU body while maintaining contact with the swiveled SSU head, thereby preserving the codon–anticodon register and maintaining the reading frame. In this conformation, the tRNAs adopt ap/P (A-site tRNA) and pe/E (P-site tRNA) positions on the SSU (Table 2), while their 3'-CCA ends remain anchored in the P and E-sites on the LSU (Ratje et al. 2010; Ramrath et al. 2013; Zhou et al. 2013; Carbone et al. 2021; Rundlet et al. 2021; Poulis et al. 2023).

Whether EF-G actively drives tRNA–mRNA movement by a true power stroke or merely reshapes the free-energy landscape to bias intrinsic Brownian fluctuations of the ribosome has been a long-standing and unresolved debate. In the power-stroke model, the chemical energy liberated by GTP hydrolysis and Pi release is directly converted into mechanical force that actively displaces the tRNAs and mRNA. In the Brownian ratchet model, the ribosome acts as a thermally driven machine. In this view, EF-G-GTP binding and subsequent structural rearrangements do not actively push the components forward; instead, they alter the free-energy landscape, lowering activation barriers and sequentially trapping (or "ratcheting") the favorable forward fluctuations of the ribosome-tRNA-mRNA complex. The current consensus, supported by time-resolved cryo-EM and rapid kinetics, presents a hybrid of these two models: GTP hydrolysis and Pi release drive the initial ribosome-unlocking step via a power-stroke-like mechanism, while the subsequent large-scale tRNA–mRNA translocation is largely driven by the intrinsic thermal dynamics of the ribosome, with EF-G ensuring that these fluctuations are unidirectional (Frank and Agrawal 2000; Yao et al. 2013; Chen et al. 2016; Petrychenko et al. 2021; Rodnina 2023).

Further progression from INT2 involves exaggerated SSU head-swivel motions that drive rapid and reversible transitions into a third transient intermediate, INT3. From INT3, the SSU head undergoes relocking — the reversal of its swivel, returning to the unswiveled position through re-engagement of the head domain with the SSU body via intersubunit bridges — coinciding with the repositioning of the mRNA and peptidyl-tRNA into their final POST-state E/E and P/P configurations and dissociation of EF-G–GDP, leaving the A-site available for the next aminoacyl-tRNA (Ermolenko and Noller 2011; Belardinelli et al. 2016; Wasserman et al. 2016; Carbone et al. 2021; Rundlet et al. 2021). Throughout this late phase, the L1 stalk passes through a half-closed intermediate conformation as it accompanies the deacylated tRNA from the P/E hybrid to the E/E classical position, ultimately opening to release the E-site tRNA (Cornish et al. 2009; Fei et al. 2009).

After translocation is complete, the POST ribosome bears a P-site peptidyl-tRNA and an E-site deacylated tRNA, with a vacant A-site, 0° of intersubunit rotation, and a fully back-swiveled SSU head. The complete translocation cycle thus couples the energy of GTP hydrolysis to an orchestrated sequence of conformational transitions that advance the ribosome by precisely one codon while preserving the translational reading frame.

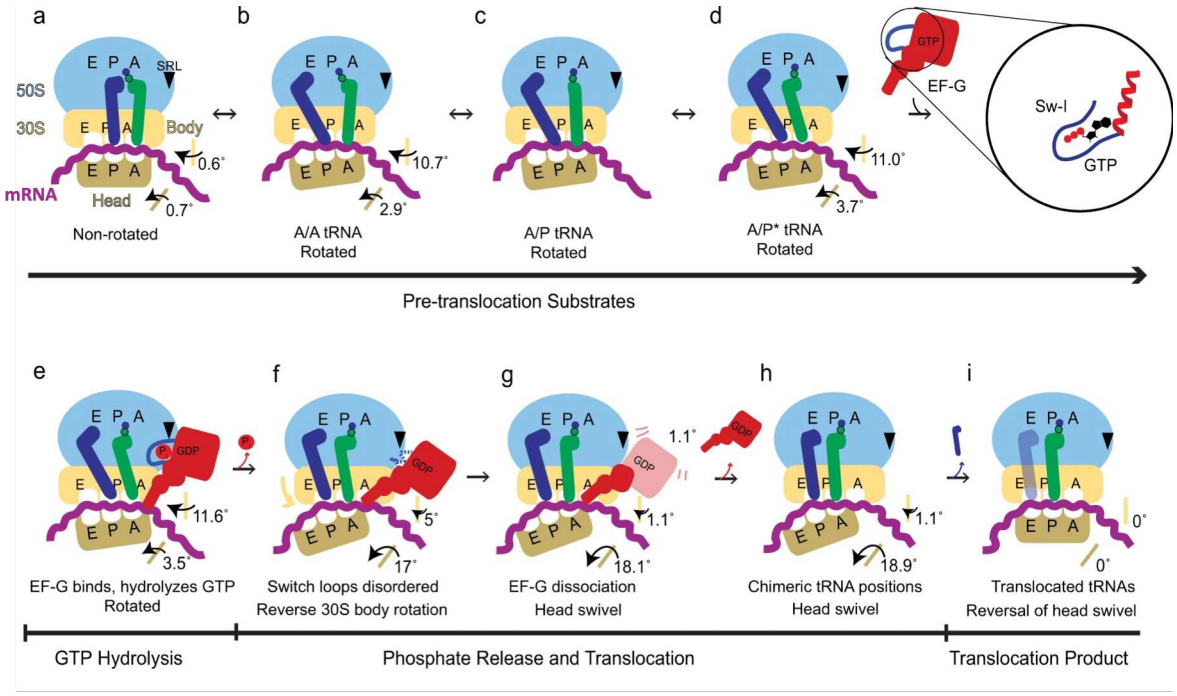

Figure 11: Overview of translocation. The sequential steps of translocation, as described in the text, are shown schematically (a-i). The ordered conformation of the switch I (Sw-I) of EF-G-GTP is shown in the inset. The indicated angles of 30S head and body rotations were observed in time-resolved cryo-EM structures (Carbone et al. 2021), from which this figure is adapted, licensed under CC BY 4.0 (https://creativecommons.org/licenses/by/4.0/).

Table 2: Nomenclature of tRNAs based on ribosomal positions during translation

Adapted from Korostelev 2022 with permission from Annual Reviews (License 1762320-1).

tRNA Nomenclature	Aminoacylation Status	Position in ribosome structure	
		Anticodon stem-loop (ASL)	Acceptor CCA end
A/T	Aminoacyl	A-site of SSU	Bound to EF-Tu, hence “T”
A*/T (used to indicate A/T tRNA when the 30S is in an open conformation)	Aminoacyl	A-site of SSU	Bound to EF-Tu, hence “T”
A or A/A	Aminoacyl or peptidyl	A-site of SSU	A-site of LSU

P or P/P	Peptidyl or deacyl (or aminoacyl during initiation)	P-site of SSU	P-site of LSU
E or E/E	Deacyl	E-site of SSU	E-site of LSU
A/P	Peptidyl	A-site of SSU	P-site of LSU
A/P*	Peptidyl	A-site of SSU	P-site of LSU, with the elbow of the tRNA shifted ~20Å towards the P-site relative to the A/P state
P/E	Deacyl	P-site of SSU	E-site of LSU
ap/P	Peptidyl	A-site elements of SSU head domain & P-site elements of SSU body domain	P-site of LSU
pe/E	Deacyl	P-site elements of SSU head domain & E-site elements of SSU body domain	E-site of LSU

1.2.3. SSU-binding antibiotics that affect decoding, accommodation and translocation

As mentioned in Section 1.1, ribosome-targeting antibiotics account for nearly half of all antibiotics in current therapeutic use (Lin et al. 2018). In this section, I provide a brief overview of a subset of these antibiotics, focusing on those that bind the 30S subunit and target the decoding, accommodation and translocation steps of translation elongation, as described in the preceding section. Many of these antibiotics possess overlapping binding sites but exhibit divergent mechanisms of action in inhibiting protein synthesis. In the context of my thesis, this overview aims to contextualize my experimental findings and delineate the mechanistic distinctions between known antibiotics in the literature.

Antibiotics that cause misreading of the genetic code

Several 30S subunit-binding antibiotics target the function of the decoding center, causing misreading of the genetic code and the resultant production of proteins with misincorporated amino acids, which in turn hamper cellular function and survival.

Aminoglycosides (e.g., streptomycin, kanamycin, tobramycin, gentamicin, among others) are one of the most widely known antibiotic classes with this mechanism of action – they are broad-spectrum antibiotics that inhibit protein synthesis by binding to h44 of the 16S rRNA near the A-site. They induce a structural rearrangement in the decoding center that stabilises the "flipped-out" conformation of the monitoring bases A1492 and A1493, permitting incorporation of near-cognate (single mismatch in the codon-anticodon complex) and non-cognate (two or three mismatches in the codon-anticodon complex) aa-tRNAs during decoding (Fourmy et al. 1996; Pape et al. 1999; Carter et al. 2000; Jingji Zhang et al. 2018). Aminoglycosides also induce formation of error clusters with multiple successive translation errors – this suggests that the antibiotic stays bound to the ribosome for several successive elongation cycles, and during this "residence time," stabilizes an error-prone conformation of the decoding center, forcing it to make multiple mistakes before the drug eventually dissociates (Wohlgemuth et al. 2021). Such erroneous decoding of the mRNA causes misincorporation of amino acids in translated proteins, leading to detrimental effects on cell membrane integrity and initiating a lethal self-promoted uptake loop of the drug, resulting in

cell death (Davis et al. 1986; Kohanski et al. 2008; reviewed in Davis 1987; Magnet and Blanchard 2005; Krause et al. 2016).

Another well-known example is that of tuberactinomycins like capreomycin and viomycin, which are circular peptide antibiotics that bind to the decoding center at the interface between h44 (SSU) and H69 (LSU). They stabilise A1492 and A1493 in their "flipped out" states and lock the 23S rRNA residue A1913 into a distinct conformation that allows it to stack with A1493 and form a stable hydrogen bond with the accommodated A-site tRNA (Modolfll and Vázquez 1977; Peske et al. 2004; Ermolenko, Spiegel, et al. 2007; Stanley et al. 2010; Brilot et al. 2013; L. Zhang et al. 2020; Holm et al. 2016, 2019). This structural stabilization creates a positive cooperative feedback loop, where the affinity of tuberactinomycins for the ribosome significantly increases upon A-site tRNA binding, preventing dissociation of near- and non-cognate tRNAs, enhancing errors during initial selection (Holm et al. 2016, 2019).

Two other recently discovered antibiotic classes that cause misreading are the peptide antibiotics odilorhabdins (Pantel et al. 2018), and the lasso peptides lariocidins (Jangra et al. 2025). Both classes bind the SSU near the decoding center, establishing multiple contacts with the sugar-phosphate backbone of residues of 16S rRNA helices h31, h32 and h34 and interact with the anticodon loop of the A-site tRNA, increasing the affinity of the aa-tRNA for the ribosome, leading to error-prone translation. However, despite targeting the same helices, their binding sites only partially encroach into each other, with overall distinct and unique interactions with the ribosome. The mechanism of action of odilorhabdins is one of the core studies performed during this thesis, and it has been discussed in detail in Chapter 3.

Antibiotics that impede the accommodation of aminoacyl tRNA

Several antibiotics that target the SSU can inhibit translation elongation by preventing the accommodation of an incoming aminoacyl tRNA into the A-site.

Tetracyclines are one of the most well-known antibiotics that function in this manner. They are broad-spectrum antibiotics that bind the ribosome primarily in a pocket formed by the 16S rRNA helices h31 and h34, which interferes with the accommodation of an incoming aa-tRNA into the ribosomal A-site by creating a steric clash with the ASL of the tRNA (Brodersen et al. 2000; Pioletti 2001; Jenner et al. 2013; Schedlbauer et al. 2015). Due to the widespread

clinical use of classical tetracyclines since the Golden Age of antibiotic discovery, resistant pathogens harbouring ribosomal protection proteins (e.g., TetM) or efflux pumps have emerged over the years. This has led to the chemical improvement of tetracyclines to second-generation derivatives with optimised pharmacokinetics (e.g., doxycycline) and subsequently, third-generation glycylcyclines (e.g., tigecycline). As elaborated in Chapter 4, these advanced third-generation derivatives feature engineered structural modifications that establish additional, high-affinity interactions with the 16S rRNA pocket (e.g., stacking interactions with C1054 in tigecycline). These structural adaptations allow them to physically block the access of ribosomal protection proteins, thereby evading resistance mechanisms and displaying significantly enhanced antibacterial potency (Olson et al. 2006; Jenner et al. 2013; Schedlbauer et al. 2015; Grossman 2016).

Thermorubin is chemically related to tetracyclines but binds to the ribosome at the interface between the small and the large subunits, where h44 and H69 form the intersubunit bridge B2a. It stacks between the C1409-G1491 base pair within helix 44 (h44) of 16S rRNA and A1913 within helix 69 (H69) of 23S rRNA and induces C1914 to flip out from H69 and adopt a conformation where it would collide with an A-site tRNA. Hence, thermorubin also impedes A-site delivery and accommodation of aa-tRNA, thereby impairing elongation, albeit via a pathway distinct from tetracyclines (Bulkley et al. 2012; Parajuli et al. 2023).

Antibiotics that inhibit translocation

Certain antibiotics that bind to the SSU can also impede translation elongation by inhibiting the translocation of the ribosome.

For example, spectinomycin binds to h34 of the 16S rRNA at the junction between the head and shoulder domains of the SSU (Carter et al. 2000; Borovinskaya et al. 2007). This interaction traps the 30S head domain in a conformation that is refractory to the swivelling motion required for tRNA translocation on the SSU (Peske et al. 2004; Borovinskaya et al. 2007). Kinetic studies further show that spectinomycin uncouples LSU and SSU translocation: while movement of the acceptor end of peptidyl-tRNA on the large subunit proceeds at an increased rate, translocation of the anticodon stem-loop on the small subunit becomes severely

impaired, leading to translation inhibition (Borovinskaya et al. 2007; Pan et al. 2007; Holtkamp et al. 2014; Rundlet et al. 2021).

Further, GE82832 and dityromycin are structurally and functionally related cyclic peptide antibiotics – differing by a mass of only two units – that specifically target the SSU by binding exclusively to the ribosomal protein uS12. This sterically blocks the interaction between domain 3 of EF-G and protein uS12, trapping EF-G in a compact conformation on the ribosome, and inhibiting EF-G-mediated translocation (Ōmura et al. 1977; Brandi et al. 2006, 2012; Bulkley et al. 2014; Jinzhong Lin et al. 2015).

PamB2 is another example of a translocation inhibitor. It is a hybrid non-ribosomal peptide - polyketide antibiotic that binds to the SSU between the P-site and accommodated A-site tRNAs, interacting with 16S rRNA helices h24 and h44, 23S rRNA H69 (notably A1913), first and third bases of the P-site codon of the mRNA, and the A-site tRNA (residues 37 and 38). PamB2 binds to the ribosome after aa-tRNA accommodation and traps a pre-translocation state of the ribosome that does not allow stable binding of EF-G, preventing subsequent steps of translocation. The mode of translation inhibition by PamB2 is also context-dependent – its activity is influenced by the presence of modifications at position 37 of the A-site tRNA (Müller et al. 2014; Bulatov et al. 2022; Koller et al. 2024).

Aminoglycosides can also affect translocation – for example, kanamycin, gentamicin, and tobramycin induce translocation inhibition in addition to misreading (Jesús Cabañas et al. 1978; Carter et al. 2000; Gromadski and Rodnina 2004; Peske et al. 2004; Tsai et al. 2013; Wohlgemuth et al. 2021), and hygromycin B does not stimulate miscoding, but instead, by inducing a unique orientation of A1493, stabilises the A-site tRNA and sterically blocks its translocation to the P-site (Peske et al. 2004; Borovinskaya et al. 2008; Holtkamp et al. 2014).

Similarly, lariocidins can also cause translocation inhibition – their interactions with the head and shoulder domains of the SSU restrict conformational transitions for EF-G-catalysed translocation of mRNA and tRNAs, thereby inhibiting elongation (Jangra et al. 2025).

Tuberactinomycins like viomycin have also been shown to inhibit translocation by stabilizing a rotated conformation of the ribosome that traps the tRNAs in hybrid P/E and A/P* intermediate states – by locking this specific intermediate step along the translocation pathway, the drug prevents the coordinated subunit back-rotation and EF-G-mediated

movement necessary for elongation (Peske et al. 2004; Shoji et al. 2006; Ermolenko, Spiegel, et al. 2007; Pan et al. 2007; Cornish et al. 2008; Ly et al. 2010; Wang et al. 2012; Holm et al. 2016, 2019; Carbone et al. 2021).

Antibiotics that target multiple steps of translation elongation

Some antibiotics binding the SSU can also inhibit multiple steps during translation elongation. For example, odilorhabdins are reported to cause misreading at low concentrations, and inhibit translocation at high concentrations (Pantel et al. 2018) (elaborated in Chapter 3). Further, the binding site of negamycin overlaps with tetracyclines, in the pocket formed by the 16S rRNA helices h31 and h34, but negamycin is smaller than tetracycline and exhibits more interactions with the backbone of residues of the h31 helix compared to tetracyclines. Consequently, it stabilises tRNA-binding in the A-site, increasing the affinity of the tRNA to the ribosome, stimulating misreading of the mRNA and inhibiting translocation (Polikanov, Szal, et al. 2014). Aminoglycosides, lariocidins and tuberactinomycins can also inhibit both decoding and translocation, as described in preceding paragraphs.

To cite another example, saskemycin is a cationic glycolipid antibiotic that binds between 16S rRNA helices h18 and h34. From this site, it prevents the latching of the decoding center and locks the SSU in an open conformation, thereby destabilizing aa-tRNA binding in the A-site. However, despite the SSU remaining in an open state, saskemycin-bound ribosomes can occasionally accommodate aa-tRNA in the A-site, catalyse peptide bond formation, and successfully advance to a rotated intermediate state along the translocation pathway. However, the ribosome is unable to complete the translation cycle, and it is hypothesised that the drug immobilizes parts of the SSU that need to have a sufficient degree of mobility for successful translocation. Further, saskemycin exhibits a context-dependent activity whereby it preferentially stalls ribosomes when an Asp or Thr codon in the mRNA is positioned in the A-site. Because structural data indicate that saskemycin does not directly interact with either the mRNA template or the nascent peptide chain, its codon specificity is hypothesized to rely on yet-uncharacterized, sequence-specific tRNA body or anticodon stem-loop properties (Wright et al. 2025).

To summarize, the diverse mechanisms of action displayed by this subset of antibiotics targeting the small subunit underline how chemically distinct antibiotics can exploit overlapping binding sites to drive divergent pathways of translation elongation inhibition, ranging across the steps of decoding and translocation. The recently characterized context-dependent activity in antibiotics like paenilamicin B2 and saskemycin further indicates that their inhibitory activity is modulated by the specific mRNA-tRNA combinations present in the ribosomal P and A-sites. However, the extent to which sequence-dependent inhibition applies to major classes of decoding center targeting drugs remains largely unexplored. Investigating these potential context-dependencies can bring novel insights into the structural mechanisms of elongation inhibition, providing the basis for the research presented in this thesis.

1.3. Aims and Objectives

Antibiotic resistance is a critical contemporary public health concern which necessitates robust strategies for combating drug-resistant pathogenic bacteria. While innovation is urgently needed to introduce new antibiotic classes capable of overcoming existing resistance mechanisms, several classes currently in clinical use still lack a complete molecular and structural understanding of their mechanisms of action. Although over half of the clinically used antibiotics target the bacterial ribosome, our understanding of their inhibitory mechanisms is evolving. As introduced in the preceding sections, over the last decade, our understanding of translation inhibition is shifting away from global sequence-independent mechanisms toward context-dependent translation arrest, offering novel frameworks for targeting unique, species-specific translation pathways in multidrug-resistant pathogenic bacteria.

The decoding center of the ribosome is an efficient antibiotic target since it ensures the fidelity of translation of the genetic information from mRNA into protein. Consequently, perturbations in this function can result in lethal mistranslation and/or ribosome stalling. At the onset of my PhD, most of the characterized context-specific drugs were known to bind at the nascent peptide exit tunnel (NPET), and it was not sufficiently clear whether similar selectivity exists for drugs targeting the decoding center of the ribosome. Hence, during my PhD, I aimed to characterize the sequence-specific mode of action of two classes of antibiotics that bind at unique sites of the decoding center and obtain a better understanding of their mechanism of translation inhibition.

In this work, I have studied odilorhabdins, which are a relatively novel class of peptide antibiotics discovered in the previous decade (Pantel et al. 2018), and tigecycline, which is a third-generation tetracycline well-established in clinical use. While both antibiotics disrupt translation elongation, they do so through distinct mechanisms: odilorhabdins induce genetic code misreading and inhibit translocation, whereas tigecycline prevents incoming aminoacyl-tRNAs from binding to the ribosomal A-site (Jenner et al. 2013; Schedlbauer et al. 2015). Additionally, tigecycline has been recently shown to impair translation initiation as well (Nakahigashi et al. 2016; Barrenechea et al. 2021).

The first objective of my thesis was to investigate the context-dependent inhibition of translation by each of these antibiotics. Specifically, I aimed to map the landscape of sequence motifs that preferentially arrest translation in *E. coli* across a gradient of drug concentrations relative to untreated controls. To accomplish this, I used inverse toeprinting coupled to high-throughput sequencing (iTP-Seq), an *in vitro* profiling technique developed by our group to locate stalled ribosomes on mRNA with codon-level resolution without degrading the upstream translated mRNA sequence (Seip et al. 2018; Gillard et al. 2026). iTP-Seq was performed on a template library encoding over 10^{12} short peptides featuring an N-terminal variable region of 15 randomized (NNN) codons, where N denotes equal proportions of the four possible canonical nucleotides. For tigecycline, this high-throughput screen was used to reveal the specific sequence motifs where drug-bound ribosomes stall during elongation and initiation. Conversely, because odilorhabdins exert a dual effect on decoding and translocation, iTP-Seq was used to specifically capture ribosome stalling. While iTP-Seq cannot detect amino acid misincorporation, I used it to map the specific sequence motifs where misreading leads to severe translocation defects.

My second objective, specific to odilorhabdins, was to investigate the structures of drug-bound ribosomes stalled on specific arrest motifs identified by iTP-Seq, to find out how decoding center perturbations by odilorhabdins can lead to downstream translocation defects. To achieve this, I first screened drug-specific stalling sequences from the iTP-Seq data using classical toeprinting to identify motifs that lead to homogeneous stalling of the ribosomes on specific codons. Homogeneous stalling on a specific arrest motif refers to ribosomal complexes that are stalled on a particular codon of the open reading frame, encompassing several conformations of the ribosomes translating the same sequence. Identifying such homogeneous complexes is interesting because they bypass the need for post-*in vitro* translation purification steps and can be directly applied to grids for cryo-EM single-particle analysis (SPA). Using this workflow, I identified two stalling motifs for structural characterization and subsequently processed and analyzed the cryo-EM dataset for one representative motif, as detailed in the subsequent chapters of the thesis. Together, this work contributes to the foundational knowledge needed for structure-guided development of next-generation ribosome-targeting antibiotics.

Chapter 2

Methodological Overview and Methods

To study the context-dependent mechanisms of action of odilorhabdins (specifically, NOSO-502 and NOSO-96624) and tigecycline, I used a combination of two *in vitro* techniques – classical toeprinting and inverse toeprinting coupled to next-generation sequencing (iTP-Seq). Additionally, to elucidate the high-resolution architecture of stalled ribosomal complexes bound to the odilorhabdin NOSO-502, I used single-particle cryo-electron microscopy. In this chapter, I first provide an overview of these techniques and then describe the experimental protocols used throughout this work, the results of which are presented in the subsequent chapters.

2.1. Methodological Overview

2.1.1. Investigation of ribosomal stalling landscapes with classical and inverse toeprinting

Primer extension inhibition, or classical toeprinting, was developed in the late 1980s to study translation initiation complexes at codon resolution (Hartz et al. 1988) and was subsequently adapted to monitor specific patterns of drug-induced ribosome stalling on individual mRNA templates in cell-free translation systems (Orelle, Carlson, et al. 2013; Orelle, Szal, et al. 2013). This is a reverse-transcription-based *in vitro* assay (Fig. 12) where, following translation, a 5'-fluorescently-labelled DNA oligonucleotide primer is annealed to the 3' region of the mRNA template to initiate reverse transcription. As the reverse transcriptase moves along the template, it falls off upon encountering a stalled ribosome, producing a fluorescently labelled single-stranded cDNA whose length marks the leading edge of the stalled complex, 16-17 nucleotides downstream of the first nucleotide of the P-site codon of the stalled ribosome. Sanger sequencing of the template is performed in parallel, and when both the toeprinting-generated cDNA and sequencing reactions are visualized on the same gel, the precise location of the mRNA codon on which the ribosome has stalled can be mapped.

Despite its codon resolution, this is a low-throughput technique that relies on testing each mRNA of interest in a separate reaction. As such, to study drug-dependent ribosomal stalling on a variety or library of sequences, this is not the most practical choice.

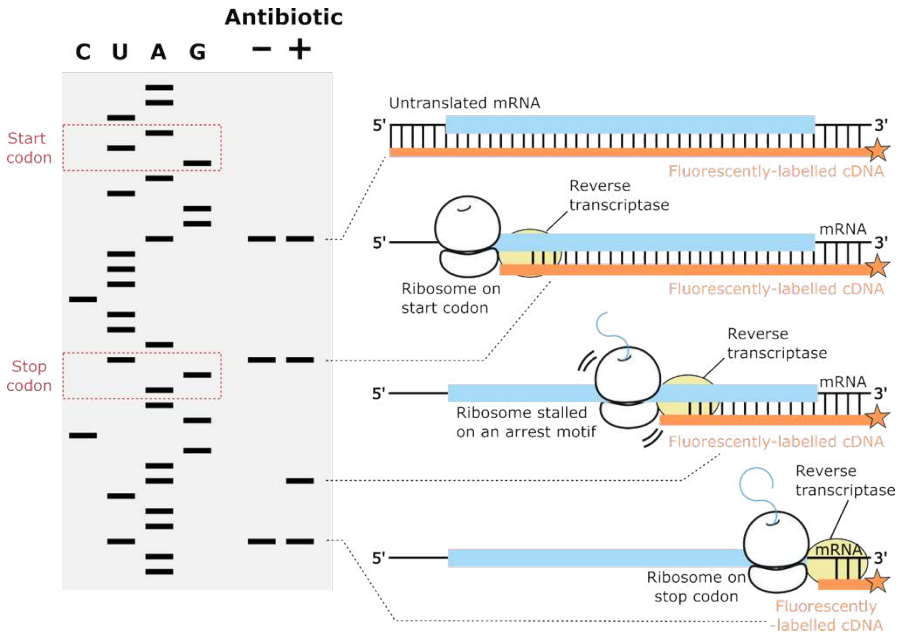

Figure 12: Principle of classical toeprinting. Left: Schematic gel displaying Sanger sequencing lanes (C, U, A, G) alongside toeprinting reaction lanes in the absence (–) or presence (+) of an antibiotic that can cause stalling of ribosomes on a specific arrest motif. Start and stop codons are highlighted in red dashed boxes. The 3' end of the cDNA product is separated by 16-17 nucleotides from the first nucleotide of the codon in the P-site of the stalled ribosome. **Right:** Fluorescently labelled cDNA fragments (in orange) are synthesized by reverse transcriptase (in yellow), extending from a 5'-labelled primer annealed to the 3' region of the mRNA template until enzyme progression is physically blocked by the leading 70S ribosome. Corresponding states during reverse transcription: full-length cDNA generated from untranslated mRNA (top); cDNA when the leading ribosome is on the start codon (second from top); cDNA when the leading ribosome is stalled on a specific arrest motif yielding a distinct drug-dependent cDNA band (third from top); and cDNA when the ribosome has a stop codon in the A-site (bottom).

Hence, to scale up this method to study context-dependent ribosomal stalling in the presence of antibiotics, the high-throughput approach of ribosome profiling or Ribo-Seq was used (reviewed in Vázquez-Laslop and Mankin 2018). Ribo-Seq is an *in vivo* technique that determines transcriptome-wide translation rates. An RNA endonuclease, typically micrococcal nuclease or MNase for bacteria, is used to digest unprotected mRNA, leaving short fragments of ribosome-protected mRNA, called ribosome footprints. These footprints are isolated, converted into a cDNA library and analyzed by next-generation sequencing. Upon mapping these reads onto a reference genome, a quantitative snapshot of ribosome occupancy across cellular mRNAs is generated, and comparing control and drug-treated conditions can reveal

antibiotic-induced sequence-dependent stalling patterns of ribosomes (Ingolia et al. 2009; Kannan et al. 2014; Marks et al. 2016; McGlincy and Ingolia 2017; Vázquez-Laslop and Mankin 2018; Mohammad and Buskirk 2019; Ingolia et al. 2019; Choi et al. 2020; Mangano et al. 2022; Y. Zhang et al. 2022; Wright et al. 2025; Kaur et al. 2026). However, this method has a few limitations. For example, the footprints are short (15-40 nucleotides in bacteria) and rely on alignment to a well-annotated reference genome. Moreover, the reads cannot be recovered for weakly expressed genes in the transcriptome, precluding their evaluation. As such, ribosome profiling cannot be performed on customized transcript libraries or on organisms whose genome sequences are poorly characterized. Ribo-Seq can also be limited to compounds that can readily enter cells and are retained in the cytoplasm, and being an *in vivo* technique, requires medium to large bacterial culture volumes and high sequencing depth (Ingolia et al. 2009; Glaub et al. 2020), which can make the comprehensive analysis of stalling landscapes of multiple antibiotics at different concentrations cost-prohibitive.

To overcome these limitations, our group developed inverse toeprinting coupled to next-generation sequencing (iTP-Seq), an *in vitro* high-throughput profiling workflow designed to map bacterial translation landscapes. This method enables the systematic characterization of context-dependent ribosomal stalling across diverse antibiotic conditions at a significantly lower sequencing depth, while offering precise control over *in vitro* translation conditions (Seip et al. 2018; Leroy et al. 2023; Gillard et al. 2026). Like classical toeprinting and ribosome profiling, iTP-Seq also locates ribosomes stalled on mRNA with codon resolution. However, instead of discarding the translated transcript or relying on short footprint fragments, iTP-Seq captures the entire mRNA sequence from the 5’ end of the mRNA up to where the leading ribosome stalls, generating fragments termed “inverse toeprints”. A comparative overview of classical toeprinting, ribosome profiling and inverse toeprinting is illustrated in Fig. 13.

In a standard iTP-Seq experiment, a complex transcript library consisting of ~10^{12} mRNA molecules is translated *in vitro*, following which a highly processive 3’ to 5’ exonuclease, RNase R, is used to degrade the transcripts from their 3’ ends up to the point where it encounters the leading stalled ribosome on the mRNA, and falls off. Therefore, the entire coding sequence from the 5’ end of the transcript to the RNase R cleavage site is preserved. These inverse toeprints are then reverse-transcribed into cDNA, PCR-amplified, size-selected and analysed

via next-generation sequencing. Since RNase R degrades transcripts 17-19 nucleotides downstream of the first nucleotide of the P-site codon (Seip et al. 2018), the 3' end of each inverse toeprint can be mapped to the location of the stalled ribosome on the mRNA with codon resolution.

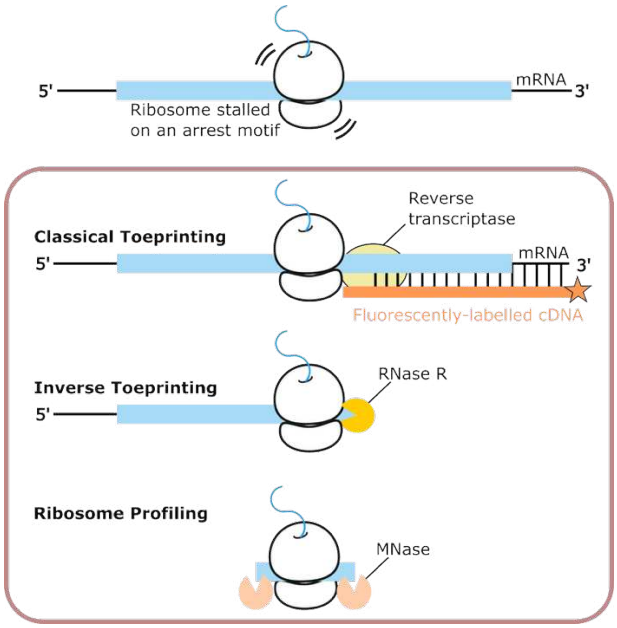

Figure 13: Comparison of toeprinting and ribosome profiling techniques. Schematic highlighting how each method isolates mRNA regions relative to a stalled 70S ribosome. In classical toeprinting, reverse transcriptase extends a 5'-fluorescently-labelled primer from the 3' end of the mRNA until blocked by the ribosome, yielding a labelled cDNA fragment representing the sequence downstream of the arrest site. In inverse toeprinting, RNase R degrades the untranslated 3' mRNA region up to the leading edge of the stalled ribosome, preserving the entire upstream 5' translated sequence ("inverse toeprint"). In ribosome profiling, micrococcal nuclease (MNase) digests unprotected mRNA on both the 5' and 3' sides, isolating only the short ribosome-protected footprint.

In this work, I first used iTP-Seq on an (NNN)15 transcript library composed of short ORFs with a randomized N-terminal sequence of 15 NNN (where N denotes any nucleotide) codons downstream of an AUG start codon. By translating this library in the absence and presence of varying concentrations of odilorhabdins or tigecycline, I characterized the sequence-dependent stalling profiles of *E. coli* 70S ribosomes *in vitro* using the PURExpress system (New England Biolabs), which is based on the PURE system technology originally described in Shimizu et al. 2001. The detailed experimental workflow is depicted in Fig. 14 and elaborated

in Section 2.2. This revealed a series of distinct arrest motifs that cause drug-induced ribosomal stalling, as described in the subsequent chapters. To further characterize the precise stalling patterns of ribosomes on these motifs, I used classical toeprinting on certain arrest sequences. This combination of low- and high-throughput classical and inverse toeprinting methods revealed novel insights into the mechanism of inhibition by these two antibiotic classes.

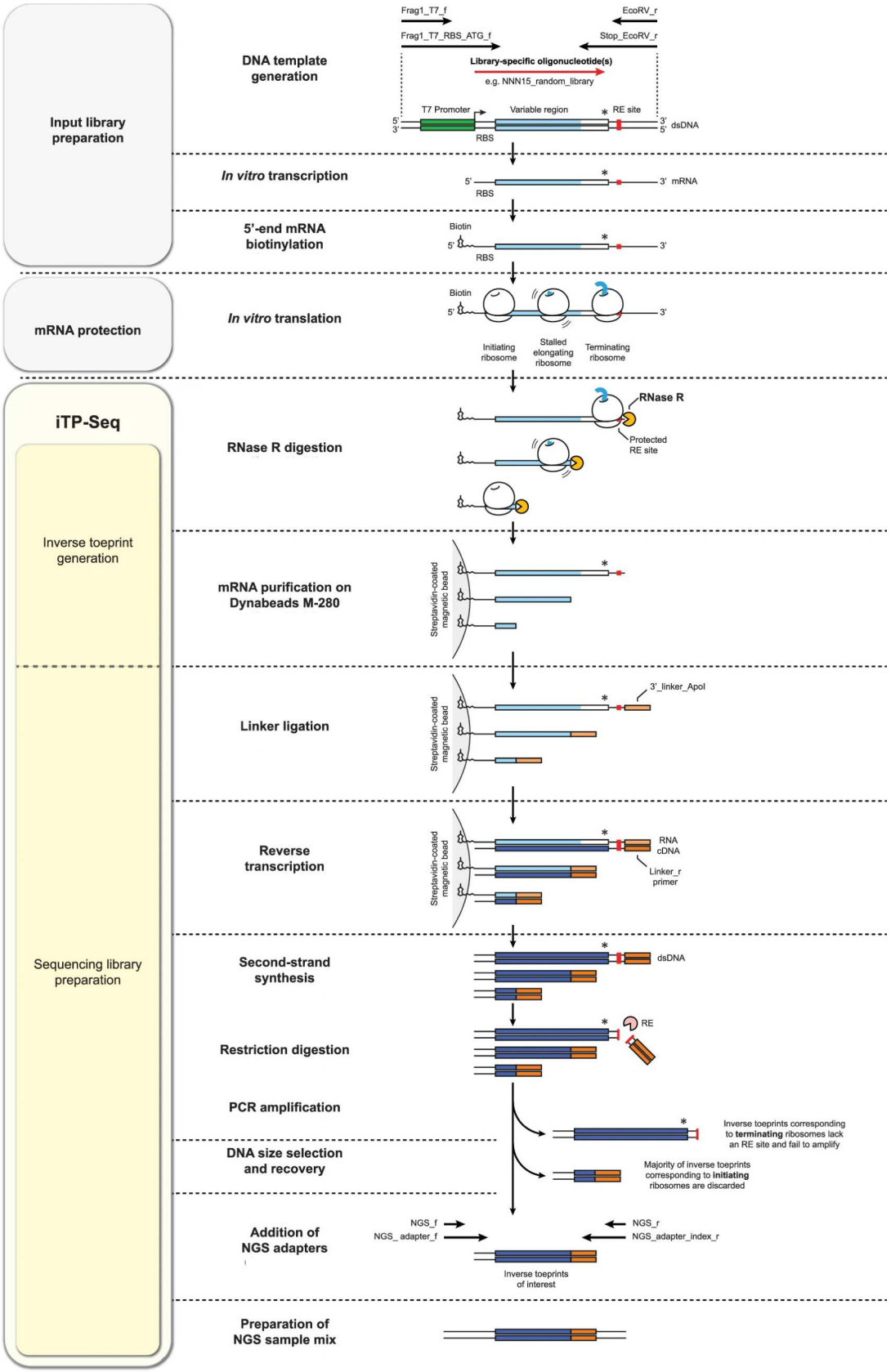

Figure 14: Overview of the experimental steps of iTP-Seq. Adapted and modified from Gillard et al. 2026 with permission from Springer Nature (License No. 6334821131237).

To delve deeper into the mechanism of action of the odilorhabdin NOSO-502, I reproduced the *in vitro* translational conditions used in the toeprinting experiments to obtain stalled ribosomal complexes. Specifically, these complexes were stalled during the *in vitro* translation of an arrest motif identified via the iTP-Seq experiments and were subsequently characterized structurally using single-particle cryo-EM.

2.1.2. Visualisation of stalled ribosomal complexes using cryo-EM

Structural analyses of bacterial ribosomes bound to antibiotics have led to the foundational understanding of not only drug mechanisms, but also of the process of translation per se, as exemplified in Chapter 1. Historically, such studies have been performed using X-ray crystallography, yielding structures of ribosomes in complex with nearly all major classes of antibiotics (reviewed in Wilson 2014). While high-resolution structural information could be obtained using X-ray crystallography, ribosomes are trapped in a static state within the crystal lattice, which can limit the understanding of the precise molecular mode of inhibition of ribosome-targeting antibiotics. Specifically, the molecular size of the ribosome, coupled to its complexity and flexibility, and difficulties in purifying sufficient quantities of ribosome-antibiotic complexes for crystallization and structural determination, often limit the efficiency of this technique. As such, improvements in the high-resolution single-particle cryo-EM technique over the last decades have been monumental in studying the mechanism of action of small molecules targeting the ribosome, including antibiotics (reviewed in Herrero del Valle and Innis 2020).

Cryo-EM is an imaging technique where an electron beam is transmitted through a frozen sample to generate 2D projected images on a detector; by computationally averaging these projections from multiple identical biomolecules trapped in vitreous ice in different orientations, single-particle analysis (SPA) enables their 3D structures to be reconstructed at high resolutions comparable to or exceeding those that can be achieved by X-ray crystallography. Compared to X-ray crystallography, this method is particularly useful in studying ribosome-antibiotic complexes due to several key advantages. For example, significantly lower sample quantities and screening parameters are required in cryo-EM compared to crystallography, which may be particularly useful in limiting drug availability.

Further, cryo-EM allows the visualization of molecules in solution, including various conformations – this tolerance for heterogeneity, coupled with the ability of computational classification of individual particles, allows comprehensive study of distinct functional states of drug-bound ribosomal complexes (reviewed in Cheng 2015; Herrero del Valle and Innis 2020; Tsegaye et al. 2021; historical perspective in Frank 2016). Initial cryo-EM reconstructions of the bacterial ribosome yielded modest average resolutions of 25Å (Frank et al. 1995) – over subsequent decades, continuous innovations in microscopes, direct electron detectors, energy filters, sample preparation techniques and data processing algorithms propelled the field into the "resolution revolution", a milestone formally recognized by the 2017 Nobel Prize in Chemistry awarded to Jacques Dubochet, Joachim Frank and Richard Henderson. Today, cryo-EM of bacterial ribosomes routinely achieves sub-2Å resolutions (e.g., 1.55Å reported in Fromm et al. 2023).

In this work, I used cryo-EM SPA to determine the structures of *E. coli* 70S ribosomes stalled while translating an arrest-motif-coding mRNA sequence in the PURExpress *in vitro* translation system in the presence of NOSO-502. Following translation, the sample was diluted and directly applied onto cryo-EM grids and vitrified. This strategy preserves the weakly bound ribosomal components, such as elongation factors, which frequently dissociate during conventional purification methods like sucrose density gradient centrifugation prior to grid vitrification. Grid preparation, vitrification and data collection for the dataset presented in this thesis were performed by Dr Fanny Boissier at the IECB (Pessac, France), and I subsequently processed the collected data using CryoSPARC v4.7.1 (Punjani et al. 2017). The experimental and analytical pipelines are illustrated in Figures 15 and 32 and detailed in Section 2.2.



Figure 15: Schematic overview of the cryo-EM workflow for NOSO-502-stalled *E. coli* 70S ribosomal complexes. Arrest motif-coding mRNA was translated *in vitro* in the PURExpress system (New England Biolabs) by *E. coli* 70S ribosomes in the presence of 40µM NOSO-502. The sample was diluted and frozen on glow-discharged carbon-coated grids using the Vitrobot (Thermo Fisher Scientific). After screening of grids, data were collected on a Glacios 2 (Thermo Fisher Scientific) microscope equipped with a Falcon 4 camera and a Selectris filter. Micrographs were processed using CryoSPARC v4.7.1, starting with patch motion correction and contrast transfer function (CTF) estimation, followed by particle picking and 2D classification. Subsequent 3D classification and non-uniform refinement yielded the final cryo-EM density maps, which were used for atomic model building. Images partially created with BioRender.com.

2.2. Methods

2.2.1. Inverse toeprinting coupled to next-generation sequencing (iTP-Seq)

iTP-Seq was performed in quadruplicate as previously described (Leroy et al. 2023; Gillard et al. 2026), with certain modifications. The detailed experimental workflows are described as follows. The reagents used are the same as those listed in Gillard et al. 2026 unless otherwise mentioned. The sequences of the DNA oligonucleotides used in this work are listed in Supplementary Tables 7 and 8.

Luciferase assay to determine odilorhabdin concentrations for iTP-Seq

To determine the optimal concentrations of odilorhabdins for iTP-Seq, serial 2-fold dilutions of NOSO-502 and NOSO-96624 dissolved in molecular biology grade water, ranging from 655µM to 0.04µM, were evaporated in distinct wells in a white opaque 96-well plate with clear bottom using a miVac DNA concentrator (Fisher Scientific, cat. no. DNA-23050-B00). Untreated control wells contained evaporated molecular biology grade water alone. mRNA coding for firefly luciferase (sequence indicated in Supplementary Fig. 61) at a final amount of 200ng was added to each well and translated *in vitro* in a 5µl reaction volume using a PURExpress kit (New England Biolabs cat. no. E6800) for 20 minutes at 37°C. All low-volume liquid dispensation steps were executed with a Formulatrix® Mantis® liquid dispenser to ensure volume accuracy. Following translation, 50µl of Steady-Glo® Reagent (mixture of Steady-Glo® Buffer and Steady-Glo® Substrate in a 1:1 ratio according to manufacturer's instructions) (Promega, cat. no. E2510) was added to the wells and mixed thoroughly. The plate was centrifuged at 100 x g for 1 minute, and 40µl aliquots from each reaction were transferred to clean wells on the same plate. After 2 minutes of incubation, the luminescence signal was measured on a CLARIOstar plate reader (BMG Labtech) at 550-570 nm. Experiments were performed in technical triplicates, i.e., three independent assay wells prepared from a single master mix per antibiotic concentration. Luminescence values were normalized as a percentage relative to the untreated control, and half-maximal inhibitory concentration (IC_{50}) values were calculated by fitting normalized dose-response data to a sigmoidal curve using the SciPy library in Python.

Preparation of an (NNN)15 mRNA library

A DNA library composed of short ORFs with a random N-terminal stretch of 15 NNN (N denotes any nucleotide base) codons was purchased from Eurogentec as a single-stranded oligonucleotide (iTP_NNN15), and it was used to assemble an expression cassette for *in vitro* transcription using PCR with other template oligonucleotides. A 50µl PCR was performed with Phusion DNA polymerase (6 cycles [98°C, 10 s; 62°C, 5 s; 72°C, 10 s]), with oligonucleotides iTP_NNN15, Frag_1_T7_RBS_ATG_f and Stop_EcoRV_r (final concentration, Cf, of each being 20nM) used as templates, and oligonucleotides Frag1_T7_f (Cf 200nM) and EcoRV_r (Cf 200nM) used as amplification primers. The PCR product was purified using the QIAquick PCR purification kit (Qiagen, cat. no. 28106) according to the manufacturer's instructions. The sequence of the final (NNN)15 DNA template was:

CGATCGAATTCTAATACGACTCACTATAGGGCTTAAGTATAAGGAGGAAAAAAT**ATGNNNNNNNNNN NNNNNNNNNNNNNNNNNNNNNNNNNNNNNNNNNNGCGATCTCGGTG**TGATGA*GATATC*AA TATCAAAAAGGATCCATATA (the T7 promoter is underlined, the translated region is in bold; the EcoRV site for iTP-seq is in italics) (also illustrated in Supplementary Fig. 54).

To generate the mRNA library for iTP-seq, *in vitro* transcription was performed at 37°C for 3 h, in a 60µl reaction volume containing 30pmol of the (NNN)15 library, 30µl RiboMAX™ Express T7 2X Buffer (contains NTPs) and 6µl Enzyme Mix T7 Express as per manufacturer's instructions (T7 RiboMAX™ Express Large Scale RNA Production System Promega, cat. no. P1320). Transcripts were purified using an RNA Clean & Concentrator-5 purification kit (Zymo Research, cat. no. R1015 or R1016) according to the manufacturer's instructions. The concentration of mRNA was determined using a NanoDrop spectrophotometer (Thermo Fisher Scientific). As illustrated in Fig. 14, 5'-biotinylation of the mRNA templates for *in vitro* translation is required – this facilitates the various downstream enzymatic reactions performed for iTP-seq since biotinylated transcripts can be attached to magnetic beads coated with streptavidin, thereby allowing easier washing steps without the need for exhaustive purification steps. For the biotinylation reaction, 672pmol of mRNA template was incubated at 65°C for 5 minutes after which 7µl 10X Capping Buffer, 14µl 3'-Biotin-GTP 5mM (70000pmol) (New England Biolabs, cat. no. N0760S) and 7µl Vaccinia Capping Enzyme (70 units) (New England Biolabs, cat. no. M2080S) were added in order and incubated at 37°C for

30 minutes as per manufacturer's instructions. Transcripts were again purified using the RNA Clean & Concentrator-5 purification kit (Zymo Research) according to the manufacturer's instructions. The biotinylation efficiency was determined using a dot blot, as follows. Amersham Hybond-N+ membrane (Cytiva, cat. no. RPN2020B) was treated with 6X SSC (Saline sodium citrate) buffer (0.9 M NaCl, 90 mM Na_3-citrate, pH 7.0) for 10 min and dried briefly between two pieces of Whatman paper. Biotinylated (NNN)15 mRNA and a 5'-biotinylated oligonucleotide standard (iTP_Biotin_standard) were diluted in 6X SSC buffer to 5, 2.5, 1.25, and 0.625 pmol/µl, and 1µl of each dilution was pipetted onto the membrane. The membrane was baked for 2 h at 80°C to adsorb nucleic acids and subsequently blocked in 5% [wt/vol] powdered milk in TBS-T (Tris-buffered saline-Tween) (50 mM Tris–HCl, 150 mM NaCl, and 0.05% [vol/vol] Tween-20, pH 7.5) for 1 h at room temperature. The TBS-T-milk solution was removed, and the membrane was incubated with a 1:1666 dilution of streptavidin-alkaline phosphatase antibody (Promega cat. no. V5591) in TBS-T for 1 h at room temperature. Unbound antibody was removed by washing three times with TBS-T buffer. Colorimetric detection was performed using an NBT/BCIP (Nitro blue tetrazolium / 5-bromo-4-chloro-3-indolyl-1-phosphate) detection kit (Promega cat. no. S3771) according to the manufacturer's instructions. The membrane was washed twice with TBS-T to stop the reaction and then imaged on a Bio-Rad Imager. The biotinylation efficiency was estimated by comparing the intensity of the sample dots with the intensity of the standard dots (Supplementary Fig. 54).

In vitro translation and generation of inverse toeprints

In vitro translation was carried out with a PURExpress ΔRF123 kit (New England Biolabs cat. no. E6850S), using ~5 pmol of 5'-biotinylated mRNA as a template. For odilorhabdins, NOSO-502 and NOSO-96624 (compounds provided by Dr Maxime Gualtieri, former CSO of Nosopharm) dissolved in molecular biology grade water were added at the bottom of 1.5mL tubes and evaporated using a miVac DNA concentrator (Fisher Scientific, cat. no. DNA-23050-B00) to obtain final concentrations of 0.3µM (NOSO-96624), 0.4µM (NOSO-502) and 40µM (both NOSO-502 and NOSO-96624) in separate 5µl reactions. Similarly, for tigecycline (tigecycline hydrate, Sigma-Aldrich, cat. no. PZ0021-25MG, lot no: 0000108201), a 10mM stock was prepared in DMSO and diluted in filtered DEPC (diethyl pyrocarbonate)-treated water to be added at the bottom of 1.5mL tubes and evaporated to reach final concentrations

of 0.05µM, 0.5µM, 5µM, 50µM and 500µM in separate 5µl reactions. Master mixes for translation reactions were prepared as per the manufacturer's instructions for a final volume of 5µl and added to each reaction tube with the dried antibiotic. Release factors 1 and 3 were added to the translation reaction according to the manufacturer's instructions, while release factor 2 was omitted to allow stalling of ribosomes that did not stall elsewhere on the coding sequence at the trap UGA stop codon at the end of the ORF. Elongation factor P (EF-P) was also added in the translation reaction mix to a final concentration of 10µM. *In vitro* translation was performed at 37°C for 30 min, after which the samples were placed on ice and 5µl ice-cold Mg2+ buffer (50 mM HEPES-KOH, 100 mM K-glutamate, 87 mM Mg-acetate, and 1 mM DTT, pH 7.5) was immediately added to the reactions. 1µl of truncated RNase R (3 mg/ml) (purified previously in the lab from plasmids gifted by Dr John Hunt and Dr Grégory Boël) was added, followed by an additional incubation for 30 min at 37°C to ensure complete mRNA degradation. 140µl of 1x BWT (Bind & Wash and Tween) buffer (5 mM Tris–HCl pH 7.5, 0.5 mM EDTA pH 8, 1 M NaCl, and 0.05% [vol/vol] Tween-20) was added to stop the reaction and increase the salt concentration to ensure that the ribosomes dissociate and inhibit RNase R. For each sample, 5µl of M-280 streptavidin Dynabeads (Thermo Fisher Scientific, cat. no. 11205D) were washed three times with 1x BWT buffer in DNA LoBind tubes (Eppendorf) and resuspended in 50µl of the same buffer. Each biotinylated mRNA library was then individually combined with Dynabeads and incubated on a tube rotator for 15 min at room temperature to allow biotin to bind to streptavidin. After incubation, beads were collected using a 16-tube SureBeads magnetic rack (Bio-Rad, cat. no. 1614916) and the supernatant was discarded. The beads were washed once with 1x BWT buffer to remove unbound RNA, followed by two washes with molecular biology grade H_2O to remove the 1x BWT buffer.

Library preparation for next-generation sequencing

The beads coated with RNA were resuspended in 4.5µl of H_2O, and 5.5µl of linker ligation reaction mixture was added to each reaction, reaching a final volume (Vf) of 10µl. The ligation mixture contained 1µl of 10x T4 RNA ligase 2 (truncated) buffer (New England Biolabs, cat. no. M0242L), 3µl of 50% PEG 8000 (New England Biolabs, included in cat. no. M0242L), 1µl oligonucleotide 3'_linker_ApoI (Cf 1µM in Vf 10µl) and 0.5µl of ligase (T4 RNA ligase 2, truncated Cf 9 U/µl, New England Biolabs, cat. no. M0242L). Linker ligation was allowed to

proceed on a tube rotator for 2 h at room temperature. Following ligation of the linker, beads were washed once with molecular biology grade water to remove unincorporated linker oligonucleotide and were resuspended in 11.5µl of water. Next, 1µl of dNTPs (10 mM of each – New England Biolabs, cat. no. N0447S) and reverse transcription primer oligonucleotide Linker_r (Cf 0.1µM) were added to each reaction and incubated at 65°C for 5 mins with 500rpm shaking for pre-annealing of the primer to its complementary sequence in the mRNA template. Samples were then placed on ice, and then reverse transcription mix containing 4µl of 5X First Strand synthesis buffer (Cf 1X, Thermo Fisher, cat. no. 18080044), 1µl of 100mM DTT (Cf 5mM – included in Thermo Fisher, cat. no. 18080044) and 1µl of reverse transcriptase (Superscript III – Cf 10U/µl – Thermo Fisher, cat. no. 18080044) was added to each sample and incubated at 55°C for 30 min at 500 rpm. Reverse transcribed cDNA was used without further purification as a template for PCR.

Pilot PCRs with 6-22 cycles were performed (98°C, 10s; 42°C, 10s; 72°C, 10 s) with oligonucleotides cDNA_Fwd (Cf 200nM) and Linker_r (Cf 200nM) to establish the optimal number of PCR cycles for obtaining a visible band on the gel while minimizing non-specific byproducts, as described in Gillard et al. 2026. Next, to generate double-stranded DNA for restriction digestion, a fill-up reaction was performed on the reverse transcribed cDNA using oligonucleotide cDNA_Fwd (Cf 200nM) by consecutive incubation at 98°C, 10s; 42°C, 10s; 72°C, 30s. The resulting double-stranded DNA was digested with 2.5µl of EcoRV-HF restriction enzyme (New England Biolabs, cat. no. R3195S), and the sample was incubated at 37°C for 1 h. Preparative PCR was then performed with the digested DNA as template and Linker_r (Cf 200nM) as reverse primer for the optimal number of cycles determined, and the same cycle conditions. The samples were then loaded on medium-sized 12% TBE-polyacrylamide gels and run at 175V for 18 hours. Bands containing inverse toeprints corresponding to stalled ribosomes from the initiation codon to the last NNN codon were excised from the gel with a clean scalpel. Excision of the band corresponding to stalling at the initiation codon was deliberately restricted to its upper half to bias the recovered fragments toward elongation stalls rather than initiation stalls within the available NGS sequence space (Supplementary Fig. 55). Gel pieces were crushed through 5mL syringes into 15mL Falcon tubes, and 10mL of gel extraction buffer (10 mM Tris–HCl pH 8, 500 mM NH_4-Acetate, and 10 mM EDTA pH 8) was

added. The tubes were incubated on a tube rotator at room temperature for 72 hours. Gel debris was separated from the extraction solution by filtering through 0.2µm Vivaspin 6 centrifugal concentrators (Sartorius, cat. no. VS0672). Each sample was then concentrated to ~1.2 mL using a miVac DNA concentrator (Fisher Scientific, cat. no. DNA-23050-B00). DNA was precipitated in 5mL Eppendorf tubes using ~1.2mL of isopropanol with 4µl GlycoBlue coprecipitant (Invitrogen, cat. no. AM9515) and incubated at −80°C overnight. After precipitation, DNA was recovered by centrifugation at 20000 × g for 45 min at 4°C. The supernatant was removed, and DNA pellets were resuspended in 20µl H_2O and used as templates for subsequent addition of the next-generation sequencing (NGS) adaptors.

Pilot PCRs with 10-18 cycles were performed (98°C, 10s; 42°C, 10s; 72°C, 10s) with long oligonucleotides NGS_adapter_f (Cf 20nM), NGS_adapter_index_r (Cf 20nM), and amplification primers NGS_f (Cf 200nM) and NGS_r (Cf 200nM) to establish the optimal number of PCR cycles for obtaining visible bands on the gel while minimizing non-specific byproducts, as described in Gillard et al. 2026. Both the forward and reverse long oligonucleotides contain Illumina TruSeq adapter sequences followed by 18 nucleotides complementary to the 5' or 3' region of the cDNA; the long reverse oligonucleotides also contain barcode sequences for multiplexing according to the commercially available Illumina TruSeq protocols. As such, a unique long reverse oligonucleotide was chosen per sample per replicate. Once the optimal number of PCR cycles was determined, preparative PCRs were performed under the same cycling conditions. PCR products were purified using the QiaQuick PCR purification kit. The size and concentration of the fragments obtained were measured using a 2100 Agilent Bioanalyzer (Agilent Technologies, cat. no. G2939A) with the DNA 1000 kit (Agilent, cat. no. 5067-1504).

Next-generation sequencing and analysis of iTP-Seq data

Next-generation sequencing was performed by the BGI Genomics Facility in Hong Kong on an Illumina HiSeq X Ten system to obtain 150bp paired-end reads. The reads were paired using PEAR v0.9.10 (Jiajie Zhang et al. 2014) with the maximal proportion of uncalled bases in a read set to 0 (-u option) and the upper bound for the resulting quality score set to 126 (-c option). Then, the reads were parsed and analyzed using the itpseq (v1.0.0) open-source Python library (https://pypi.org/project/itpseq/) developed to process inverse-toeprinting data (Gillard et al.

2026). During the parsing step, the script extracted the sequences flanked by the TruSeq adapter sequences GTATAAGGAGGAAAAAAT and GGTATCTCGGTGTGACTG, which were introduced during library preparation. A maximum of two mismatches within each of these flanking regions was permitted, and all other reads were discarded. Common lab-specific and experiment-specific contaminant sequences were also filtered out during this step. A quality control was then applied that retained reads starting with an ATG initiation codon and having a minimum Phred Q-score of 30. Differential ribosomal stalling analysis in antibiotic-treated versus untreated samples was also performed using the itpseq analysis library, which serves as a Python wrapper executing differential expression (DE) analysis via PyDESeq2 (Muzellec et al. 2023), an implementation of the DESeq2 framework (Love et al. 2014). Statistically significant enriched or depleted arrest motifs were identified using an adjusted p-value threshold 0.05 adjusted via the Benjamini-Hochberg false discovery rate (FDR) procedure.

Software versions

Python 3.12.7; Matplotlib 3.9.2; NumPy 2.1.3; SciPy 1.15.2; Pandas 2.2.3; Seaborn 0.13.2

2.2.2. Classical Toeprinting/Primer Extension Inhibition

Toeprinting reactions

Toeprinting was performed as described previously (Orelle, Carlson, et al. 2013), with modifications. Briefly, gBlocks Gene Fragments (Integrated DNA Technologies) were designed containing a T7 promoter, a ribosome binding site, a sequence coding for the arrest motif of choice, followed by a spacer with stop codons and a sequence for the binding of the reverse transcription primer (denoted as NV1, as described in Vazquez-Laslop et al. 2008). The gBlocks were then amplified using the oligonucleotides T7_TP (Cf 200nM) and TP_Rev_Short (Cf 200nM).

The sequence of the toeprinting mRNA templates was:

CGATCGAATATTAATACGACTCACTATAGGGCTTAAGTATAAGGAGGAAAAAAT**ATG**-arrest_motif-*AGCGAATAATAACTGACTCTGAACAACATCCGTACTCTTCGTGCGCAGGCAAGGTTAATAAGCAAAATTCATTATAACC* (the T7 promoter is underlined; the start codon is in bold; the NV1 sequence is in italics; the sequences for arrest_motif are indicated in Fig. 31 and Supplementary Fig. 56).

In vitro transcription was then performed at 37°C for 1 h, in a 20µl reaction volume containing

500ng DNA, 10µl RiboMAX^{TM} Express T7 2X Buffer (contains NTPs) and 2µl Enzyme Mix T7 Express as per manufacturer's instructions (T7 RiboMAX^{TM} Express Large Scale RNA Production System Promega, cat. no. P1320). Transcripts were purified using the RNA Clean & Concentrator-5 purification kit (Zymo Research, cat. no. R1015 or R1016) according to the manufacturer's instructions. The concentration of mRNA was determined using a NanoDrop spectrophotometer (Thermo Fisher Scientific). *In vitro* translation was carried out with a custom PURExpress ΔRF123 kit ΔRibosome Kit (New England Biolabs, cat. no.: Solution A - B0229B-001; Solution FM (without RF123) - P0825B-001; *E. coli* ribosomes (RFs free) - P0824B-001), using 5pmol of mRNA as a template and a final concentration of 1.62µM *E. coli* ribosomes in 5µl reactions. Antibiotics were supplemented at necessary concentrations by drying at the bottom of tubes using a miVac DNA concentrator (Fisher Scientific, cat. no. DNA-23050-B00) at the beginning of the reaction. Elongation factor P (EF-P) (PURERFrex, cat. no. PFS052) was added to a final concentration of 2µM. Translation was performed at 37°C for 15 min, after which the Yakima Yellow-labelled primer complementary to the 3' end of the NV1 sequence (oligonucleotide NV_YY) (1µl from 2µM stock, hence Cf 0.33µM in 6µl) was pre-annealed for 5 min at 37°C. Reverse transcription was then performed with 50U of Avian Myeloblastosis Virus reverse transcriptase (Promega, cat.no. M5108) for 20 min at 37°C. Alkaline hydrolysis of the template RNA was then performed by incubating each reaction with 0.5µl of 10M NaOH at 37°C for 15 min. Samples were then neutralized with 0.7µl of 7.5M HCl, and the cDNA was purified using the QIAquick nucleotide removal kit (QIAGEN cat. no. 28306). The purified samples were dried using a miVac DNA concentrator (Fisher Scientific, cat. no. DNA-23050-B00) and resuspended in 6µL Formamide Loading Dye (0.25% wt/vol of Bromophenol blue and 20 mM EDTA pH8 in formamide).

Sanger sequencing reactions

Before Sanger sequencing, DNA templates were treated with ExoSAP-IT reagent (Thermo Fisher Scientific, cat. no. 78200.200.U) as per the manufacturer's instructions to remove excess dNTPs and primers. Dideoxynucleoside Triphosphate Set (ddNTP) was purchased from Sigma-Aldrich (cat. no. 03732738001) as 10mM solutions. ddNTP mixes for the sequencing were prepared as follows with dNTPs mix (10 mM of each – New England Biolabs, cat. no. N0447S): ddATP mix (350µM ddATP + 20µM dNTPs mix), ddCTP mix (200µM ddCTP + 20µM

dNTPs mix), ddGTP mix (30µM ddGTP + 20µM dNTPs mix) and ddTTP mix (600µM ddTTP + 20µM dNTPs mix). 17µl of a master mix containing 1pmol Exo-SAP-IT-treated DNA template and 1µl Hemo KlenTaq enzyme (New England Biolabs, cat. no. M0332S) was prepared, with final concentrations of 1X Hemo KlenTaq Buffer 5X (New England Biolabs, cat. no. B0332S), 120nM NV_YY primer, and 0.6mM $MgCl_2$. 4µl of this master mix was added to 2µl of each of the ddNTP mixes, and the following thermocycler program was used for each of the 6µl reactions: 2 mins denaturation at 95°C, 40 cycles of (95°C, 30s; 42°C, 30s; 70°C, 1min), 5 mins elongation at 70°C. The samples were purified using the QIAquick nucleotide removal kit (QIAGEN), dried using a miVac DNA concentrator (Fisher Scientific, cat. no. DNA-23050-B00) and resuspended in 3µL Formamide Loading Dye.

Toeprinting and sequencing samples were heated for 5 min at 80°C to denature secondary structures, and 1.5µl of each of the sequencing and toeprinting reactions were separated by 5.8% TBE-Urea PAGE (2000 V, 300mA, 40W for 2.5 h) followed by detection on an Amersham Typhoon Gel and Blot Imaging System (GE Healthcare Life Sciences).

2.2.3. Cryo-EM single particle reconstruction of NOSO-502-bound *E. coli* 70S ribosomes stalled on the mDDP motif

Preparation of an *E. coli* mDDP-70S-NOSO-502 40µM complex for cryo-EM

Stalled ribosomal complexes for cryo-EM were obtained by *in vitro* translation of the mDDP-containing template used for toeprinting reactions. *In vitro* translation was carried out using a custom PURExpress ΔRF123 kit ΔRibosome Kit (New England Biolabs, cat. no.: Solution A - B0229B-001; Solution FM (without RF123) - P0825B-001; *E. coli* ribosomes (RFs free) - P0824B-001), with final concentrations of 3.26µM mRNA template and 1.63µM purified *E. coli* KC6 70S ribosomes. NOSO-502 was added at a final concentration of 40µM by drying at the bottom of a 1.5mL tube using a miVac DNA concentrator (Fisher Scientific, cat. no. DNA-23050-B00) at the beginning of the reaction. Elongation factor P (EF-P) (PURERex, cat. no. PFS052) was added to a final concentration of 2µM. Translation was performed at 37°C for 15 min and then diluted in NOSO-502-supplemented Polymix Buffer B (30mM HEPES-KOH pH 7.5, 5mM $MgCl_2$, 50mM NH_4Cl, 5mM 2-mercaptoethanol, 2mM spermidine, 5mM putrescine, 40µM NOSO-

502) (recipe from Rundlet et al. 2021 and similar to Leroy et al. 2023), to yield a final concentration of 400nM ribosomes.

Cryo-EM grid preparation (performed by Dr Fanny Boissier)

Quantifoil carbon grids (QF-R2/2-Cu, 300 mesh) were coated with a thin carbon layer (~2 nm) using a Safematic ccu-010 HV carbon coater. Grids were glow-discharged for 20 s at 2.5 mA before application of 4µl of mDDP-70S-NOSO-502 40µM complex. After blotting for 3 s and waiting for 30 s (blotting force 5), grids were plunge-frozen in liquid ethane using an FEI Vitrobot Mark IV (Thermo Fisher Scientific) set to 4 °C and 100% humidity.

Cryo-EM data acquisition (performed by Dr Fanny Boissier)

Cryo-EM data were collected on a Glacios 2 (Thermo Fisher Scientific) microscope operated at 200kV and equipped with a Falcon 4 camera and a Selectris filter at the IECB in Pessac, France. Images were recorded with SerialEM with a pixel size of 0.694Å at a magnification of 165,000X to record 44 movie frames with an exposure time of 2.58 seconds using a dose rate of 0.918 $e^{-}/Å^2$ per frame for a total accumulated dose of 40.41 $e^{-}/Å^2$ (Table 3 in Chapter 3). The initial dataset was composed of 12,374 micrographs with defocus values ranging from -0.5 to -1.9 µm.

Cryo-EM image processing

Data were processed in CryoSPARC v4.7.1 (Punjani et al. 2017) according to the workflow in Fig. 32 (Chapter 3). Briefly, the raw movie frames were summed and corrected for drift and beam-induced motion at the micrograph level using Patch Motion Correction, and the contrast transfer function (CTF) was estimated using Patch CTF Estimation. Micrographs were subsequently curated using Curate Exposures based on average intensity, defocus, astigmatism, relative ice thickness, and total motion drift, retaining 12,101 micrographs. Initial particle picking was performed using Blob Picker, yielding 1,126,564 picked particles. Next, well-defined two-dimensional classes were selected by 2D classification, and using these classified particles as templates, cleaned particles were picked from the micrographs with Template Picker, retaining 745,601 particles. Particles were 2.8X downsampled and subjected to 6 rounds of iterative Ab-initio reconstruction and Heterogenous refinement, following the decoy classification strategy proposed by Oliver Clarke (https://discuss.cryosparc.com/t/new-cryosparc-tutorial/14188), to remove junk particles from the dataset. Duplicate particles

within a 100Å separation distance were removed, and full-size particles were re-extracted; these 519,225 particles were refined with Non-uniform (NU) refinement. Subsequent Global CTF refinement, Local CTF refinement, Reference-based motion correction and final NU refinement produced a consensus reconstruction of the *E. coli* 70S ribosome at 2.1Å resolution based on the gold-standard FSC=0.143 cutoff, from 517,053 particles. Three-dimensional classification was performed in three steps: (i) a focused 3D classification using a 30S subunit mask (derived from PDB 7ZTA (Leroy et al. 2023)), separating 50S subunits and unclassified low-quality or artifactual particles from intact 70S ribosomes, (ii) a second focused 3D classification on the intact 70S population from the previous round, with the 30S mask, yielding 10 initial classes, and (iii) focused 3D classifications on each of the 10 initial classes with masks targeting elongation factors EF-Tu, EF-G, and E-, P- and A-site tRNAs (classical and hybrid states) (masks derived from PDB 5UYM (Loveland et al. 2017), PDB 6WDF (Loveland et al. 2020), PDB 7SSD (Carbone et al. 2021) and PDB 7ZTA (Leroy et al. 2023)). This yielded 27 distinct classes with a total of 388,256 particles. Each of the 27 final classes was subjected to independent NU refinement to produce 27 reconstructed maps across a resolution range of 2.57-6.73Å, based on the gold-standard FSC=0.143 cutoff. Local resolution estimation for the 27 reconstructions was performed in CryoSPARC using the Local Resolution Estimation job with a local FSC threshold of 0.5, and local resolution maps were visualized in UCSF ChimeraX v1.10 (Goddard et al. 2018; Meng et al. 2023) (Supplementary Fig. 57). Pixel size was optimized by calculating model-to-map correlation coefficients at multiple pixel sizes in ChimeraX v1.10, selecting the pixel size that yielded the highest coefficient value.

Initial Model Building and Structural Analysis

Published atomic models of *E. coli* translation elongation intermediates (Loveland et al. 2017, 2020; Carbone et al. 2021; Petrychenko et al. 2021; Rundlet et al. 2021) were rigid-body fitted into the 27 reconstructed maps using the “fitmap” function in UCSF ChimeraX v1.10 to identify functional states of the maps and additional density for NOSO-502. For each map, the closest published conformation was selected as a template and fitted via rigid-body alignment followed by molecular dynamics flexible fitting (MDFF) in ISOLDE (Croll 2018), yielding initial models. Ligand restraints for NOSO-502 were generated from *T. thermophilus* NOSO-502-bound 70S X-ray structure coordinates shared by collaborators Elena Aleksandrova and Yury

Polikanov (UIC, Chicago), using PHENIX (Liebschner et al. 2019) ReadySet! The drug was refined against a representative map via PHENIX real-space refinement, rigid-body-fitted into all 27 maps, and merged with the initial models. Domain rotations of the 30S head (residues 921-1397 of the 16S rRNA) and body (residues 2-920 and 1398-1540 of the 16S rRNA) were quantified using the Ribosome Angle Decomposition Tool (RADTool) (Hassan et al. 2023), relative to an unrotated reference 70S structure (PDB 4V9D; Dunkle et al. 2011).

Figures showing cryo-EM density or atomic models were prepared using ChimeraX v1.10.

Chapter 3

Mechanism of inhibition of translation by the odilorhabdin class of peptide antibiotics

The first class of antibiotics I studied during my thesis is odilorhabdins, a novel class of peptide antibiotics that were discovered and characterized in the last decade. At the onset of this work, it was known that these are miscoding drugs that target the decoding center of the bacterial ribosome and interfere with the decoding and translocation steps of translation elongation in a concentration-dependent manner (Pantel et al. 2018). It was also suspected that these drugs act in a sequence-dependent manner, but this aspect was not characterized extensively.

My first aim, as mentioned in Chapter 1, was to investigate the sequence-dependent inhibition of translocation by odilorhabdins and identify the landscape of arrest motifs on which drug-bound *E. coli* ribosomes stall during translation, using the iTP-Seq method. Further, I aimed to investigate the structures of drug-bound ribosomes stalled on the mRNA while translating specific sequence motifs, using cryo-EM SPA, to find out how decoding center perturbations by odilorhabdins can lead to downstream translocation defects.

The discovery of odilorhabdins and their characterization was headed by Nosopharm, a former startup based in Nîmes, France. Their CSO, Dr Maxime Gualtieri, provided our lab with two odilorhabdin compounds, NOSO-502 and NOSO-96624, for this research – NOSO-502 was in pre-clinical studies against *Enterobacteriaceae*-caused catheter-associated urinary tract infections (cUTIs), while NOSO-96624 was in a patenting process at the time. Unfortunately, Nosopharm was liquidated in 2024, and although NOSO-96624 was eventually patented and its chemical structure was published (Gualtieri et al. 2024), industrial research and development of odilorhabdins is currently not known to be ongoing.

In this chapter, I first introduce the background of the discovery of odilorhabdins, their chemical compositions, and the X-ray crystallographic structure of the NOSO-95179-bound *Thermus thermophilus* ribosome, which captured the first snapshot of an odilorhabdin-bound bacterial ribosome (Pantel et al. 2018). I then describe and explain the results obtained from the iTP-Seq and toeprinting experiments, based on which I arrived at two representative arrest motifs that stall translating ribosomes in the presence of NOSO-502 and NOSO-96624. For the iTP-Seq analyses, I worked together with Dr Thibaud Renault, the author of the now open-source itpseq Python library (https://pypi.org/project/itpseq/) (Gillard et al. 2026), which was still in development and improvement when I analyzed the data. Structural analyses were

subsequently done on odilorhabdin-bound ribosomes stalled on both arrest motifs, separately. Due to legal and intellectual property uncertainties surrounding the proprietary status of NOSO-96624 during the active experimental phase of this project, structural determination was focused exclusively on the advanced lead candidate, NOSO-502. Three cryo-EM datasets were collected for two chosen arrest motifs – all grids were prepared by Dr Fanny Boissier, who also performed two collections (one for each arrest motif) at the IECB in Pessac using a Glacios 2 microscope with a Falcon 4 camera and a Selectris energy filter. Another data collection was performed at the ESRF in Grenoble by Dr Pauline Juyoux using a Titan Krios G4 microscope with a Falcon 4i camera and a Selectris X energy filter, for one of the arrest motifs. At the stage of structural analyses, I shared the work with Dorian Gayral, another PhD student in our group, who analyzed the two datasets for one arrest motif, and I analyzed one dataset for the other arrest motif. As such, in the latter part of this chapter, I describe the cryo-EM ensemble reconstructions only from the dataset that I analyzed.

Finally, I discuss the current hypothesis, based on my results, on how NOSO-502 inhibits translation elongation by targeting the decoding and translocation steps.

3.1. Introduction: Odilorhabdins - a Novel Class of Peptide Antibiotics

3.1.1. From the discovery of odilorhabdins to the optimisation of lead compounds

Gram-positive actinomycetes have represented a major traditional source of natural antibiotics since the Golden Age of antibiotic discovery. These were identified using early methods of screening soil-derived actinomycetes for antimicrobial activity against a susceptible test microorganism by detecting zones of growth inhibition on an overlay plate – however, in the post-genomics era, it is now understood that these bacteria produce antibiotics as secondary metabolites using biosynthetic gene clusters (BGCs) like non-ribosomal peptide synthetases (NRPSs) and polyketide synthases (PKSs), which are giant multimodular enzymes involved in the production of a variety of secondary metabolites (reviewed, among others, in Walsh 2008; Lewis 2013; Bloudoff and Schmeing 2017; Süssmuth and Mainz 2017; Liu et al. 2019). In the wake of the antibiotic resistance crisis, the search for novel potential antibiotic-producing biosynthetic gene clusters has continued in previously untapped microbial resources, using sequencing-based whole-genome mining, coupled with mass spectrometric analyses of gene products. This has led to the discovery of such NRPS and PKS genes also in the Gram-negative gammaproteobacterium *Xenorhabdus nematophila*, belonging to the *Morganellaceae* family of the *Enterobacterales* order, making it an additional source for novel bioactive compound discovery, including antibiotics (Akhurst 1982; Forst et al. 1997; Bode 2009; Gualtieri et al. 2009; Tobias et al. 2017).

Xenorhabdus sp. is an entomopathogenic symbiotic bacterium which inhabits the intestine of the soil-dwelling nematodes *Steinernema* sp. and *Heterorhabditis* sp. The dauer stage of the nematodes, known as infective juveniles, infects the larvae of soil-inhabiting insects and releases the bacteria into the haemocoel of the insects. The bacteria specifically kill the insect by releasing toxins and immunomodulators but benefit the nematode by releasing antibiotics that protect the insect carcass from competing microorganisms. This allows the entire insect biomass to act as an energy source for nematode reproduction and proliferation (Gualtieri et al. 2009; Tobias et al. 2017; Pantel et al. 2018; Racine and Gualtieri 2019) (Fig. 16). One such class of antibiotics is odilorhabdins (ODLs) (initially, odilomycins), which are linear polycationic bactericidal peptides with six standard proteinogenic amino acids and four to six non-standard amino acids (Gualtieri et al. 2016; Pantel et al. 2018).

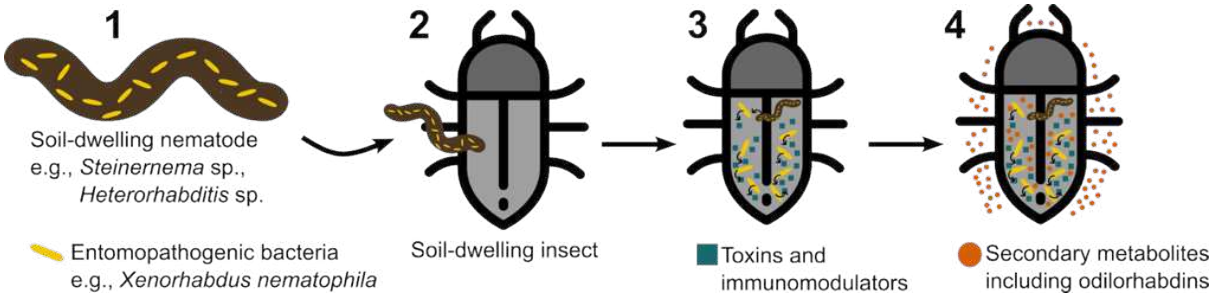

Figure 16: Odilorhabdin production by entomopathogenic bacteria. (1) Entomopathogenic bacteria like *Xenorhabdus nematophila* (in yellow) are symbiotic to and inhabit the intestine of soil-dwelling nematodes (in brown). When the nematode infects an insect (2), the released bacteria produce toxins and immunomodulators (in teal) which kill specifically the insect but not the nematode (3). (4) The bacteria also produce a set of antibiotics called odilorhabdins (in orange) as secondary metabolites, which kill other neighboring microbial competitors.

The odilorhabdin biosynthetic gene cluster (*odl*-BGC) in the genome of *X. nematophila* contains four core genes (*odlS1-odlS4*), which encode NRPS proteins responsible for ODL biosynthesis, and ten putative tailoring genes, *odlA-J*, predicted to be responsible for modification of the compounds (Lanois-Nouri et al. 2022; Präve et al. 2024). Each NRPS module of the *odlS* genes comprises i) an adenylation domain (A) which selects and activates specific amino acids, ii) a thiolation/peptide carrier protein domain (T/PCP) that binds the amino acid via thioester bond formation, iii) a condensation domain (C) that forms the peptide bond between the nascent peptide chain and the subsequent amino acid, and iv) a termination or thioesterase/reductase module (Te/R) that releases the peptide from the enzyme (Süssmuth and Mainz 2017; Pantel et al. 2018; Präve et al. 2024) (Fig. 17). Of the three conserved accessory genes (*odlA-C)* upstream of the *odlS1-S4* core, *odlA* encodes a diamino butyrate (Dab) aminotransferase, which is suggested to be involved in the synthesis of the Dab precursor, one of the non-standard amino acids involved in ODL synthesis. *odlB* encodes a β-hydroxylase to synthesise Dab(βOH) from Dab, which is a substrate used by the *odlS* domains, and *odlC* encodes a Gcn-5-related N-acetyltransferase, involved in self-resistance of the drug in *X. nematophila*, which is elaborated in Section 3.1.3. *odlD-odlH* are situated downstream of the core NRPS genes – *odlD* encodes a predicted ABC transporter-related protein, *odlE* encodes a lysine δ-hydroxylase, *odlF* encodes an L-arginine β-

hydroxylase, *odlG* encodes a periplasmic deacylase with a specificity for peptides with lysine in the N-terminus, *odlH* is a yet uncharacterized putative acylase (Präve et al. 2024), and *odlI* and *odlJ* are conserved hypothetical proteins belonging to the superfamily of clavanimate synthase-like domains (Lanois-Nouri et al. 2022). Overall, it is hypothesized that odilorhabdins are synthesized in an acylated inactive pre-odilorhabdin form, which OdlD then exports to the periplasm, where OdlG deacylates the pre-odilorhabdin, creating the active compound, which can be secreted as an antibiotic to other microbes (Präve et al. 2024).

The first three natural ODLs isolated from the supernatant of cultured *X. nematophila* strain K102 (CNCM I-4530) were called NOSO-95A, NOSO-95B and NOSO-95C (Fig. 17) (Pantel et al. 2018), identified and developed by Nosopharm, a biotechnology company in Nîmes, France, specialising in the discovery and development of odilorhabdins. The sequences of the peptides, solved by nuclear magnetic resonance (NMR) studies and verified by *de novo* chemical synthesis, were revealed to be:

- NOSO-95A:

  Lys_1-Dab(β-OH)$_2$-Dab(β-OH)$_3$-Gly_4-D-Orn_5-Pro_6-His_7-Dhl_8-Dha_9-Dhl_{10}-Dbt_{11}

- NOSO-95B:

  Lys_1-Dab(β-OH)$_2$-Dab(β-OH)$_3$-Gly_4-D-Orn_5-Pro_6-His_7-Dhl_8-Dha_9-**Lys_{10}**-Dbt_{11}

- NOSO-95C:

  Lys_1-Dab(β-OH)$_2$-Dab(β-OH)$_3$-Gly_4-D-Orn_5-Pro_6-His_7-**Lys_8**-Dha_9-**Lys_{10}**-Dbt_{11}

The residues other than the standard amino acids in these antibiotics are α, γ-diamino-β-hydroxybutyric acid (Dab(β-OH)), D-ornithine (D-Orn), δ-hydroxylysine (Dhl), α, β-dehydroarginine (Dha), and α, δ -diaminobutane (Dbt). As indicated in bold, the Dhl10 of NOSO-95A is substituted by Lys10 in both NOSO-95B and NOSO-95C, while the Dhl8 of NOSO-95A is substituted by Lys8 in NOSO-95C (Pantel et al. 2018).

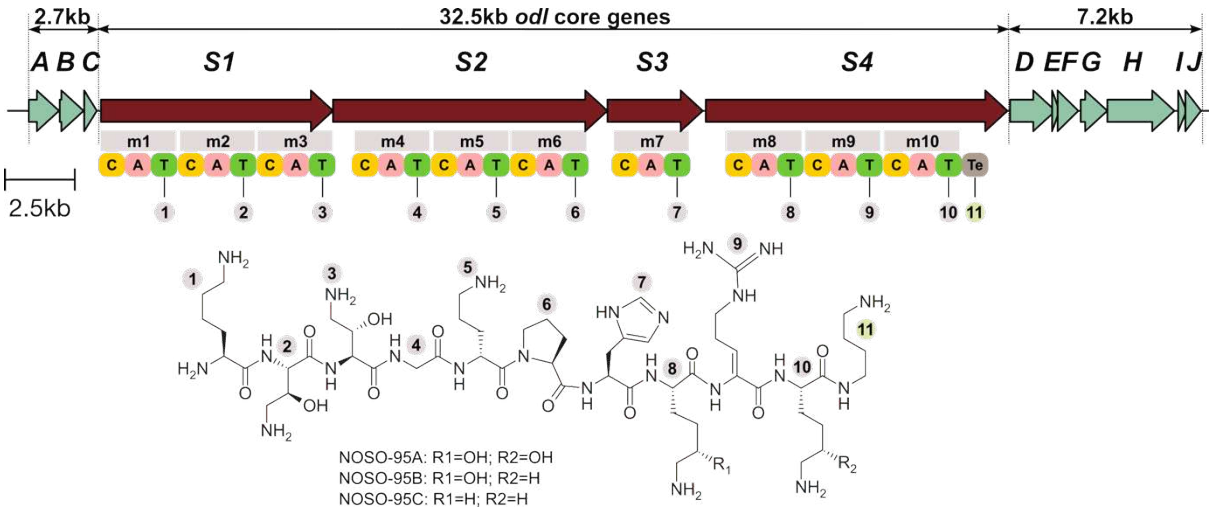

Figure 17: Odilorhabdin biosynthetic gene cluster in *Xenorhabdus nematophila*. The core *odl(S1-S4)* genes (in brown) of the biosynthetic gene cluster encode NRPS modules (m1-m10) responsible for odilorhabdin biosynthesis, and the ten putative tailoring genes, *odl(A-J)* (in light green), are predicted to be responsible for the modification of the compounds. Each NRPS module of the *odlS* genes comprises an adenylation domain (A) (in pink), a thiolation domain (T) (in green), a condensation domain (C) (in yellow), and a termination module (Te) (in grey). Each of the ten modules contributes a residue of the natural odilorhabdin peptide (NOSO-95A/B/C), as indicated from 1 to 10. The Dbt_{11} residue is a modification introduced by the *odlS4* Te domain. Source: Sequence accession number LT966404 from project PRJEB17644, European Nucleotide Archive (Pantel et al. 2018). Figure generated using anti-SMASH 8.0 (Blin et al. 2025) and Clinker (Gilchrist and Chooi 2021), adapted and modified from (Pantel et al. 2018; Lanois-Nouri et al. 2022; Präve et al. 2024).

The peptidic nature of ODLs allowed room for modification of the structures by *de novo* chemical synthesis, and extensive structure-activity relationship (SAR) studies were performed on synthetic NOSO-95C to improve drug activity (Sarciaux et al. 2018). NOSO-95C was systematically modified via alanine-scanning mutagenesis, side-chain alterations of non-standard amino acids, and truncation of the C- and N-termini. The antibacterial efficacy of these novel derivatives against *Enterobacteriaceae* (*E. coli* and *K. pneumoniae*) was evaluated by determining their minimum inhibitory concentrations (MICs) using standard broth microdilution methods. Further, incorporation of radiolabeled precursors into biopolymers (e.g., protein, DNA, RNA, peptidoglycan) of *E. coli* cells revealed that ODLs primarily interfere with protein synthesis in bacteria (Pantel et al. 2018). Additionally, the capacity of ODLs to inhibit bacterial translation was quantified by determining half-maximal inhibitory concentration (IC_{50}) values using cell-extract-based *in vitro* coupled transcription-translation (IVTT) systems. Such studies further helped to identify or predict which side chains of the

peptides were essential for translation inhibition. IC_{50} assays were also performed in rabbit reticulocyte cell-free IVTT systems to check if the drugs additionally inhibit eukaryotic translation. The combination of the best modifications led to the first synthetic ODL, NOSO-95179, which was used as the starting point for a lead-optimization campaign. In NOSO-95179, the Dab(β-OH)$_3$ of NOSO-95C is replaced by Ala and the Lys_{10} and Dbt_{11} are removed. NOSO-95179 is also 300-fold more active in translation inhibition in bacteria than in eukaryotes, compared with only 16-fold for NOSO-95C (Pantel et al. 2018; Sarciaux et al. 2018; Racine and Gualtieri 2019). Further lead optimization to enhance *in vitro* antibacterial activity and *in vivo* efficacy, while having no cytotoxicity in the HepG2 human cell line, led to the synthesis of around 500 analogues. These were in turn examined for MICs against a large and heterogeneous panel of resistant bacterial strains, ADME-Tox properties (blood stability, acute toxicity and hemolysis in mouse models), and pharmacokinetic properties (plasma protein binding and efficacy in murine sepsis infection model) (Racine et al. 2018; Racine and Gualtieri 2019). NOSO-502 showed the best profile, where the Ala_3 and His_7 of NOSO-95179 are substituted with Dab_3 and ortho-fluorophenylalanine (o-F-Phe_7), respectively (Fig. 18).

NOSO-502 is active against several multidrug-resistant *Enterobacteriaceae* strains, including polymyxin-resistant, ESBL (extended spectrum β-lactamase)-resistant, colistin-resistant and carbapenem-resistant *Enterobacteriaceae* (CRE). For example, NOSO-502 is active against CRE with MICs in the range of 0.5-4μg/mL (Racine et al. 2018). Experiments with clinical isolates further demonstrated the potent *in vitro* activity of NOSO-502 against *Escherichia coli, Klebsiella pneumoniae*, *Enterobacter* spp., *Citrobacter* spp., and *Serratia marcescens* (Attwood et al. 2025). NOSO-502 is also effective against *E. coli* in several models of infection *in vivo*, as demonstrated by dose-dependent bactericidal activity in neutropenic murine thigh infection models of hospital-acquired infections like sepsis, complicated urinary tract infections (cUTIs), and lung infections, protecting against the highest-incidence hospital pathogens *E. coli* and *K. pneumoniae*, including an *E. coli* strain expressing the metallo-β-lactamase NDM-1, resistant to major antibiotic classes (Racine et al. 2018; Racine and Gualtieri 2019). NOSO-502 also exhibited a good safety profile based on data from *in vitro* nephrotoxicity, cardiotoxicity, genotoxicity and cytotoxicity standard studies in murine thigh infection models (Racine et al. 2018; Zhao et al. 2018; Attwood et al. 2025). NOSO-502 was hence chosen as the first pre-

clinical odilorhabdin candidate against *Enterobacteriaceae*-caused catheter-associated urinary tract infections (cUTI), approaching Phase 1 human studies (Attwood et al. 2025).

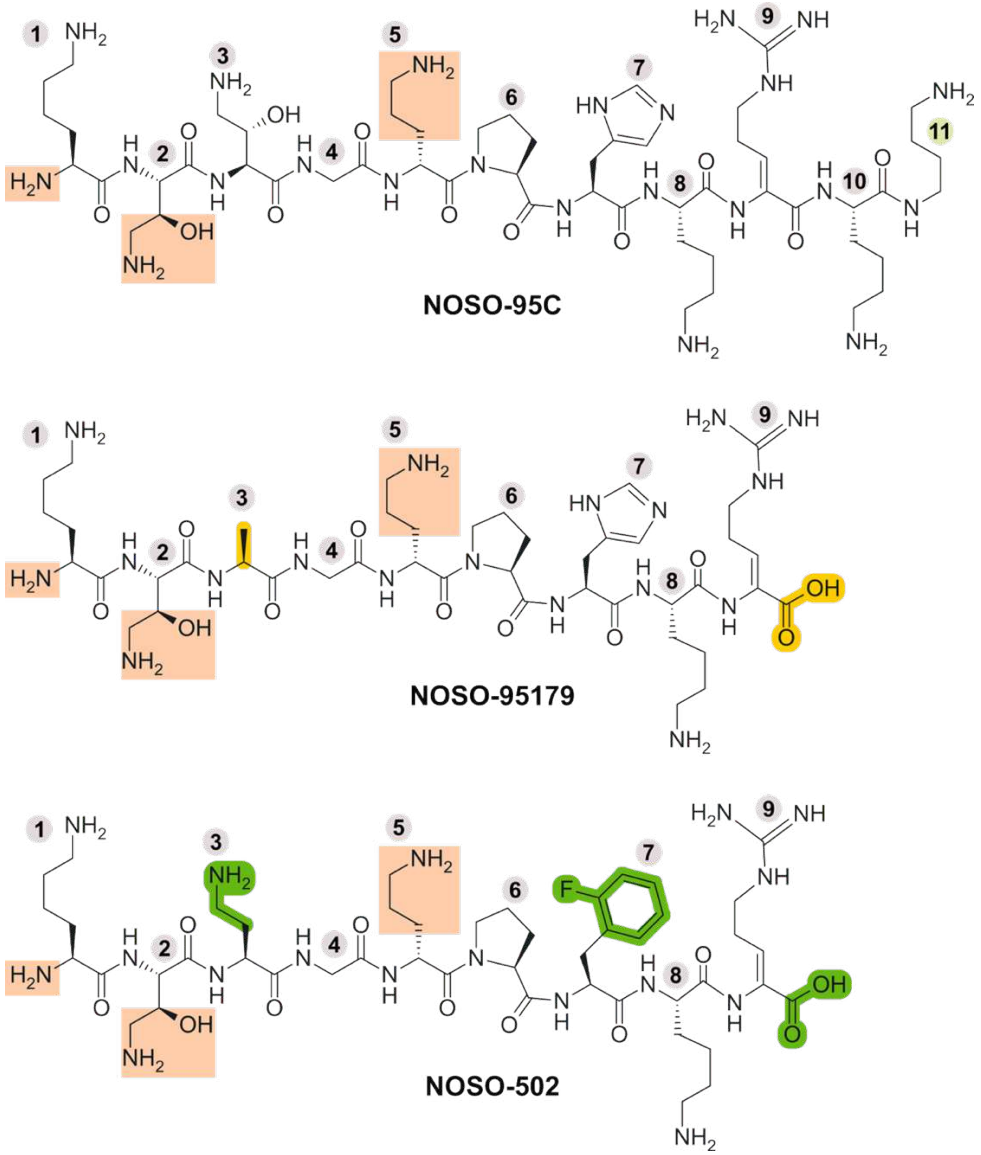

Figure 18: Chemical structures of odilorhabdin lead compounds. The synthetic odilorhabdin NOSO-95179 is obtained chemically by replacing the Dab(β-OH)$_3$ of NOSO-95C with Ala, and by removing the Lys$_{10}$ and Dbt$_{11}$. Changes in NOSO-95179 from NOSO-95C are highlighted in yellow. NOSO-502 is obtained chemically by replacing the Ala$_3$, and His$_7$ of NOSO-95179 with Dab$_3$, and o-F-Phe$_7$, respectively. Changes in NOSO-502 from NOSO-95C are highlighted in green. Side chains of residues 1, 2 and 5 (highlighted in salmon) have been reported to interact with the ribosome, involving roles in inhibition of bacterial translation, and remain unchanged in all three compounds (Pantel et al. 2018; Racine et al. 2018; Sarciaux et al. 2018; Racine and Gualtieri 2019).

3.1.2. Odilorhabdins target the decoding center of the bacterial ribosome

When evaluated in bacterial cell-free IVTT systems, the translation inhibition profiles of odilorhabdins yielded IC_{50} values within the same range (~0.5-0.6µM) as established ribosome-targeting antibiotics such as chloramphenicol and spectinomycin (Pantel et al. 2018; Racine and Gualtieri 2019). Hence, to identify the primary target of NOSO-95179 within the bacterial ribosome, bacteria that were resistant to odilorhabdins at 10-fold MIC were screened for mutations in ribosomal RNA. This selection is a powerful tool, since surviving clones are expected to carry mutations that reduce drug binding and sequencing these clones can reveal the drug target. However, this process in wild-type bacteria is typically hindered by genetic redundancy, as *E. coli* carries seven identical, redundant copies of the rRNA operon. A mutation in a single operon is recessive and masked by the remaining wild-type copies, which continue to bind the drug, arrest translation, and cause cell death. To circumvent this limitation, the screening strategy used the engineered *E. coli strain* SQ110, which lacks six of its seven chromosomal rRNA operons (Orelle, Carlson, et al. 2013; Quan et al. 2015; Pantel et al. 2018). Subsequent whole-genome sequencing of the selected single-operon ODL-resistant clones revealed a distinct clustering of mutations within the 16S rRNA gene localized near the decoding center, directly confirming the ribosome as the primary functional target. Interestingly, none of the resistance mutations conferred cross-resistance to other known ribosome-targeting antibiotics, such as tetracycline, tigecycline, gentamicin, kanamycin or chloramphenicol, indicating that odilorhabdins have a unique binding site, distinct from other antibiotics (Pantel et al. 2018). Further, the crystal structure of the *Thermus thermophilus* 70S ribosome associated with mRNA, A-, P- and E-site tRNAs and 250µM NOSO-95179 at 2.6-Å resolution, confirmed that odilorhabdins bind near the decoding center in the 30S ribosomal subunit (Pantel et al. 2018; Racine and Gualtieri 2019).

Odilorhabdins were shown to form multiple hydrogen bonds with the sugar-phosphate backbone atoms of the 16S rRNA residues of helices 31, 32 and 34, rather than to the rRNA bases directly. The α-amine of the Lys_1 residue of NOSO-95179 also forms a hydrogen bond with the non-bridging phosphate oxygen of C32 of the anticodon loop of the A-site tRNA (Fig. 19). This simultaneous interaction of the drug with the ribosome and the tRNA was hypothesized to potentially decrease the accuracy of translation by increasing the affinity of

the tRNA to the ribosome during decoding, allowing the binding of near-cognate aminoacyl-tRNAs and additionally interfering with the translocation of the A-site tRNA to the P-site. A secondary binding site of NOSO-95179 was also found at the interface of the 30S and 50S subunits, near the site where h44 of the 16S rRNA and H64 of the 23S rRNA interact with each other – the drug here interacts with the backbones of nucleotides 1472-1474 of the 16S rRNA, nucleotides 1987-1989 of the 23S rRNA, and the Glu45 side chain of the uL14 ribosomal protein. This site is far from known functional centers of the ribosome, and unlikely to interfere with translocation; hence it was deemed to be functionally irrelevant since under the experimental condition of 250μM antibiotic, there is also a possibility of the positively charged flexible ODL to bind promiscuously to the polyanionic rRNA scaffold (Pantel et al. 2018).

Toeprinting analysis of ribosomes stalling during translation on *E. coli* genes such as *ompX* and *csrA* further revealed that NOSO-95179 preferentially induces pausing at certain codons such as Leu (CUG and CUU), Gln (CAA), Arg (CGA), Ile (AUU) and Lys (AAA). The mode of translation inhibition was not only indicated to be sequence-dependent, but also concentration-dependent. At lower concentrations of the drug (~0.6μM), the fidelity of decoding is reduced, exemplified by bypass of hungry codons during *in vitro* cell-free translation, readthrough of premature stop codons *in vivo*, and amino acid misincorporation at sites of inactivating missense mutations *in vivo* (Pantel et al. 2018). Additionally, at higher concentrations (≥ 20μM), toeprinting analyses showed ribosomes primarily arrested at early codons, indicating that the progression of the ribosome along the mRNA is deterred (Pantel et al. 2018). This was attributed to a slowdown in translocation caused by drug-induced binding of near-cognate tRNAs in the A-site, which leads to inefficient accommodation of the mismatched codon–anticodon pair in the P-site (Pantel et al. 2018).

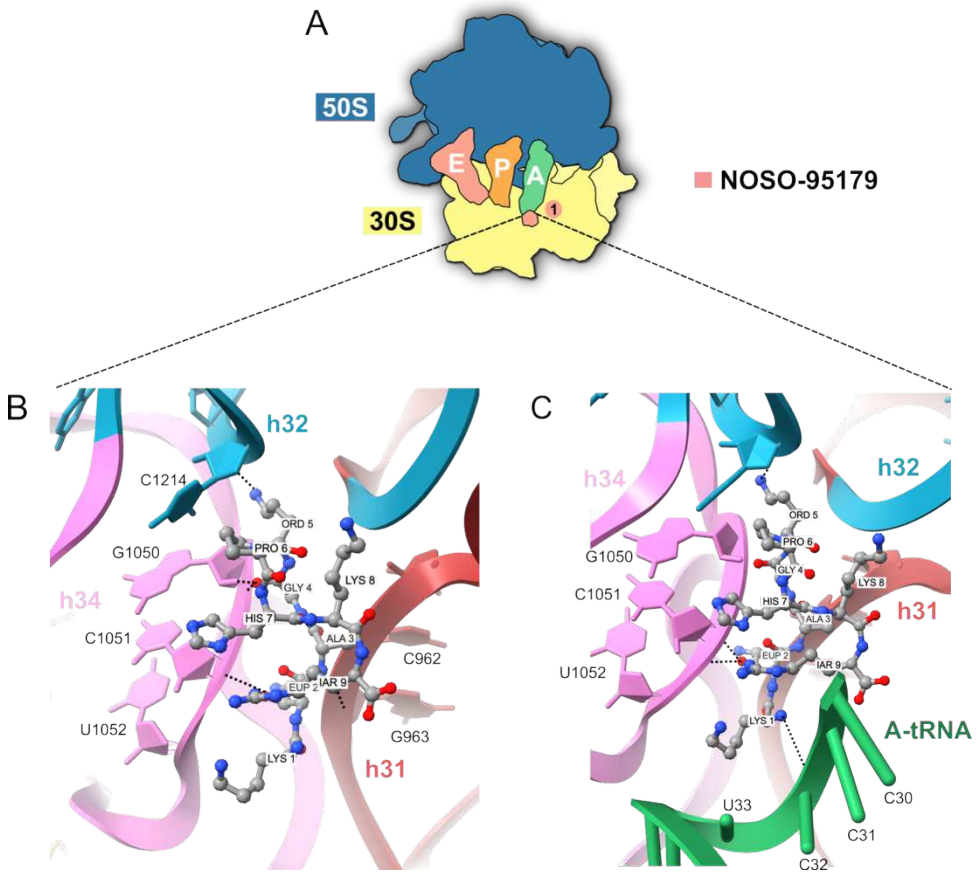

Figure 19: NOSO-95179 bound to the *T. thermophilus* 70S ribosome (*E. coli* numbering). (A) NOSO-95179 primarily binds to the bacterial ribosome at the decoding center of the 30S subunit near the anticodon stem-loop of the A-site tRNA. (B, C) NOSO-95179 (shown in ball-and-stick) interacts with the sugar-phosphate backbone atoms of the 16S rRNA residues of helices 31 (in brown red), 32 (in light blue) and 34 (in pink), and simultaneously with C32 of the anticodon loop of the A-site tRNA (in green). Source: PDB ID 6CAE (Pantel et al. 2018).

3.1.3. Resistance to odilorhabdins

As discussed in Section 3.1.1, the ODL-producing *Xenorhabdus nematophila* protect themselves from the produced antibiotics due to the selective resistance conferred by the Gcn-5 related N-acetyltransferase (GNAT)-encoding *oatA* or *odlC*, which has been found only in *X. nematophila* and a single phylogenetic clade of *Photorhabdus* sp (Lanois-Nouri et al. 2022). OdlC catalyses the transfer of an acetyl group from acetyl-CoA to a primary amine, causing the mono-, bi- or tri-acetylation of the amines in the side chains of Dab(βOH) or D-Orn in the peptide antibiotic, which decreases the inhibitory and antibacterial activity of the altered compound (Sarciaux et al. 2018; Lanois-Nouri et al. 2022). Since the N-terminal free

α-amine of the ODL is essential for translation inhibition via direct interaction with the sugar-phosphate backbone of helix 34 of the 16S rRNA (Pantel et al. 2018), acetylation hinders antibiotic action (Lanois-Nouri et al. 2022).

Although horizontal gene transfer of *odlC* has not yet been reported, a few other ODL-resistance mechanisms have been identified and explored in recent years. For example, *Klebsiella pneumoniae* strains with missense mutations in the *crrB* gene are NOSO-502-resistant. *crrB* belongs to the crrAB two-component system, which is variably present in *K. pneumoniae* but absent in *E. coli*. CrrB is a signal-transducing histidine kinase, while CrrA is an adjacent response regulator, and mutations in the *crrB* gene are responsible for NOSO-502 resistance via upregulation of the *kexD* gene, which is predicted to encode an energy-dependent resistance nodulation division (RND) efflux pump component. KexD is hypothesized to pump NOSO-502 out of the cell, probably in conjunction with the AcrAB-TolC efflux system (Racine et al. 2018; Pantel et al. 2021, 2022). Further, clinical isolates of *Pseudomonas aeruginosa* have shown variable levels of resistance to NOSO-95C and NOSO-502, due to overexpression of the MexXY-OprM efflux pump, which extrudes the antibiotic out of the cell (Gualtieri et al. 2024). Recent studies with clinical isolates have also shown that *Proteus mirabilis* and *Morganella morganii* are intrinsically resistant to NOSO-502, with MICs exceeding 16 µg/mL. This resistance is hypothesized to stem from their taxonomic classification within the *Morganellaceae* family, which also includes the ODL-producing *Xenorhabdus* sp., suggesting potential similarities in protein synthesis machinery and mechanisms of ODL resistance (Attwood et al. 2025).

Although resistance mechanisms to NOSO-502 have been identified, their overall impact appears limited, and the drug retains activity against a broad spectrum of susceptible bacterial species, supporting the continued therapeutic potential of odilorhabdins.

3.1.4. Towards further characterization of odilorhabdins

As mentioned at the beginning of the chapter, during my PhD, I have studied two odilorhabdin compounds – NOSO-502 and NOSO-96624. The structure of NOSO-96624 is:

Lys_1–Dab(β-OH)$_2$–Dab_3–Gly_4–D-Orn_5–Pro_6–(**p-carboxy-Phe)$_7$**–Lys_8–Dha_9**–Lys_{10}–Nspd(β-OH)$_{11}$**

where the o-F-Phe$_7$ of NOSO-502 is substituted with (para-carboxy-Phe)$_7$ and a Lys$_{10}$ has been added, followed by a 2-hydroxynorspermidine (Nspd(β-OH)) polyamine tail (Fig. 20).

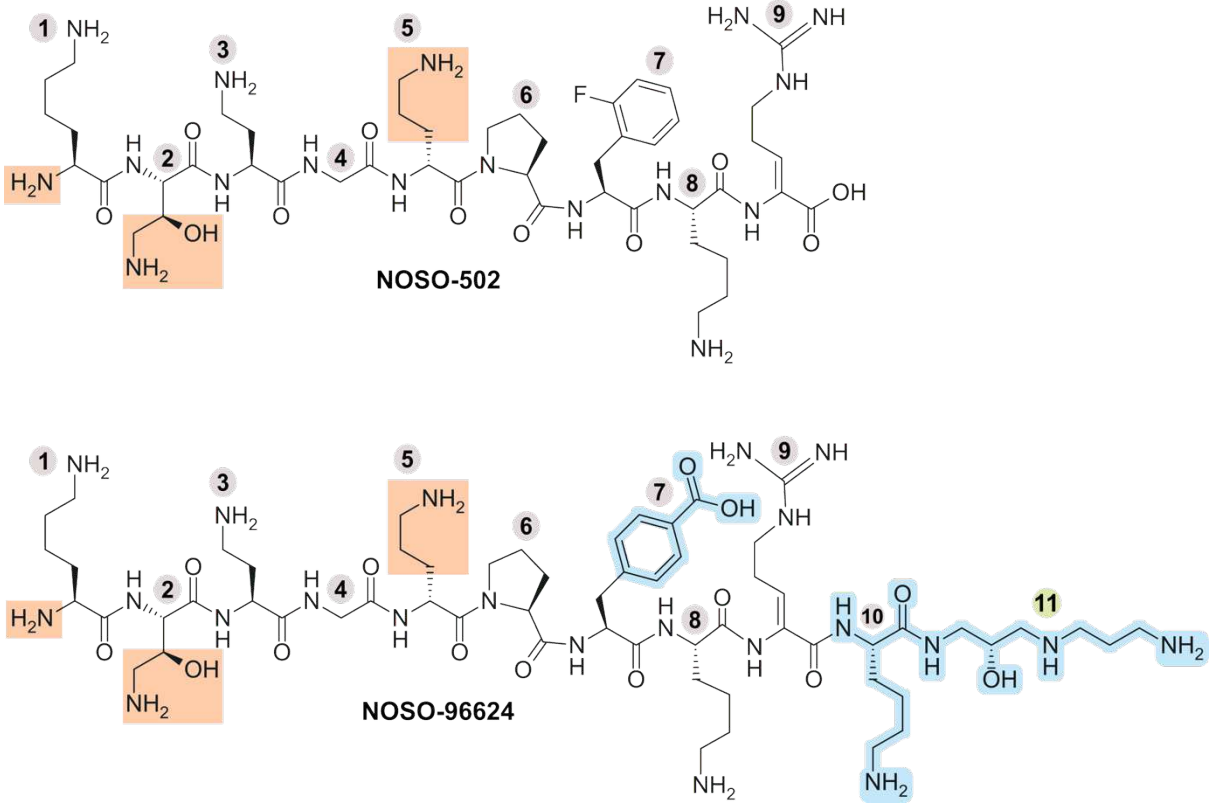

Figure 20: Chemical structures of NOSO-502 and NOSO-96624. NOSO-96624 is obtained chemically by replacing the o-F-Phe$_7$ of NOSO-502 with p-carboxy-Phe$_7$ and adding a Lys$_{10}$ followed by an Nspd(β-OH) polyamine tail. Changes in NOSO-96624 from NOSO-502 are highlighted in blue. Side chains of residues 1, 2 and 5, which are considered important for the inhibition of bacterial translation by odilorhabdins, remain unchanged in both compounds and have been highlighted in salmon (Racine et al. 2018; Gualtieri et al. 2024).

Given that the structure of the parent compound NOSO-95179 in complex with the ribosome is already available (Pantel et al. 2018), and the specific side chains driving its ribosomal interactions are conserved in the derived NOSO-502 and NOSO-96624, it is logical to assume both compounds share a similar mechanism of action as NOSO-95179. However, several questions about the mechanism have remained unanswered.

For example, although the context-dependent activity of odilorhabdins was first reported in that work, stalling of ribosomes in the presence of NOSO-95179 was tested on a limited number of genes and codon sequences, and was not characterized extensively. Hence,

questions such as – why only certain codons lead to ribosomal stalling, whether sequence-dependence is a function of the codon, the tRNA reading the codon or the amino acid that gets incorporated, and how the sequence-dependence can be linked to misreading of the genetic code – remained to be explored. In this regard, by studying two different compounds that have certain side chain differences among themselves, I wanted to also check whether the context-dependence of odilorhabdins changes based on modifications in residues that are not yet reported to interact with the ribosome. Further, while the X-ray crystallographic structure captured the binding sites of the drug and characterized its interaction with the A-site tRNA, the ribosomal complex for crystallization was assembled *in vitro* with tRNAi in the P-site and cognate tRNA-Val in the A-site (Pantel et al. 2018). This complex, constrained by the crystal lattice, is not representative enough to capture the exact context of translation, and hence the question remains regarding how actively translating ribosomes with an available pool of tRNAs would behave when they encounter the drug.

Thus, one of the objectives towards my goal of finding a comprehensive mechanism of action of odilorhabdins was to determine the structure of a ribosome that cannot continue translocation due to the binding of NOSO-502 and is hence stalled. For this purpose, I decided to perform *in vitro* translation using the PURE system (Shimizu et al. 2001), which contains the minimal set of factors necessary for *in vitro* protein translation in *E. coli*. Notably, this provides a pool of tRNAs, purified from *E. coli* B cell extracts, for ribosomes to choose from and incorporate during translation. Further, I sought to determine the structure of the drug-bound stalled ribosome using cryo-EM single-particle analysis, as this technique can provide better insights than X-ray crystallography into the different conformational states of the ribosome during the specific stages of decoding and translocation. However, to capture a high-resolution structural snapshot of a stalled ribosome, I needed to identify an mRNA sequence whose translation could lead to defective translocation and hence, ribosomal stalling. The suspected context-dependent mode of action of odilorhabdins, in addition to the need for a specific mRNA sequence to be translated, led me to perform a systematic characterization of the sequence-dependent stalling of ribosomes using the high-throughput technique of iTP-Seq. By performing iTP-Seq on a template library featuring an N-terminal variable region of 15 randomized (NNN) codons, in the presence or absence of two related but different

odilorhabdins - NOSO-502 and NOSO-96624 - I aimed to identify the sequences that stall translating ribosomes specifically in the presence of odilorhabdins. Unlike performing low-throughput toeprinting experiments on different gene sequences, performing high-throughput iTP-Seq on a randomized library could cover a much deeper sequence space and provide a broader overview of how odilorhabdins can change the translational landscape. Based on these iTP-Seq findings, I could then identify sequences that can homogeneously stall drug-bound ribosomes on a particular codon, in a specific sequence context, using classical toeprinting experiments. This would be the sequence of mRNA that I would use during *in vitro* translation for cryo-EM sample preparation and subsequent structural data collection without necessitating any intermediate purification steps. This pipeline combining high-throughput iTP-Seq and low-throughput classical toeprinting, followed by cryo-EM structural analysis, was deemed promising to obtain a comprehensive understanding of the odilorhabdin-induced sequence-dependent stalling of ribosomes, shedding deeper insights into a more detailed mechanism of action than already described in the literature.

In the following sections of this chapter, I discuss the results obtained from these outlined experimental designs.

3.2. Results and Discussion

3.2.1. Determination of concentrations of odilorhabdins to be used in iTP-Seq experiments

iTP-Seq is a technique that identifies at which mRNA sequences ribosomes stall during *in vitro* translation; it does not provide any information on misreading of the mRNA and/or misincorporation of amino acids by tRNAs. While it was indeed reported that ribosomal stalling is observed at high concentrations of odilorhabdins, and that low concentrations lead to misreading (Pantel et al. 2018), I performed iTP-Seq at both low and high concentrations to check if certain mRNA-sequence-dependent stalling events are observable at low concentrations as well. The chosen "low" and "high" concentrations for experiments with NOSO-95179 were 0.6µM and ≥20µM respectively. However, since NOSO-502 and NOSO-96624 are both slightly chemically different from NOSO-95179, I decided to first perform a luciferase expression inhibition assay with a titration of odilorhabdin concentrations as described in Section 2.2.1, to find out their half-maximal inhibitory concentrations (IC_{50}). As illustrated in Fig. 21, the IC_{50} of NOSO-502 and NOSO-96624 were found to be 0.4µM and 0.3µM respectively, and hence these were chosen as the "low" concentrations for the drugs. Despite the minimal difference between them, I maintained two separate "low" concentrations to compare both drugs at equivalent functional activity. For the "high" concentration condition, 40µM (~100-fold above IC_{50} and also exceeding the minimum ≥20µM threshold previously defined for ribosomal stalling) was chosen for both drugs to ensure complete drug saturation of the ribosomal decoding center.

Therefore, iTP-Seq was performed in biological quadruplicates, for five conditions:

i) no antibiotic (negative control)
ii) 0.4µM NOSO-502 ("low" concentration, IC_{50})
iii) 40µM NOSO-502 ("high" concentration)
iv) 0.3µM NOSO-96624 ("low" concentration, IC_{50})
v) 40µM NOSO-96624 ("high" concentration)

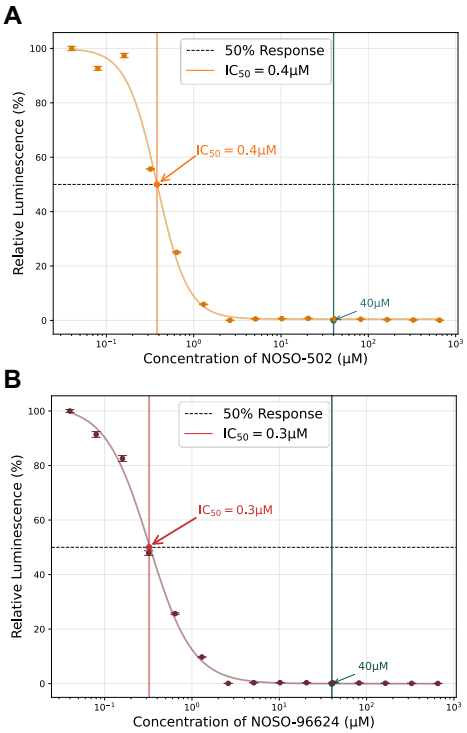

Figure 21: Half-maximal inhibitory concentrations (IC_{50}) of NOSO-502 and NOSO-96624. Luciferase-based reporter assays involving the *in vitro* translation of the firefly luciferase gene were performed in serial dilutions of NOSO-502 and NOSO-96624, in technical triplicate (i.e., three independent assay wells prepared from a single master mix per antibiotic concentration), and relative luminescence was measured and plotted as shown in panels A and B, respectively. The IC_{50} of NOSO-502 is 0.4µM, and that of NOSO-96624 is 0.3µM. iTP-Seq experiments were performed at the IC_{50} of each drug, considering them as "low" concentrations. A common high concentration of 40µM was also tested in iTP-Seq for each of the two drugs.

3.2.2. Processing of next-generation sequencing reads and quality control

iTP-Seq was performed using an (NNN)15 template DNA library as described in Section 2.2.1, and the reads obtained from short-read (paired-end, 150bp) next-generation Illumina sequencing were paired using PEAR v0.9.10 (Zhang et al. 2014), parsed, and analyzed using the itpseq open-source Python library (https://pypi.org/project/itpseq/) developed to process inverse-toeprinting data (Gillard et al. 2026).

During the parsing step, the script extracted the sequences flanked by the TruSeq adapter sequences GTATAAGGAGGAAAAAAT and GGTATCTCGGTGTGACTG, which were introduced during library preparation using oligonucleotides. A maximum of two mismatches within each of these flanking regions was permitted, and all other reads were discarded. Common lab-

specific and experiment-specific contaminant sequences were also filtered out during this step. A quality control was subsequently applied that retained reads starting with an ATG initiation codon and having a minimum Phred Q-score of 30, corresponding to 99.9% base call accuracy, meaning that the probability of an incorrect base call is 10^{-3} (Ewing et al. 1998; Ewing and Green 1998). To distinguish between an ATG codon for the initiator fMet and an elongating Met, the initiation codon at the start of a read is designated as atg in lowercase in the itpseq analysis software, with the corresponding amino acid denoted as m for fMet, while all other ATG codons are designated in uppercase, with the corresponding amino acid denoted as M for methionine. The analysis of the processed reads indicated a tri-nucleotide periodicity for fragments where RNase R cleavage had occurred 21–48 nucleotides downstream from the start codon (Fig. 22). Since the RNase R cleavage site is positioned +17-19 nucleotides downstream from the first nucleotide of the P-site (Seip et al. 2018), these fragments corresponded to 3-30 nucleotides (or 1-10 codons) downstream from the start codon, indicating that the first peak (~20nt, Fig. 22) corresponds to the initiation peak where the atg start codon occupies the P-site and one additional codon is present in the protected inverse toeprint. Further, while the triplet periodicity was reproducible, inter-replicate variations were observed at the initiation peak (codon 1 in Fig. 22), reflecting technical differences introduced while manually excising the high-intensity initiation gel bands as described in Section 2.2.1 and illustrated in Supplementary Fig. 55. Longer fragments that did not follow this triplet periodicity were excluded from further analysis. The proportion of the finally retained processed reads relative to the total reads collected per condition per replicate is shown in Fig. 23.

Finally, the script split the processed reads into codons, translated them into their corresponding amino acids and aligned the inverse toeprints relative to the ribosomal P-site. By convention, inverse toeprints are mapped by defining the P-site of the stalled ribosome as position 0 (Fig. 24). From the P-site towards the 5’ end of the mRNA (corresponding to the N-terminus of the nascent peptide), the numbering decreases, i.e., the E-site is designated as -1, the site further upstream as -2, and so on. Conversely, from the P-site towards the 3’ end of the mRNA (corresponding to the amino acid that has not yet been incorporated), the numbering increases, i.e., the A-site is designated as +1 or 1.

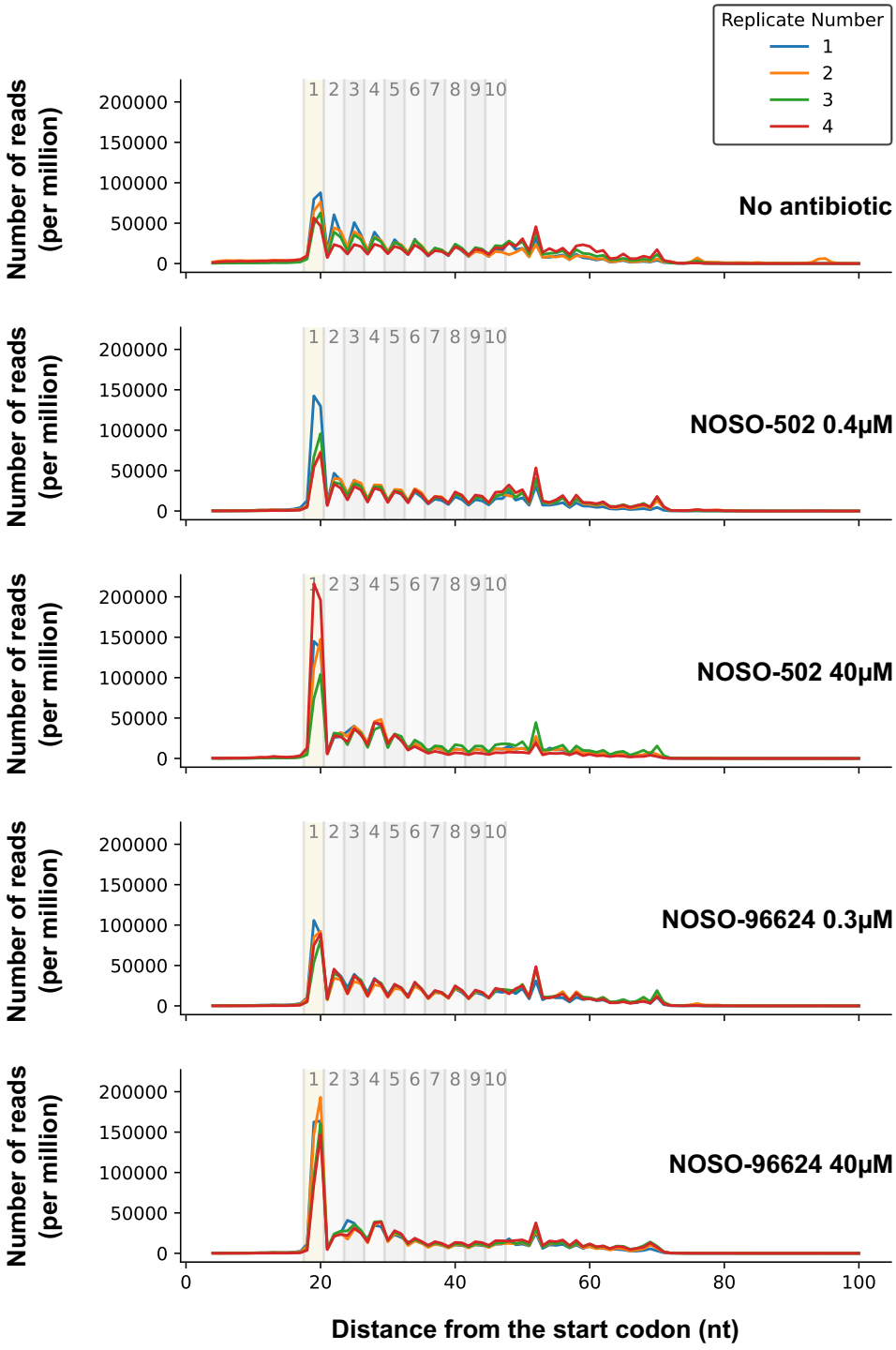

Figure 22: Distribution of obtained sequencing reads. Read counts, normalized to reads per million to adjust for differences in sequencing depth, are represented as a function of the distance from the start codon for untreated (no antibiotic) and odilorhabdin-treated samples across all four replicates. The shaded area (codons 1–10) highlights the reads selected for analysis, corresponding to the region where the three-nucleotide periodicity is well-defined. The first column in this shaded region is highlighted in yellow; this corresponds to ribosomes stalled at the initiation step of translation.

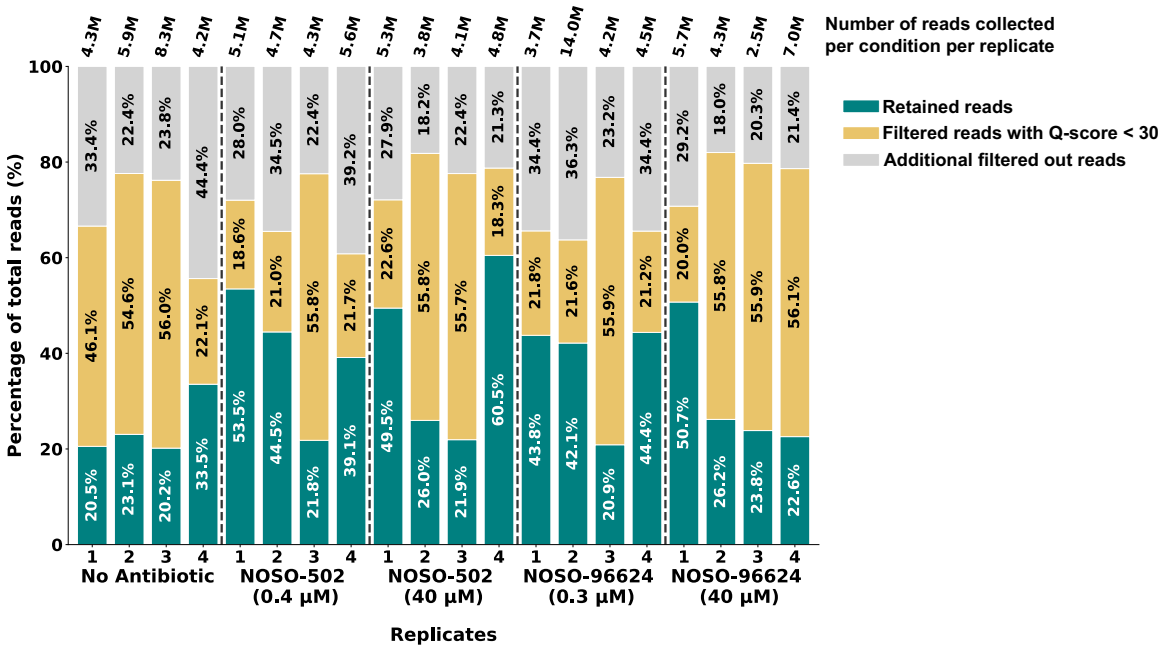

Figure 23: Proportion of sequencing reads retained after data processing and quality control. For each replicate of each experimental condition, the total number of collected sequencing reads is indicated at the top of the bar (M = millions), alongside the percentage of reads filtered out during quality control (in yellow) and additional data parsing (in grey). The retained reads (in teal) represent the percentage of reads that displayed well-defined triplet periodicity (codons 1-10) and were used for downstream analyses.



Figure 24: Schematic illustration of the nomenclature applied to the different ribosome sites on an inverse toeprint. The numbering of nucleotides and amino acids relative to the first nucleotide of the P-site codon (defined as position 0) is shown. The "protected overhang" represents the portion of the mRNA sequence physically covered by the stalled ribosome, which extends to the RNase R cleavage site (+17-19 nucleotides downstream from the first nucleotide of the ribosomal P-site) (Seip et al. 2018), indicated in dashed grey lines.

3.2.3. iTP-Seq reveals sequence- and concentration-dependent stalling of elongating ribosomes in the presence of NOSO-502 and NOSO-96624

Since odilorhabdins inhibit the decoding and translocation steps of translation elongation (Pantel et al. 2018), I focused my analysis on ribosomes stalled during elongation, i.e., inverse toeprints which do not contain the initiating formyl-methionine in the P-site. These reads were analyzed using the itpseq analysis library, which serves as a Python wrapper executing differential expression (DE) analysis via PyDESeq2 (Muzellec et al. 2023), an implementation of the DESeq2 framework (Love et al. 2014). To quantify motif enrichment between antibiotic-treated samples and the no-antibiotic reference control, the pipeline uses read counts for distinct sequence motifs across specified ribosome positions relative to the P-site using a negative binomial generalized linear model. The motif enrichment is expressed as the $\log_2$ (FoldChange) (LFC_i) for a given motif i as follows:

$$\text{Motif Enrichment } (LFC_i) = \log_2\left(\frac{\overline{K}_{i,\text{antibiotic}}}{\overline{K}_{i,\text{control}}}\right), \text{ and } \overline{K}_{ij} = \frac{K_{ij}}{s_j}, \text{ where}$$

K_{ij} = raw read counts for motif i in sample j,

s_j = DESeq2 size factor for sample j, calculated using median-of-ratios normalization to adjust for differences in sequencing depth, and

$\overline{K}_{ij}$ = normalized read count for motif i in sample j

To evaluate the statistical significance of these changes, the pipeline computes unadjusted p-values via Wald tests (Wald 1943) within the DESeq2 framework, followed by Benjamini-Hochberg adjustments (Benjamini and Hochberg 1995) to control the false discovery rate. Therefore, if we consider motif sequences with an adjusted p-value ≤ 0.05, the expected proportion of false discoveries within that set of motifs is 5%. Thus, a statistically significant (adjusted p-value ≤ 0.05), positive enrichment value indicates motif sequences where the antibiotic preferentially induces translation arrest or ribosomal stalling. Conversely, a significant negative enrichment value denotes sequences that are depleted in the antibiotic-

treated condition relative to the no-antibiotic condition, indicating motifs that the ribosome translates efficiently even in the presence of the antibiotic.

First, I analyzed the pairwise enrichment based on amino acid sequence across the -2, E, P and A-sites, for each of the four odilorhabdin-treated conditions, relative to the control (Fig. 25-28). I focused on the core E, P, and A-sites since they correspond to the primary mRNA-tRNA complexes within the stalled ribosome, and I included the -2 site to capture the sequence context in its immediate upstream vicinity. It is important to note here that while this analysis maps enrichment by amino acid identities, these designations reflect the coding capacity of the mRNA at the stalling site rather than the physical incorporation of these amino acids into the nascent peptide during an antibiotic-dependent arrest event.

At a low concentration of NOSO-502 (0.4µM) (Fig. 25), some of the most significant enrichment trends included the pairing of Pro codons in the P-site with several codons in the -2 and A-sites, Pro codons in the P-site with Glu/Asp/Pro codons in the E-site, Phe/Tyr codons in the A-site with several codons in the -2 and E-sites, and Lys/Pro codons in the E-site with several codons in the A-site. The most significant depletion trends included the pairing of Asp/stop codons in the A-site with several codons in the -2, E and P-sites.

At a low concentration of NOSO-96624 (0.3µM) (Fig. 26), the significant enrichment trends included the pairing of Pro codons in the P-site with several codons in the -2 and A-sites, Pro codons in the P-site with Glu/Asp/Pro codons in the E-site, Pro codons in the E-site with several codons in the A-site. Notably, no significant depletion trend could be observed for NOSO-96624 at this concentration.

These observations suggested that at their respective IC_{50}, both drugs induce sequence-specific stalling of ribosomes on similar motifs.

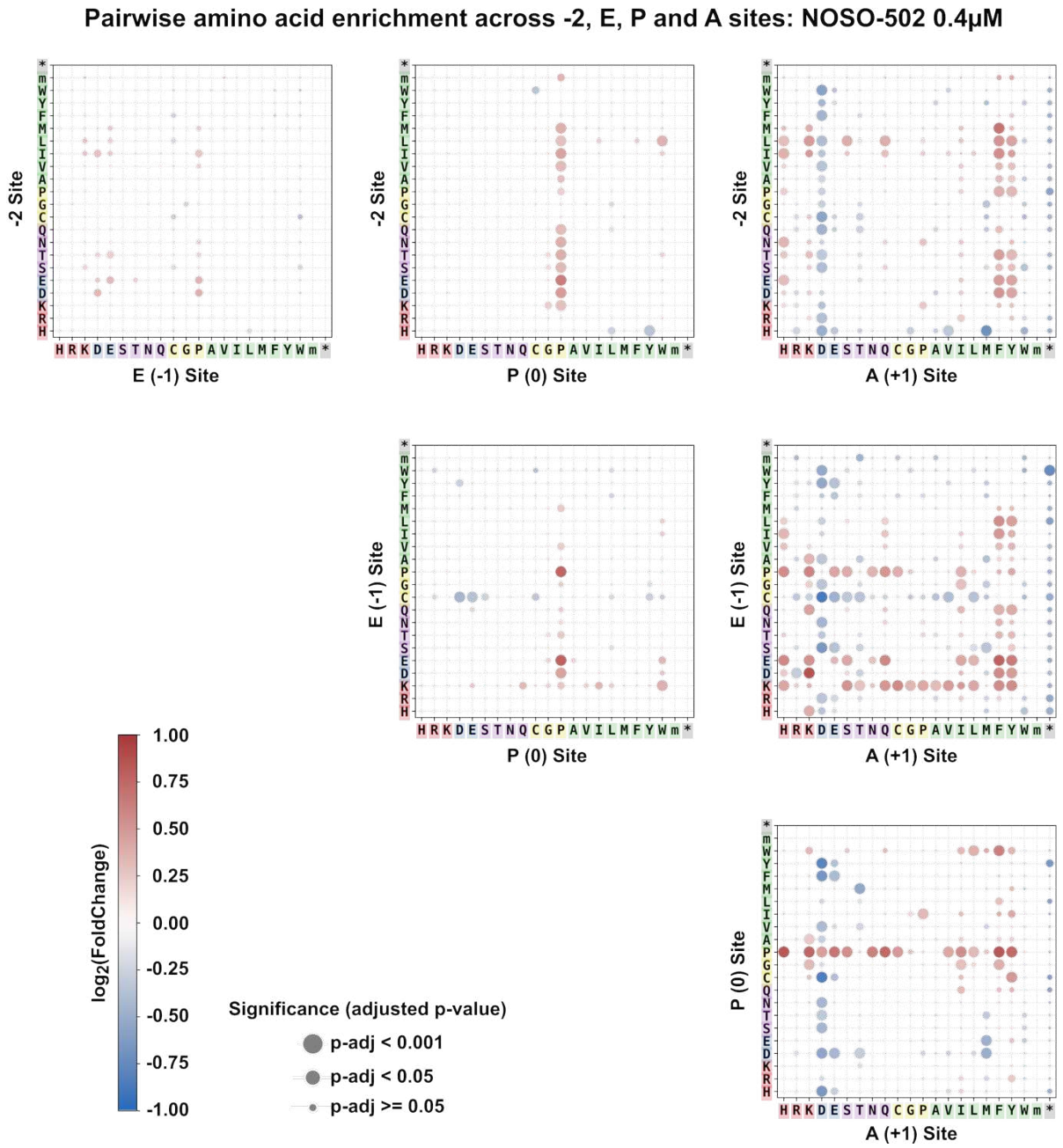

Figure 25: Heatmap grid representing the di-amino acid motifs enriched across -2, E, P and A-sites in the presence of 0.4µM of NOSO-502. Amino acid labels on the two axes are colored as follows: red – positively charged, blue – negatively charged, purple – polar, yellow – specific amino acids like Cys, Gly and Pro, and green – hydrophobic. Formyl methionine or fMet is denoted as m, while a stop codon is represented as an asterisk (*) symbol shaded in grey.

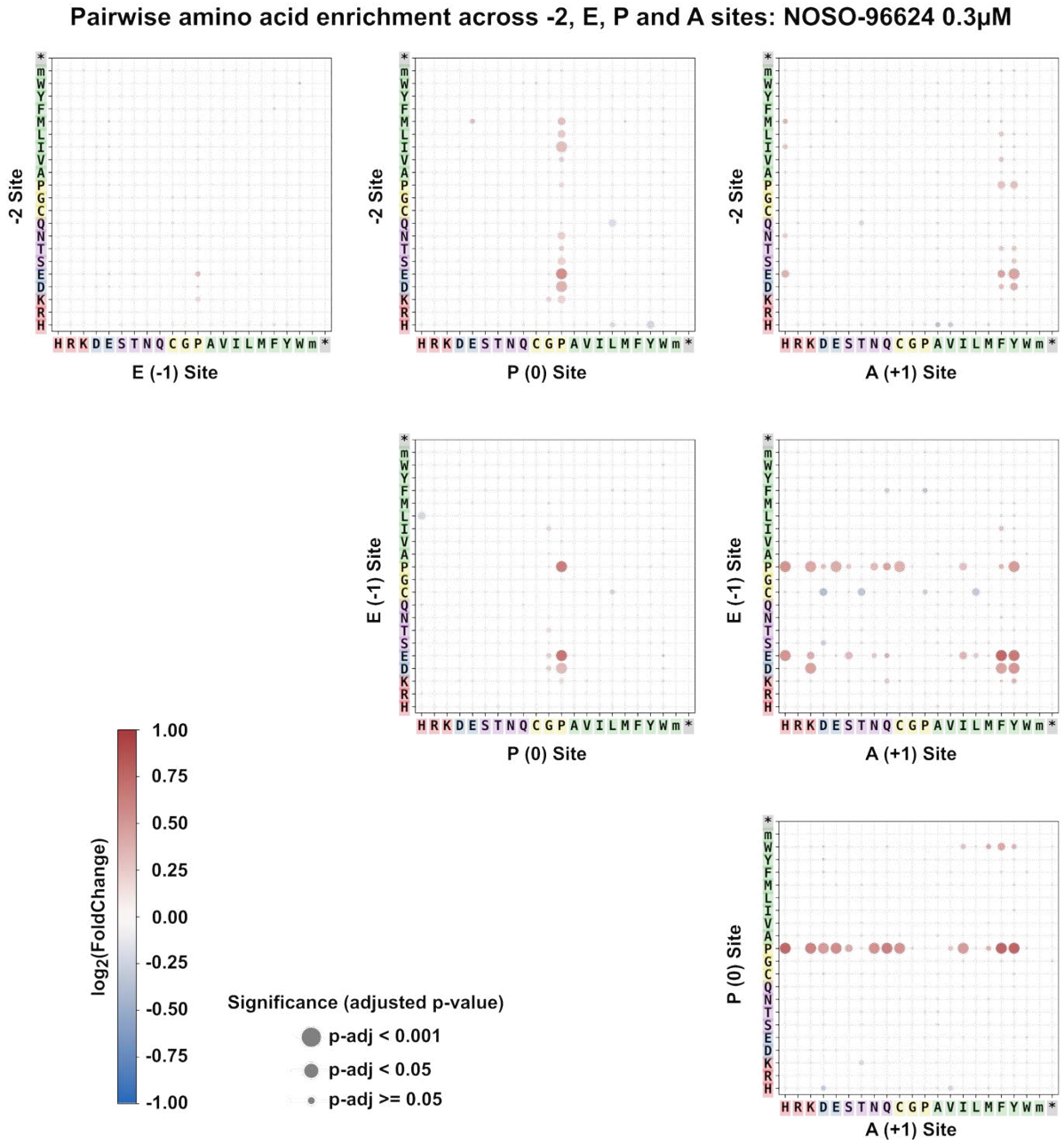

Figure 26: Heatmap grid representing the di-amino acid motifs enriched across -2, E, P and A-sites in the presence of 0.3µM of NOSO-96624. Amino acid labels on the two axes are colored as follows: red – positively charged, blue – negatively charged, purple – polar, yellow – specific amino acids like Cys, Gly and Pro, and green – hydrophobic. Formyl methionine or fMet is denoted as m, while a stop codon is represented as an asterisk (*) symbol shaded in grey.

In contrast to the low concentration conditions, analysis of the higher concentration (40µM NOSO-502 or NOSO-96624) samples (Fig. 27-28) revealed a more expanded repertoire of enriched di-amino acid motifs that were distinct from those observed at low concentrations, agreeing with previously reported findings that translocation inhibition is a feature characteristic of a higher drug concentration rather than a lower concentration (Pantel et al. 2018). For both NOSO-502 and NOSO-96624, the most significantly enriched motifs either featured Pro/Gln/Glu/Lys/His codons in the A-site or Cys/Pro/Phe/Tyr/Trp codons in the P-site. Further trends included the pairing of codons for hydrophobic amino acids like Met/Leu/Ile at the -2 site with several codons in the E, P and A-sites, and codons for the charged amino acids Glu/Asp/Lys at the E-site with several codons in the -2, P and A-sites. A variety of significant motif depletion trends were also observed in both high antibiotic concentration conditions, with pairing of Gly/Val/Ala codons in the -2 site with several codons in the E, P and A-sites; Cys/Ser/Phe/Tyr/Trp codons in the E-site with several codons in the -2, P and A-sites; Asp/Ile/Leu/Met codons in the P-site with several codons in the -2, E and A-sites; Asp/Thr/Asn/Ile/Met/Trp/stop codons in the A-site with several codons in the -2, E and P-sites.

Despite the differences in motif enrichment and depletion trends across different concentrations of the antibiotics, a few trends remained the same. For example, for both NOSO-502 and NOSO-96624, Pro codons were significantly enriched in the P-site for almost any codon combination, along with the signature enrichment of Pro codons in the P-site with Glu/Asp/Pro codons in the E-site. Similarly, Asp or stop codons were depleted in the A-site for most codon combinations at both high and low concentrations of NOSO-502.

This concentration-dependent increase in the variety of stalling motifs identified may be attributed to sub-stoichiometric drug occupancy at lower concentrations, where a lower fraction of antibiotic-bound ribosomes stalling at specific sequences is outnumbered by drug-free elongating complexes that do not stall at the arrest motifs. In contrast, increasing to high drug concentrations likely saturates occupancy, efficiently trapping translating ribosomes in a wider variety of sequences. However, future kinetic studies to validate drug binding and dissociation need to be performed to confirm this.

Finally, the distinct depletion of A-site stop codons may be explained by the fact that odilorhabdins are not known to interact with release factors, and hence when a release factor recognizes the stop codon, canonical translation termination proceeds without inducing ribosomal stalling. However, since odilorhabdins are known to induce stop codon readthrough (Pantel et al. 2018), i.e., they allow the misincorporation of aminoacyl tRNAs even when there is a stop codon at the A-site, this depletion signal possibly reflects both normal termination clearance and misreading events.

Taken together, these observations indicate that odilorhabdins like NOSO-502 and NOSO-96624 induce both sequence- and concentration-dependent ribosomal stalling, including subtle variations, possibly attributable to chemical differences in side-chains among themselves.

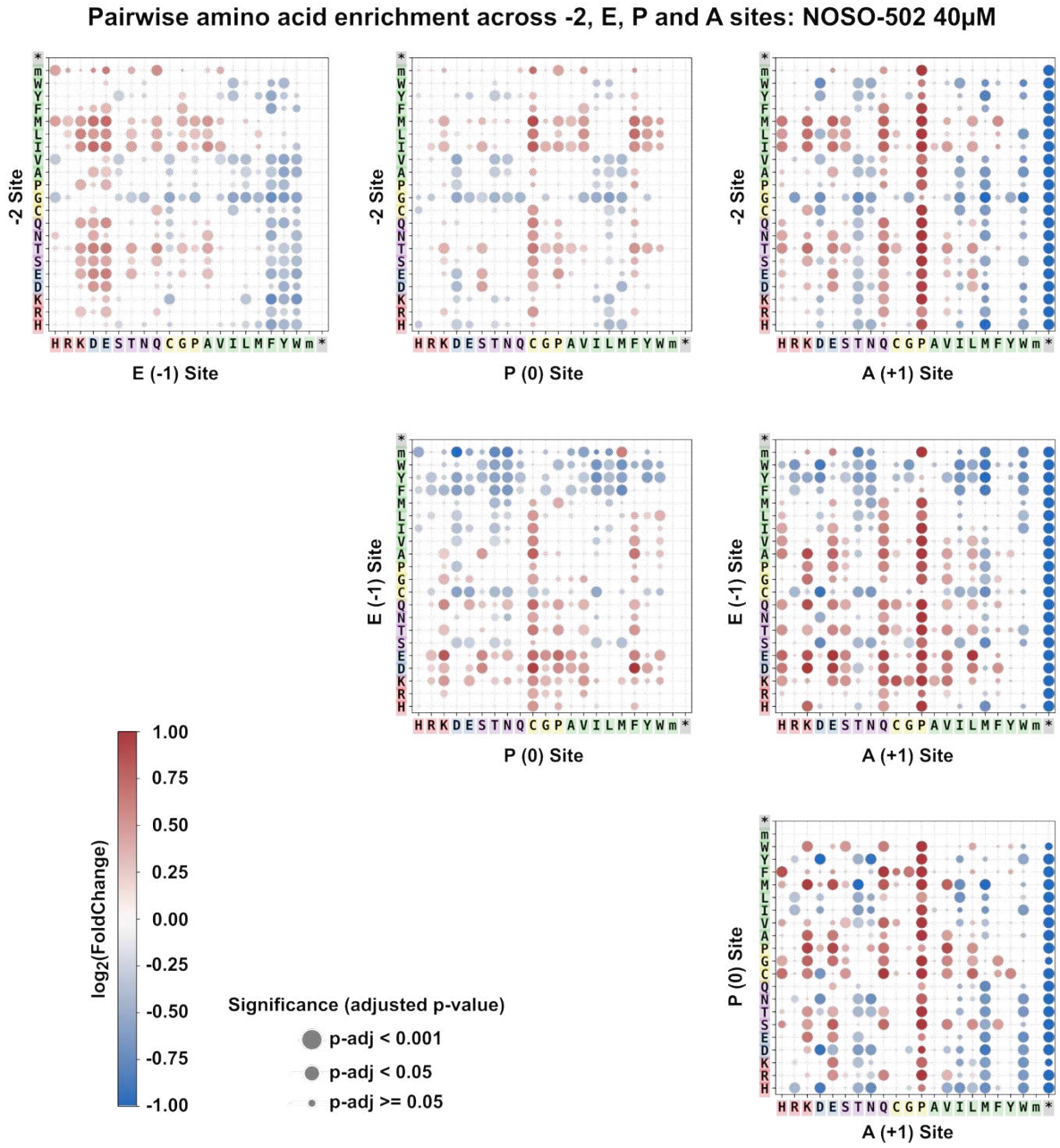

Figure 27: Heatmap grid representing the di-amino acid motifs enriched across -2, E, P and A-sites in the presence of 40µM of NOSO-502. Amino acid labels on the two axes are colored as follows: red – positively charged, blue – negatively charged, purple – polar, yellow – specific amino acids like Cys, Gly and Pro, and green – hydrophobic. Formyl methionine or fMet is denoted as m, while a stop codon is represented as an asterisk (*) symbol shaded in grey.

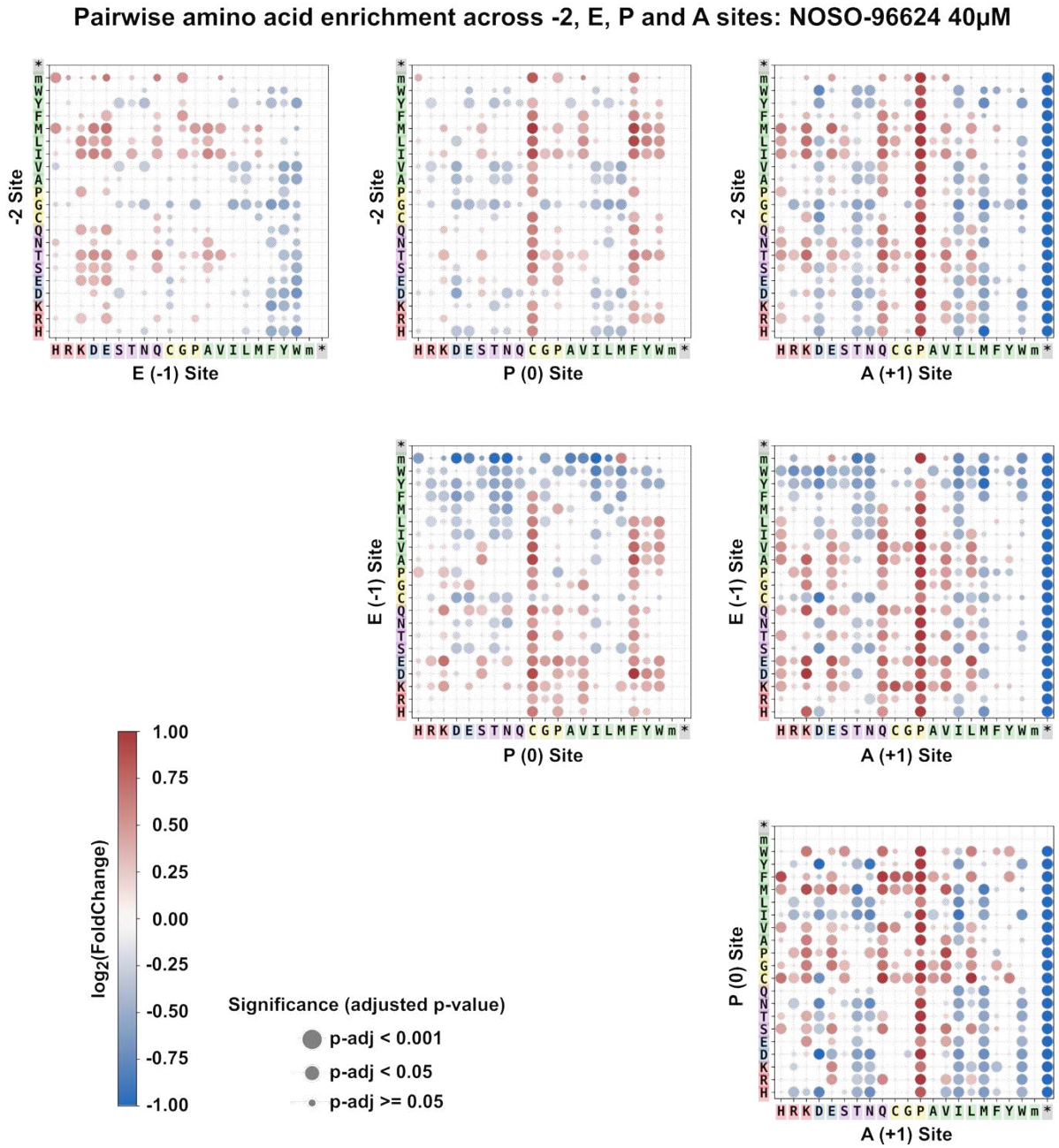

Figure 28: Heatmap grid representing the di-amino acid motifs enriched across -2, E, P and A-sites in the presence of 40µM of NOSO-96624. Amino acid labels on the two axes are colored as follows: red – positively charged, blue – negatively charged, purple – polar, yellow – specific amino acids like Cys, Gly and Pro, and green – hydrophobic. Formyl methionine or fMet is denoted as m, while a stop codon is represented as an asterisk (*) symbol shaded in grey.

Next, I expanded the analysis for enrichment of codons for di-amino acid motifs to those combining four contiguous amino acids across the -2, E, P and A-sites to assess the global multi-site changes in the translational landscape induced by odilorhabdins, and also to check if the core di-amino acid motifs are conserved within longer sequence contexts or are modulated by the flanking residues.

To identify significant trends in sequences, motifs were filtered based on i) a $\log_2$(Fold-Change) ≥ 1, corresponding to at least a 2-fold enrichment compared to the control condition, ii) a statistical significance cutoff of adjusted p-value ≤ 0.05, corresponding to -$\log_{10}$(adjusted-p-value) ≥ 1.3. Motifs containing stop codons in the A-site were also filtered out to focus analyses on drug-induced elongation arrest and avoid signal due to translation termination. The filtered motifs were subsequently used to construct Sankey flow diagrams (Fig. 29). In these diagrams, each node corresponds to a specific amino acid residue at a given ribosomal position, with taller nodes reflecting higher relative abundance of motifs containing that residue within the filtered dataset. The width of the connecting links is proportional to the relative frequency of co-occurring amino acid pairs across adjacent sites. Together, these diagrams enable mapping of combinatorial sequence preferences and multi-site residue dependencies across the -2, E, P and A-sites.

The key takeaways from the analyses were the following. At 0.4µM NOSO-502, most four-residue motifs contained codons for Pro/Glu in the E-site and Pro in the P-site, with a strong preference for fMet/Ser/Thr codons in the -2 site. The trend was similar at 0.3µM NOSO-96624, although with a lesser number and variety of stalled motifs, consistent with the pairwise enrichment analysis. Additionally, at the -2 site, a strong preference was shown for motifs with fMet/Pro codons. At 40µM, for both NOSO-502 and NOSO-96624, more combinations of four-residue motifs were observed, consistent with the concentration-dependent increase in the number of observed stalling motifs. Most of these motifs contained codons for Pro in the A-site and fMet/Ser/Thr in the -2 site, with a more relaxed preference for Cys/Ser/Gly/Pro/Thr/Arg codons in the P-site. The enrichment of fMet or initiator codon across the conditions at the -2 site suggests that the antibiotic causes ribosomal stalling within the first few codons of the open reading frame, preventing translation from progressing beyond a few elongation cycles. In fact, this is also supported by the observations on the

distribution of sequencing reads in Fig. 22. Overall, these observations for the four-residue motifs mostly echo the trends from the pairwise enrichment analysis. However, not all motifs identified and discussed in the pairwise analysis are represented with equal prominence in the four-residue flow diagrams (e.g., the signature DP motif across E and P-sites in low-concentration datasets). This can be attributed to limitations in the sequence context: although a di-residue motif may show high statistical enrichment during pairwise analysis, its representation across the four-residue landscape can remain low if it occurs only in a narrow sequence context, resulting in minor nodes in the global flow.

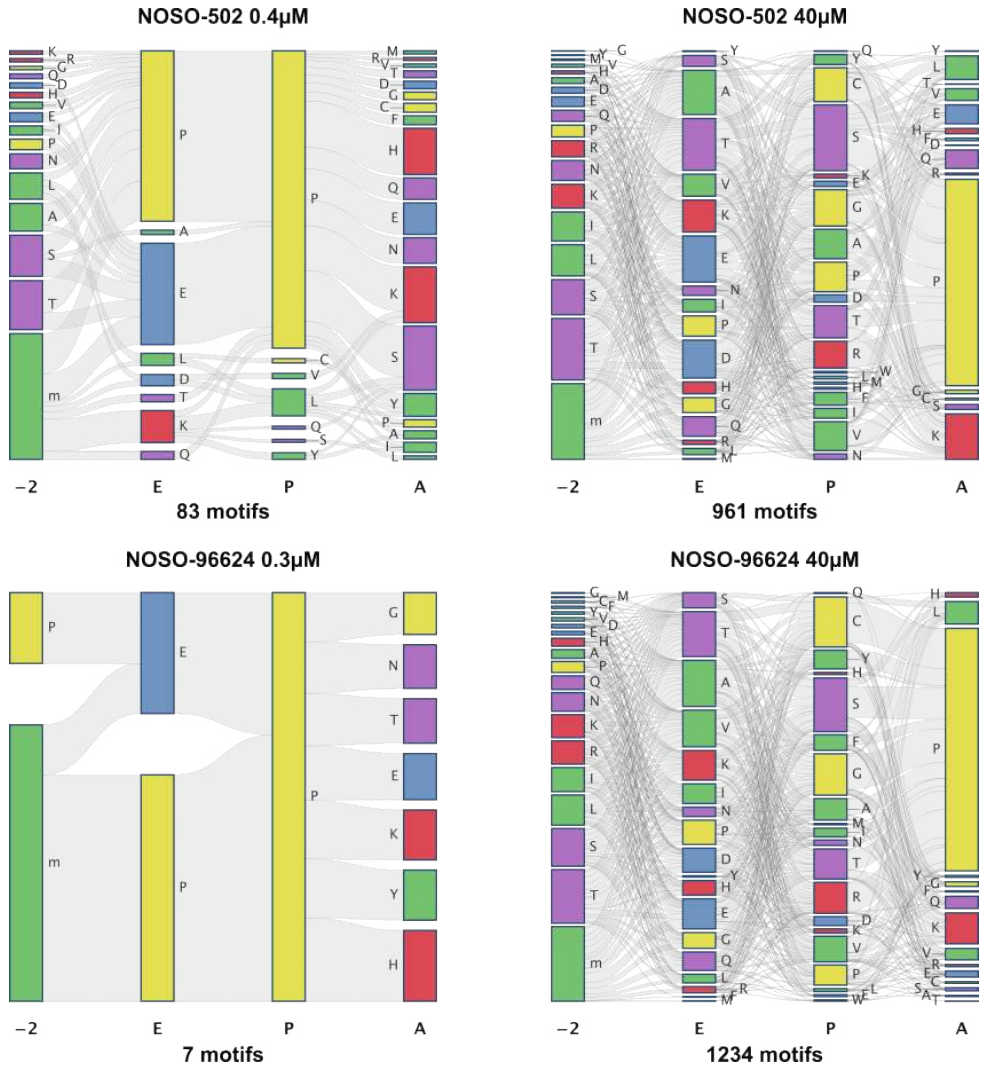

Figure 29: Combinatorial sequence preferences across -2, E, P and A-sites during odilorhabdin-induced translation arrest. Sankey flow diagrams illustrating multi-site amino acid dependencies across the -2, E, P, and A-sites for NOSO-502 (top) and NOSO-96624 (bottom) at low (left) and high (right) concentrations. Vertical blocks (nodes) represent individual amino acid residues at each site,

with node height proportional to the relative abundance of motifs containing that residue. Amino acid nodes are colored as follows: red – positively charged, blue – negatively charged, purple – polar, yellow – specific amino acids like Cys, Gly and Pro, and green – hydrophobic. Formyl methionine or fMet is denoted as m. Grey connector ribbons (links) depict transitions between adjacent sites, with ribbon width proportional to the co-occurrence of specific residue pairs. Data were filtered for $\log_2$(FoldChange) ≥ 1 using a statistical cutoff of -$\log_{10}$(adjusted p-value) ≥ 1.3, excluding stop codons in the A-site.

Since the genetic code is degenerate, i.e., multiple synonymous codons can encode one amino acid, evaluating the iTP-Seq data solely at the amino acid level might mask important variations. Therefore, I also looked at individual codon enrichment at the -2, E, P and A-sites to check for differential stalling patterns at the nucleotide level (Fig. 30). The variations in enrichment patterns were consistent across NOSO-502 and NOSO-96624, but varied at different concentrations of the drugs, and also at different sites. While the complete 64 X 4 codon matrix across the four sites yields numerous localized shifts across the four conditions, several prominent trends represent this position-dependent behaviour, as listed below, alongside comparisons with published trends (Pantel et al. 2018), wherever applicable. In this list, 'X-site stalling' refers to stalling of the ribosome with the codon for the corresponding residue positioned at site X.

- Amino acids encoded by 6 codons in *E. coli*:
    - Serine (S): At high antibiotic concentrations, P-site stalling (i.e., ribosomal stalling with a Ser codon at the P-site) is preferentially driven by the TCA codon, whereas A-site stalling is preferentially due to the AGC codon.
    - Leucine (L): At high antibiotic concentrations, P-site stalling preferentially occurs with either the TTG or CTT codons, while A-site stalling displays a codon block dependence - the TTX codons (TTG and TTA) are distinctly depleted, while the CTX codons, notably CTT, are enriched. This agrees with previously reported toeprinting-based studies (Pantel et al. 2018), where A-site stalling was observed with CTG or CTT codons at 50µM NOSO-95179.
    - Arginine (R): Across all sites and conditions, the AGX codons (AGG and AGA) and the CGA codon preferentially lead to stalling. However, previous studies reported stalling with the CGT codon in the P-site and the CGA codon in the A-site at 50µM

NOSO-95179, partially agreeing with the findings in this work. While the CGT codon in the P-site is not depleted in the high-concentration conditions (40µM) in this dataset, it is not significantly enriched either. This difference can be attributed to the low-throughput nature of single-template toeprinting assays, which do not systematically screen all possible codons and sequence context combinations evaluated in high-throughput library approaches like iTP-Seq.

- Amino acids encoded by 4 codons in *E. coli*:
    - Glycine (G): At high antibiotic concentrations, P-site stalling preferentially occurs with the GGG and GGT codons, but A-site stalling preferentially occurs with the GGC and GGA codons. Previous studies reported stalling with the GGT codon in the P-site, agreeing with the findings in this work.
    - Proline (P): At low antibiotic concentrations, stalling preferentially occurs with the CCG or CCA codons. At high antibiotic concentrations, while P-site stalling follows this trend, A-site stalling is observed to occur significantly with all four codons. Further, E-site stalling at high antibiotic concentrations preferentially occurs with the CCC codon.
    - Alanine (A): E-site stalling preferentially occurs with the GCC codon, but stalling at the P-site preferentially occurs with the GCA codon.
- Amino acids encoded by 3 codons in *E. coli*:
    - Isoleucine (I): At low antibiotic conditions, A-site stalling preferentially occurs with the ATA codon, while at high concentrations, P-site stalling preferentially occurs with the ATT codon. This is consistent with previous studies that reported stalling with the ATT codon in both P and A-sites at 50µM NOSO-95179.
- Amino acids encoded by 2 codons in *E. coli*:
    - Lysine (K): A-site stalling occurs with both the AAG and AAA codons, but AAG is preferred more than AAA. Similar to the situation for Arg (R) described before, previous studies reported stalling with the AAA codon in both the P and A-sites at 50µM NOSO-95179, which is consistent with the findings in this work, but is not found to be the most preferred codon choice.

- Aspartate (D): At high antibiotic concentrations, A-site stalling preferentially occurs with the GAC codon rather than the GAT codon.
- Glutamate (E): A-site stalling preferentially occurs with the GAG codon rather than the GAA codon, consistent with previous studies reporting stalling with the GAG codon in the A-site at 50µM NOSO-95179.
- Asparagine (N): At high antibiotic concentrations, A-site stalling preferentially occurs with the AAC codon.
- Glutamine (Q): While no major preferential enrichment is observed for either the CAG or CAA codons across all sites at high antibiotic concentrations in this dataset, previous studies reported stalling with the CAA codon in the A-site at 50µM NOSO-95179.
- Cysteine (C): At high antibiotic concentrations, A-site stalling preferentially occurs with the TGC codon rather than TGT. While no such distinct preference is observed during stalling at the P-site in this dataset, previous studies have reported stalling with the TGT codon in the P-site at 50µM NOSO-95179.
- Tyrosine (Y): At high antibiotic concentrations, P and A-site stalling preferentially occur with the TAC codon rather than the TAT codon.

Indeed, these observations suggest that the sequence-dependent action of odilorhabdins varies at the nucleotide (codon) level, rather than at the amino acid level. It is, however, important to note that the *in vitro* iTP-Seq experiments were performed using the PURExpress system from New England Biolabs, which uses purified total *E. coli* tRNA, while the (NNN)15 template library translated by the ribosomes is designed to represent all codons with equal frequency, regardless of endogenous codon usage frequencies in *E. coli*. This could affect the interpretation of codon-level enrichment results, where stalling may occur not solely due to the effect of the drug, but also due to potential kinetic delays caused by a limited supply of cognate tRNAs for specific lower-efficiency codons. Additionally, since synonymous codons recruit distinct tRNA isoacceptors, the codon-dependent stalling profiles strongly hint at context-dependent antibiotic action at the tRNA level. Mass spectrometric analyses have demonstrated that even in control conditions, the degeneracy of the genetic code, maintained

by isoaccepting tRNA species and Wobble base-pairing, can lead to the incorporation of mismatched amino acids. The most frequent misincorporation events in *E. coli* involve G:U (codon: anticodon) mismatched base pairs in the first and second codon positions, G:G in the first position, and U:G in the second position (Mordret et al. 2019). Subsequent high-sensitivity mass spectrometry studies comparing missense error frequencies in the presence and absence of miscoding aminoglycoside antibiotics (Garofalo et al. 2019; Wohlgemuth et al. 2021) revealed antibiotic-specific misincorporation trends and the formation of "error clusters", which indicate a series of consecutive translational errors where downstream misreadings occur up to 10^4-fold more frequently following an initial error. As such, since iTP-Seq captures only the mRNA sequence associated with stalled ribosomes, it cannot directly resolve the specific misincorporation events induced by miscoding drugs like odilorhabdins. To accurately map the profile of near-cognate tRNAs that can be accommodated during an odilorhabdin-induced miscoding event, quantitative mass spectrometric experiments are required in both the presence and the absence of the antibiotic. This approach will allow the identification of precise amino acid substitution patterns and the correlation of tRNA misincorporation preferences with the enriched codons identified in the iTP-Seq data. To address this question, we established a recent collaboration with Dr Ingo Wohlgemuth and Dr Marina Rodnina (MPI Göttingen, Germany) to evaluate context-dependent mistranslation at the tRNA level; these analyses are currently ongoing.

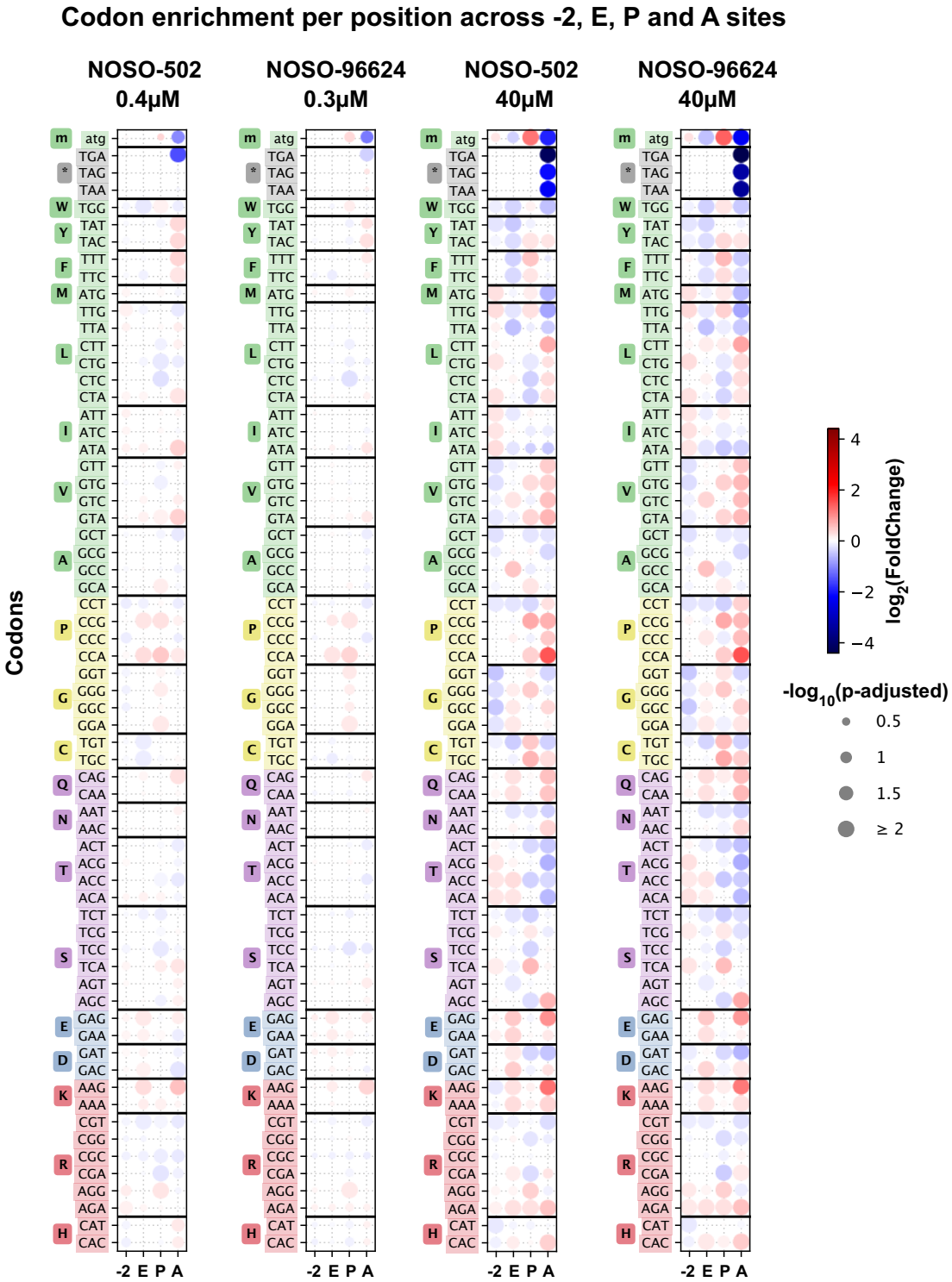

Figure 30: Heatmaps representing per-position codon enrichment (*Escherichia coli* codons) across -2, E, P and A-sites in the presence of NOSO-502 and NOSO-96624 at low and high concentrations. Amino acid labels on the Y-axis are colored as follows: red – positively charged, blue – negatively charged, purple – polar, yellow – specific amino acids like Cys, Gly and Pro, and green – hydrophobic. Formyl methionine or fMet is denoted as m, while a stop codon is represented as an asterisk (*) symbol shaded in grey.

In summary, the odilorhabdins NOSO-502 and NOSO-96624 are both context-dependent antibiotics that induce ribosomal stalling in a distinct sequence-dependent manner depending on the concentration of the drug. While my results are in overall agreement with previously reported stalling preferences, the differences observed can be attributed to the low-throughput nature of the reported single-template toeprinting assays, which did not systematically screen all possible codons and sequence context combinations that can be evaluated in high-throughput library approaches like iTP-Seq used in this work. As such, this work identifies and delineates a more exhaustive profile of context-dependent translocation inhibition. Further, the findings suggest that rather than acting as an inhibitor stalling translation at an isolated, canonical motif, which has been observed for several context-dependent antibiotics documented in the literature (reviewed in Bhattacharya et al. 2024, Appendix B), odilorhabdin-induced translation arrest is characterized by a broader context-dependence, modulated by tRNA-level misincorporation dynamics that remain to be fully deciphered.

However, in an attempt to elucidate the molecular mechanism behind this sequence-dependent stalling, I decided to look at the structures of antibiotic-bound, stalled ribosomal complexes. This approach aimed to determine the conformational state of the decoding center within the stalled complexes and investigate the basis of tRNA misincorporation and resultant stalling at a particular codon, as described in the following sub-sections.

As mentioned at the beginning of this chapter, due to legal and intellectual property uncertainties surrounding the proprietary status of NOSO-96624 during this stage of the project, structural characterization was focused exclusively on NOSO-502-bound stalled ribosomal complexes.

3.2.4. Arrest motifs selected for structural analyses

iTP-seq analyses showed that a wide variety of four-amino-acid motifs can lead to stalling of ribosomes in the presence of different concentrations of odilorhabdins. Hence, to find suitable motif candidates for obtaining structures of NOSO-502-bound stalled ribosomes, I performed toeprinting experiments on a subset of these motifs. Toeprinting, or primer extension inhibition, as described in Chapter 2, locates stalled ribosomes on a single mRNA sequence at codon resolution. Ideally, I sought to choose a motif that minimizes the number of codons on which ribosomes can stall so that I could have a pool of homogeneously stalled ribosomes at a particular sequence context, for structural analyses. This could allow me to know the mRNA sequence at the different ribosomal sites of the stalled complexes, helping me during my structural analyses to track the codon-anticodon interactions at the decoding center. Since toeprinting is a low-throughput process, I selected a few candidate stalling motifs and performed toeprinting experiments on them to check their stalling patterns (Fig. 31 and Supplementary Fig. 56). Following *in vitro* transcription, 1µM mRNA was translated *in vitro* using the PURExpress Δ RF123 Δ Ribosomes Kit from New England Biolabs, maintaining an optimal final concentration of ~1.62 µM *E. coli* ribosomes. Release factors RF1, RF2 and RF3 were omitted from the reaction so that ribosomes that bypassed the expected stalling motif were ultimately arrested at a termination codon designed into the template. Experiments for each arrest motif were performed at both low (0.4µM) and high (40µM) concentrations of NOSO-502. Next, reverse transcription was performed on these mRNA templates with stalled ribosomes, using a fluorescently labelled DNA primer. By convention, when the reverse transcriptase encounters a stalled ribosome, the 3' end of the synthesized cDNA maps 16-17 nucleotides downstream from the first nucleotide of the P-site codon (Orelle et al. 2013). Sanger sequencing of the corresponding DNA template was performed in parallel and visualized on the same toeprinting gel to locate the exact codon positions of the stalled ribosomes.

Each toeprinting experiment included three controls – (i) an "mRNA-only" reaction that did not contain the PURE system translational components, but only the buffers and RNA – this assessed the secondary structure of the mRNA template – if bands were observed in this lane, it indicated where the reverse transcriptase faced obstacles on the RNA and hence

dissociated; (ii) a no-drug reaction which allowed translation of the mRNA without any antibiotics, to test how efficiently this sequence can be translated and if any inherent sequences are difficult for the ribosome to translate, and (iii) a reaction with retapamulin, a pleuromutilin antibiotic that prevents peptide bond formation and acts as an initiation inhibitor (Schlünzen et al. 2004; Davidovich et al. 2007), stalling translating ribosomes on the start codon – this allows locating the initiating AUG codon, and hence the initiation complex on the toeprinting gel.

Finally, I selected two motifs spanning the -2, E, P and A-sites – mDDP and TDCL (Fig. 31) – for structural analyses because they exhibited minimal stalling bands at 40μM NOSO-502, compared to the rest of the motifs (Supplementary Fig. 56). For TDCL, at 40μM NOSO-502, elongation arrest was observed with the majority of the drug-bound ribosomal complexes stalled homogeneously with Cys4 in the P-site, alongside minor populations stalled with Thr2 in the P-site or at initiation. A faint elongation stalling band with Thr2 in the P-site was also observed at 0.4μM NOSO-502, which was not present in the no-antibiotic control, highlighting the concentration-dependent stalling pattern. For mDDP, at 40μM NOSO-502, two major elongation arrests were observed, at the initiation codon and with Asp3 in the P-site, along with a minor population stalled with Pro4 in the P-site. A faint elongation stalling band with Pro4 in the P-site was also detectable at 0.4μM NOSO-502, which was absent in the no-antibiotic control.

The primary objective of screening motifs from the iTP-Seq analyses using the toeprinting assay was to identify motifs capable of inducing distinct, strong, drug-dependent translation arrest to capture complexes for cryo-EM studies. Since both TDCL and mDDP reproducibly met these requirements, they were selected as candidates for downstream structural analyses.

In each of the cases, structural studies were performed at 40μM NOSO-502, since more intense stalling bands, indicating stronger stalling, were observed at high concentrations.

As mentioned at the beginning of this chapter, two cryo-EM datasets were collected for the TDCL motif, which were analyzed by Dorian Gayral, a PhD student in our group. The cryo-EM dataset collected for the mDDP motif was processed and analyzed by me.

The following sub-sections present my structural findings and analyses for ribosomal complexes stalled on this motif.

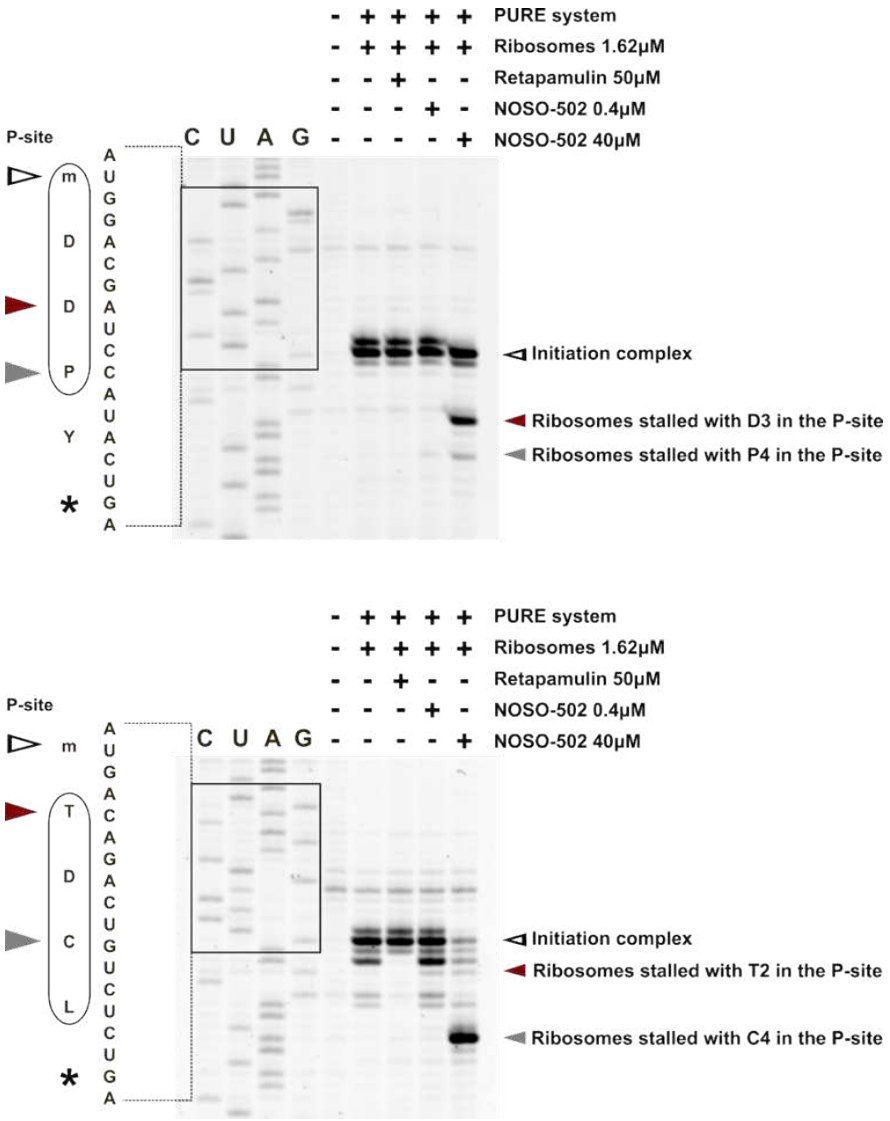

Figure 31: Stalling patterns of odilorhabdin-bound ribosomal complexes on selected arrest motifs. Representative toeprinting gels (from n=3 independent replicates) are shown for mDDP (top panel) and TDCL (bottom panel) motifs. Lanes C, U, A, and G show Sanger sequencing reactions along with the mRNA sequence and the corresponding amino acid sequence. Open arrowheads mark initiation complexes on the start codon (AUG or m denoting fMet). Colored arrowheads identify motif-specific elongation stalls with the indicated amino acid positioned in the P-site. Asterisks (*) indicate the stop codon. Experimental conditions and antibiotic concentrations are labelled above each gel.

3.2.5. Cryo-EM single particle reconstruction of NOSO-502-bound *E. coli* 70S ribosomes stalled on the mDDP motif

To prepare the sample for cryo-EM analysis, I performed *in vitro* translation of an mRNA transcript encoding the fMet-Asp-Asp-Pro (mDDP) motif, in the PURExpress system from New England Biolabs, with *E. coli* 70S ribosomes in the presence of 40µM NOSO-502, as described in Section 2.2.3. Upon dilution, the sample was directly applied onto cryo-EM grids and vitrified. This strategy preserves the weakly bound ribosomal components, such as elongation factors, which frequently dissociate during conventional purification methods like sucrose density gradient centrifugation prior to grid vitrification. Cryo-EM data were then collected on a Glacios 2 (Thermo Fisher Scientific) microscope equipped with a Falcon 4 camera and a Selectris filter. The data collection and processing statistics are shown in Table 3. The initial dataset comprised 12,374 micrographs, which were processed using CryoSPARC v4.7.1 (Punjani et al. 2017) according to the workflow shown in Fig. 32. An initial 70S *E. coli* consensus reconstruction was reached at 2.1Å overall resolution, encompassing 517,053 particles. These particles were then subjected to multiple rounds of focused 3D classification using different masks. In the first round, they were classified using a 30S mask, which separated the 70S ribosome particles from isolated 50S subunit particles and unclassified low-quality or artifactual particles. The remaining 400,666 particles corresponding to the 70S ribosomes were then further classified using the 30S mask to achieve 10 distinct classes corresponding to different 30S subunit conformations, encompassing 390,870 particles. These classes corresponded to different combinations of 30S head and body rotational states, along with a mixture of tRNA conformations and elongation factor associations, which required further classification. Hence, each of these 10 classes was subsequently sub-classified using focused masks corresponding to the E, P and A-site tRNAs (in classical or hybrid states), as well as the elongation factors EF-Tu and EF-G, used either individually or in combination. This classification scheme ultimately yielded 27 distinct classes representing unique combinations of 30S subunit conformations, tRNA compositional states and bound elongation factors. The 27 reconstructed maps, colored according to their local resolution, are represented in Supplementary Fig. 57.

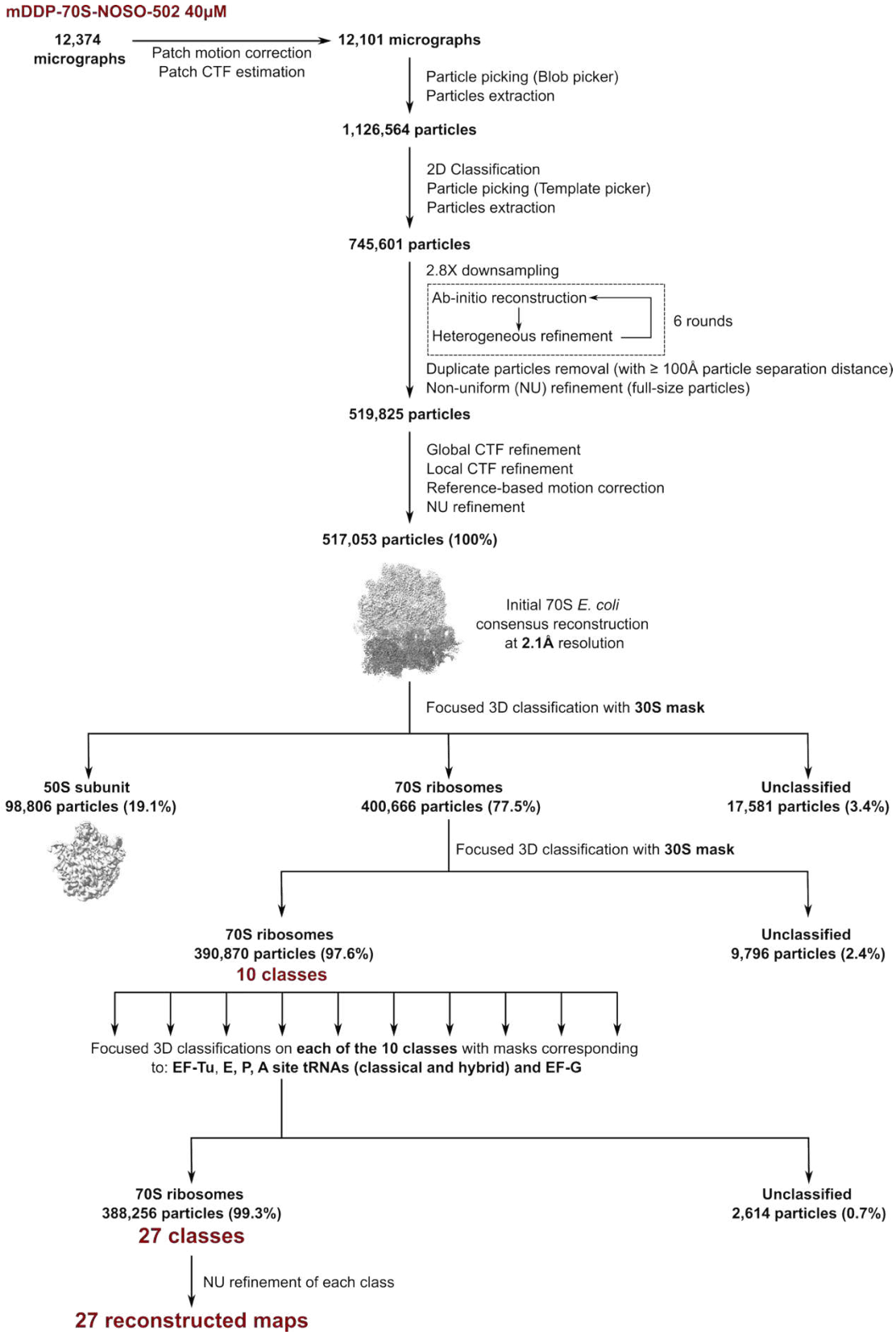

Figure 32: Cryo-EM data processing workflow using CryoSPARC for *E. coli* mDDP-70S-NOSO-502 40µM complexes.

Table 3: Cryo-EM data collection and processing details

Data collection and processing	mDDP-70S-NOSO-502-40µM
Magnification	165,000
Voltage (kV)	200
Electron exposure ($e^-/Å^2$)	40.41
Defocus range (µm)	-0.5 to -1.9
Pixel size (Å)	0.694
Symmetry imposed	C1
Initial particle images (no.)	1,126,564
Final particle images (no.)	388,256
Map resolutions (Å) FSC threshold	2.57-6.73 0.143

To analyze the reconstructed maps corresponding to these 27 classes, I grouped them according to their tRNA and elongation factor compositions. This gave rise to 9 functional states spanning the 27 classes (hereon referred to as “sub-states”), as described in Table 4 and Fig. 33.

Table 4: Distribution of 27 ribosomal 3D classes into functional states by composition of tRNA and associated elongation factors

Functional state	Composition (tRNAs and EFs)	Classes or sub-states	Resolution range (in Å)	Number of particles per functional state	Percentage of total number of particles
A	E and P site tRNAs	A1-A2	3-3.17	11,616	2.99%
B	E, P and A site tRNAs; EF-Tu	B1-B7	2.66-3.52	86,412	22.26%
C	E, P and A site tRNAs	C1-C10	2.57-3.05	206,851	53.28%
D	P/E and A/P hybrid tRNAs	D	3.35	3,884	1%
E	P/E and A/P* hybrid tRNAs	E1-E3	2.57-3.21	64,571	16.63%
F	pE/E and ap/P chimeric tRNAs; EF-G	F	6.73	1,628	0.42%
G	E and A site tRNAs; EF-Tu	G	3.52	4,397	1.13%
H	E and A site tRNAs	H	3.12	4,290	1.10%
I	E and A site tRNAs with fainter density for P site tRNA	I	3.08	4,607	1.19%
				Total = **388,256**	

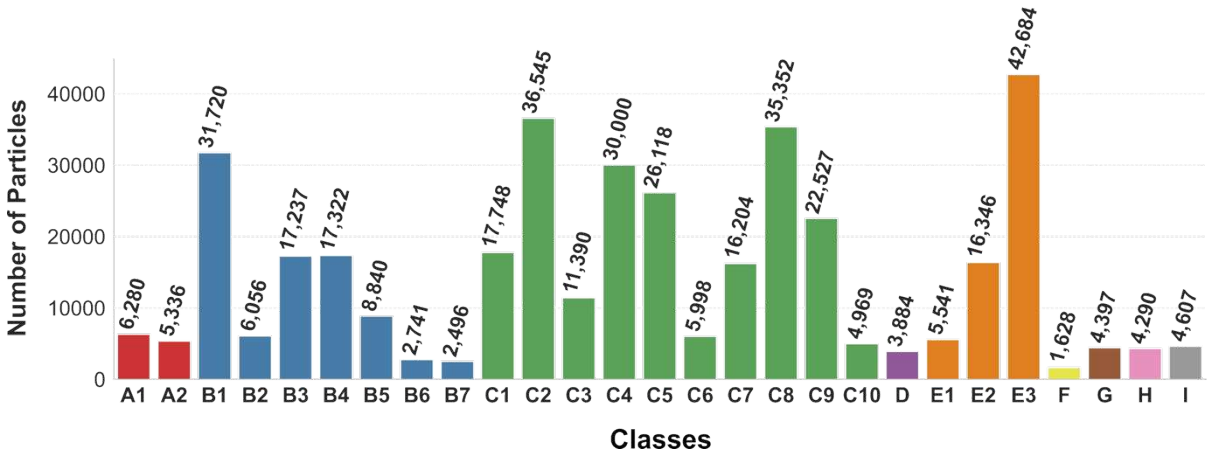

Figure 33: Bar plot showing the distribution of particles in each of the 27 ribosomal 3D classes. The classes are labelled and colored by their functional state, as described in Table 4.

3.2.6. Conformational landscape of NOSO-502-bound *E. coli* 70S ribosomes stalled on the mDDP motif

For each of the 9 functional states encompassing the 27 reconstructions, I characterized their structural features, focusing on the tRNA conformations at the E, P and A-sites, the conformations of the key monitoring bases in the decoding center (G530, A1492, A1493 of 16S rRNA and A1913 of 23S rRNA), and the conformational states of the elongation factors EF-Tu and EF-G. For this comparative characterization, I used published atomic models from recent ensemble and time-resolved cryo-EM studies, representing various translation elongation intermediates (Loveland et al. 2017, 2020; Carbone et al. 2021; Petrychenko et al. 2021; Rundlet et al. 2021), and rigid-body fitted them into the 27 reconstructed maps. This also identified the additional density for NOSO-502 in the 30S subunit near the decoding center, matching the previously reported major binding pocket of NOSO-95179 (Pantel et al. 2018). Consequently, in relation to the sequential events of the translation cycle, I mapped these 9 functional states to 6 canonical translational states and 3 off-pathway states (Fig. 34). For each of the 27 reconstructions, I then selected the published atomic model with the nearest conformational match as a template and generated initial models by rigid-body fitting these template models into the corresponding maps, followed by molecular dynamics flexible fitting (MDFF) in ISOLDE (Croll 2018). The crystal structure of NOSO-502 bound to *Thermus thermophilus* 70S ribosome was solved by our collaborators, Elena Aleksandrova and Dr Yury Polikanov (UIC, Chicago, USA). I processed these NOSO-502 coordinates using the Phenix (Liebschner et al. 2019) ReadySet! program to generate ligand restraints, and then refined it against a representative map (sub-state C8) using Phenix real space refinement, to obtain an optimized starting conformation of the drug (Fig. 34). This refined drug model was then docked into the remaining density maps by rigid-body fitting and merged with the corresponding initial models to yield the atomic models for all 27 sub-states. These models have been used in this work to visualize and interpret the map densities. Further, although the reconstructed maps were categorized into 9 functional states based on their tRNA and elongation factor compositions, the individual sub-states within a functional state differed in their 30S conformations. This structural heterogeneity, particularly angular changes along the rotational axes of the 30S head (residues 921-1397 of the 16S rRNA) and body (residues 2-920

and 1398-1540 of the 16S rRNA) (Fig. 37 Panel C) domains, were then quantified in these models using the Ribosome Angle Decomposition Tool (RADTool) (Hassan et al. 2023), which measures directional angular differences in the small subunits of ribosome models with respect to a standard, unrotated reference structure (PDB 4V9D; Dunkle et al. 2011).

In the following pages, I describe the observations, analyses and structural interpretations derived from the reconstructions of these 27 sub-states.

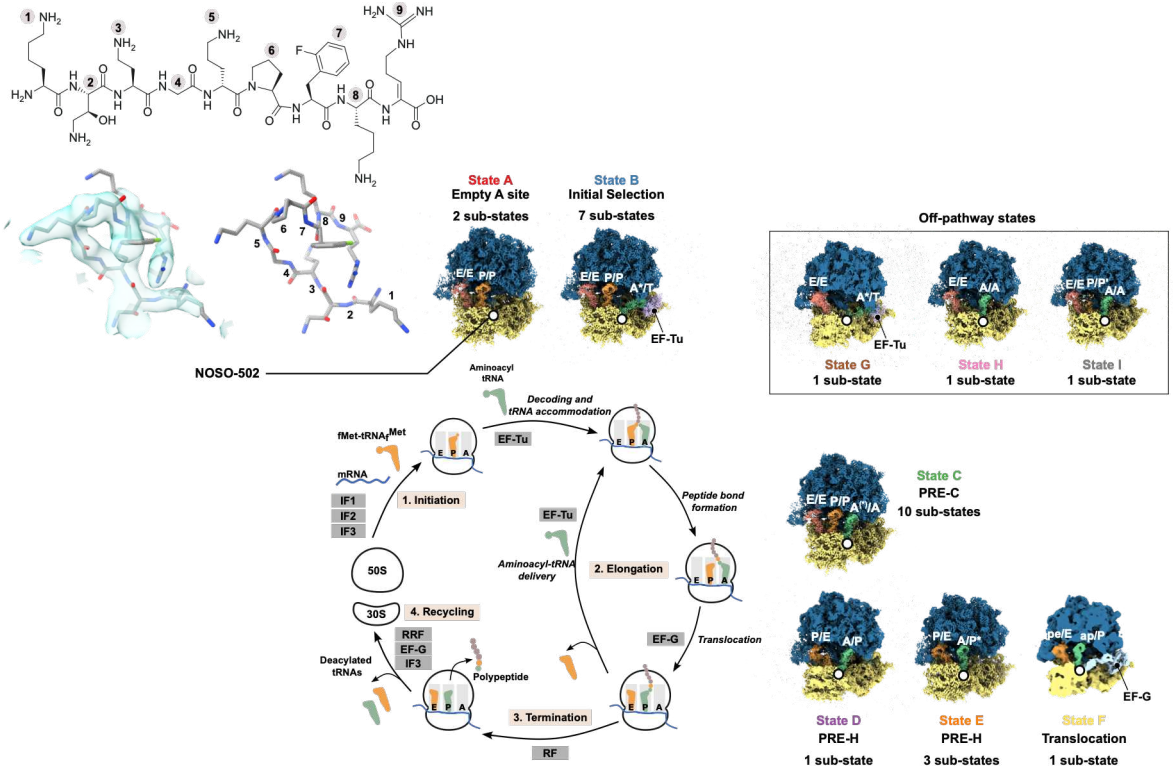

Figure 34: Conformational landscape of 9 functional states of the NOSO-502-bound 70S *E. coli* ribosome across the translation cycle. Representative reconstructed maps are shown for each functional state. In the maps, the 50S subunit is indicated in dark blue, the 30S subunit in yellow, the E, P, and A-site tRNAs in pink, orange, and green, respectively, EF-Tu in purple, EF-G in light blue, and NOSO-502 is indicated as a white circle. The density (in light blue, sub-state C9) and corresponding fitted 3D model of NOSO-502 are shown beside state A, with carbon atoms in grey, nitrogen atoms in blue, oxygen atoms in red and a fluorine atom in green. The residues of the peptide antibiotic have been indicated from 1 to 9, in accordance with the 2D chemical structure. States A-F correspond to six canonical states along the translation cycle: State A (empty A-site) represents a post-translocation state; State B (with EF-Tu) corresponds to initial selection during decoding and tRNA accommodation; State C maps to the classical pre-translocation (PRE-C) stage following tRNA accommodation and peptide bond formation; States D and E both represent hybrid pre-translocation (PRE-H) stages differing in their hybrid tRNA conformations; and State F represents a translocation intermediate bound to EF-G. States G, H and I (in inset) represent three off-pathway states that either lack (States G and H), or exhibit partial P-site tRNA density (State I, where the P-site tRNA conformation has been designated as P/P' for this work).

In an attempt to determine the identities of the tRNAs present in the stalled ribosomal complexes, I first analyzed the densities corresponding to the mRNA codons, the interacting tRNA anticodons and the nascent peptide or amino acid attached to the acceptor stems of the tRNAs. Based on the toeprinting experiments described before (Fig. 31), the two major complexes expected to be captured by cryo-EM were the following – an initiation complex, with initiator tRNA in the P-site interacting with the AUG codon on the mRNA, and an elongation complex, with the GAU codon (for Asp) in the P-site interacting with possibly a near-cognate tRNA that got misincorporated during decoding of the GAU codon in the A-site, before its translocation to the P-site. Hence, I looked at the codon-anticodon densities in the P and A-sites for each of the 27 maps and tried to assign purine versus pyrimidine bases. However, in all cases, the observed base densities could not be distinguished as corresponding to a purine or a pyrimidine at the codon-anticodon regions, since both options seemed possible. For example, in the absence of unambiguous base assignment, a Purine-Pyrimidine-Purine (AUG, for Met) and a Purine-Purine-Pyrimidine (GAU, for Asp) codon at the P-site could not be distinguished from each other (Fig. 35 Panels A and B).

Next, I tried to isolate initiation complexes by looking for specific structural features of the P-site tRNA. An initiator tRNA has several identifying features, viz., an absence of base-pairing between the C1 and A72 residues in the acceptor stem (which is otherwise a canonical Watson-Crick base pairing in elongator tRNAs) (Lee et al. 1991; RajBhandary 1994); a purine: pyrimidine pair at positions 11:24 in the D loop (which is otherwise pyrimidine: purine in elongator tRNAs); and the presence of 3 consecutive G: C base pairs in the anticodon stem at positions 29:41, 30:40 and 31:39 (Seong and RajBhandary 1987; Varshney et al. 1991; Mandal et al. 1996; Shetty et al. 2015). I compared the densities for each of these cases by fitting initiator tRNA and aspartyl-tRNA models. As exemplified in Fig. 35 Panel C with sub-state B1, the bases in positions 1 and 72 indicated continuous density suggestive of possible base pairing, whereas bases 11, 24, 29-31 and 39-41 could not be identified with confidence due to ambiguous assignment of base densities as purine or pyrimidine.

All of these observations suggested that a mixture of ribosomal complexes stalled with different codons in the P and A-sites had been captured.

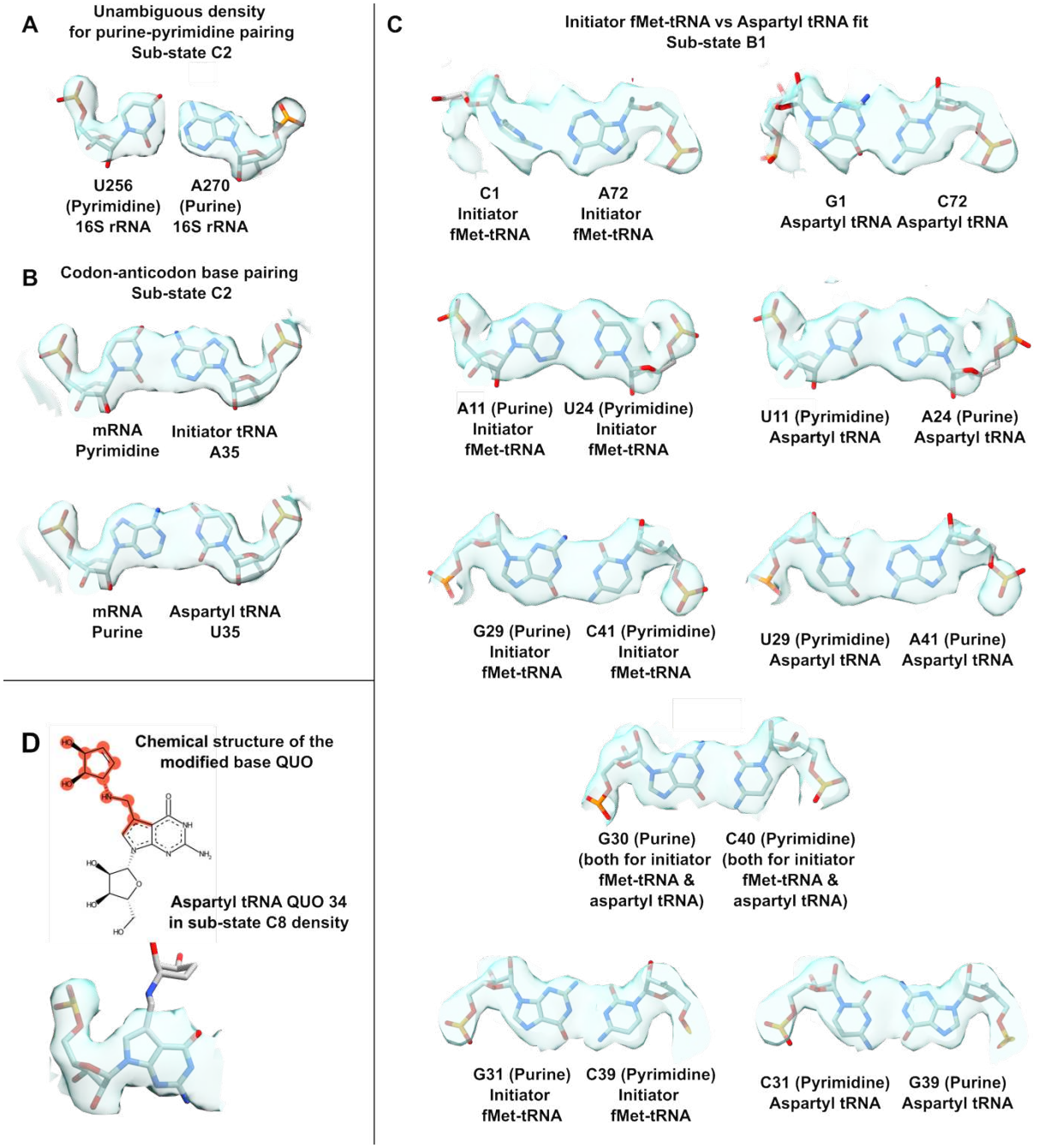

Figure 35: Analysis of density features for mRNA and tRNA sequence assignment. A. Example showing unambiguous purine-pyrimidine base-pairing density (in blue) from a well-resolved region corresponding to 16S rRNA (helix 11, U256:A270) in the sub-state C2 map (resolution 2.57Å). **B**. Ambiguous codon–anticodon density in sub-state C2 at the same contour level as in panel A. The density can accommodate both an mRNA pyrimidine paired with a tRNA purine (e.g., the initiator tRNA A35), and an mRNA purine paired with a tRNA pyrimidine (e.g., the aspartyl tRNA U35). **C.** Comparison of fit in density for initiator fMet-tRNA versus aspartyl tRNA in the P-site tRNA, shown in sub-state B1, resolution 2.66Å. **D.** Chemical structure of queuosine (QUO), highlighting the bulky modification (Source: MODOMICS database)**,** and the absence of density for this modification at position 34 of the P-site tRNA in sub-state C8 (resolution 2.66Å).

As a complementary identification strategy, I searched for map densities corresponding to bulky tRNA-specific base modifications described in the public database MODOMICS (Dunin-Horkawicz 2006; Sordyl et al. 2026). For example, aspartyl tRNAs contain a bulky queuosine at the Wobble position. The density corresponding to this modification was absent in all the maps (exemplified in Fig. 35 Panel D). On one hand, this could suggest that even in complexes that stalled at the GAU codon, a cognate aspartyl tRNA had not been successfully incorporated. Alternatively, it could also be a result of local map attenuation due to conformational flexibility of the modification, or compositional heterogeneity due to an unresolved mixture of initiator and elongator tRNAs, or the presence of an unmodified near-cognate tRNA.

Further, peptidyl densities attached to the acceptor stem of P and A-site tRNAs were generally poorly resolved across all sub-states, and only their presence or absence could be detected, in agreement with their respective functional states. Peptidyl densities were observed on the P-site tRNA in states A (empty A-site or POST-translocation) and B (initial selection), and on the A-site tRNA in states C (PRE-C) and E (PRE-H) (Fig. 36). In contrast, peptidyl densities were fragmented or unidentifiable in off-pathway states (G, H and I), the PRE-H state D and the lower-resolution state F (translocation intermediate). Even in the states where peptidyl density was visible, side-chain identification was not possible due to fragmented densities. Moreover, without knowing the specific tRNA species bound, especially given the possible mixture of stalled ribosomal complexes bearing different tRNAs, sequence assignment for the nascent peptide was not feasible. Notably, the E-site tRNAs in all sub-states showed density consistent with aminoacylation. While this is not biologically expected, this phenomenon is not uncommon in *in vitro* translation systems, where charged tRNAs from the reaction mixture can passively occupy an empty E-site.

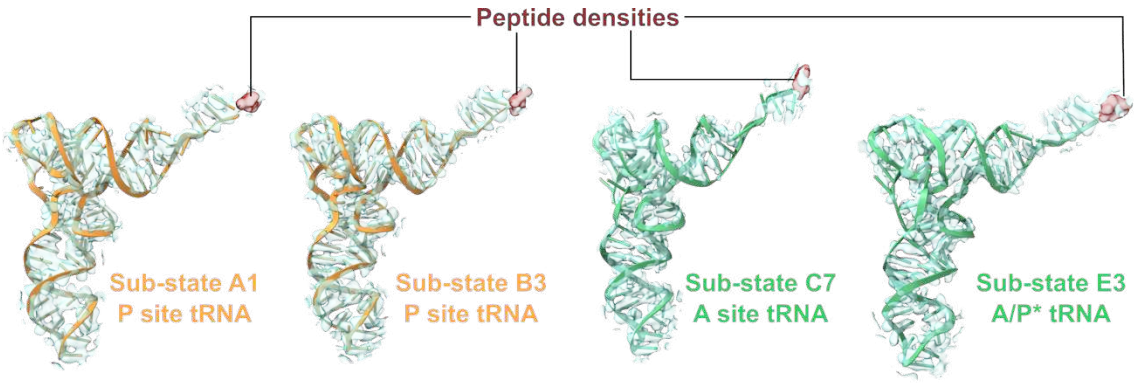

Figure 36: Analysis of peptide density on tRNAs in different sub-states. Representative cryo-EM density maps (in blue) depicting peptidyl tRNA density fitted with corresponding models for P-site tRNAs (sub-states A1 and B3, in orange), and A-site or A/P* tRNA (sub-states C7 and E3, respectively, in green). Nascent peptides are modelled as maroon spheres within the density maps to indicate their spatial location.

Despite these ambiguities in base identities and the presence of a mixture of stalled initiation and elongation complexes, the 27 reconstructions capture the different conformations of the NOSO-502-bound ribosome along the translation cycle.

In the following pages, I will first describe the structural features of each functional state (A-I), elaborating, wherever applicable, on the interactions of NOSO-502 with the 30S subunit and the A-site tRNA, the organization of the monitoring bases in the decoding center (G530, A1492, A1493 of 16S rRNA and A1913 of 23S rRNA), and the conformational changes among the sub-states in the 30S subunit, specifically, the head swivel and body ratchet angles. I also compared the observed states with various translation elongation intermediates from recent ensemble and time-resolved cryo-EM studies (Loveland et al. 2017, 2020; Carbone et al. 2021; Petrychenko et al. 2021; Rundlet et al. 2021), aiming to reach an understanding of the mechanism of translation inhibition by NOSO-502, which will be discussed in the next sub-section.

Functional state A (POST-translocation state)

This state is defined by the presence of E/E and P/P tRNA conformations in the E and P-sites (tRNA nomenclatures detailed in Table 2), respectively, and comprises two sub-states, A1 and A2, reconstructed at 3Å and 3.17Å resolutions, respectively (Fig. 37 Panel A). The density for NOSO-502 indicates that it can interact with the sugar-phosphate backbones of 16S rRNA residues in helices h31 (C962, interacting with the side chain of Dab_3 of NOSO-502), h32 (C1214, interacting with the side chain of D-Orn_5 of NOSO-502), and h34 (G1050, interacting with the side chain of D-Orn_5 of NOSO-502, and U1052, interacting with Dab(β-$OH)_2$ of NOSO-502) (Fig. 37 Panel B). This is in agreement with the previously reported interactions of NOSO-95179 with the ribosome, which was also shown to interact with the backbones of residues in these three helices (Pantel et al. 2018). The two sub-states also exhibit distinct head swivel and body ratchet angles, which, when compared to published structures, cluster with different post-translocation intermediates lacking an A-site tRNA before the next round of elongation (Fig. 37 Panels D and E).

Hence, overall, functional state A corresponds to ribosomes at a post-translocation state, waiting for the next aminoacyl-tRNA to be incorporated into the empty A-site.

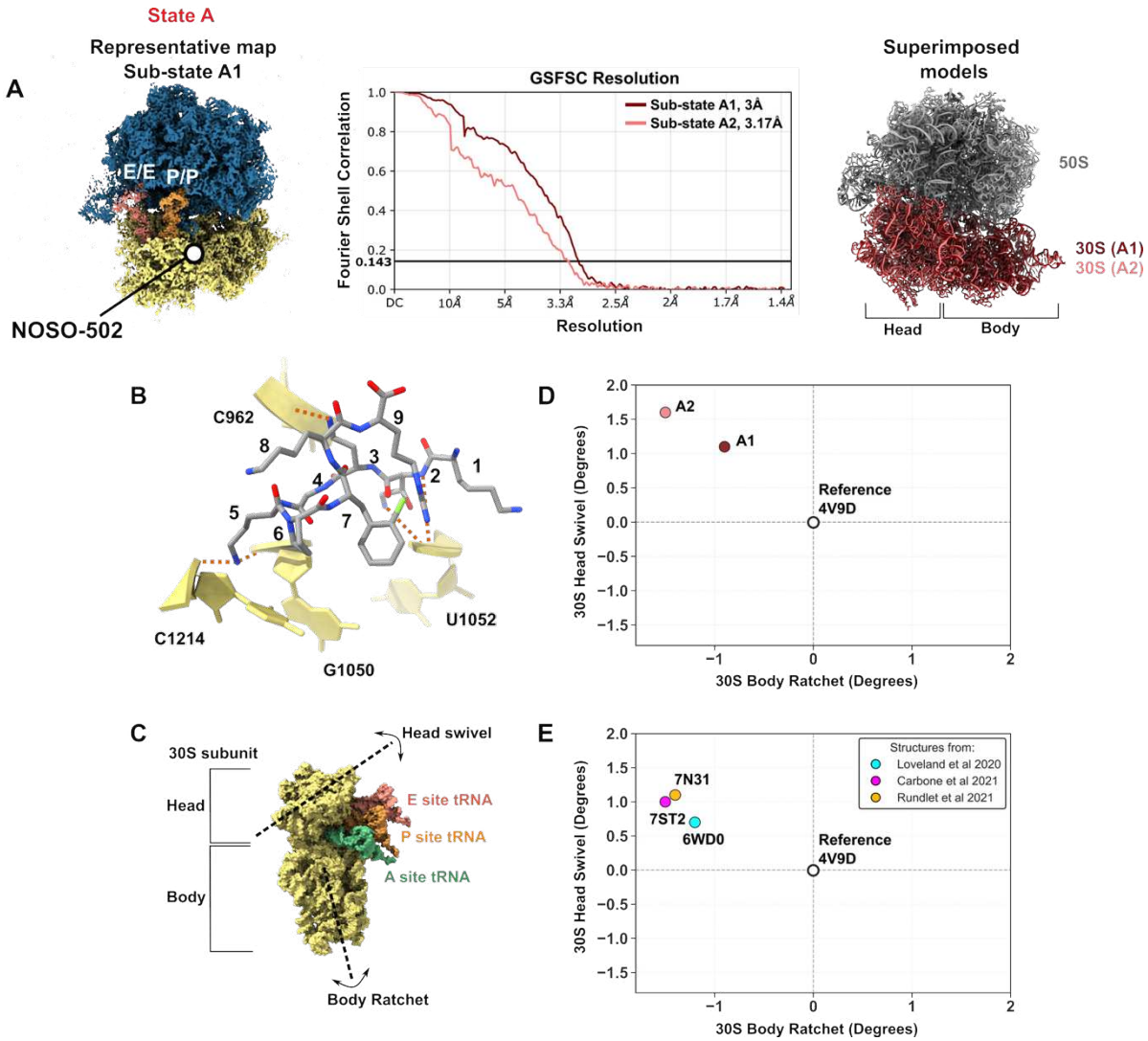

Figure 37: Structural and conformational features of functional state A: **A**. Cryo-EM density map for sub-state A1 (left), Fourier Shell Correlation (FSC) curves for the final reconstructions of sub-states A1 and A2 determined using the gold-standard FSC cutoff of 0.143 (middle), and superimposed atomic models of both sub-states (right). The 30S subunits in the models are colored differently to highlight subtle conformational shifts in head and body domains of the SSU. **B.** Interactions between NOSO-502 and surrounding 16S rRNA residues (yellow) are shown with orange dashed lines. **C.** Location of head swivel and body ratchet rotational axes used in RADTool for conformational analyses of the 30S subunit. Represented for reference with an atomic model with three tRNAs (model for sub-state C8). **D, E.** Graphs generated using RADTool, plotting 30S body ratchet and head swivel angles for sub-states A1 and A2, and published post-translocation intermediates (PDB 7N31, 7ST2, 6WD0), calculated relative to a reference non-rotated PRE-C state (PDB 4V9D).

Functional state B (Initial selection state)

This state is defined by the presence of E/E, P/P, and A*/T tRNA conformations at the E, P, and A-sites, respectively, with the A*/T tRNA bound to the elongation factor EF-Tu. This state comprises seven sub-states, B1-B7, resolved between 2.66Å and 3.52Å (Fig. 38 Panel A).

Structurally, EF-Tu can adopt two distinct conformations on the ribosome – a GTP-bound compact form, and a GDP-bound extended form (Fig. 38 Panel F), and the cryo-EM density for all 7 sub-states corresponded to the compact GTP-bound form (exemplified by sub-state B1 in Fig. 38 Panel C). The reconstructions also showed distinct density for NOSO-502, which interacts with the backbones of 16S rRNA helices h31 (C962), h32 (C1214), and h34 (G1050, U1052), consistent with state A. Additionally, the densities indicated interactions of NOSO-502 with the sugar-phosphate backbone of the A-site tRNA at residues 31 (with Dha_9 of NOSO-502), 32 and 34 (both with Lys_1 of NOSO-502) (Fig. 38 Panels B and D). Such interactions with the backbone of the A-site tRNA were also reported for NOSO-95179 (Pantel et al. 2018).

As described in Chapter 1, during the initial selection step of decoding, the 30S subunit of the EF-Tu-bound ribosome can adopt two conformations – an open conformation where the decoding center is in an “unlocked” or “OFF” state with the monitoring bases not engaging with the A-site tRNA, and a closed conformation, where the 30S head and shoulder move towards the 50S subunit, engaging with a cognate tRNA in the A-site, and the decoding center is in a “locked” or “ON” state (Fig. 9). By convention, the A-site tRNA is named A*/T when the 30S subunit is in its open conformation, and A/T when the 30S is in its closed conformation. Time-resolved cryo-EM studies have isolated several EF-Tu•GTP-bound elongation intermediates differing in their conformations of switch regions and states of the GTP-binding pocket (Loveland et al. 2020), and upon plotting their 30S head swivel and body ratchet movements (Fig. 38 Panel G), these intermediates formed two distinct clusters for open (PDB 6WD2-6WD4) and closed (PDB 6WD8 and 6WD9) 30S subunits with A*/T and A/T tRNA conformations, respectively. Further, ensemble cryo-EM studies have also been conducted on complexes where EF-Tu was bound to a non-hydrolysable GTP analogue, GDPCP (guanosine-5’-[(β,γ)methyleno]triphosphate), to capture aminoacyl-tRNA binding states before GTP hydrolysis and EF-Tu dissociation (Loveland et al. 2017). This study specifically compared the structures of ribosomes with cognate (PDB 5UYL and 5UYM) and near-cognate (PDB 5UYP and

5UYQ) aminoacyl-tRNAs delivered by EF-Tu. The results from this study indicated that when the 30S is in its open conformation, there is a difference at the monitoring base G530 – it is in a SEMI-ON state (anti-conformation but not interacting with the OFF A1492) in the cognate complex (PDB 5UYL), but an OFF state (syn-conformation) in the near-cognate complex (PDB 5UYP). However, the structures with near-cognate tRNA overall resemble the structures with cognate tRNA when the 30S subunit is in its closed conformation. This indicated that a near-cognate tRNA can also result in a closed 30S conformation with a locked decoding center, and the presence of the near-cognate tRNA also did not cause any dramatic changes in 30S head swivel or body ratcheting movements, as revealed in the comparison with the complexes containing cognate tRNA (Fig. 38 Panel G).

The densities for sub-states B1-B7 indicated an open 30S subunit conformation, with the monitoring bases of the decoding center adopting an unlocked state, albeit with G530 in its SEMI-ON conformation (Fig. 38 Panels B and D). The time-resolved cryo-EM studies (Loveland et al. 2020) have shown that this open state is a transient intermediate where cognate tRNA accommodation rapidly leads to a closed 30S state within 17-29 seconds. Since the translation reaction in my work proceeded for 15 minutes, the long-term persistence of the open state, despite the SEMI-ON decoding conformation, coupled with the known miscoding activity of NOSO-502 and the ambiguous codon-anticodon base densities, suggests that these sub-states represent a near-cognate tRNA in the ribosome rather than a cognate one.

Further analysis of the 30S head swivel and body ratchet angles of sub-states B1-B7 indicated that they cluster in the same region as published structures with an open 30S and unlocked decoding center, although spanning a slightly wider angular range for individual sub-states (Fig. 38 Panels E and G).

Hence, overall, functional state B corresponds to ribosomes stalled at the initial selection step of decoding, bound to EF-Tu•GTP.

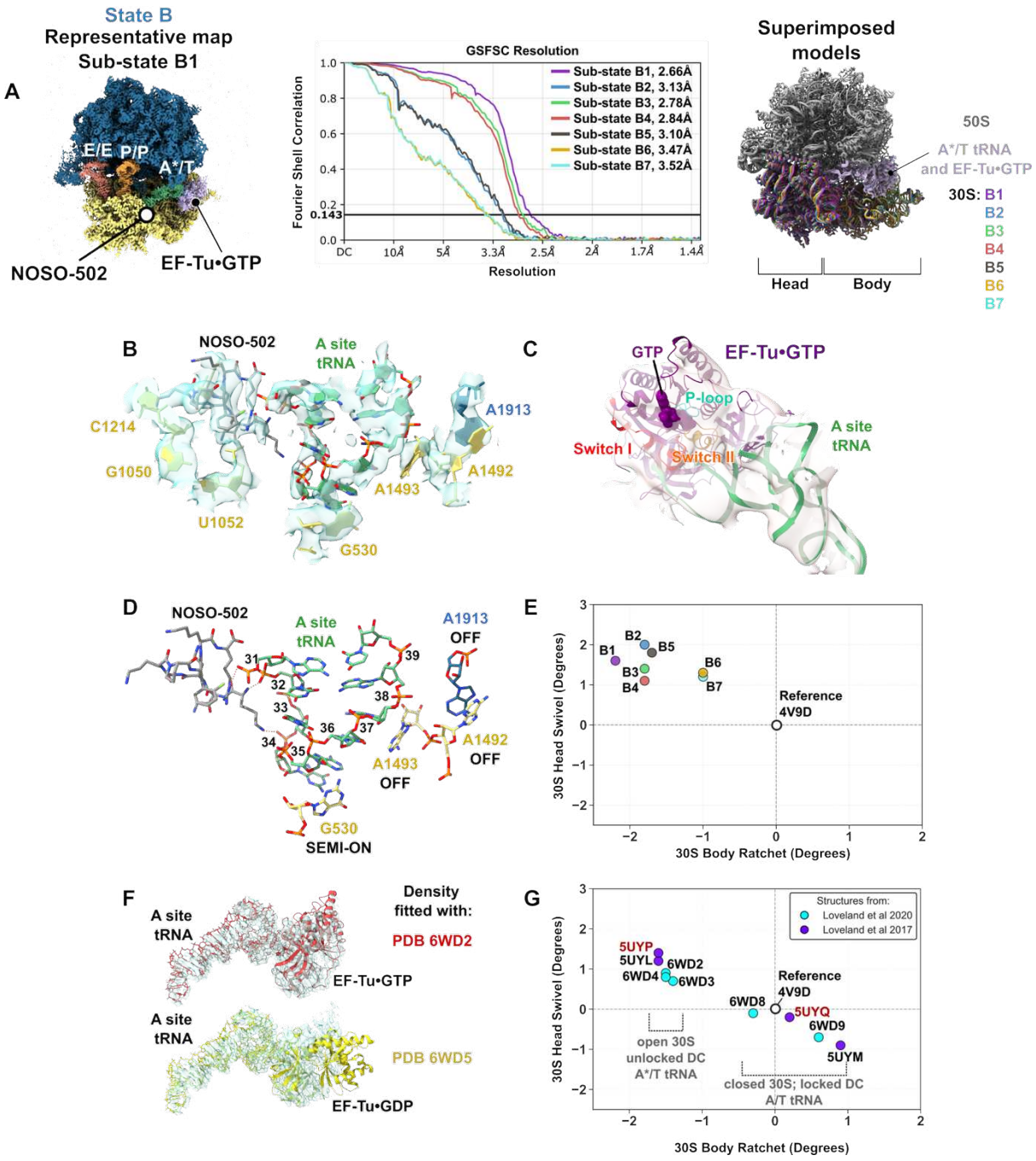

Figure 38: Structural and conformational features of functional state B: **A**. Cryo-EM density map for sub-state B1 (left), Fourier Shell Correlation (FSC) curves for the final reconstructions of sub-states B1-B7 determined using the gold-standard FSC cutoff of 0.143 (middle), and superimposed atomic models of all 7 sub-states (right). The 30S subunits in the models are colored differently to highlight subtle conformational shifts in head and body domains of the SSU. **B.** Cryo-EM density (in light blue) fitted with the structural model of NOSO-502, 16S rRNA residues G1050, U1052, C1214 (in yellow), the monitoring bases of the decoding center (G530, A1492, A1493 of 16S rRNA, in yellow, and A1913 of 23S rRNA in blue), and the A-site tRNA (in green). **C**. Gaussian-filtered (σ = 0.73Å) density (in grey) of sub-state B1 fitted with the structural model of EF-Tu•GTP (in purple) and A-site tRNA (in green). The compact nature of EF-Tu•GTP is indicated with the structured switch I (in red), switch II (in orange) and

P loop (in cyan) regions, and the GTP molecule is represented in purple spheres. **D.** Interactions between NOSO-502 and the A-site tRNA (residues 31, 32 and 34) are shown with orange dashed lines. The four monitoring bases of the decoding center are shown in their unlocked conformations. **F.** Sub-state B1 density for A-site tRNA and EF-Tu fitted with PDB 6WD2 (with compact EF-Tu•GTP) and PDB 6WD5 (with extended EF-Tu•GDP) to show that the density corresponds to the compact GTP-bound form. **E, G.** Graphs generated using RADTool, plotting 30S body ratchet and head swivel angles for sub-states B1-B7, and published EF-Tu•GTP-bound (PDB 6WD2-6WD4, 6WD8, 6WD9) and EF-Tu•GDPCP-bound (5UYL, 5UYM, 5UYP, 5UYQ) elongation intermediates, calculated relative to a reference non-rotated PRE-C state (PDB 4V9D). PDB 5UYP and 5UYQ represent structures with near-cognate tRNA and have been labelled in red.

Functional state C (PRE-C state)

This state is defined by the presence of E/E and P/P tRNAs at the E and P-sites, along with an aminoacylated A/A or A*/A tRNA at the A-site. This state is the most populated in the dataset (206,851 particles) and comprises ten sub-states, C1-C10, resolved between 2.57Å and 3.05Å (Fig. 39 Panel A). In existing literature, these tRNA arrangements correspond to the pre-translocation classical (PRE-C) stage following A-site tRNA accommodation. Time-resolved cryo-EM studies of elongation intermediates (Loveland et al. 2020) have demonstrated that upon accommodation of a cognate tRNA into the A-site, the closed 30S subunit can sample two rotational states of the body domain (Fig. 39 Panel B, PDB 6WDD and 6WDE, in green), both harboring an A/A tRNA at the A-site. The same time-resolved studies also investigated PRE-C complexes bound to a near-cognate tRNA in the A-site, which showed certain structural differences compared to their cognate counterparts. First, near-cognate PRE-C complexes sample open, intermediate semi-open and fully closed conformations of the 30S subunit, varying in their head swivel and body ratchet angles. In the open and semi-open 30S states (Fig. 39 Panel B, PDB 6WDJ and 6WDL, in red), the A-site tRNA was designated A*/A, denoting a nearly accommodated tRNA paired with a non-closed 30S subunit. Conversely, in the closed 30S states (Fig. 39 Panel B, PDB 6WDK and 6WDM, in red), the A-site tRNA is in a fully accommodated A/A state. Second, contrary to the cognate complexes where the decoding center is consistently in a locked conformation, the near-cognate complexes represented decoding centers that were either partially locked (open 30S) or locked (semi-open or closed 30S), as described in Table 5. Although the experimental conditions in the time-resolved cryo-EM studies were optimized to favor miscoding by adding a single near-cognate tRNA-

containing ternary complex with EF-Tu and excluding other tRNAs, these findings indicated that while near-cognate tRNAs frequently sample open or semi-open 30S conformations, they can nevertheless drive full 30S subunit closure. Further, upon comparison of the published structure for the NOSO-95179-bound ribosome (PDB 6CAE, Pantel et al. 2018), which also contains E/E, P/P and cognate A/A tRNAs with a locked decoding center, its head swivel and body ratchet angles placed it close to both the cognate 6WDE and near-cognate 6WDM structures (Fig. 39 Panel B).

In the NOSO-502-bound maps, the density of the drug indicated interactions with the sugar-phosphate backbones of 16S rRNA helices h31 (C962), h32 (C1214), and h34 (G1050, U1052), consistent with the binding mode observed in states A and B. Additionally, the densities also indicated interactions of NOSO-502 with the sugar-phosphate backbones of residues 31, 32 and 34 of the A-site tRNA (Fig. 40). Across the sub-states, there were variations in the 30S subunit and decoding center, closely resembling the conformations from the time-resolved studies. The 30S subunit was open in sub-states C1-C6, with unlocked decoding centers in C1-C3 and partially locked decoding centers in C4-C6. A semi-open 30S subunit with a locked decoding center was observed for sub-state C7, and closed 30S subunits with locked decoding centers were observed for sub-states C8-C10 (Fig. 40). Notably, several maps showed a dynamic behaviour of the decoding center, with densities corresponding to multiple unlocked conformations of a particular monitoring base (e.g., Fig. 40 Panel A), or both locked (ON) and unlocked (OFF) conformations (e.g., Fig. 40 Panel B) in the same map. The details of the monitoring bases for each of the sub-states have been summarized in Table 6.

Further, the densities of the A-site tRNAs indicated similarities with the A*/A versus A/A distinctions based on overall 30S domain closure (Fig. 39 Panel C), and upon comparing the 30S head swivel and body ratchet angles for each of the sub-states, they clustered into similar quadrants for open, semi-open and closed conformations as in existing literature, while displaying a range of minor variations among themselves.

Hence, overall, functional state C corresponds to ribosomes stalled at the post-accommodation and pre-translocation PRE-C step, with the multiple open 30S subunit structures being a strong indication that this NOSO-502-bound state represents near-cognate tRNA incorporation.

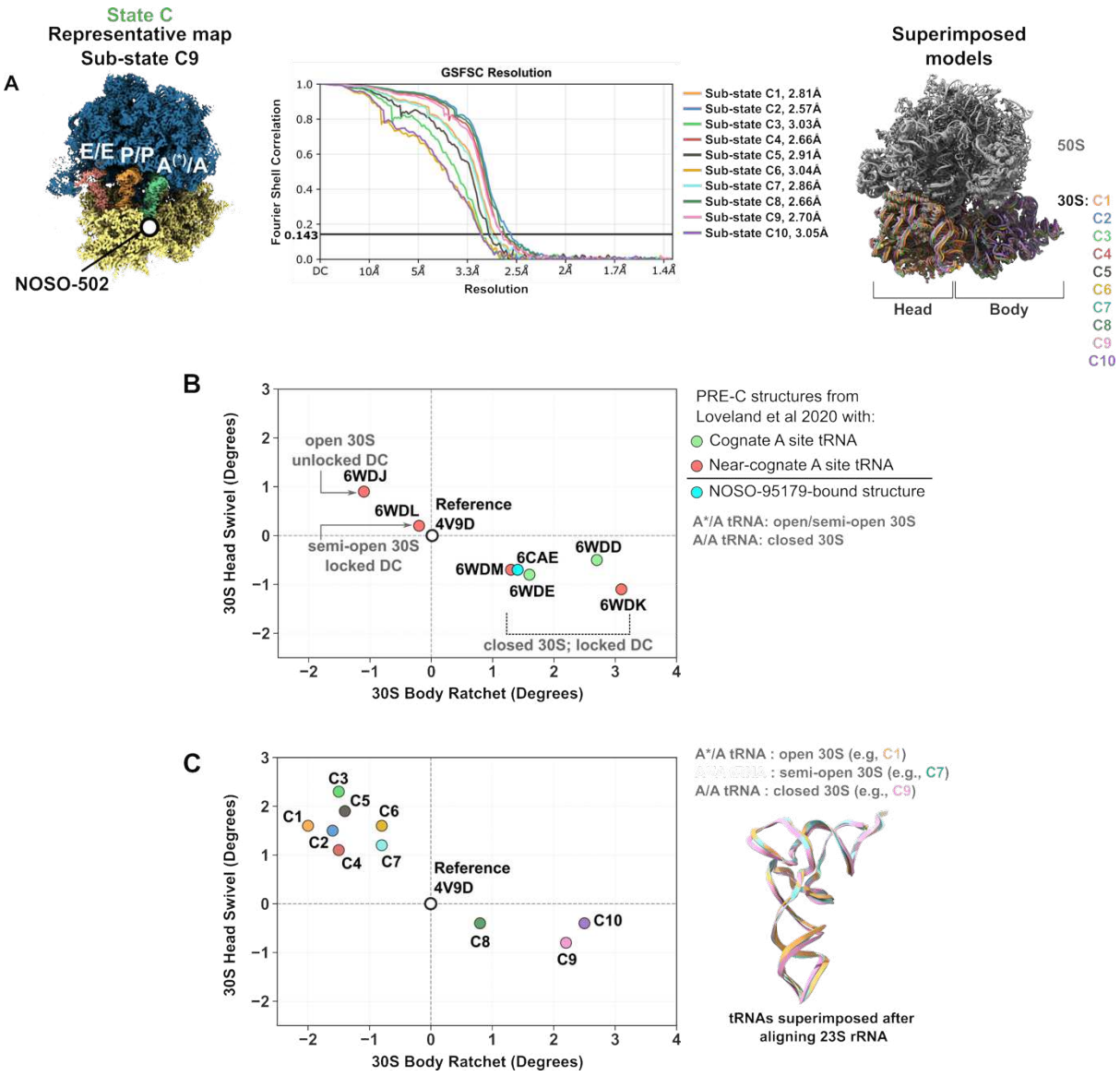

Figure 39: Structural and conformational features of functional state C, Part 1: **A**. Cryo-EM density map for sub-state C9 (left), Fourier Shell Correlation (FSC) curves for the final reconstructions of sub-states C1-C10 determined using the gold-standard FSC cutoff of 0.143 (middle), and superimposed atomic models of all 10 sub-states (right). The 30S subunits in the models are colored differently to highlight subtle conformational shifts in head and body domains of the SSU. **B, C.** Graphs generated using RADTool, plotting 30S body ratchet and head swivel angles for published PRE-C elongation intermediates with cognate (green) (PDB 6WDD, 6WDE) and near-cognate (red) (PDB 6WDJ-6WDM) A-site tRNAs, the NOSO-95179-bound structure (PDB 6CAE) and sub-states C1-C10, calculated relative to a reference non-rotated PRE-C state (PDB 4V9D). The conformations of the A*/A and A/A tRNA are also represented for sub-states C1 (in orange), C7 (in cyan) and C9 (in pink).

Table 5: Architecture of monitoring bases of the decoding center and corresponding 30S conformation in published time-resolved cryo-EM PRE-C structures (Loveland et al. 2020)

PDB ID	A site tRNA	Monitoring base conformation				Decoding center status	30S conformation
		G530	A1492	A1493	A1913		
6WDD	Cognate A/A	ON				Locked	Closed
6WDE	Cognate A/A	ON					
6WDJ	Near-cognate A*/A	SEMI-ON	OFF	ON	OFF	Partially locked	Open
6WDK	Near-cognate A/A	ON				Locked	Closed
6WDL	Near-cognate A*/A	SEMI-ON	ON	ON	ON	Locked	Semi-open
6WDM	Near-cognate A/A	ON				Locked	Closed

Table 6: Architecture of monitoring bases of the decoding center and corresponding 30S conformation in sub-states C1-C10 (this work)

Sub-state (% of total number of state C particles)	Monitoring base conformation				Decoding center status	30S conformation
	G530	A1492	A1493	A1913		
C1 (8.58%)	SEMI-ON	OFF	OFF	OFF	Unlocked	Open
C2 (17.67%)	SEMI-ON	OFF	OFF	OFF		
C3 (5.51%)	SEMI-ON	OFF	OFF	OFF		
C4 (14.5%)	ON	ON/OFF	ON	ON/OFF	Partially locked	
C5 (12.63%)	SEMI-ON	OFF	ON	ON		
C6 (2.9%)	SEMI-ON	ON/OFF	ON	ON		
C7 (7.83%)	ON	ON	ON	ON	Locked	Semi-open
C8 (17.09%)	ON	ON	ON	ON	Locked	Closed
C9 (10.89%)	ON	ON	ON	ON		
C10 (2.4%)	ON	ON	ON	ON		

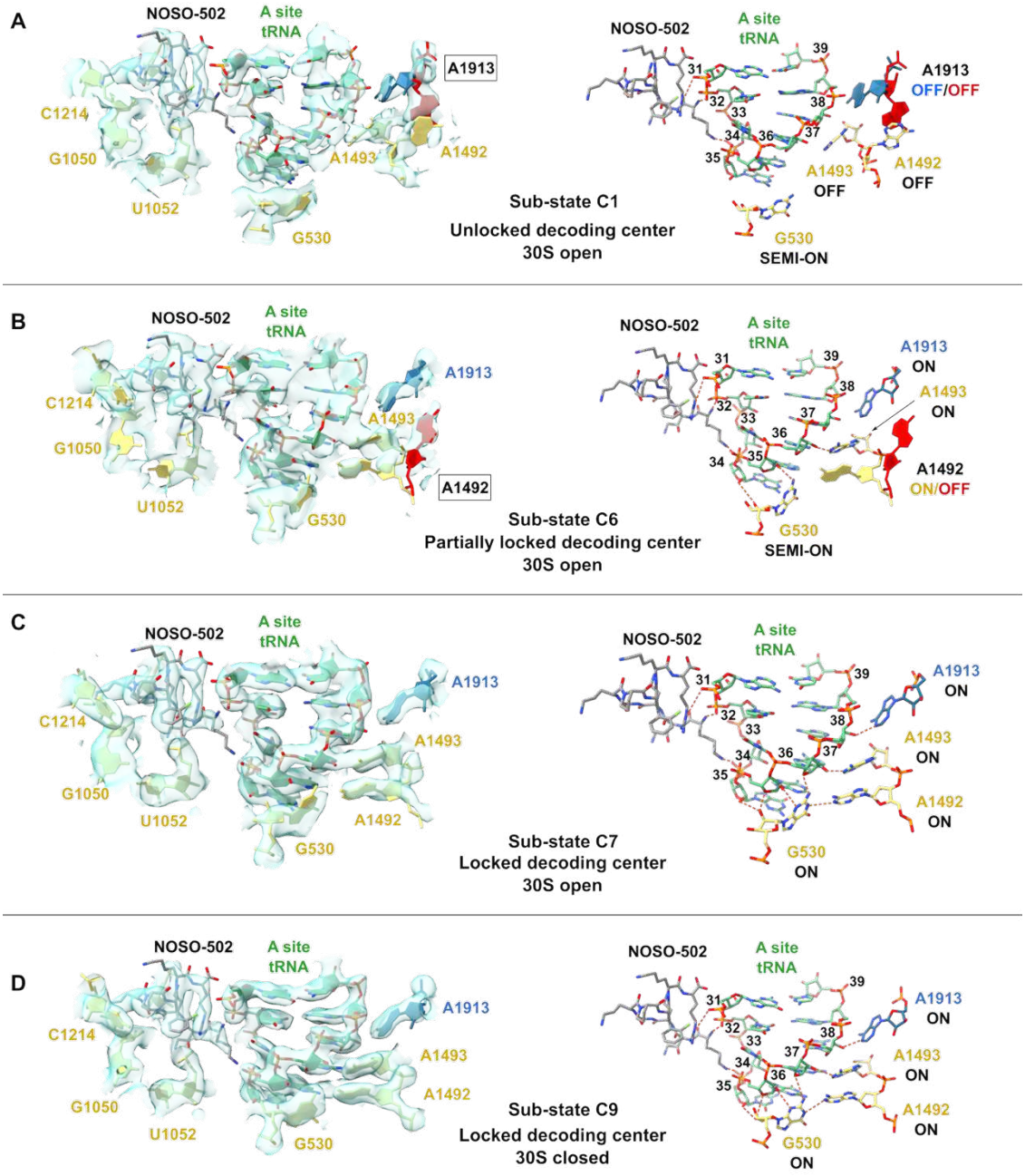

Figure 40: Structural and conformational features of functional state C, Part 2: Cryo-EM density (in light blue) and structural model of NOSO-502, 16S rRNA residues G1050, U1052, C1214 (in yellow), the monitoring bases of the decoding center (G530, A1492, A1493 of 16S rRNA, in yellow, and A1913 of 23S rRNA in blue), and the A-site tRNA (in green). Interactions between NOSO-502, the A-site tRNA (residues 31, 32 and 34) and the monitoring bases of the decoding center are shown with orange dashed lines. **A:** Sub-state C1 with open 30S and unlocked decoding center – A1913 in this sub-state had density corresponding to two alternative OFF conformations, shown in filled blue and red base representations. **B:** Sub-state C6 with open 30S and partially locked decoding center – A1492 in this sub-state had density corresponding to both ON and OFF conformations, shown in filled yellow and red base representations, respectively. **C:** Sub-state C7 with open 30S and locked decoding center. **D:** Sub-state C9 with closed 30S and locked decoding center.

Functional states D and E (PRE-H states)

The defining features of states D and E are the presence of hybrid tRNAs accompanied by a rotated 30S subunit, both of which are characteristic of the pre-translocation state, as described in Chapter 1. While the classical P/P tRNA adopts the P/E hybrid conformation, the classical A/A tRNA can adopt two hybrid conformations – A/P and A/P* – where the elbow of the tRNA shifts ~20Å towards the P-site relative to the A/P state. In the NOSO-502-bound dataset, both hybrid tRNA conformations are observed – in state D (3.35Å resolution), the tRNAs are in the P/E and A/P conformations, while in state E (comprising three sub-states, E1-E3, resolved between 2.57Å and 3.21Å), the tRNAs are in the P/E and A/P* conformations (Fig. 41 Panel A).

The density for NOSO-502 in state D is fragmented and poorly resolved, and hence its interactions with the 30S subunit and the A/P tRNA could not be studied. In contrast, the reconstructions for sub-states E1-E3 were better resolved (exemplified with sub-state E3 in Fig. 41 Panel B). Here, NOSO-502 is found to interact with the backbones of 16S rRNA helices h31 (C962), h32 (C1214), and h34 (G1050, U1052), and the backbones of residues 31, 32 and 34 of the A/P* tRNA, consistent with states A-C. In state E, the decoding center remains in a locked state, with the monitoring bases adopting conformations consistent with the pre-translocation PRE-H stage of translation (Fig. 41 Panel C).

Further, upon comparison of 30S head swivel and body ratchet angles for published structures in their PRE-H state, they were found to cluster together, with A/P* tRNA-containing complexes usually exhibiting higher degrees of head swivel and body ratchet compared to A/P tRNA-containing complexes (Fig. 41 Panel E). States D and E follow the same trend (Fig. 41 Panel D), with sub-states E1-E3 displaying larger body ratchet and head swivel angles than state D.

Overall, states D and E correspond to pre-translocation hybrid (PRE-H) ribosomal complexes stalled before EF-G recruitment, characterized by significantly body-ratcheted and head-swiveled 30S subunit conformations. Their presence in the dataset suggests that NOSO-502 allows translation to proceed towards translocation, despite near-cognate tRNA incorporation.

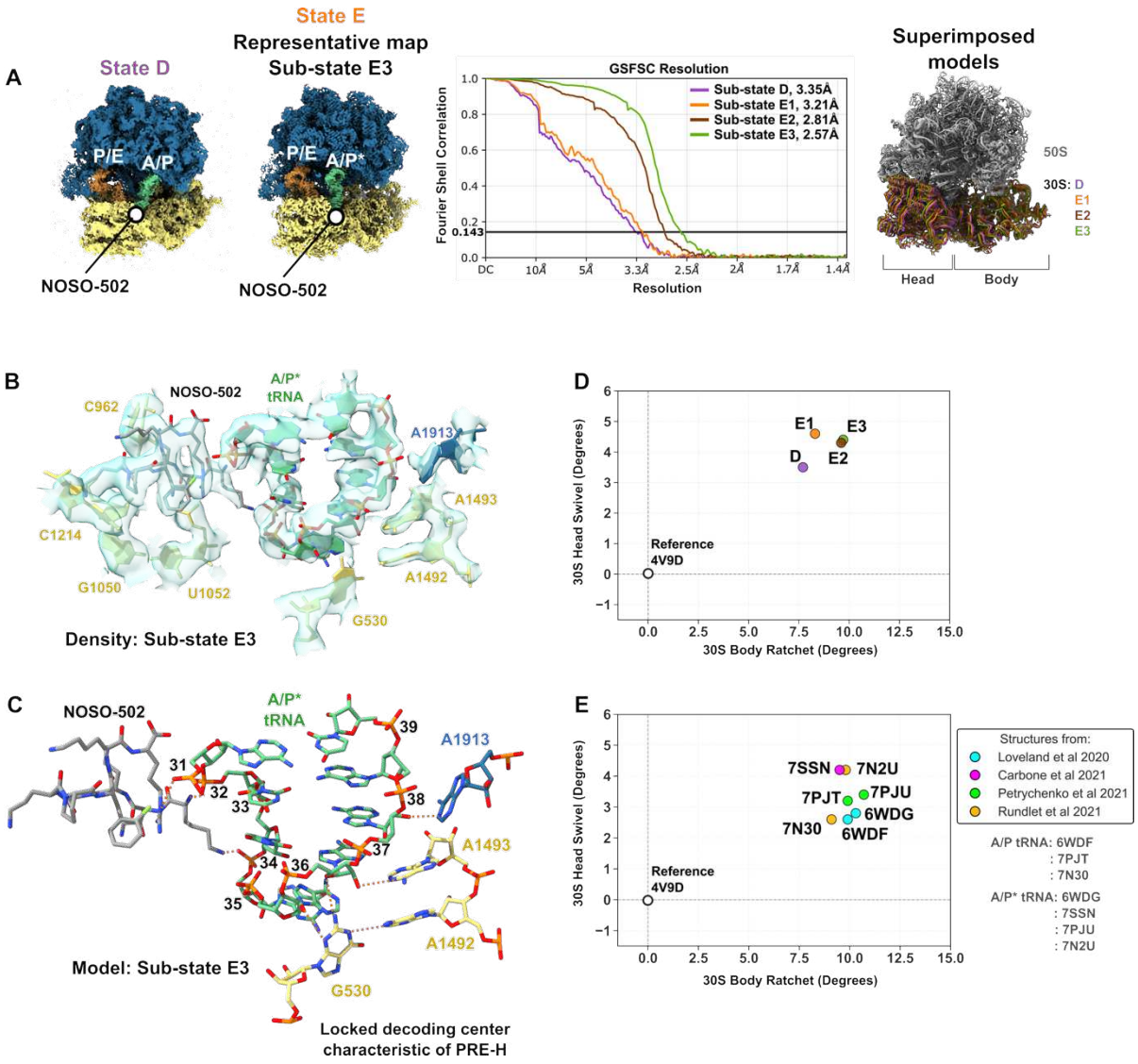

Figure 41: Structural and conformational features of functional states D and E: **A**. Cryo-EM density map for states D and E (exemplified by sub-state E3) (left), Fourier Shell Correlation (FSC) curves for the final reconstructions of sub-states D and E1-E3 determined using the gold-standard FSC cutoff of 0.143 (middle), and superimposed atomic models of all 4 sub-states (right). The 30S subunits in the models are colored differently to highlight subtle conformational shifts in head and body domains of the SSU. **B.** Cryo-EM density (in light blue) of sub-state E3 fitted with the structural model of NOSO-502, 16S rRNA residues G1050, U1052, C1214 (in yellow), the monitoring bases of the decoding center (G530, A1492, A1493 of 16S rRNA, in yellow, and A1913 of 23S rRNA in blue), and the A/P* tRNA (in green). **C.** Interactions between NOSO-502 and the A/P* tRNA (residues 31, 32 and 34) are shown with orange dashed lines. The four monitoring bases of the decoding center are shown in their locked conformations, interacting with the A/P* tRNA. **D, E.** Graphs generated using RADTool, plotting 30S body ratchet and head swivel angles for state D and sub-states E1-E3, and for published PRE-H complexes with hybrid tRNAs (PDB 6WDF, 6WDG, 7SSN, 7PJT, 7PJU, 7N30 and 7N2U), calculated relative to a reference non-rotated PRE-C state (PDB 4V9D).

Functional state F (EF-G-bound translocation intermediate)

This is the least-populated state in the dataset (1,628 particles) and consequently has the lowest resolution (6.73Å) (Fig. 42 Panel A). While the density does not allow a detailed characterization of the state, the map fits published ribosome models containing chimeric tRNAs (conventionally named pe/E and ap/P, as explained in Chapter 1, Table 2) and EF-G•GDP (represented with PBD 7SSD in Fig. 42 Panel B). Density corresponding to NOSO-502 is visible between the chimeric ap/P tRNA and the domain D4 of EF-G near the decoding center (Fig. 42 Panel C), but the resolution is insufficient to understand the conformation of NOSO-502 or its interactions with the 30S subunit and the ap/P tRNA. However, the anticodon loop of the ap/P tRNA is distant from the monitoring bases of the decoding center, which is presumably in its unlocked state, and does not interact with the tRNA (Fig. 42 Panel D).

Analysis of the 30S head and body rotation angles of this state and comparison with published structures (Fig. 42 Panels E and F) confirmed that it was a back-rotated hyper-swiveled conformation. Specifically, it is characterized by reduced 30S body ratcheting compared to the PRE-H states (Fig. 41 Panels D and E), alongside a markedly higher degree of 30S head swivel. This observed conformation of the 30S subunit in the NOSO-502-bound state F more closely resembles that of a fusidic acid-inhibited complex (INT2 state, PDB 7N2C; Rundlet et al. 2021), rather than drug-free translocation intermediates. While fusidic acid binds directly to EF-G after GTP hydrolysis, locking it to the bacterial ribosome (Gao et al. 2009), NOSO-502 binds at an entirely different site near the decoding center of the 30S subunit – despite these distinct binding sites, both antibiotics stall the ribosome in similar conformations. Further, it is also interesting to note that the conformation of the head and body domains of the 30S subunit in state F is distinctly different from the viomycin-bound pre-translocation intermediate with hybrid tRNAs and EF-G•GDP+Pi (PDB 7ST7; Carbone et al. 2021; also plotted in Fig. 42 Panel E). Tuberactinomycins like viomycin stabilize the monitoring bases of the decoding center in their “flipped out” states (elaborated in Section 1.2.3), preventing unlocking of the decoding center required for complete EF-G-mediated translocation, leading to translation inhibition. The distinct conformation of the NOSO-502-bound state F, coupled with the anticodon loop of the ap/P tRNA at a non-interacting distance from the decoding center, together suggest

that unlike viomycin, NOSO-502 does not inhibit translocation by preventing decoding center unlocking.

Overall, functional state F corresponds to a late translocation intermediate bound to EF-G•GDP. The presence of the chimeric tRNAs (which is reported in the literature to be associated with the EF-G•GDP state) alongside a possibly disordered switch I region (Fig. 42 Panel D) suggests that this represents a state post-hydrolysis of GTP and release of Pi.

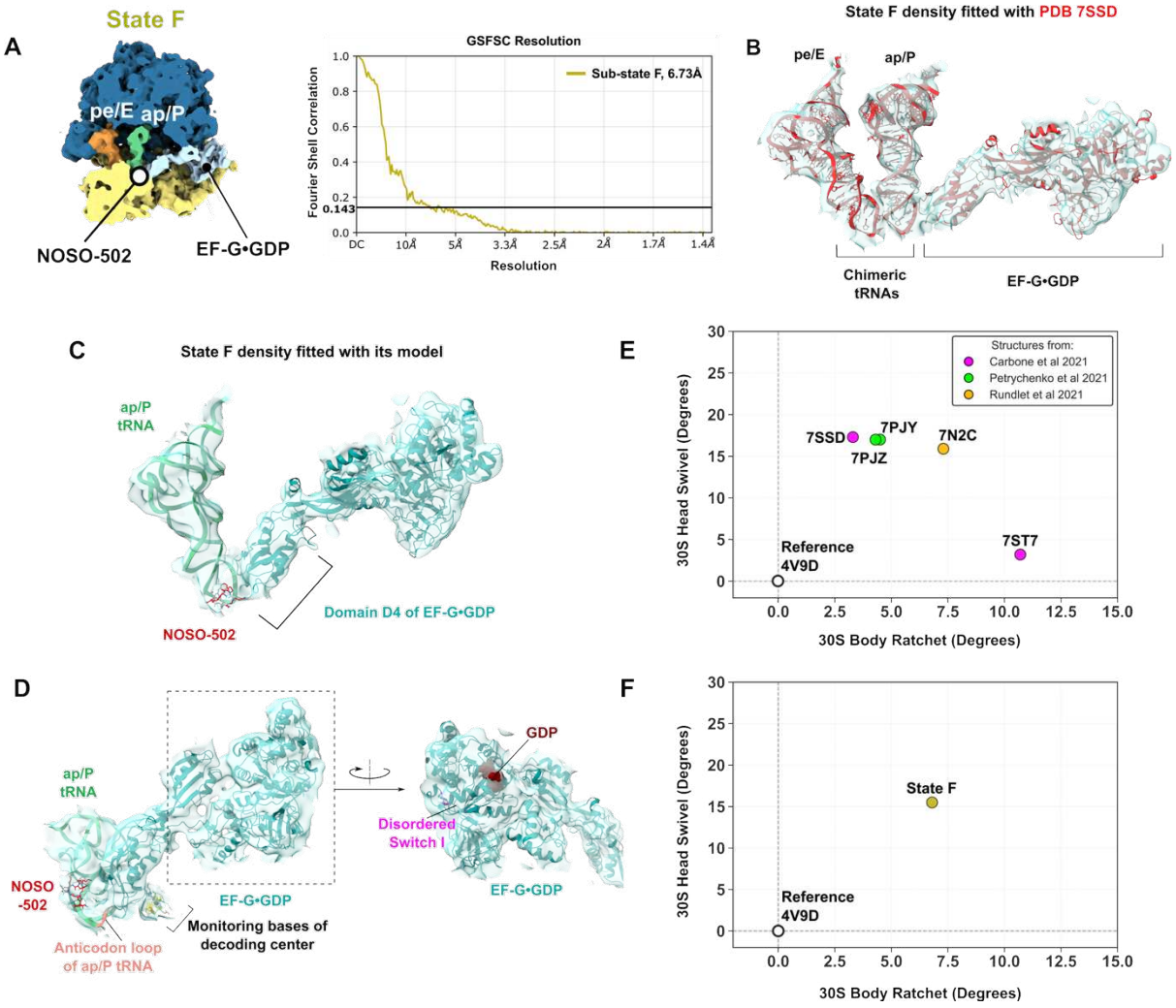

Figure 42: **Structural and conformational features of functional state F**: **A**. Cryo-EM map for state F (left) and Fourier Shell Correlation (FSC) curve (right) for the final reconstruction, determined using the gold-standard FSC cutoff of 0.143. **B.** Cryo-EM density (in light blue) fitted with a structural model (in red) with chimeric tRNAs and EF-G•GDP (PDB 7SSD). **C**. Cryo-EM density (in light blue) fitted with the structural model of state F, indicating the binding site of NOSO-502 (in red) between the ap/P tRNA (in green) and domain D4 of EF-G•GDP (in cyan). **D.** Cryo-EM density (in light blue) fitted with the structural model of state F, indicating the locations of the anticodon loop (in salmon) of the ap/P tRNA (in green) and the monitoring bases of the decoding center (in yellow). A rotated and zoomed-in view

of the density with the fitted model of EF-G•GDP is also shown, indicating the location of GDP (in maroon spheres) and the possibly disordered switch I region (in dashed lines in fuchsia). **E, F.** Graphs generated using RADTool, plotting 30S body ratchet and head swivel angles for published EF-G-•GDP-bound translocation intermediates with chimeric tRNAs (PDB 7SSD, 7PJY, 7PJZ and 7N2C), and for state F, calculated relative to a reference non-rotated PRE-C state (PDB 4V9D). The viomycin-bound translocation intermediate with hybrid tRNAs and EF-G•GDP+Pi (PDB 7ST7) is also plotted for comparison, as elaborated in the text.

Functional states G, H and I (Off-pathway states)

These states are characterized by the near or complete absence of P-site tRNA. State G (resolution 3.52Å) contains an E/E tRNA at the E-site and an A*/T tRNA bound to EF-Tu•GTP at the A-site; state H (resolution 3.12Å) contains an E/E tRNA at the E-site and an A/A tRNA at the A-site; and state I (resolution 3.08Å) contains an E/E tRNA at the E-site, an A/A tRNA at the A-site, and partial density for tRNA at the P-site, which I have designated as P/P' for this work (Fig. 43 Panels A, B and D).

Upon analysis of the 30S head swivel and body ratchet angles for these three states and comparing them with the other sub-states in the dataset, states G, H and I were found closest to sub-states B2, C6 and C10, respectively (Fig. 43 Panel C). State G exhibits a markedly greater head swivel compared to EF-Tu•GTP-bound sub-states with P-site tRNA (e.g., B2), while states H and I display none or only slightly increased head swivel compared to sub-states with P-site tRNA (e.g., C6 and C10).

Although the densities for NOSO-502, the monitoring bases of the decoding center, and the A*/T tRNA are poorly resolved in state G, preventing analysis of their interactions, these are well-resolved in states H and I. In both of these states, NOSO-502 is found to interact with the backbones of 16S rRNA helices h31 (C962), h32 (C1214), and h34 (G1050, U1052), and also with the backbones of residues 31, 32 and 34 of the A-site tRNA, consistent with states B and C. State H map density indicated an interaction network between the monitoring bases of the decoding center, the A-site tRNA and NOSO-502 which is identical to that in sub-state C6 (Fig. 40 Panel B) – the only structural difference between them is the absence of the P-site tRNA in state H. In state I, the map density revealed a closed 30S subunit with the decoding center in a locked conformation (Fig. 43 Panel E).

While the three states cannot be directly mapped into the canonical translation elongation pathway, these stalled P-site tRNA-depleted complexes may represent functional consequences of NOSO-502-binding and failed translocation, as discussed in the following sub-section.

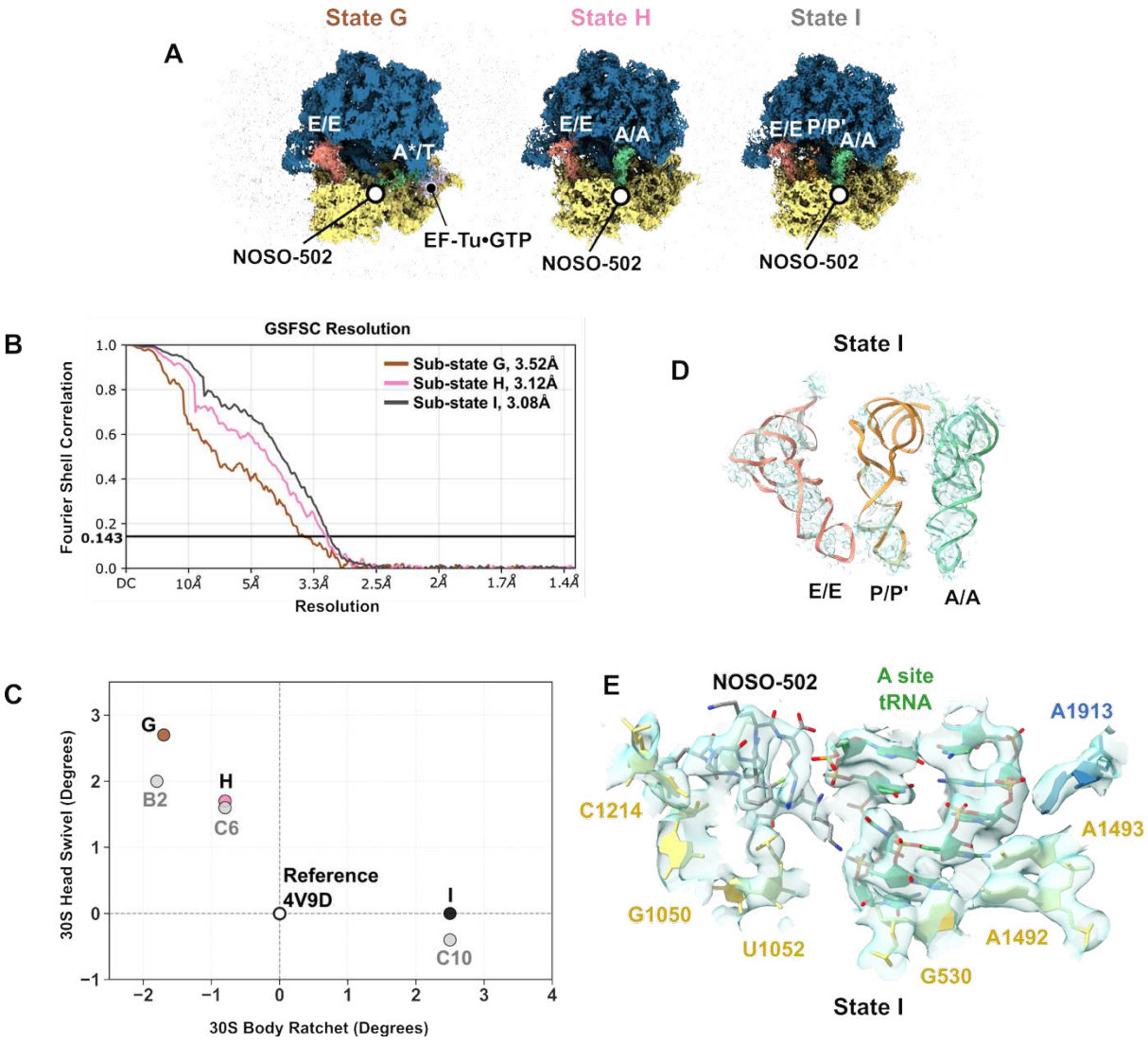

Figure 43: Structural and conformational features of functional states G, H and I: **A**. Cryo-EM maps for states G (left), H (middle) and I (right). **B.** Fourier Shell Correlation (FSC) curves for the final reconstructions, determined using the gold-standard FSC cutoff of 0.143. **C.** Graph generated using RADTool, plotting 30S body ratchet and head swivel angles for states G, H and I, and the corresponding nearest sub-states from the dataset – B2, C6 and C10, respectively (in grey), relative to a reference non-rotated PRE-C state (PDB 4V9D). **D.** Cryo-EM density (in light blue) of state I, showing the partial density corresponding to the P/P' tRNA (nomenclature for this work only), versus complete density for E/E and A/A tRNAs. **E.** Cryo-EM density (in light blue) of state I fitted with the structural model of NOSO-502, 16S rRNA residues G1050, U1052, C1214 (in yellow), the monitoring bases of the decoding center (G530, A1492, A1493 of 16S rRNA, in yellow, and A1913 of 23S rRNA in blue), and the A-site tRNA (in green).

3.2.7. Structural basis of proofreading impairment and translocation inhibition revealed by the conformational landscape of NOSO-502-bound stalled ribosomes

As described in the previous sub-section, NOSO-502 binds near the decoding center of the *E. coli* ribosome, in the 30S subunit. This binding site agrees with the previously reported crystal structure of NOSO-95179-bound *T. thermophilus* ribosome (Pantel et al. 2018), and the interactions of the drug with the sugar-phosphate backbones of residues in the 16S rRNA helices h31, h32 and h34 are conserved in both NOSO-502 and NOSO-95179. However, while the previously reported X-ray structure trapped a single conformation of the NOSO-95179-bound ribosome containing cognate tRNAs in the PRE-C state, the cryo-EM data in this work revealed a broad conformational landscape of NOSO-502-bound ribosomes comprising 27 distinct sub-states that capture a range of tRNA compositions and 30S rotational states. In all cases, the binding site and hence the interactions of NOSO-502 and the 16S rRNA are conserved, suggesting that the drug remains bound and moves with the SSU together, as a unit. NOSO-502-bound ribosomes stalled at the PRE-C stage (State C) represents the dominant population in the dataset, accounting for 53.28% of all analyzed particles (Fig. 44), followed by complexes trapped at the initial selection stage (State B) bound to EF-Tu•GTP (22.26%), the PRE-H stage with A/P* tRNA (State E) (16.63%), and a post-translocation stage with an empty A-site (State A) (2.99%). The remaining conformations (states D, F, G, H and I) each represent minor populations, ranging between 0.42 and 1.19% of the dataset. Together, these populations revealed the key steps of the decoding and translocation pathways that are targeted by NOSO-502, leading to ribosomal stalling.

The unambiguous assignment of tRNA identities in these stalled complexes was not possible due to a mixture of indistinguishable initiation and elongation complexes stalled with initiation (AUG) and Asp (GAU) codons in the P-site, respectively. However, parallel analyses on the TDCL motif (results from Dorian Gayral, not discussed in this thesis), which only exhibited a major stalling band with a Cys (UGU) codon in the P-site (Fig. 31), also did not allow unambiguous base assignment at the anticodons and hence, tRNA identities could not be ascertained. Further, in both cases, while simultaneously interacting with the 16S rRNA, NOSO-502 was also found to interact with the phosphate backbones of A-site tRNA residues in the anticodon stem-loop, in all the applicable conformational states, and not the nucleotide bases, as was

also reported for the NOSO-95179-bound structure. This is expected to increase the affinity of any incoming aminoacyl-tRNA during decoding and potentially decrease the accuracy of translation by allowing the stabilization of near-cognate aminoacyl-tRNAs. Hence, together, these observations strongly suggested that in both the NOSO-502-bound datasets, ribosomes stalled with a mixture of near-cognate tRNAs had been captured. Moreover, analyses on ribosomes stalled on the TDCL motif showed similar conformational distributions as on the mDDP motif, strengthening the hypothesis that during translation of a stalling motif, odilorhabdins, specifically NOSO-502, trap a variety of distinct functional intermediates of the ribosome across the decoding and translocation pathways.

NOSO-502 primarily impairs the proofreading capacity of the ribosome, permitting translation to proceed despite the incorporation of near-cognate tRNAs. This is principally reflected by the capture of states A, B and C.

As discussed in Chapter 1, initial binding of the ternary complex of EF-Tu, GTP and an aminoacyl-tRNA to the ribosome is codon-independent (Kothe et al. 2004; Diaconu et al. 2005; Rodnina 2012), allowing different tRNAs to sample the codon in the A-site. Usually, only the presence of a cognate tRNA can achieve the correct geometry of the codon-anticodon mini-helix necessary to obtain a locked decoding center and the induced-fit closure of the 30S subunit (Ogle et al. 2001, 2002, 2003; Agris 2004). Near-cognate tRNAs do not meet these geometric requirements, and hence the 30S remains open, the decoding center remains unlocked, with reduced GTPase activation and a higher probability of rejection of the A-site tRNA before GTP hydrolysis (Pape et al. 1998, 1999; Rodnina and Wintermeyer 2001; Ogle et al. 2002). State B captures this initial selection stage of translation where the 30S is in its open conformation, the decoding center is unlocked, and EF-Tu is in its GTP-bound conformation, with near-cognate tRNAs sampling the A-site codon. However, although the decoding center is in an overall unlocked conformation, the density of the monitoring base G530 indicates a SEMI-ON conformation, which has been shown by time-resolved cryo-EM (Loveland et al. 2017) to be characteristic of cognate tRNA recognition. This could be hypothesised as a consequence of NOSO-502-induced stabilisation of the near-cognate codon-anticodon mini-helix, which allows the syn- to anti-conformational change of G530. From state B, the structural landscape shows two possible fates – rejection and dissociation of the near-cognate

A-site tRNA, leading to an empty A-site (represented by State A), or progression towards accommodation of the near-cognate tRNA and subsequent peptide bond formation (represented by State C). It is notable here that intermediates between states B and C, such as domain closure of the 30S subunit, GTP hydrolysis by EF-Tu resulting in an EF-Tu•GDP-bound ribosome followed by EF-Tu dissociation, are not trapped in the dataset, possibly because they are too transient in the NOSO-502-bound state to accumulate and be captured without time-resolved cryo-EM strategies. It can be argued that GTP hydrolysis itself is also a very rapid process and hence the GTP-bound state should not have been observable – a possible explanation behind its appearance in the dataset is that the closure of the 30S subunit in the presence of cognate tRNA is the key rate-limiting step before GTP hydrolysis, which is slowed down in the NOSO-502-bound state due to near-cognate tRNA stabilization. However, specific kinetic studies need to be performed to precisely map the reaction rates.

Besides representing the most populated state in the dataset, state C is also the most structurally heterogeneous, comprising 10 distinct sub-states, of which 6 feature distinct rotational states with an open 30S, 1 has a semi-open 30S, while the remaining 3 have a closed 30S subunit. The sub-states with an open 30S further sample a variety of conformations of the decoding center, ranging from unlocked and partially locked to fully locked. Under canonical conditions, the PRE-C state is characterized by a locked decoding center and a closed 30S subunit. Hence the capture of these non-canonical sub-states depicts how the preceding checkpoints of initial selection and proofreading are impaired by NOSO-502, which, via its interactions with the A-site tRNA backbone, stabilizes near-cognate tRNAs during accommodation, effectively decoupling the decoding center locking and 30S domain closure from tRNA selection. Although the A*/A tRNA conformations in the open 30S sub-states (C1-C6) reflect non-optimal accommodation of the tRNA, they have peptidyl density attached to them. This suggests that in the presence of the antibiotic, peptide bond formation proceeds despite an open 30S subunit and an unlocked or partially locked decoding center, indicating that the closure of the 30S and locking of the decoding center are decoupled from peptide bond formation. The ambiguous base densities at the codon-anticodon mini-helix, in part due to the mixture of stabilized near-cognate tRNAs, did not allow analyses of NOSO-502-induced distortion of the mini-helix backbone, if any, which could provide further mechanistic detail.

However, the observations overall suggest that NOSO-502 also impairs the post-accommodation proofreading at the PTC, since if it were operative, the near-cognate tRNA would be rejected, yielding a higher population of the empty A-site-containing state A, rather than undergoing peptidyl transfer. Sub-states C7-C10 capture a progressive transition towards 30S domain closure and a locked decoding center, underlining that while NOSO-502 permits peptide bond formation in open 30S conformations, it also allows translation to proceed via the canonical pathway towards translocation. However, the incorporation of a mismatched peptidyl tRNA does have functional consequences. For example, state H represents a minor off-pathway intermediate characterized by a closed 30S subunit and lacking P-site tRNA density. This is likely a result of dissociation or "drop-off" of the misincorporated peptidyl tRNA from the mRNA, which stops elongation – a mechanism consistent with smFRET studies on miscoded peptidyl-tRNAs (Alejo and Blanchard 2017). Peptidyl tRNA drop-off may also proceed via an open 30S intermediate such as state I, which exhibits a partially locked decoding center and partial P-site tRNA density. Nevertheless, both states H and I represent minor populations (1.1% and 1.19%, respectively), whereas the PRE-H state E represents a substantially larger population (16.63%), suggesting that from the PRE-C state C, most ribosomes proceed toward translocation rather than exiting the translation cycle.

The transition from state C (PRE-C) to E (PRE-H with A/P* peptidyl tRNA) proceeds through a minor intermediate population of ribosomes stalled in state D (PRE-H with A/P peptidyl tRNA). Analysis of PRE-H complexes in state E revealed a locked conformation of the decoding center, consistent with canonical drug-free conditions, suggesting that once the NOSO-502-bound ribosomes overcome the PRE-C stage, the decoding center maintains its locked conformation through the PRE-H stage. The only other translocation intermediate observed among the stalled ribosomal complexes is a minor population (0.42%) of back-rotated and hyper-swiveled EF-G•GDP-bound ribosomes (state F), corresponding to a late translocation intermediate (INT2) state. smFRET studies have previously shown that translocation of peptidyl-tRNA from the A-site to the P-site is rate-limited by the recognition of a cognate peptidyl-tRNA within the P-site, and hence a mismatched peptidyl-tRNA-mRNA pairing within a PRE complex severely impairs and delays translocation. Specifically, these defects have been shown to occur during late steps of translocation, with extended periods of fluctuation between the INT2 and INT3

states (Alejo and Blanchard 2017). This is consistent with the structural landscape captured in the NOSO-502-bound dataset, where translocation inhibition is represented by the accumulation of PRE-H complexes carrying misincorporated peptidyl tRNA, and the trapping of the INT2 intermediate, both arising as a consequence of delayed translocation caused by mismatched peptidyl-tRNA-mRNA pairing. These states may also be linked to the off-pathway states. Indeed, exiting the translation cycle via peptidyl tRNA drop-off has been reported to be more likely following late translocation intermediates (Alejo and Blanchard 2017), e.g., here, after state F. Although kinetic studies are essential for validation, the observations in the NOSO-502-bound states could also lead to the hypothesis that there are repeated, futile cycles of GTP hydrolysis on EF-G as a consequence of the misincorporated peptidyl tRNA (similar to previous observations during translocation inhibition induced by viomycin (Holm et al. 2016)), leading to EF-G dissociation, causing the ribosome to revert to the PRE-H states, which are in turn in equilibrium with the PRE-C state. Such unsuccessful translocation attempts can also lead to peptidyl-tRNA-dropoff, linking state H with states D-F.

The only off-pathway state that could not be readily rationalized in this dataset is state G, which features an E/E tRNA, an A*/T tRNA bound to EF-Tu•GTP, completely lacks P-site tRNA density and exhibits a higher degree of 30S head-swivel than state B complexes. To my knowledge, peptidyl-tRNA-drop-off while the ribosome is still bound to EF-Tu at the initial selection stage is not reported in the translation literature. Further, previous independent cryo-EM datasets in our laboratory using PURE *in vitro* translation system have also indicated a similar P-site-tRNA-depleted, EF-Tu-bound conformation. Given these factors, coupled with the limited map resolution of state G that did not allow interpretation of NOSO-502 interactions with the ribosome, this state could also represent a reconstruction or cryo-EM grid preparation artifact. Nevertheless, since state G comprises 1.13% of the dataset – a proportion comparable to other biologically relevant, NOSO-502-bound functional states such as state D (1%) or state I (1.19%), I retained it as an uncharacterized state in the observed conformational landscape.

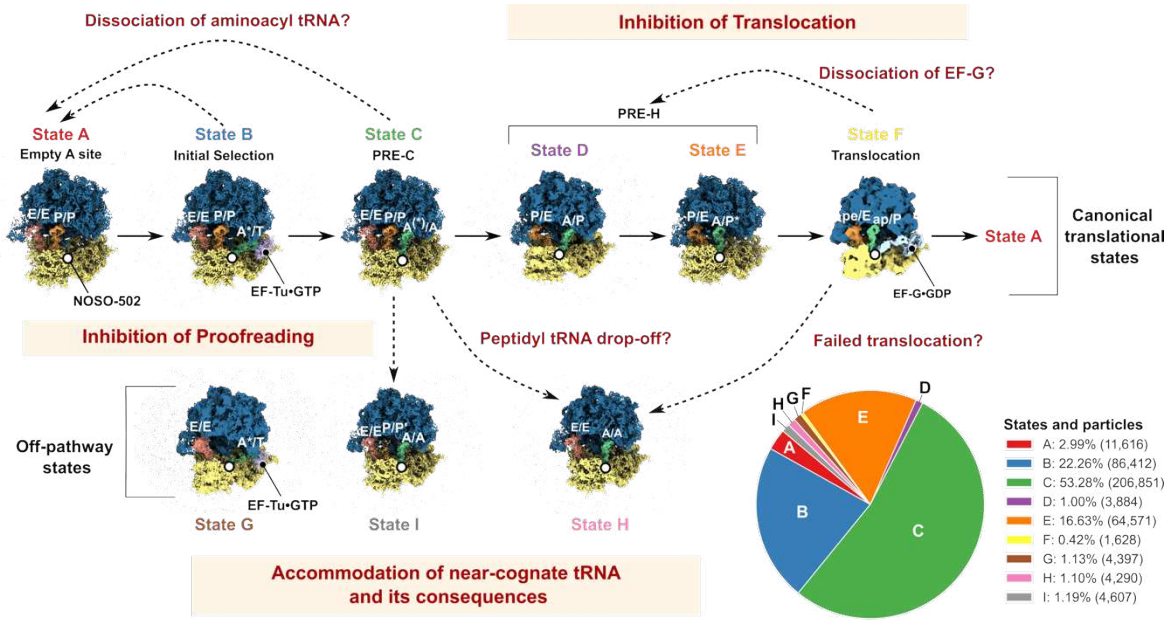

Figure 44: Conformational landscape and particle distribution of NOSO-502-bound stalled ribosomal complexes. Structural models and proposed relationships among the major functional states (states A–I) captured by cryo-EM. **Top:** Canonical elongation states trapped during translation, illustrating NOSO-502-induced inhibition of proofreading (states A-C) and inhibition of translocation (states C-F). Dotted arrows indicate proposed pathways for aminoacyl-tRNA dissociation (state B/C to state A), peptidyl-tRNA drop-off (states C/F to states H/I), and EF-G dissociation (state F to states D/E). **Bottom left:** Off-pathway intermediates (States G, H, and I) characterized by missing or partial P-site tRNA density. **Bottom right**: Pie chart showing the relative particle populations (percentage and absolute particle count) across states A–I in the dataset.

Overall, the structural states captured in this work represent high-energy elongation intermediates that are inherently transient during canonical drug-free translation and typically elude structural visualization outside of time-resolved cryo-EM analyses. Notably, these NOSO-502-bound states indicate a continuation of translation despite near-cognate tRNA incorporation, sampling a broad conformational landscape across both the decoding and translocation pathways. This structural ensemble reinstates the miscoding action of odilorhabdins, driven by non-specific interactions between NOSO-502 and the sugar-phosphate backbones of residues in the anticodon stem-loop of incoming A-site aminoacyl-tRNAs. By stabilizing near-cognate tRNAs at the A-site, NOSO-502 increases the affinity of near-cognate tRNAs to the ribosome – an effect that persists throughout subsequent steps of the translation cycle via interactions of the drug with the 16S rRNA helices h31, h32 and h34,

as well as the A-site tRNA. Ultimately, the spectrum of stalled complexes captured in this work visualizes the dual effect of NOSO-502 action – impairment of proofreading and consequent delay and inhibition of translocation, identifying the key intermediate steps of translation elongation targeted by odilorhabdins.

3.3. Conclusion and Perspectives

Before this work, the mechanism of translation inhibition by odilorhabdins was reported and discussed in one study (Pantel et al. 2018), which showed that they bind the 30S subunit of bacterial ribosomes near the decoding center, primarily causing misreading of the genetic code at low (~0.6μM) concentrations, and additionally leading to translocation inhibition at higher (20μM) concentrations. Odilorhabdin-induced ribosomal stalling was also suggested to be context-dependent, based on toeprinting experiments that showed preferential stalling on certain codons. The X-ray structure of NOSO-95179-bound *T. thermophilus* ribosome also revealed the interactions of the drug with the sugar-phosphate backbones of residues in the 16S rRNA and the A-site tRNA, suggesting that the drug stabilizes near-cognate tRNAs through non-specific backbone interactions, leading to miscoding and downstream translocation inhibition.

My thesis work advances the understanding of the mechanism of translation inhibition by odilorhabdins by providing deeper structural and functional insights. As presented in this chapter, I have first used iTP-Seq to characterize how the translational landscape is altered in a context-dependent manner during *in vitro* translation in the presence of both low (0.3-0.4μM) and high (40μM) concentrations of two odilorhabdins – NOSO-502 and NOSO-96624. This high-throughput approach revealed distinct trends in sequence-dependent stalling of ribosomes under the different odilorhabdin conditions and identified arrest motifs that induce ribosomal stalling. Further, single-particle cryo-EM analysis of ribosomes stalled on a representative arrest motif in the presence of 40μM of NOSO-502 revealed a conformational landscape that delineates key steps in the elongation pathway targeted by odilorhabdins.

However, certain questions remain. For example, the structural snapshots do not explain why the ribosome preferentially stalls on that arrest motif. Indeed, parallel structural analyses on a different stalling motif yielded a similar conformational landscape, but it also did not provide

further insights that can be linked to the sequence-dependent action. Based on our findings, it can, however, be hypothesized that sequence-dependent stalling is principally governed by the specific near-cognate tRNA species that are recruited at different sets of codons. Deciphering this specificity will require systematic investigations of mismatched codon-anticodon pairings to determine which near-cognate tRNA species stall the ribosome and shut down translation, versus which species yield released mistranslated proteins, for a particular codon. As such, to trace these misreading events, it could be interesting to examine the sequences of peptides released during *in vitro* translation of iTP-Seq-identified arrest motifs (in wild-type or mutant bacterial proteins), across a gradient of odilorhabdin concentrations using mass spectrometry. This approach could provide further insights into the sequence-dependent action of odilorhabdins by identifying which near-cognate tRNAs escape proofreading without causing stalling, allowing us – by process of elimination – to get a hint of the possible tRNAs trapped within the stalled complexes. To this end, our lab has started a collaboration with Dr Ingo Wohlgemuth and Prof Marina Rodnina (MPI Göttingen, Germany), who specialize in mass-spectrometry-based quantification of antibiotic-induced mistranslation (Garofalo et al. 2019; Wohlgemuth et al. 2021). While direct identification of the tRNAs trapped within the *in vitro* translation complexes could theoretically be achieved via tRNA microarrays (Kirchner, Cai, et al. 2017; Kirchner, Robert Rauscher, et al. 2017), preliminary exploratory attempts indicated that the total RNA input required exceeds the yield practically feasible with the *in vitro* PURE system used in this work. Future cell-free extract-based *in vitro* transcription/translation assays or *in cellulo* studies can provide possible alternatives and could also be important to better understand the mechanism of action of odilorhabdins in more physiologically relevant conditions.

In summary, although certain questions regarding the sequence-dependent mechanism of action of odilorhabdins remain to be fully resolved, this work contributes structural and functional insights into NOSO-502-mediated translation arrest, providing a foundation for future biochemical and structural investigations.

Chapter 4

Context-dependent inhibition of translation by tigecycline

The second antibiotic I studied during my thesis is tigecycline, a third-generation derivative of tetracycline, developed in the late 1990s and in clinical use since the early 2000s. Tigecycline is known to bind the 30S subunit of the bacterial ribosome near the decoding center and sterically prevent the A-site tRNA from being accommodated, leading to translation inhibition and elongation stalling. The idea of checking if tigecycline is context-dependent was conceived together with our collaborators, Prof Alexander (Shura) Mankin and Dr Nora Vázquez-Laslop, at UIC Chicago, USA. Unpublished ribosome profiling data from the Mankin-Vázquez-Laslop lab revealed that tigecycline causes pronounced elongation stalls on several genes, represented by elevated read counts at certain sequence motifs, although no general trends were immediately apparent. Further, strong initiation stalls were also observed in the presence of tigecycline. While tetracyclines were long considered to be primarily elongation inhibitors, initiation inhibition by tetracyclines, including tigecycline, has also been discussed in more recent literature (elaborated later in this chapter). As such, using iTP-Seq, I decided to characterize the context-dependent action of tigecycline for both initiation and elongation stalls across a range of concentrations.

In this chapter, I will provide a brief overview of the known mechanisms of translation inhibition by tigecycline, followed by my observations and interpretation of its sequence-dependent action. For the iTP-Seq analyses, I worked together with Dr Thibaud Renault, who is the author of the now open-source itpseq Python library (https://pypi.org/project/itpseq/) (Gillard et al. 2026), which was still in development and improvement when I analyzed the data. While the results presented in this chapter are primarily observational, they nevertheless add to our knowledge and understanding of which specific sequences can preferentially lead to ribosomal stalling in the presence of tigecycline and provide insights to guide future structural and mechanistic studies.

4.1. Introduction: Tigecycline – a third-generation derivative of tetracycline

Tetracyclines are broad-spectrum aromatic polyketide antibiotics that target both Gram-positive and Gram-negative bacteria and are naturally produced by type-II polyketide synthases in soil-dwelling actinomycetes bacteria. They were first isolated as the secondary metabolite aureomycin (Duggar 1948) or chlortetracycline, during the Golden Age of antibiotic discovery, and then chemically modified and developed in the early 1950s by Pfizer and Robert B. Woodward as tetracycline, a potent drug against bacterial pathogens (Conover et al. 1953). Tetracyclines take their name from the four fused rings (A, B, C, D) of their naphthacene core (Fig. 45 Panel A) (Stephens et al. 1952). Driven by the need to improve pharmacokinetic properties, enhance antimicrobial potency, lower patient toxicity, and overcome emerging resistance to tetracycline, the antibiotic was iteratively modified and second-generation (e.g., doxycycline, minocycline) (McCormick et al. 1957; McCormick et al. 1960; Martell and Boothe 1967) and third-generation (e.g., tigecycline, eravacycline, omadacycline, sarecycline) (Barden et al. 1994; Sum et al. 1994; Ronn et al. 2013; Honeyman et al. 2015; Deeks 2019) tetracyclines were developed.

Tigecycline is a glycylcycline derived from tetracycline by modifications made in the C7 and C9 positions of ring D of the tetracycline core, by the addition of a 7-dimethylamino and a 9-t-butylglycylamido moiety, respectively (Fig. 45 Panel A) (Barden et al. 1994; Sum et al. 1994). Originally designated GAR-936, tigecycline displayed an MIC range of 0.25-0.5µg/ml against *E. coli*, *S. aureus* and *E. faecalis* strains expressing tetracycline efflux resistance determinants such as *tet(A), tet(B), tet(C), tet(D), tet(K)* and ribosomal protection genes like *tet(M)* (Petersen et al. 1999), becoming one of the most potent antimicrobials of the time to be introduced into the market (as Tygacil), approved for use by the FDA in 2005 (Senior 2005).

The primary mode of action of tigecycline is translation elongation inhibition via binding to the 30S ribosomal subunit. The X-ray crystal structure of the *T. thermophilus* 70S ribosome with 60µM tigecycline has shown that the drug binds at the head of the 30S subunit, in a pocket formed by helices h31 and h34 of the 16S rRNA. This pocket overlaps with the position of the anticodon stem-loop of an A-site-bound tRNA, thereby sterically preventing the accommodation of an incoming aminoacyl tRNA (Brodersen et al. 2000; Pioletti 2001; Murray et al. 2006; Jenner et al. 2013). The polar edge of tigecycline (encompassing the hydrophilic

functional groups around C1, C11 and C12) interacts directly with the phosphate-oxygen backbone of residues C1195 and U1196 in h34, and also indirectly, via two distinct Mg^{2+} ions, with the backbones of residues G1197, G1198 and C1054 in h34, and G966 in h31 (Fig. 45 Panel B). Notably, the glycyl nitrogen of the C9 extension of tigecycline forms a unique stacking interaction with the π-orbital of C1054, which in turn stacks against U1196. C1054 is a canonically dynamic nucleotide that is important for A-site decoding via interactions with the anticodon loop, specifically residue 34 of the incoming aminoacyl tRNA (Ogle et al. 2001, 2003). By stacking against C1054 and locking it into a rigid conformation, tigecycline mimics the local architecture observed during canonical A-site tRNA binding. This restriction of C1054 mobility, mediated by the C9 extension, accounts for the enhanced target binding and inhibitory properties of tigecycline relative to tetracycline, where the C9 extension is absent. Further, the X-ray crystal structure of the *T. thermophilus* 30S subunit with 100μM tigecycline (Schedlbauer et al. 2015) showed that tigecycline can also adopt an extended conformation where the C9-side chain peptide bond is planar and extends toward G530 in h18 (Fig. 45 Panel C). In this conformation, tigecycline is proposed to form additional interactions with the base and ribose at C1054, further restricting its mobility. Structural analyses and smFRET studies have also confirmed that the C9 extension plays an important role in evading resistance. It overlaps with the domain IV loop of the tetracycline resistance-conferring ribosome protection protein TetM, thereby preventing TetM binding, and hence overcoming the resistance by continued blocking of tRNA entry into the A-site (Jenner et al. 2013).

Beyond their role in elongation inhibition, tetracyclines, including tigecycline, have also been implicated in initiation inhibition. Earlier studies have suggested that tetracycline competes with translation initiation factors IF1 and IF3 for overlapping binding sites in the A-site of the 30S subunit, thereby destabilizing the initiation complex (Risuleo et al. 1976; Carter et al. 2001; Pioletti 2001; Simonetti et al. 2008). Additionally, *in vivo* ribosome profiling studies conducted in the presence of tetracycline have revealed enrichment of ribosome footprints at canonical translation start sites (Nakahigashi et al. 2014, 2016). More recent pre-steady-state kinetic and molecular modelling analyses have demonstrated that tetracyclines, including tigecycline, induce a structural compaction of the 30S-bound-IF3, which is a conformational rearrangement canonically associated with IF1 binding (Barrenechea et al.

2021). Notably, these studies show that rather than competing with IF1, tetracyclines and IF1 act cooperatively to stabilize this compacted 30S-IF3 state. For tigecycline, its bulky C9 modification is further proposed to establish potential contacts with Lys39, Met42, His43, Tyr44, Ile45 and Arg70 of IF1. This enhanced interaction is suggested to promote IF1 retention on the 30S subunit, delaying the 70S initiation complex assembly and the subsequent transition into translation elongation (Barrenechea et al. 2021) (Fig. 45 Panel D).

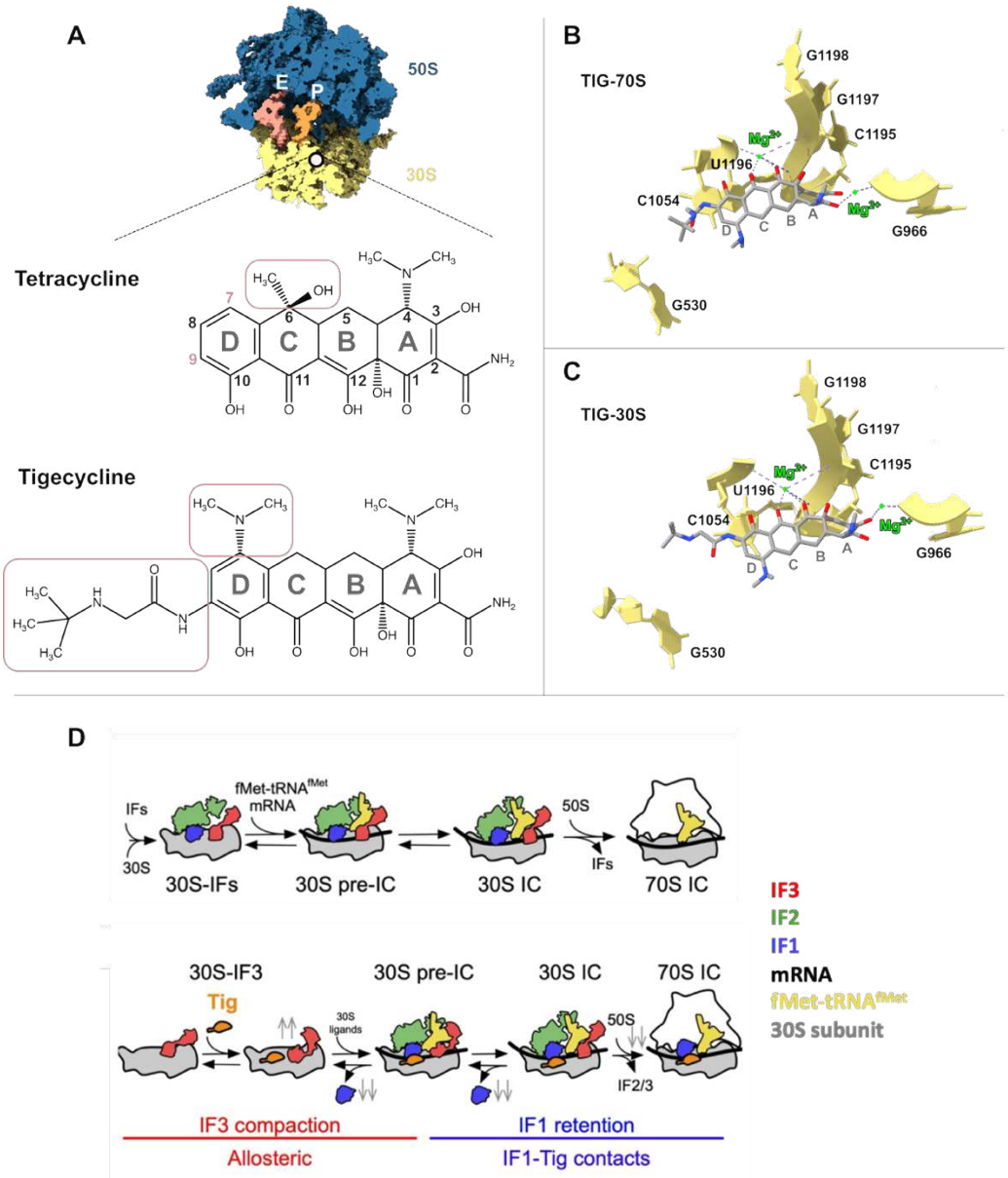

Figure 45: Binding site, chemical structures and initiation-targeting mechanism of tigecycline. A. Tigecycline (white circle) binds to the 30S subunit (in yellow) of the bacterial 70S ribosome (surface representation generated from PDB 4V9B (Jenner et al. 2013)); 50S subunit is shown in blue, the E- and P-site tRNAs are shown in pink and orange, respectively), sterically preventing accommodation of

the A-site tRNA. The binding site of tigecycline overlaps with that of its parent compound, tetracycline. The chemical structure of tetracycline with carbon atom assignments (1-12) for rings A-D are shown in the middle panel. The chemical structure of tigecycline is shown in the bottom panel with modifications in C7 and C9 boxed in light pink. The C6-methyl and C6-hydroxyl groups in tetracycline, which are absent in tigecycline, are also boxed in light pink. **B, C.** The binding site of tigecycline (A-D rings labelled in grey) surrounded by the 16S rRNA residues (in yellow) mentioned in the text is shown when bound to the 70S subunit (in B, PDB 4V9B) and the isolated 30S subunit, adopting its extended form (in C, PDB 4YHH (Schedlbauer et al. 2015)). The indirect coordination network between tigecycline and the 16S rRNA residues via the two Mg^{2+} ions (green spheres) is indicated in purple dashed lines. **D.** Schematic diagram showing the canonical translation initiation pathway (top panel) with its alteration in the presence of tigecycline (bottom panel). As mentioned in the text, tigecycline binding can allosterically lead to IF3 compaction and, via direct contacts with IF1, lead to its retention on the 30S subunit, delaying 70S initiation complex (70S IC) assembly. Grey double arrows indicate relative increases (up) or decreases (down) in specific kinetic step rates. Panel D is adapted from Barrenechea et al. 2021, licensed under CC BY 4.0 (https://creativecommons.org/licenses/by/4.0/).

However, over the years, due to widespread clinical overuse of the drug, tigecycline-resistance genes have emerged rapidly in bacteria and spread via horizontal gene transfer. Currently, the major pathways of tigecycline resistance in different *Enterobacterales* include overexpression of multidrug efflux pumps (e.g., AcrAB-TolC, MFS superfamily transporters and MexABCDXY-OprJM systems) as well as ribosomal protection via the mobile *tet* family genes that can enzymatically degrade tigecycline (*tet(X)* variants) (reviewed in Yaghoubi et al. 2022; Korczak et al. 2024). Further, several adverse effects of the use of tigecycline have been discovered in clinical trials, identifying an increased risk of all-cause mortality, prompting the FDA to issue a black box warning (last updated in 2025) that restricts its current use to monotherapy in adults only when alternative therapeutic options are unavailable. While this underscores the need for novel next-generation translation inhibitors, the rational engineering of new drugs requires a comprehensive understanding of the mechanism of action of existing drugs like tigecycline. Despite the detailed structural characterization of tigecycline bound to the bacterial ribosome, static atomic models alone cannot account for how ribosomal stalling varies across different mRNA templates. As suggested by *in vivo* ribosome-profiling experiments from our collaborators, tigecycline-mediated inhibition of initiation and elongation is not absolute – instead, the specific sequence being translated appears to impact whether the ribosome strongly stalls at initiation or can continue translation elongation for a few cycles. However, these experiments were unable to establish a specific trend in sequence-specific action of

tigecycline – indeed, the variety of sequences that can be sampled by Ribo-Seq is limited by variable transcript abundance *in vivo*, leaving vast regions of the translational sequence space unexplored. Hence, I decided to perform high-throughput iTP-Seq on a randomized (NNN)15 library (same as described in Chapters 2 and 3) that can sample ~10^{12} unique peptide sequences in one *in vitro* assay. By performing iTP-Seq across a gradient of tigecycline concentrations, I aimed to have a comprehensive understanding of which sequence contexts preferentially lead to ribosomal stalling *in vitro* in the presence of the antibiotic, versus those that allow translation to proceed.

In the next sub-section, I discuss the results and trends of sequence-dependent antibiotic behaviour that were revealed from the iTP-Seq experiments.

4.2. Results and Discussion

Tigecycline has been reported to exhibit a half-maximal inhibitory concentration (IC_{50}) of 0.3µM in an *E. coli in vitro* transcription/translation assay with GFP fluorescence as readout (Jenner et al. 2013), and our collaborators used a concentration of 9.64µM for their Ribo-Seq experiments. However, to have an exhaustive view of sequence-dependent tigecycline activity over a wider range of concentrations, I performed iTP-Seq experiments at the following five concentrations: 0.05µM (a sub-IC_{50} negative control expected to let translation continue largely unaffected), 0.5µM (a concentration near the IC_{50}), and three subsequent 10-fold serial concentrations, i.e., 5µM, 50µM and 500µM.

iTP-Seq was performed in independent biological quadruplicates for each antibiotic condition, using the same (NNN)15 template DNA library as described for the experiments with odilorhabdins in Chapter 3. The inverse toeprints from both the tigecycline and odilorhabdin experiments were sequenced together at the BGI Genomics Facility, Hong Kong, by short-read (paired-end, 150bp) next-generation Illumina sequencing, and hence they both shared the same no-antibiotic negative control described in Section 3.2.1. One replicate from the 0.05µM tigecycline condition failed to meet quality control standards before next-generation sequencing, resulting in biological triplicates for this specific condition.

The raw sequencing reads were processed and quality-filtered using the same pipeline outlined in Section 3.2.2. Similar to previous observations, processed reads demonstrated a tri-nucleotide periodicity for fragments where RNase R cleavage had occurred ~21–48 nucleotides (corresponding to 1-10 codons) downstream from the start codon (Fig. 46). Notably, despite considering inter-replicate and inter-condition variations at the initiation peak (codon 1 in Fig. 46) due to manual excision of the high-intensity initiation gel bands (Supplementary Fig. 55), the initiation peaks for conditions with 5µM, 50µM and 500µM tigecycline displayed a substantial increase in the normalized read counts compared to the control and 0.05µM and 0.5µM tigecycline conditions. This suggested that tigecycline inhibits translation initiation *in vitro*, in agreement with previously reported results. However, peaks for ribosomes stalled at codon 2 and beyond were also observed, although their relative counts decreased in a tigecycline-concentration-dependent manner. This suggested that

despite inhibiting translation initiation, tigecycline allows translation elongation to continue for a few cycles, exerting a dual role on both these steps.

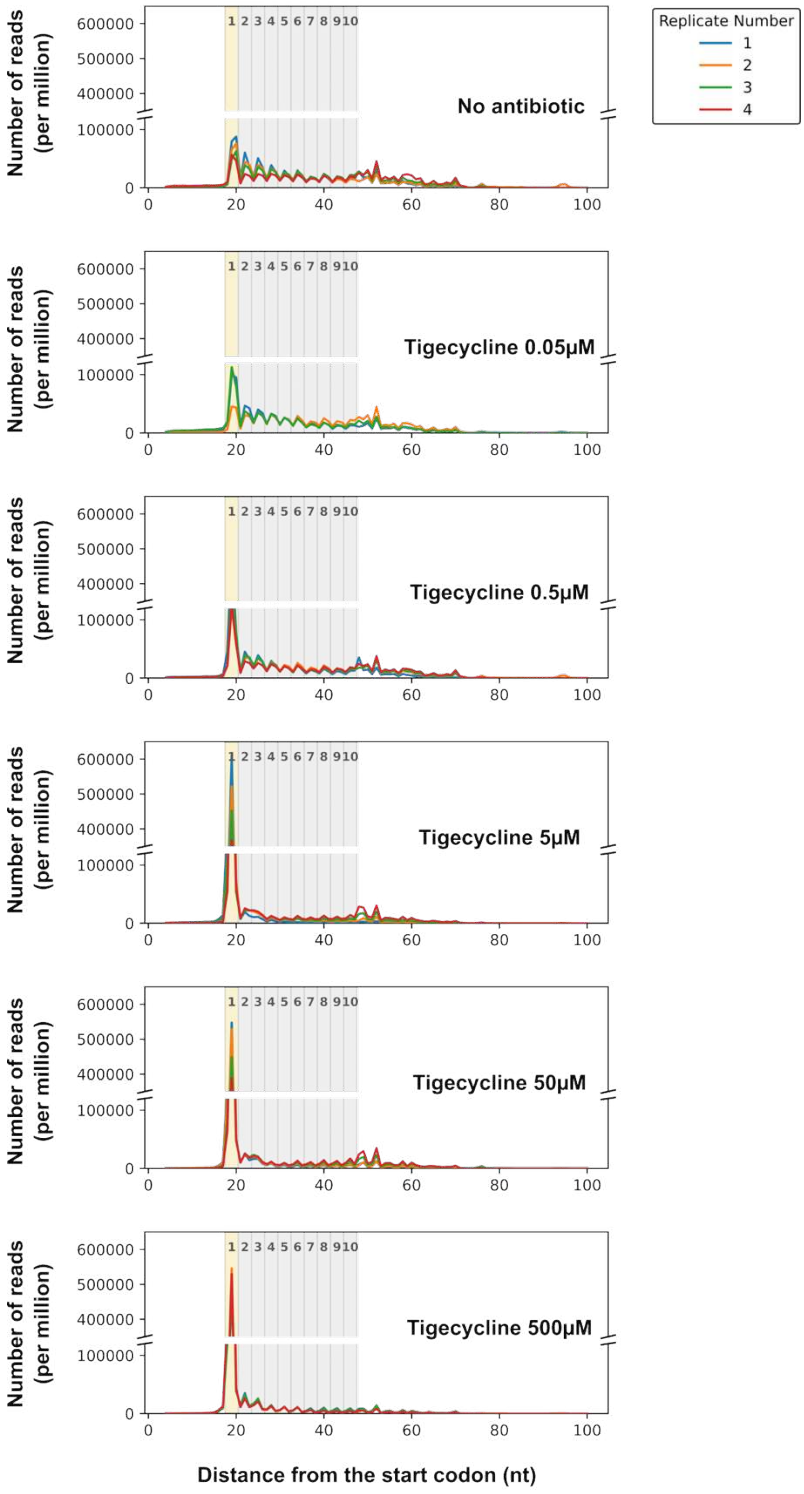

Figure 46: Distribution of obtained sequencing reads. Read counts, normalized to reads per million to adjust for differences in sequencing depth, are represented as a function of the distance from the start

codon for untreated (no antibiotic) and tigecycline-treated samples across all replicates. The shaded area (codons 1–10) highlights the reads selected for analysis, corresponding to the region where the three-nucleotide periodicity is well-defined. The first column in this shaded region is highlighted in yellow; this corresponds to ribosomes stalled at the initiation step of translation. The y-axis is represented with a scale break (split axis) to visualize both the higher-count initiation and lower-count elongation reads.

Following the removal of longer fragments outside this triplet-periodicity interval, the proportion of the finally retained reads relative to the total reads collected per condition per replicate is illustrated in Fig. 47.

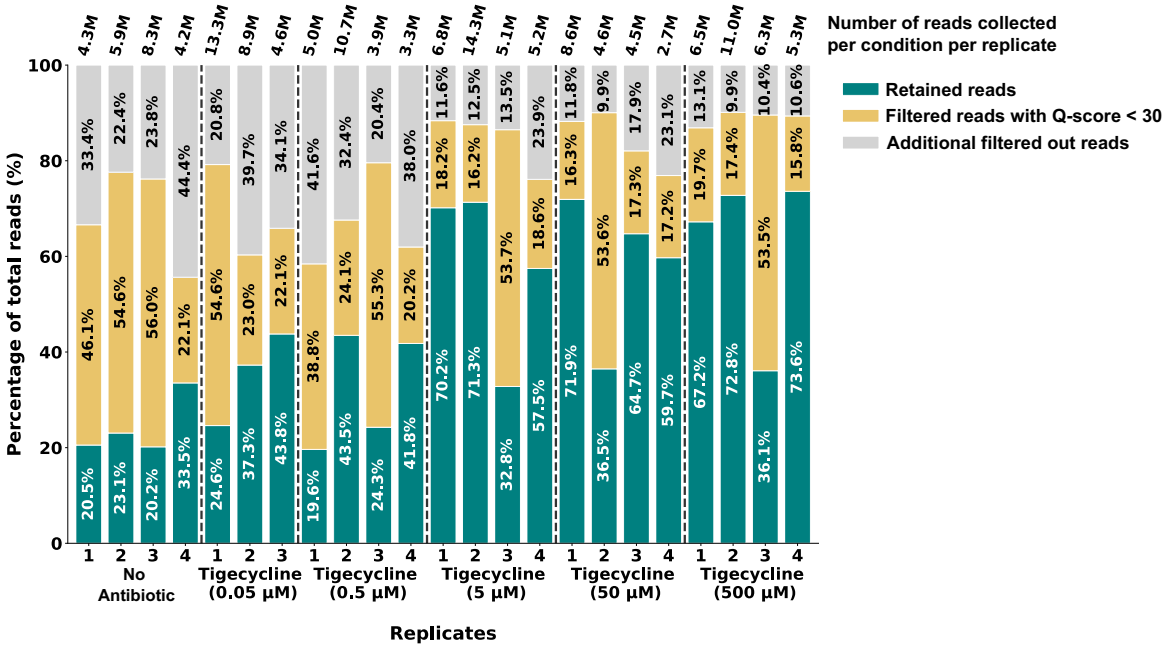

Figure 47: Proportion of sequencing reads retained after data processing and quality control. For each replicate of each experimental condition, the total number of collected sequencing reads is indicated at the top of the bar (M = millions), alongside the percentage of reads filtered out during quality control (in yellow) and additional data parsing (in grey). The retained reads (in teal) represent the percentage of reads that displayed well-defined triplet periodicity (codons 1-10) and were used for downstream analyses.

The pipeline used for downstream differential expression (DE) analysis of these processed reads was also identical to that described for odilorhabdins in Section 3.2.3.

The itpseq analysis software designates the initiation codon as atg in lowercase, with the corresponding fMet residue denoted as m, while all other ATG codons are designated in

uppercase, with the corresponding amino acid denoted as M for methionine. Thus, for characterizing tigecycline-induced sequence-dependent ribosomal stalling, I divided the dataset into two parts – inverse toeprints that do not contain fMet in the P-site, corresponding to ribosomes stalled during elongation, and those that contain the initiating fMet in the P-site, corresponding to ribosomes stalled during initiation – and analyzed them separately.

- **Tigecycline-induced context-dependent stalling of ribosomes during elongation**

As in the case of odilorhabdins, for ribosomes stalled during elongation, I first analyzed the pairwise codon enrichment based on amino acid sequence across the -2, E, P and A-sites, for each of the tigecycline-treated conditions, relative to the untreated control. While no significant enrichment or depletion patterns were observed at 0.05µM tigecycline (Supplementary Fig. 59), confirming that sub-IC_{50} concentrations of tigecycline do not induce measurable ribosomal stalling, only mild enrichment was observed for motifs with a Met codon in the P-site paired with codons for Arg/Glu/Gly/Ala in the A-site at 0.5µM tigecycline (Supplementary Fig. 60). Increasing the concentration to 5µM tigecycline and above revealed strong, highly significant enrichment trends that become more pronounced with increasing concentrations, broadening a core set of specific motif preferences (Fig. 48-50). At 5µM tigecycline concentration, stalling is predominantly observed with motifs containing an fMet codon in the -2 site, suggesting that elongation is inhibited within the first few translation cycles. Further, significant enrichment was observed in motifs with codons for hydrophobic amino acids (e.g., Ile/Leu/Met/Phe/Tyr/Trp) in the E or P-sites. Motifs with Met/Pro codons in the P-site or Trp codons in the A-site were also significantly enriched. Notably, most other di-amino acid combinations lacking a hydrophobic residue were significantly depleted. Significant depletion was also observed for stop codons in the A-site, suggesting that tigecycline does not affect canonical translation termination or recognition of stop codons in the A-site by release factors. In addition to these trends, at 50µM tigecycline, enrichment was also observed for motifs with codons for positively charged amino acids like His/Arg/Lys in the E-site or Arg/Lys in the A-site. At 500µM tigecycline, the trends broadened further, with enrichment extending to motifs with Arg/Lys codons in the P-site or codons for polar amino acids like Ser/Thr/Asn/Gln in the A-site. This concentration-dependent increase in significant stalling events is likely a consequence of increasing drug occupancy, gradually revealing the

full spectrum of sequence contexts that can lead to antibiotic-dependent ribosomal stalling. Overall, these results indicate that tigecycline induces sequence-dependent ribosomal stalling at different motif combinations in a concentration-dependent manner. While higher drug concentrations stall ribosomes on a broader motif variety, particularly those containing polar or positively charged residues, the primary, most significantly enriched motifs comprise early stalling sequences, P-site Met motifs, A-site Trp motifs, and motifs with hydrophobic amino acids across the -2, E and P-sites.

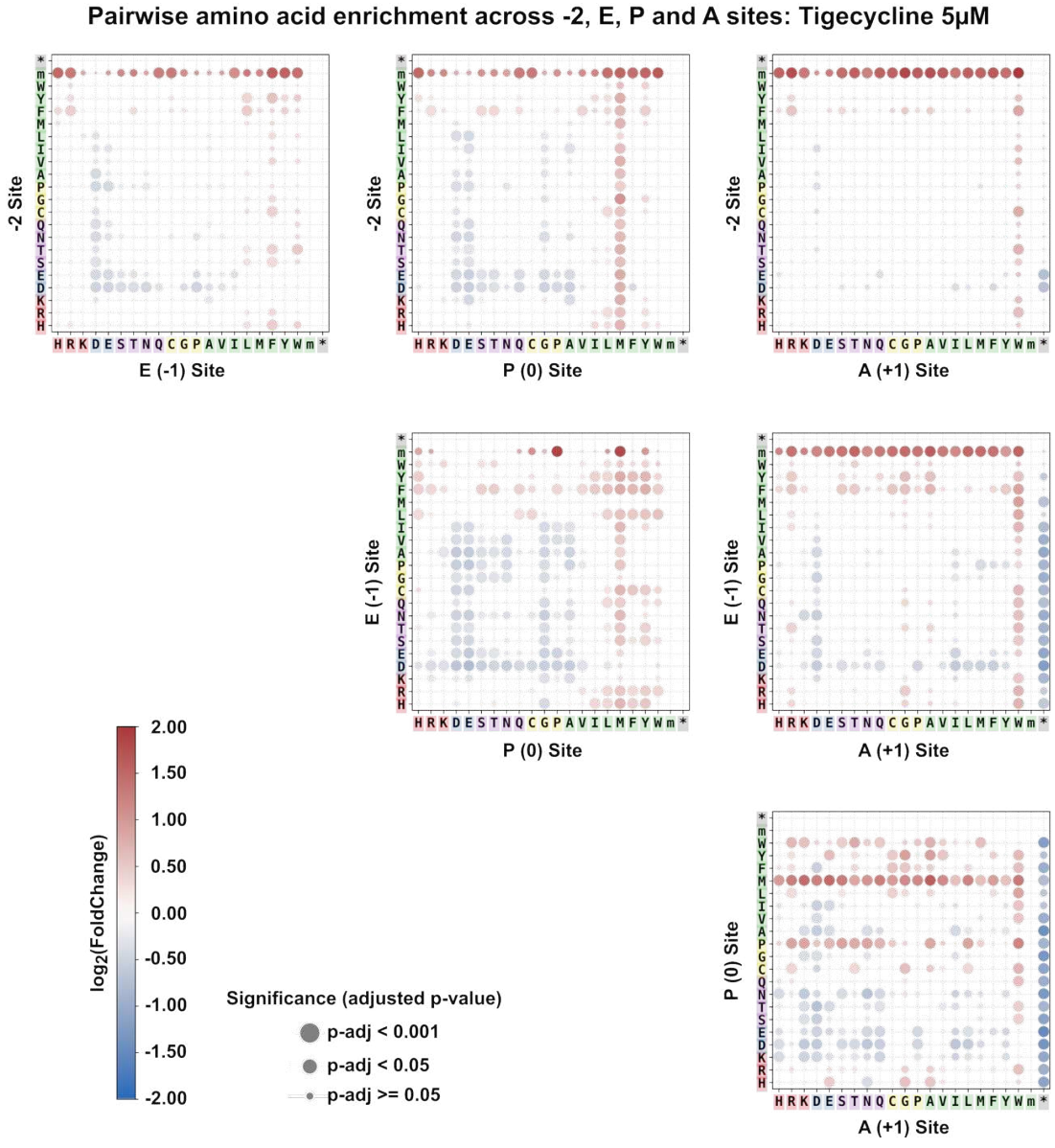

Figure 48: Heatmap grid representing the di-amino acid motifs enriched across -2, E, P and A-sites in the presence of 5µM of tigecycline. Amino acid labels on the two axes are colored as follows: red – positively charged, blue – negatively charged, purple – polar, yellow – specific amino acids like Cys, Gly

and Pro, and green – hydrophobic. Formyl methionine or fMet is denoted as m, while a stop codon is represented as an asterisk (*) symbol shaded in grey.

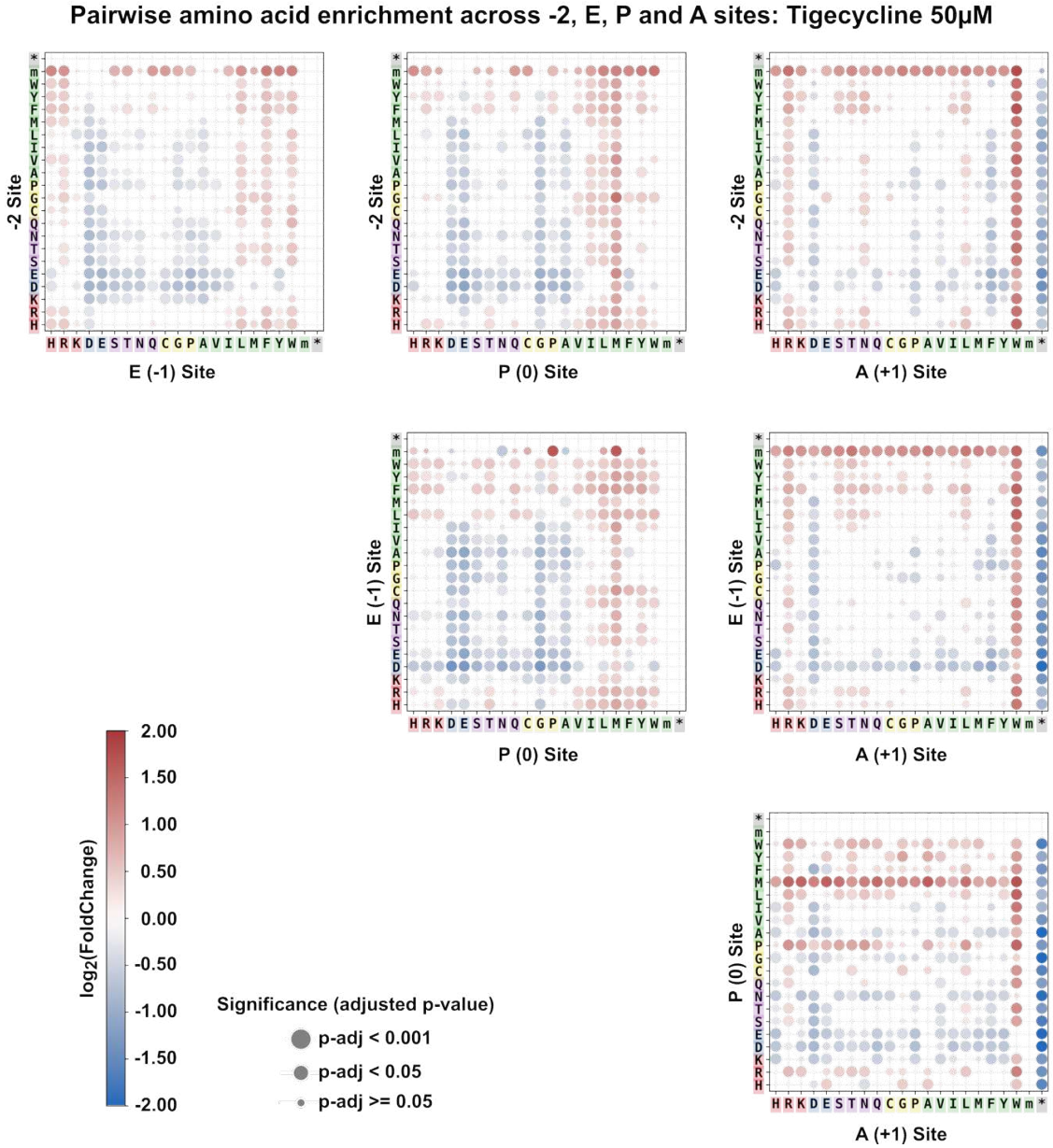

Figure 49: Heatmap grid representing the di-amino acid motifs enriched across -2, E, P and A-sites in the presence of 50µM of tigecycline. Amino acid labels on the two axes are colored as follows: red – positively charged, blue – negatively charged, purple – polar, yellow – specific amino acids like Cys, Gly and Pro, and green – hydrophobic. Formyl methionine or fMet is denoted as m, while a stop codon is represented as an asterisk (*) symbol shaded in grey.

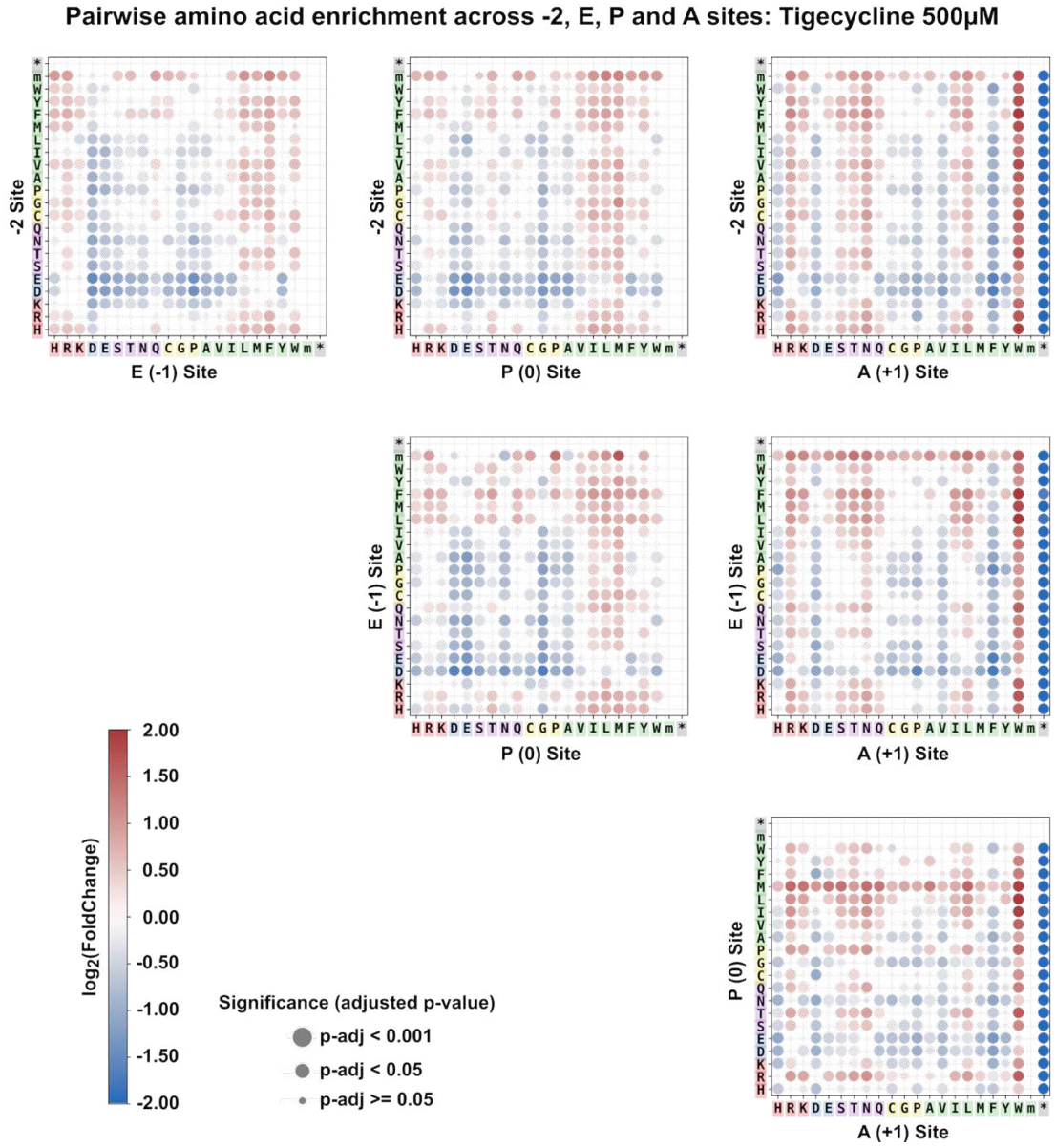

Figure 50: Heatmap grid representing the di-amino acid motifs enriched across -2, E, P and A-sites in the presence of 500µM of tigecycline. Amino acid labels on the two axes are colored as follows: red – positively charged, blue – negatively charged, purple – polar, yellow – specific amino acids like Cys, Gly and Pro, and green – hydrophobic. Formyl methionine or fMet is denoted as m, while a stop codon is represented as an asterisk (*) symbol shaded in grey.

Next, I also analyzed the enrichment of motifs combining three contiguous amino acids across the E, P and A-sites to assess multi-site changes in the translational landscape induced by tigecycline, and also to check if the core di-amino acid motifs are conserved within this sequence context. The analyses presented here focus on the 5µM, 50µM and 500µM tigecycline conditions, since stalling events were primarily identified in these three sample sets. To identify significant trends in sequences, motifs were filtered based on i) a $\log_2$(Fold-Change) ≥ 1, corresponding to at least a 2-fold enrichment compared to the control condition, ii) a statistical significance cutoff of adjusted p-value ≤ 0.05, corresponding to -$\log_{10}$(adjusted-p-value) ≥ 1.3. Motifs containing stop codons in the A-site were also filtered out to focus analyses on drug-induced elongation arrest and avoid signal due to translation termination. The filtered motifs were subsequently used to construct Sankey flow diagrams to map combinatorial sequence preferences and multi-site residue dependencies across the -2, E, P and A-sites. (Fig. 51). Consistent with the trends from the pairwise enrichment analysis, motifs with codons for hydrophobic residues across all three sites were observed, notably with Met in the P-site and Trp in the A-site.

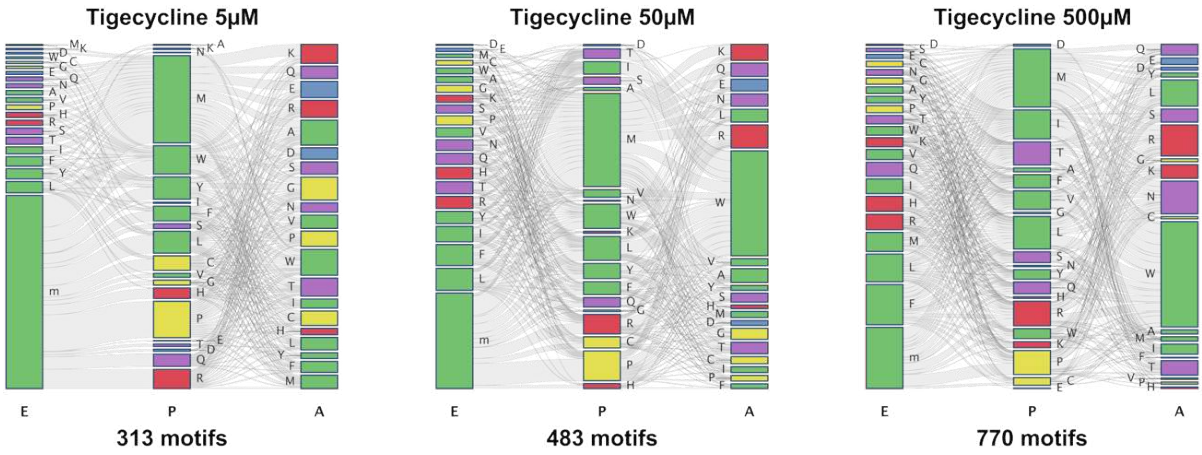

Figure 51: Combinatorial sequence preferences across ribosomal sites during tigecycline-induced translation arrest. Sankey flow diagrams illustrating multi-site amino acid dependencies across the E, P, and A-sites in the presence of 5µM, 50µM, and 500µM tigecycline. Vertical blocks (nodes) represent individual amino acid residues at each site, with node height proportional to the relative abundance of motifs containing that residue. Amino acid nodes are colored as follows: red – positively charged, blue – negatively charged, purple – polar, yellow – specific amino acids like Cys, Gly and Pro, and green – hydrophobic. Formyl methionine or fMet is denoted as m. Grey connector ribbons (links) depict transitions between adjacent sites, with ribbon width proportional to the co-occurrence of specific residue pairs. Data were filtered for $\log_2$(FoldChange) ≥ 1 using a statistical cutoff of -$\log_{10}$(adjusted p-value) ≥ 1.3, excluding stop codons in the A-site.

Finally, I also analyzed individual codon enrichment at the -2, E, P and A-sites to check for differential stalling patterns at the nucleotide level in the 5µM, 50µM and 500µM tigecycline conditions (Fig. 52). A preference was observed for Val-GTG, Pro-CCG and Arg-CGX codons over their corresponding synonymous codons in the P-site during tigecycline-induced stalling of ribosomes. Similarly, preference was observed for Gln-CAA, Ser-TCX, Leu-CTX and Pro-CC(T/A) codons over their corresponding synonymous codons in the A-site during ribosomal stalling in the presence of tigecycline. These observations suggest that the sequence-dependent action of tigecycline is modulated at the nucleotide level, and by extension, by the availability of cognate tRNAs in the vicinity. However, since the PURExpress system used for iTP-Seq uses purified total *E. coli* tRNA and the template (NNN)15 library does not take endogenous codon usage frequency into account, this could affect the interpretation of codon-level enrichment results. Possibly, codons decoded by less abundant tRNAs offer a wider temporal window for competition between the incoming aminoacyl-tRNA and tigecycline for binding the A-site, although kinetic studies are essential to confirm this.

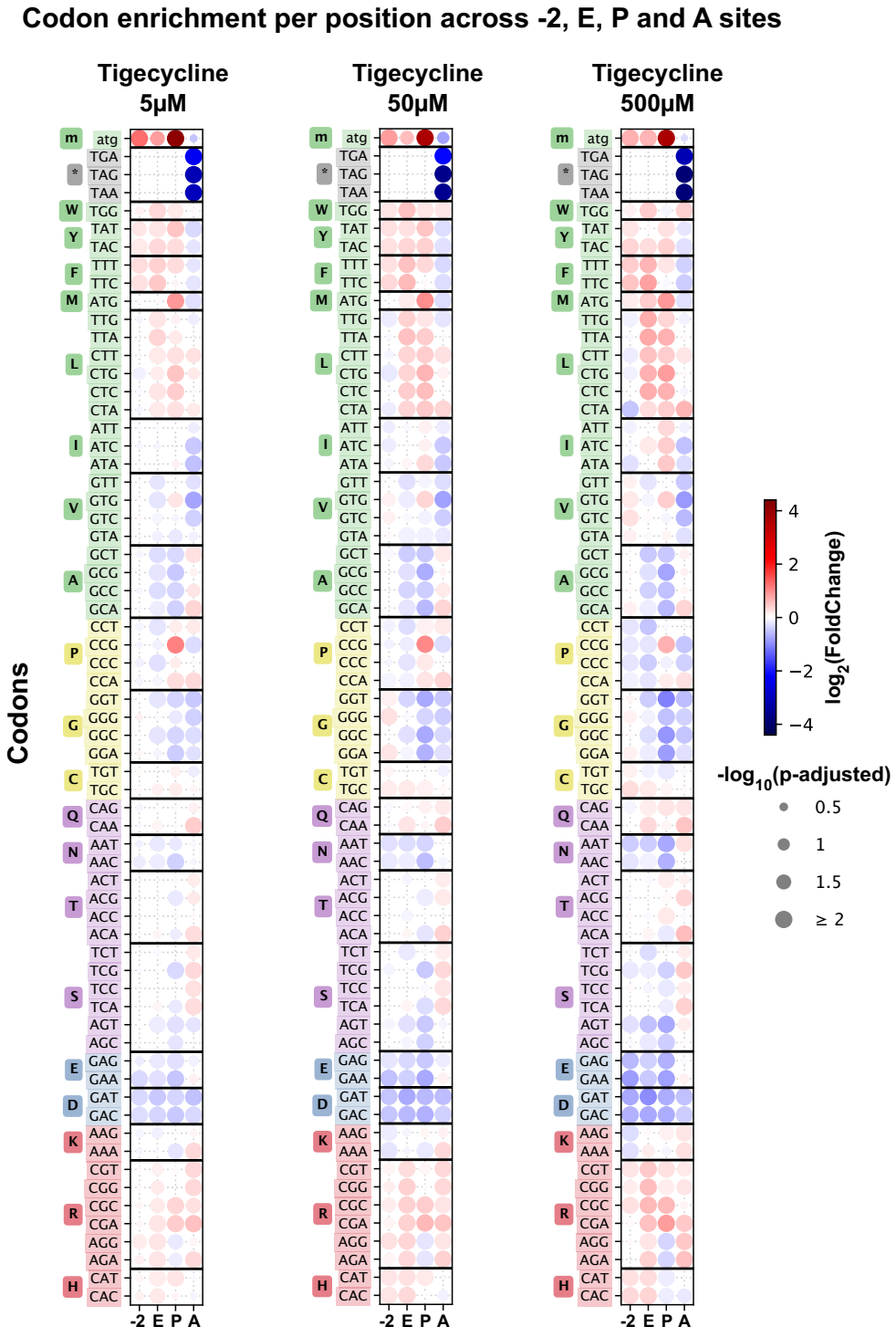

Figure 52: Heatmaps representing per-position codon enrichment (*Escherichia coli* codons) across -2, E, P and A-sites in the presence of 5μM, 50μM, and 500μM tigecycline. Amino acid labels on the Y-axis are colored as follows: red – positively charged, blue – negatively charged, purple – polar, yellow – specific amino acids like Cys, Gly and Pro, and green – hydrophobic. Formyl methionine or fMet is denoted as m, while a stop codon is represented as an asterisk (*) symbol shaded in grey.

- **Tigecycline-induced stalling of ribosomes during initiation**

To check for tigecycline-induced context-dependent stalling of ribosomes during translation initiation, I analyzed codon enrichment in the A-site of the stalled ribosomes, both at the amino acid and nucleotide levels, for sequences with an fMet (m) residue or an atg codon in the P-site (Fig. 53). At 0.05µM tigecycline concentration, no significant enrichment was observed, consistent with the fact that sub-IC_{50} concentrations of tigecycline do not induce measurable ribosomal stalling. At 0.5µM tigecycline concentration and above, significant enrichment was observed for all 20 amino acids. When compared at the nucleotide level using Sankey flow diagrams, no single nucleotide preference was observed across any of the three positions (3, 4, 5 in Fig. 53 Panel B) constituting the A-site.

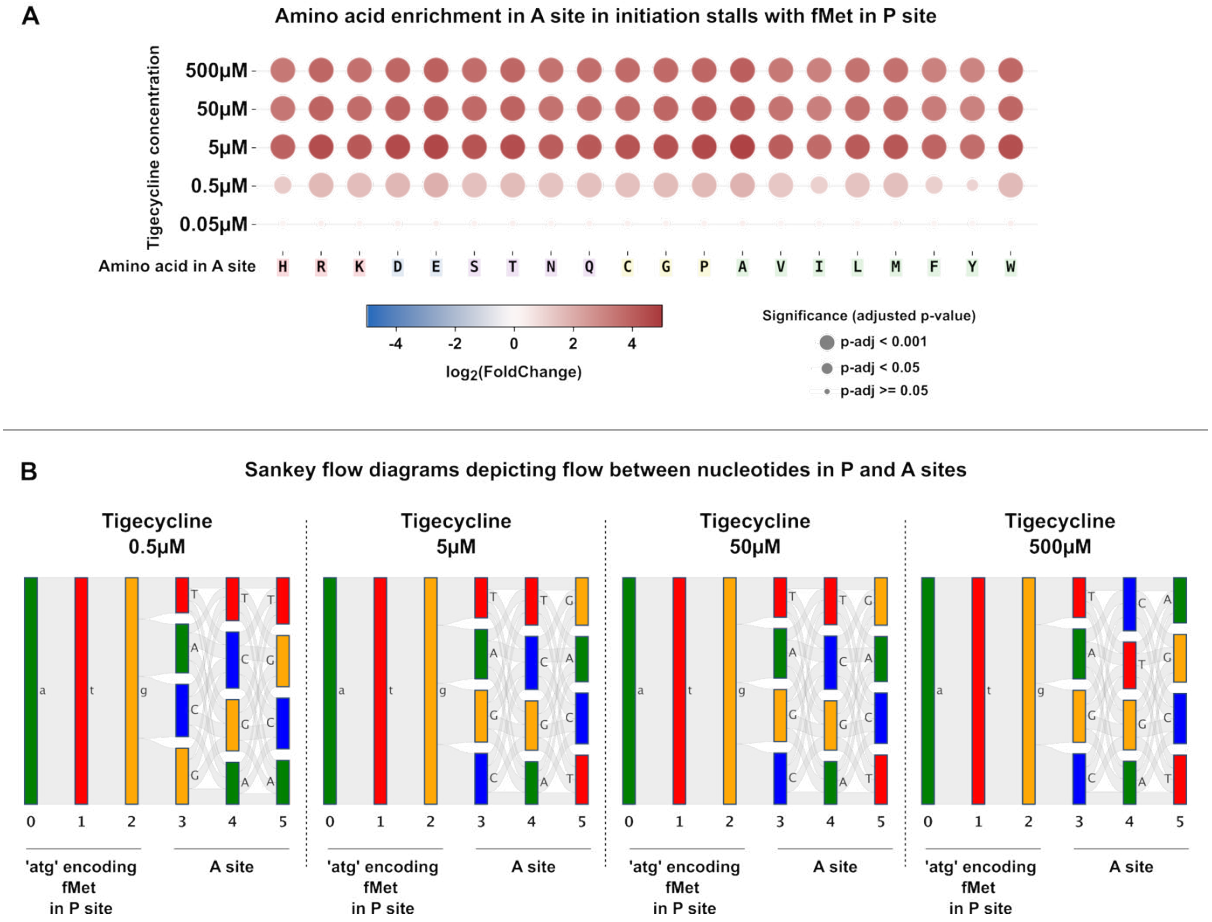

Figure 53: A. Heatmap representing amino acid enrichment in the A-site in ribosomes stalled during initiation with fMet in the P-site. B. Combinatorial nucleotide sequence preferences in the P- and A-sites during tigecycline-induced translation arrest at initiation. Sankey flow diagrams illustrating nucleotide dependencies across the P- and A-sites in the presence of tigecycline at different concentrations. The P-site nucleotides are numbered 0, 1, and 2, fixed for a, t and g to represent the initiation codon. The A-site nucleotides are numbered 3, 4 and 5. Vertical blocks (nodes) represent

individual nucleotides at each of the 6 positions, with node height proportional to the relative abundance of motifs containing that base. Nucleotide nodes are colored as follows: green – A, red – T, yellow orange – G, and blue – C. Grey connector ribbons (links) depict transitions between adjacent sites, with ribbon width proportional to the co-occurrence of specific nucleotide pairs. Data were filtered for $\log_2$(FoldChange) ≥ 1 using a statistical cutoff of -$\log_{10}$(adjusted p-value) ≥ 1.3

Together, these iTP-Seq results demonstrate that while tigecycline leads to sequence- and concentration-dependent ribosomal stalling during translation elongation *in vitro*, initiation stalling cannot be concluded to occur in a context-dependent manner from this work.

4.3. Conclusion and Perspectives

Tigecycline has been reported in existing literature to inhibit both initiation and elongation of translation by distinct mechanisms. While structural works on tigecycline bound to both the 30S and 70S have shown that it can inhibit elongation by preventing the entry of aminoacyl tRNAs in the A-site (Jenner et al. 2013; Schedlbauer et al. 2015), kinetic studies have explained that it inhibits initiation by delaying the formation of the 70S complex by allosteric compaction of IF3 and retention of IF1 to the 30S subunit by direct contacts (Barrenechea et al. 2021).

The observations in my work indicate a broadly context-dependent ribosomal stalling during tigecycline-induced elongation inhibition. It is interesting to note here that recent structural work has shown that tigecycline binds to the mitochondrial 55S ribosome in eukaryotes, revealing three binding sites. One of them is in the mtSSU A-site, which is conserved in the bacterial 30S, and two additional binding sites are in the large subunit (mtLSU) – on helix 71, and another at the peptidyl transferase center (PTC) (Li et al. 2024; Shao et al. 2025). The tigecycline binding site at the mtLSU PTC overlaps with the binding sites in the bacterial 70S for sarecycline, another third-generation derivative of tetracycline (Lomakin et al. 2023), and also for tetracenomycin X (TcmX) (Osterman et al. 2020), another aromatic polyketide antibiotic that has been further characterized to cause sequence-dependent ribosomal stalling in bacteria, preferentially at QK motifs (Leroy et al. 2023). So far, a secondary binding site for tigecycline in the bacterial ribosome, near the PTC, has not been reported in the literature. Given that the human mitoribosome is biochemically and structurally similar to the bacterial ribosome, whether tigecycline can bind to the bacterial 70S PTC at a similar site as

observed in the mitochondrial 55S PTC remains an open question, which could lead to a structural investigation for sequence- and concentration-dependent elongation stalling, complementary to the findings in this work. Hence, future structural studies with defined mRNA templates, specific stalling motifs, and isolated charged cognate tRNAs will be necessary to determine why certain codon combinations induce elongation arrest while others are bypassed.

To further elucidate the mechanism underlying selective initiation stalls on specific sequences, the influence of mRNA transcript architecture can be explored in future studies, for example, by integrating iTP-Seq data with mRNA secondary structure predictions around the start codon. Additionally, future iTP-Seq experiments could be adapted for 30S pre-initiation complexes using a focused mRNA library with varied 5' UTRs (untranslated regions) and RBS (ribosome binding sites) to investigate the role of upstream transcript architecture on initiation stalling in the presence of tigecycline.

In summary, this work revealed the concentration-dependent tigecycline-induced stalling landscape for 70S ribosomes, distinguishing sequence-independent initiation stalling and sequence-dependent elongation stalling in the PURE system and providing a foundation for future mechanistic studies into tigecycline-mediated translation inhibition.

Chapter 5

General Conclusion and Perspectives

Antibiotic resistance is currently one of the most pressing global public health threats. Addressing this crisis necessitates not only the discovery of novel drugs but also re-evaluating established antibiotic classes to better understand their mechanisms of action and develop new solutions based on that knowledge. Translation-inhibiting antibiotics targeting the bacterial ribosome are among the most widely used clinical drugs (reviewed in Lin et al. 2018), and hence they comprise an important group of antibiotics to study. Indeed, in recent literature, several ribosome-targeting antibiotics have been discovered to act in a context-dependent manner, i.e., they do not inhibit the synthesis of all bacterial proteins with similar efficiency – instead, they preferentially affect the translation of only certain sequence motifs. This selective inhibition not only reshapes the functional proteome but also plays a central role in modulating regulatory arrest peptides that control antibiotic resistance gene expression (reviewed in Ramu et al. 2009; Vázquez-Laslop and Mankin 2014, 2018; Bhattacharya et al. 2024). As such, comprehensive mapping of the sequence-dependent mode of action of ribosome-targeting antibiotics provides a foundation for rational drug design. Since different bacterial species possess distinct proteomes, often with unique essential sequence motifs, exploiting these context-dependent translational arrest patterns could enable the development of species-specific antibiotics designed to selectively disrupt protein synthesis in pathogenic antibiotic-resistant strains.

Antibiotics that inhibit bacterial translation can bind to several regions of the bacterial 70S ribosome. Of them, the decoding center in the 30S subunit is a particularly important target since it is at the heart of translational fidelity and hampering it can lead to misreading of the genetic code – the resultant synthesis of proteins with misincorporated amino acids could affect cellular physiology and even lead to cell death. Investigating the context-dependent action of antibiotics that bind the decoding center is hence interesting because it reveals which sequences are preferentially misread, leading to erroneous translation, versus which sequences are correctly read, allowing translation to continue unaffected.

In this thesis, I have elucidated the sequence-dependent inhibition of translation elongation by two antibiotic classes binding the 30S subunit near the decoding center at unique sites – odilorhabdins (specifically, NOSO-502 and NOSO-96624), and tetracyclines (specifically, the third-generation derivative tigecycline). I used the high-throughput technique of iTP-Seq to

map the landscape of sequence motifs that preferentially arrest translation in *E. coli* 70S ribosomes across different antibiotic concentrations. These experiments revealed that both antibiotics portray distinctly broad sequence- and concentration-dependent behaviour. Additionally, odilorhabdins were found to cause ribosomal stalling preferentially at certain codons coding for an amino acid and not the other synonymous codons for the same amino acid, highlighting that certain preferential codon and near-cognate anticodon interactions are stabilized in the presence of the drug. Tigecycline, on the other hand, prevents an incoming aminoacyl tRNA from binding to the A-site, and hence its context-dependence and preference for specific codons as revealed in this work, although currently observational, lay the foundation for defined structural studies in the future for a more comprehensive understanding of the drug action.

The work on odilorhabdins in this thesis builds on a single previous study (Pantel et al. 2018) and advances the understanding of the mechanism of translation inhibition with deeper structural insights. For the odilorhabdin NOSO-502, using cryo-EM single-particle analysis, this work also reveals the conformational landscape of antibiotic-bound ribosomes stalled on an arrest motif during *in vitro* translation in the PURE system. By identifying 27 distinct conformations of the NOSO-502-bound *E. coli* ribosome spread across 6 functional and 3 off-pathway states of the translation cycle, this work shows the key steps of bacterial protein synthesis that are targeted by the antibiotic. NOSO-502 interacts non-specifically with the sugar-phosphate backbones of residues in the 16S rRNA and the A-site tRNA, allowing the stabilization of near-cognate tRNAs in the A-site. Therefore, by impairing proofreading and consequently leading to delay and inhibition of translocation, NOSO-502 stabilizes several high-energy elongation intermediates that have been identified in this structural ensemble. However, future studies combining systematic kinetic assays and mass spectrometric methods are required to detail the misincorporation trends at the tRNA and protein levels.

Previous structural studies on tigecycline (Jenner et al. 2013; Schedlbauer et al. 2015) have shown that tigecycline also interacts non-specifically with the sugar-phosphate backbone of 16S rRNA residues, consistent with the mechanism of action of odilorhabdins. Further, odilorhabdins only interact with the sugar-phosphate backbone of the A-site tRNA, and not with any specific base. This shared non-specificity raises a question regarding how, despite a

lack of specific interaction with certain nucleotide bases, both drugs cause sequence-dependent translational arrest. Since neither odilorhabdin nor tigecycline interacts with the mRNA or the nascent peptide, it is most likely that in both cases, the incoming tRNA makes an essential contribution to the context-dependent inhibition of translation. Decoding is governed by a complex interplay of tRNA biochemistry, including synonymous codon usage, isoaccepting tRNA species and their relative abundance in different bacteria, Wobble base pairing, tRNA modifications, and the kinetic modulation of proofreading steps. The preferential stalling of ribosomes on certain codons in the presence of these drugs is thus a reflection of certain anticodon-codon interactions to allow the continuation of translation, albeit with misincorporated amino acid residues, while others lead to ribosomal stalling and translation inhibition. Since iTP-Seq only provides information on the mRNA sequences where the drug-bound ribosomes are stalled, this work in its current form cannot explain the contribution of preferential tRNA stabilization and incorporation. Comprehensive kinetic, biochemical and structural analyses focusing on specific codon-anticodon pairs will be essential in future studies to dissect this mechanism of action. Further, since this work focuses on the *E. coli* translation machinery and codon usage, it would be interesting to extend the analyses to other pathogenic bacteria to understand how species-specific tRNA pools can modulate stalling patterns and sequence dependence across organisms. Ultimately, scaling up these studies from *in vitro* to *in cellulo* levels could provide better insights into physiologically relevant translational arrest events.

Beyond the mechanistic basis, the breadth of context-dependence observed for odilorhabdins and tigecycline also carries implications for future rational drug design. Unlike several context-dependent antibiotics binding the 50S subunit (e.g., macrolides, TcmX among others), which induce ribosomal stalling at relatively narrower, more specific sequence contexts, the decoding center targeting drugs described here display a much broader context-dependent activity. When the translation of a narrow spectrum of motifs is affected, pathogens can sometimes evolve amino-acid substitutions in non-essential regions of the proteome to bypass arrest, mitigating the fitness cost. However, when a broader set of codons is affected, evading drug action can impose a higher fitness barrier, since it is unlikely that the pathogen will mutate all these residues without compromising its physiology. On the other hand, such

broad context-specificity may also have unwanted off-target effects on the pathogen host and/or beneficial host microbiota. Therefore, leveraging such broad context-dependence as a therapeutic strategy will require a balance between these considerations.

By mapping the sequence- and concentration-dependent inhibition of bacterial translation by odilorhabdins and tigecycline, this work reveals the extent of their context-dependence and advances the mechanistic understanding of context-dependent translation inhibition by these antibiotics, contributing to the broader effort to develop ribosome-targeted therapeutic strategies in the ongoing fight against multidrug-resistant pathogenic bacteria.

Supplementary Figures and Tables

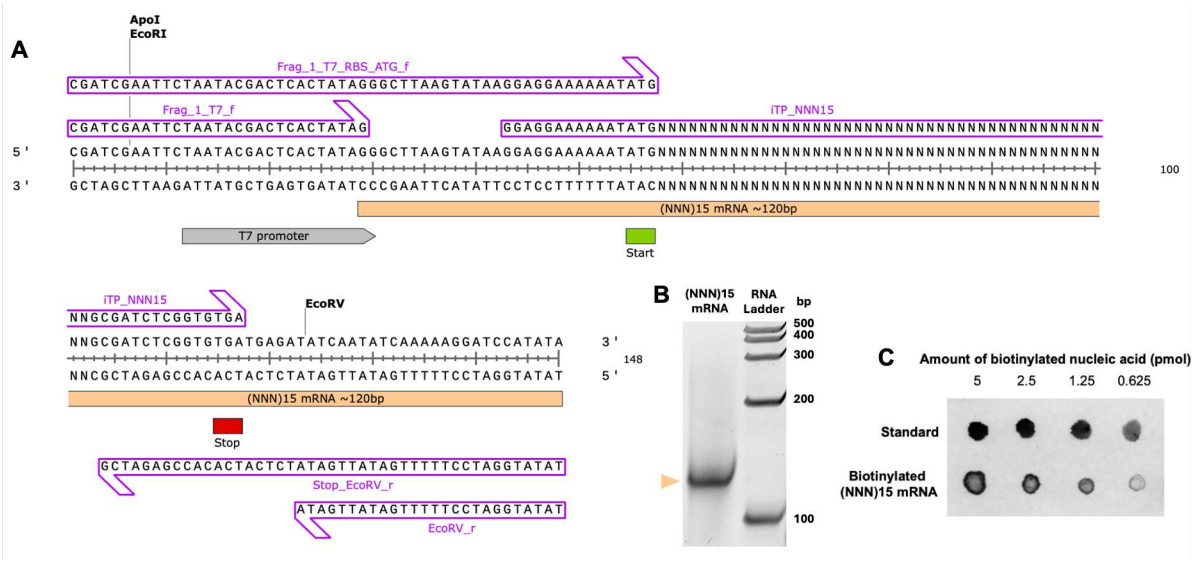

Supplementary Figure 54: A. Schematic of the DNA template library sequence used for iTP-Seq experiments, showing the oligonucleotides used for its assembly, the T7 promoter region, the start and stop codons, and the (NNN)15 mRNA transcript region. **B.** TBE-Urea-polyacrylamide gel (9%) of the (NNN)15 mRNA transcript. **C.** Dot blot for quality control of mRNA biotinylation.

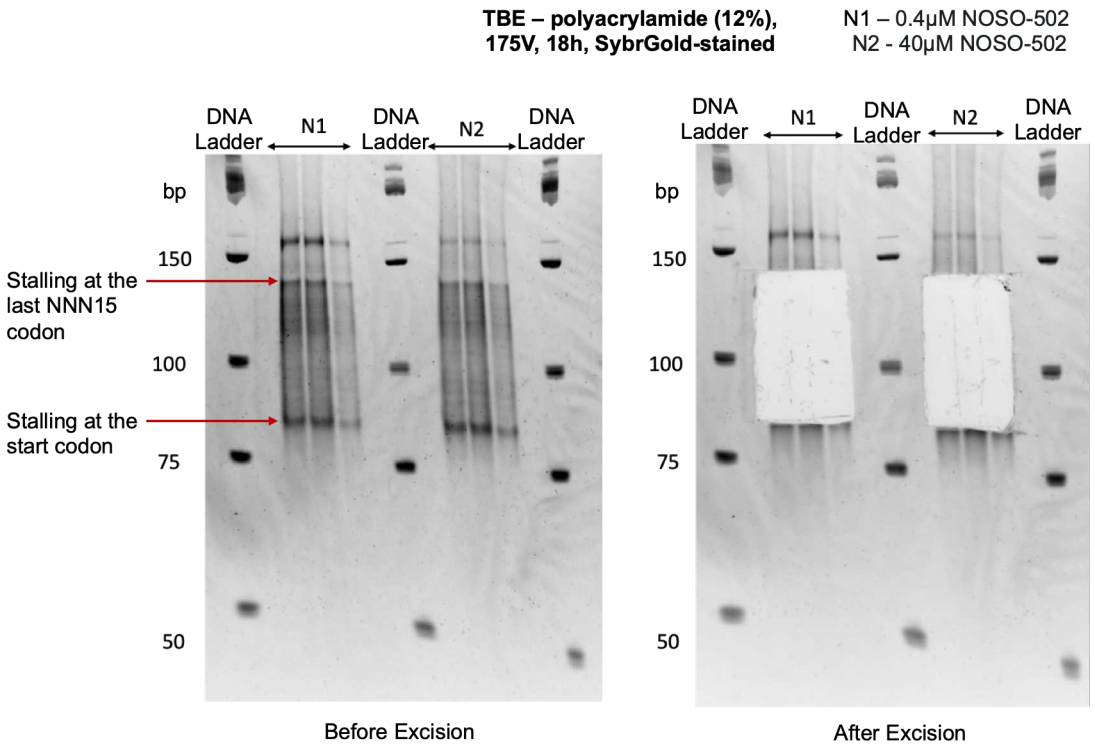

Supplementary Figure 55: Gel excision strategy for iTP-Seq library preparation for next-generation sequencing. Representative medium-sized TBE-polyacrylamide gels (12%) before (left) and after (right) excision of DNA amplified from inverse toeprints in NOSO-502-containing conditions (N1, N2). To optimise read depth for elongation stalls, the excision boundary was intentionally restricted to the upper part of the band corresponding to stalling at the initiation codon.

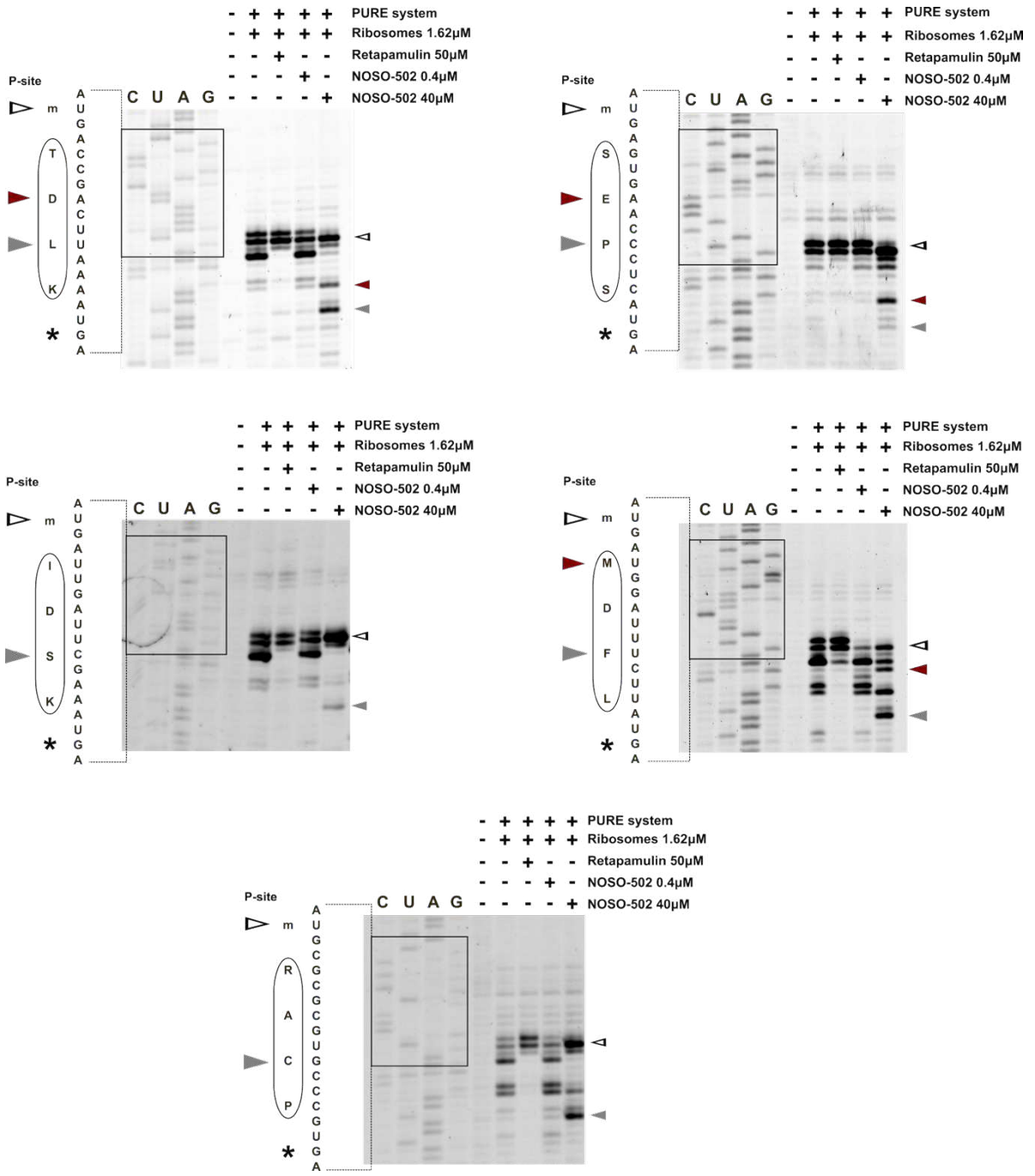

Supplementary Figure 56: Stalling patterns of odilorhabdin-bound ribosomal complexes on screened arrest motifs. Toeprinting gels are shown (n=1 replicate) for screened motifs. Lanes C, U, A, and G show Sanger sequencing reactions along with the mRNA sequence and the corresponding amino acid sequence. Open arrowheads mark initiation complexes on the start codon (AUG or m denoting fMet). Colored arrowheads identify motif-specific elongation stalls with the indicated amino acid positioned in the P-site. Asterisks (*) indicate the stop codon. Experimental conditions and antibiotic concentrations are labelled above each gel. These motifs led to multiple stalling events due to the secondary structure of the RNA or drug-induced stalling on multiple codons and hence were not deemed suitable or homogeneous for structural studies.

Supplementary Figure 57:

Cryo-EM maps of the 27 reconstructed sub-states colored by local resolution

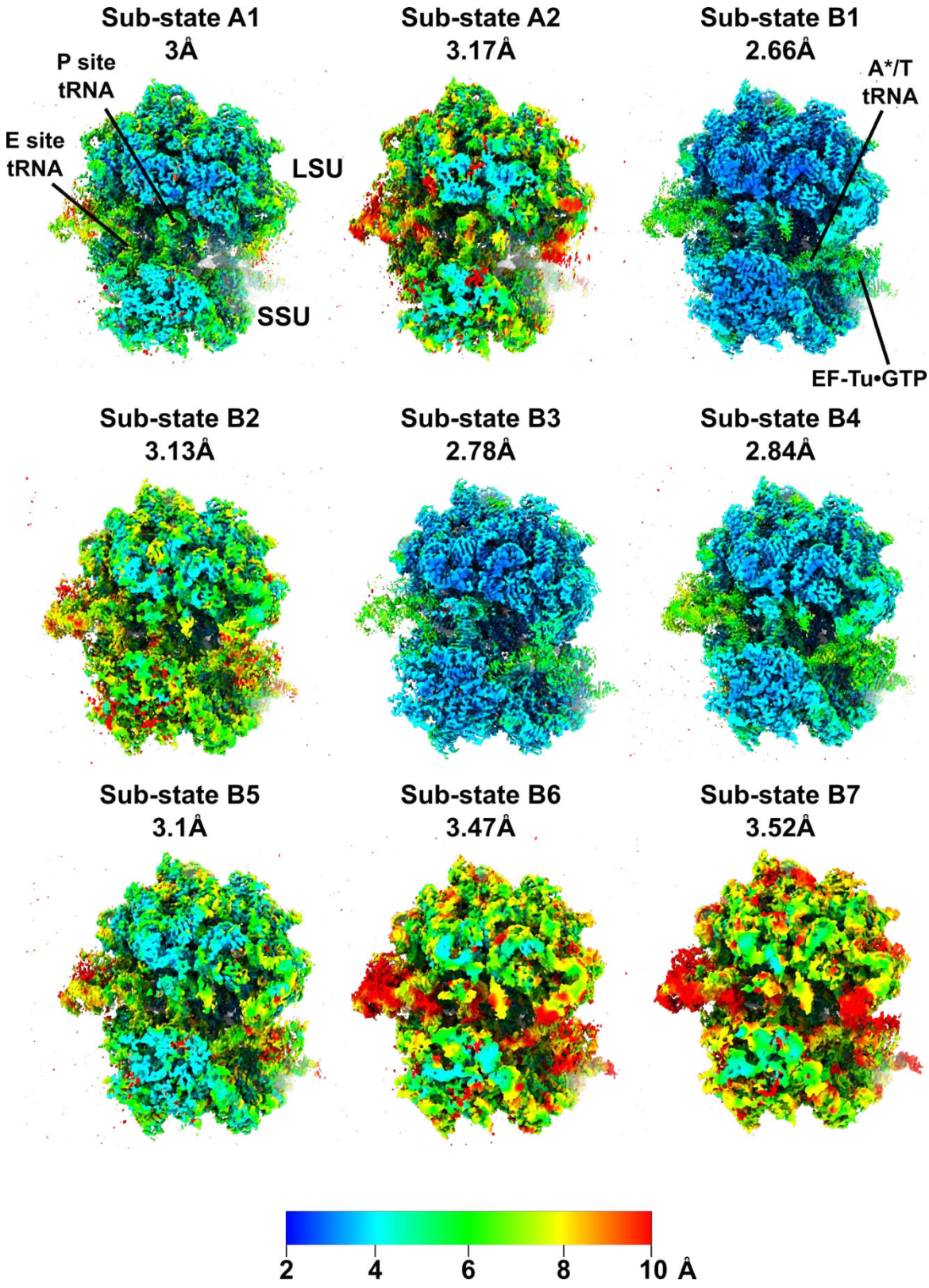

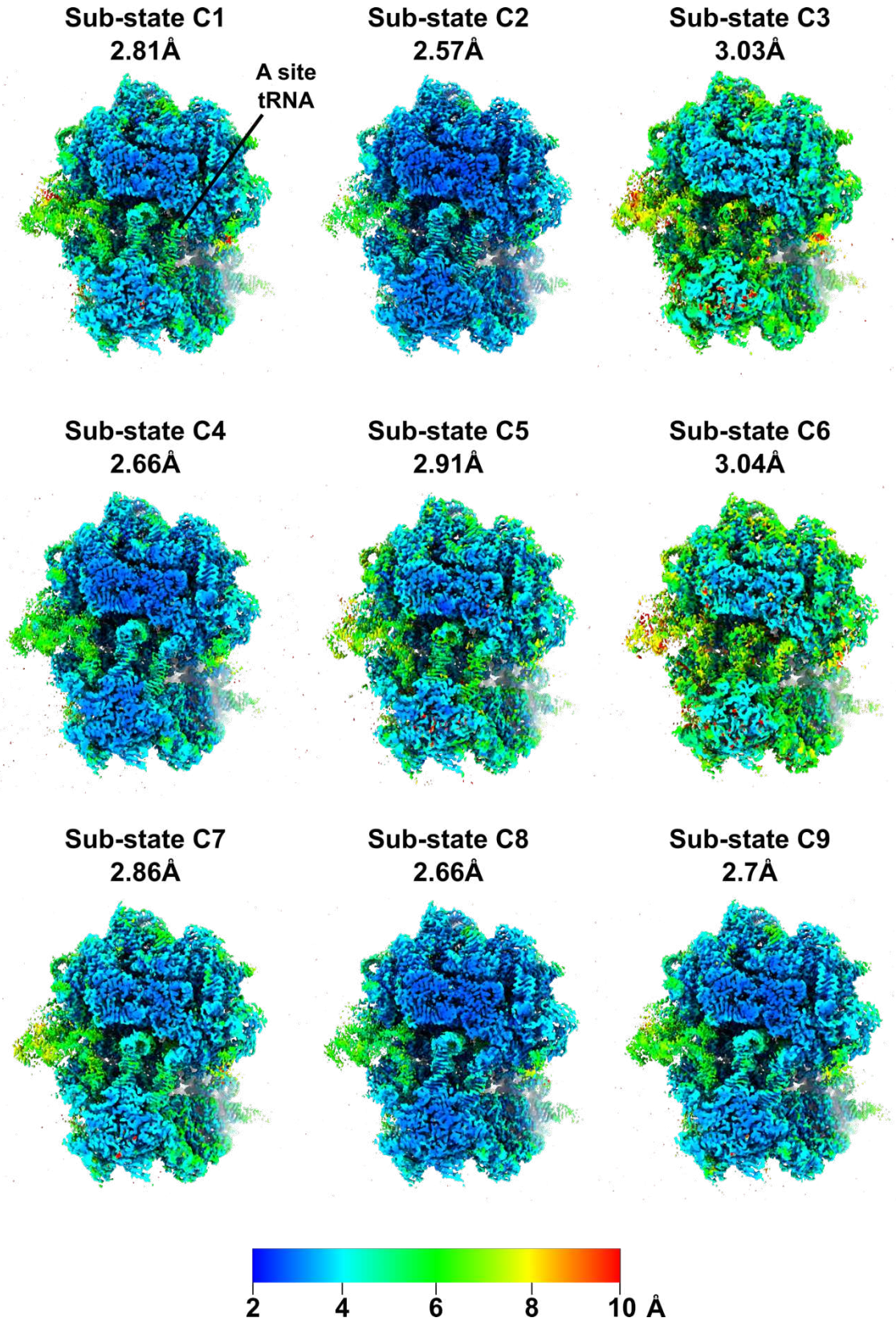
Sub-state C1
2.81Å
A site
tRNA
Sub-state C2
2.57Å
Sub-state C3
3.03Å
Sub-state C4
2.66Å
Sub-state C5
2.91Å
Sub-state C6
3.04Å
Sub-state C7
2.86Å
Sub-state C8
2.66Å
Sub-state C9
2.7Å
2
4
6
8
10 Å

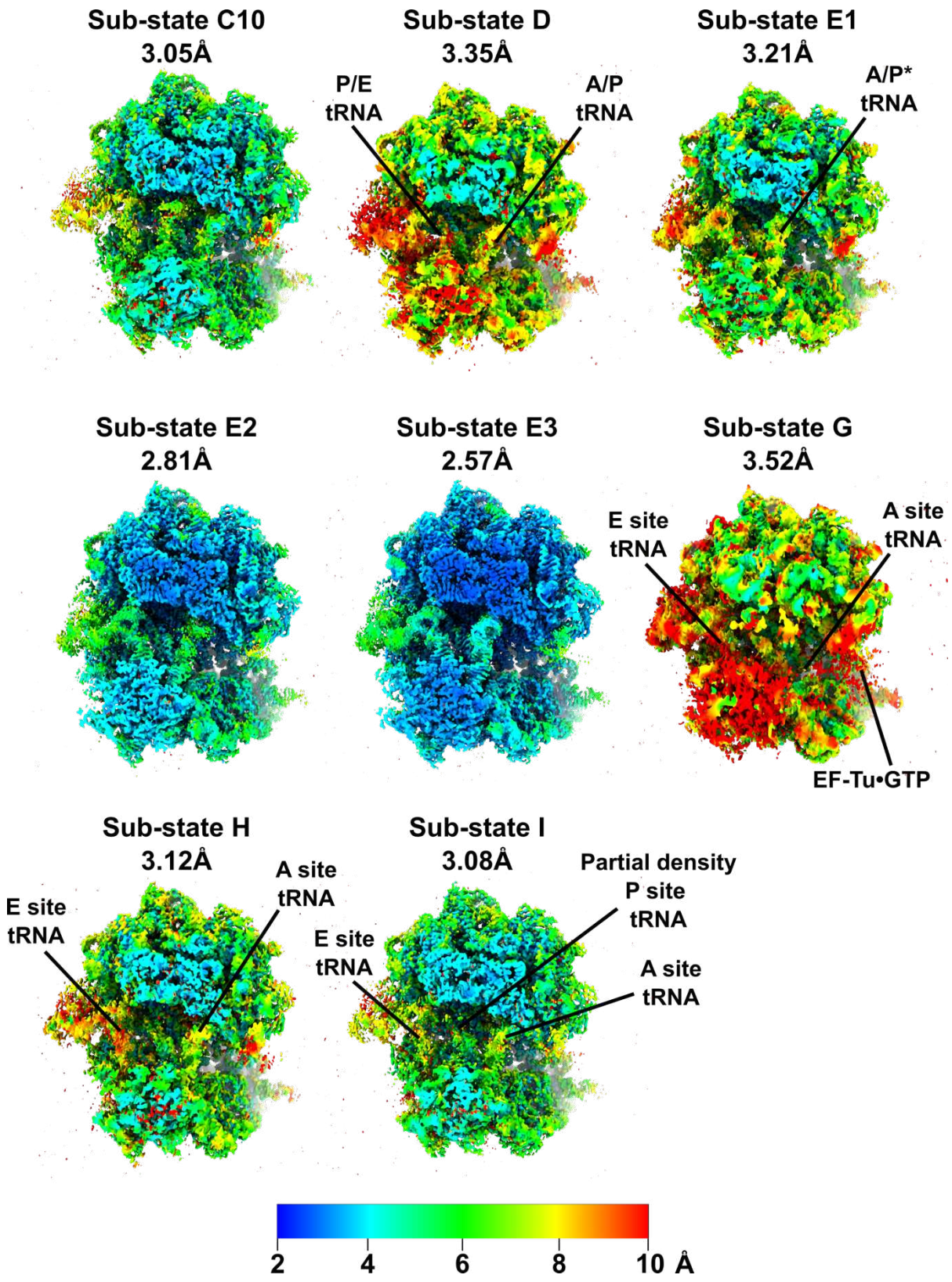
Sub-state C10
3.05Å
Sub-state D
3.35Å
P/E
tRNA
A/P
tRNA
Sub-state E1
3.21Å
A/P*
tRNA
Sub-state E2
2.81Å
Sub-state E3
2.57Å
Sub-state G
3.52Å
E site
tRNA
A site
tRNA
EF-Tu•GTP
Sub-state H
3.12Å
E site
tRNA
A site
tRNA
Sub-state I
3.08Å
Partial density
P site
tRNA
E site
tRNA
A site
tRNA
2
4
6
8
10 Å

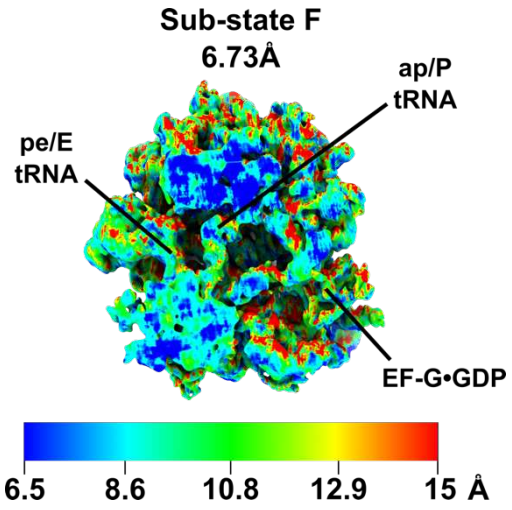
Sub-state F
6.73Å
ap/P
tRNA
pe/E
tRNA
EF-G•GDP
6.5
8.6
10.8
12.9
15 Å

Supplementary Figure 58:

Fourier Shell Correlation (FSC) curves of the 27 reconstructed sub-states

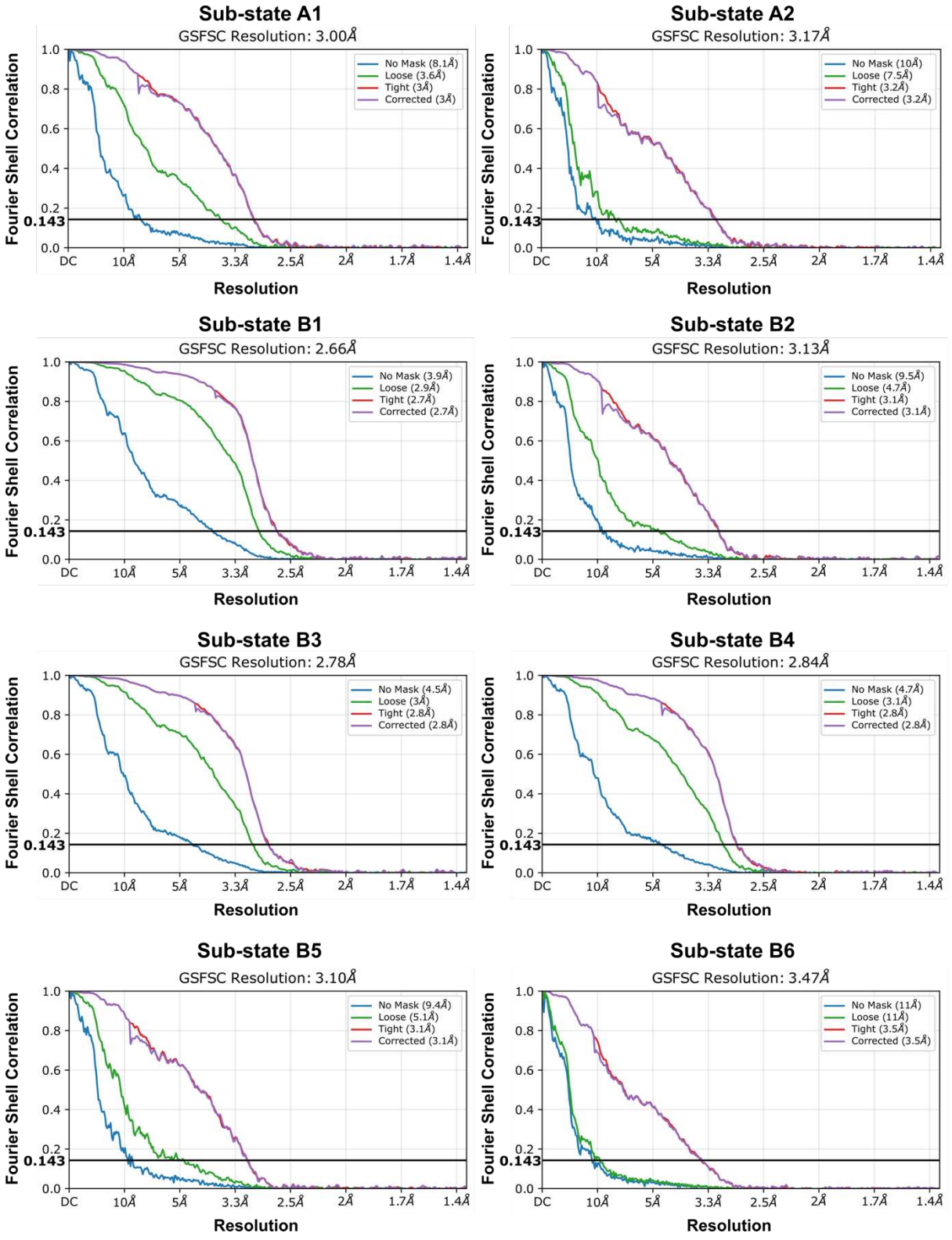

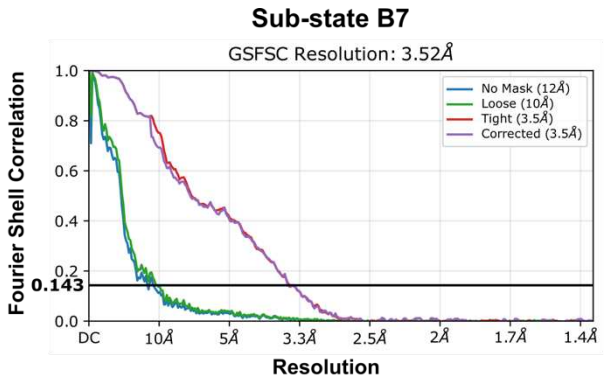
Sub-state B7
GSFSC Resolution: 3.52Å
No Mask (12Å)
Loose (10Å)
Tight (3.5Å)
Corrected (3.5Å)
Fourier Shell Correlation
0.143
DC
10Å
5Å
3.3Å
2.5Å
2Å
1.7Å
1.4Å
Resolution

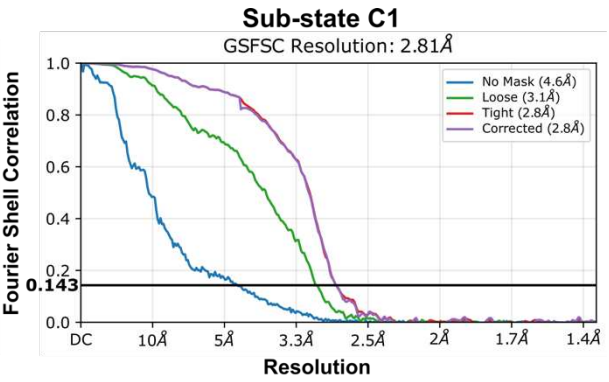
Sub-state C1
GSFSC Resolution: 2.81Å
No Mask (4.6Å)
Loose (3.1Å)
Tight (2.8Å)
Corrected (2.8Å)
Fourier Shell Correlation
0.143
DC
10Å
5Å
3.3Å
2.5Å
2Å
1.7Å
1.4Å
Resolution

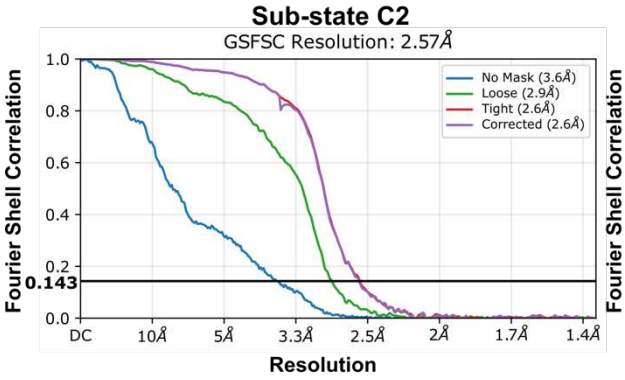
Sub-state C2
GSFSC Resolution: 2.57Å
No Mask (3.6Å)
Loose (2.9Å)
Tight (2.6Å)
Corrected (2.6Å)
Fourier Shell Correlation
0.143
DC
10Å
5Å
3.3Å
2.5Å
2Å
1.7Å
1.4Å
Resolution

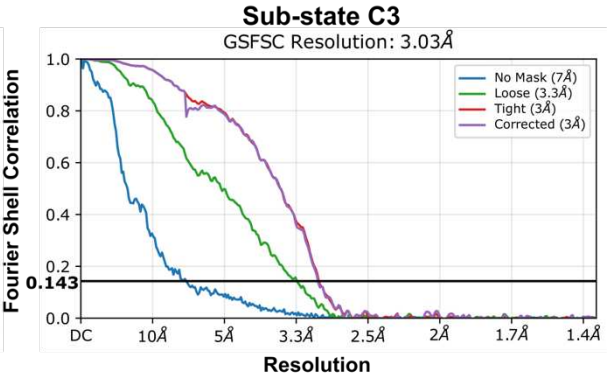
Sub-state C3
GSFSC Resolution: 3.03Å
No Mask (7Å)
Loose (3.3Å)
Tight (3Å)
Corrected (3Å)
Fourier Shell Correlation
0.143
DC
10Å
5Å
3.3Å
2.5Å
2Å
1.7Å
1.4Å
Resolution

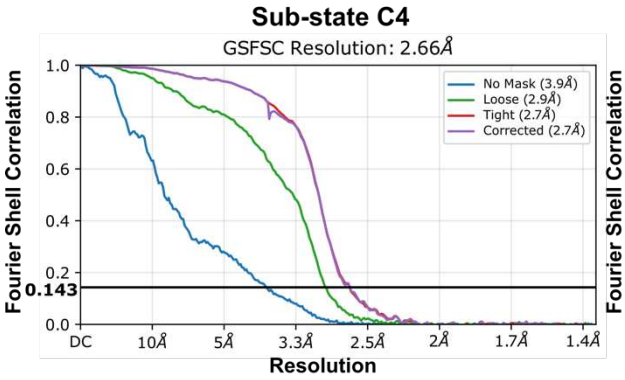
Sub-state C4
GSFSC Resolution: 2.66Å
No Mask (3.9Å)
Loose (2.9Å)
Tight (2.7Å)
Corrected (2.7Å)
Fourier Shell Correlation
0.143
DC
10Å
5Å
3.3Å
2.5Å
2Å
1.7Å
1.4Å
Resolution

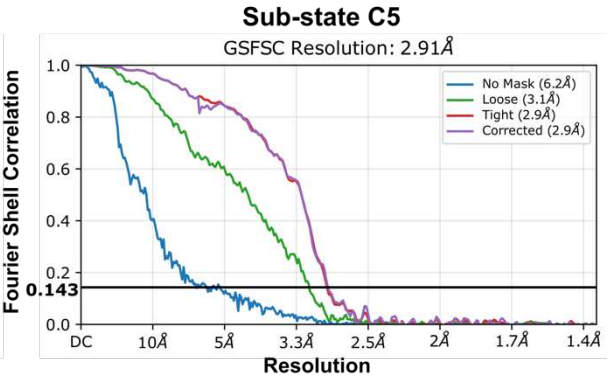
Sub-state C5
GSFSC Resolution: 2.91Å
No Mask (6.2Å)
Loose (3.1Å)
Tight (2.9Å)
Corrected (2.9Å)
Fourier Shell Correlation
0.143
DC
10Å
5Å
3.3Å
2.5Å
2Å
1.7Å
1.4Å
Resolution

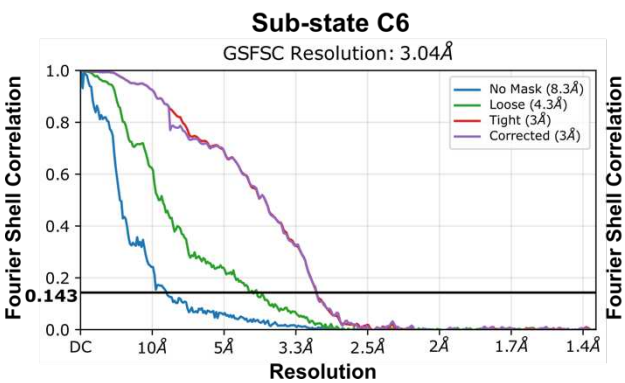
Sub-state C6
GSFSC Resolution: 3.04Å
No Mask (8.3Å)
Loose (4.3Å)
Tight (3Å)
Corrected (3Å)
Fourier Shell Correlation
0.143
DC
10Å
5Å
3.3Å
2.5Å
2Å
1.7Å
1.4Å
Resolution

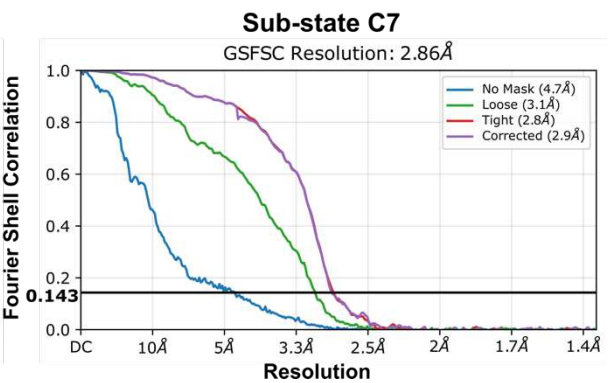
Sub-state C7
GSFSC Resolution: 2.86Å
No Mask (4.7Å)
Loose (3.1Å)
Tight (2.8Å)
Corrected (2.9Å)
Fourier Shell Correlation
0.143
DC
10Å
5Å
3.3Å
2.5Å
2Å
1.7Å
1.4Å
Resolution

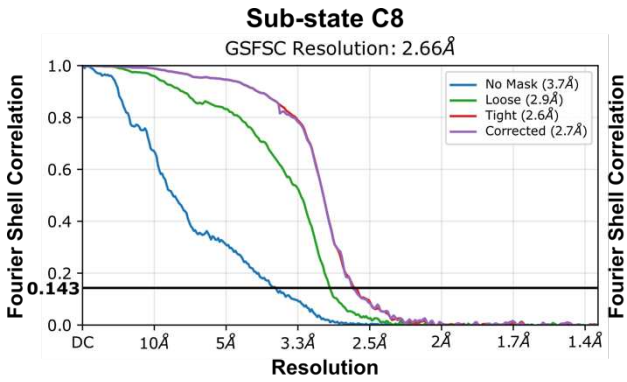
Sub-state C8
GSFSC Resolution: 2.66Å
No Mask (3.7Å)
Loose (2.9Å)
Tight (2.6Å)
Corrected (2.7Å)
Fourier Shell Correlation
0.143
DC 10Å 5Å 3.3Å 2.5Å 2Å 1.7Å 1.4Å
Resolution

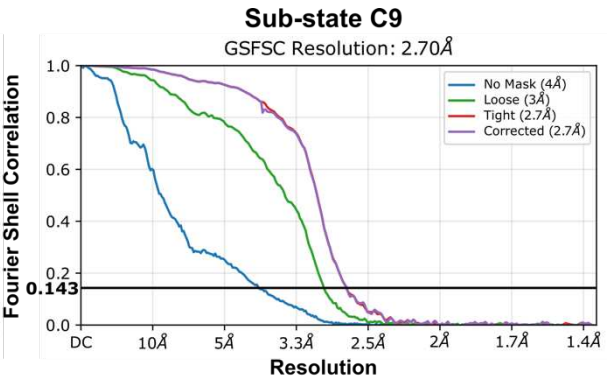
Sub-state C9
GSFSC Resolution: 2.70Å
No Mask (4Å)
Loose (3Å)
Tight (2.7Å)
Corrected (2.7Å)
Fourier Shell Correlation
0.143
DC 10Å 5Å 3.3Å 2.5Å 2Å 1.7Å 1.4Å
Resolution

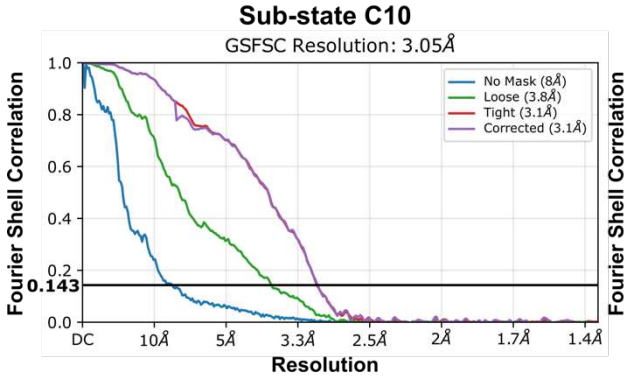
Sub-state C10
GSFSC Resolution: 3.05Å
No Mask (8Å)
Loose (3.8Å)
Tight (3.1Å)
Corrected (3.1Å)
Fourier Shell Correlation
0.143
DC 10Å 5Å 3.3Å 2.5Å 2Å 1.7Å 1.4Å
Resolution

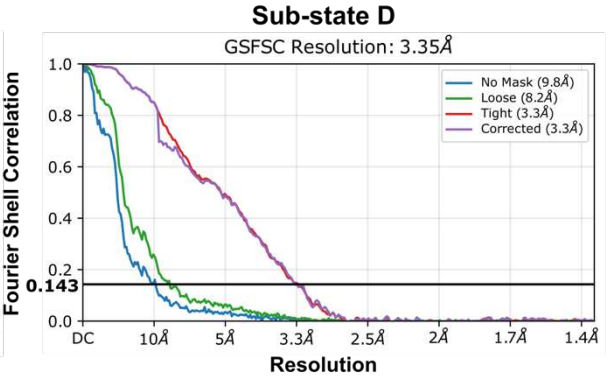
Sub-state D
GSFSC Resolution: 3.35Å
No Mask (9.8Å)
Loose (8.2Å)
Tight (3.3Å)
Corrected (3.3Å)
Fourier Shell Correlation
0.143
DC 10Å 5Å 3.3Å 2.5Å 2Å 1.7Å 1.4Å
Resolution

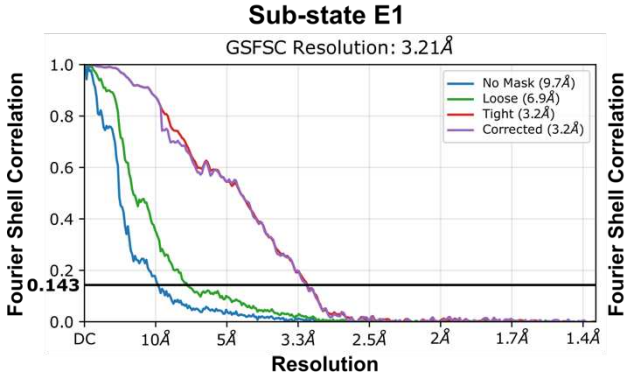
Sub-state E1
GSFSC Resolution: 3.21Å
No Mask (9.7Å)
Loose (6.9Å)
Tight (3.2Å)
Corrected (3.2Å)
Fourier Shell Correlation
0.143
DC 10Å 5Å 3.3Å 2.5Å 2Å 1.7Å 1.4Å
Resolution

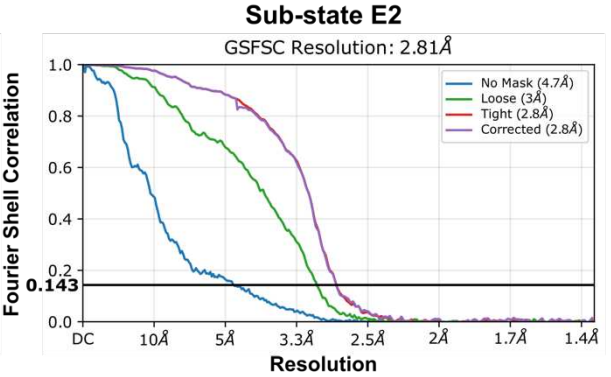
Sub-state E2
GSFSC Resolution: 2.81Å
No Mask (4.7Å)
Loose (3Å)
Tight (2.8Å)
Corrected (2.8Å)
Fourier Shell Correlation
0.143
DC 10Å 5Å 3.3Å 2.5Å 2Å 1.7Å 1.4Å
Resolution

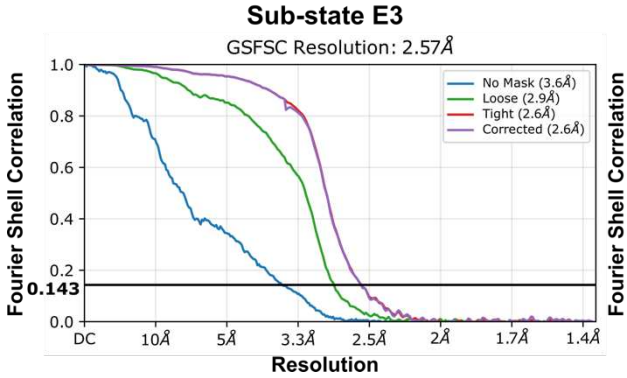
Sub-state E3
GSFSC Resolution: 2.57Å
No Mask (3.6Å)
Loose (2.9Å)
Tight (2.6Å)
Corrected (2.6Å)
Fourier Shell Correlation
0.143
DC 10Å 5Å 3.3Å 2.5Å 2Å 1.7Å 1.4Å
Resolution

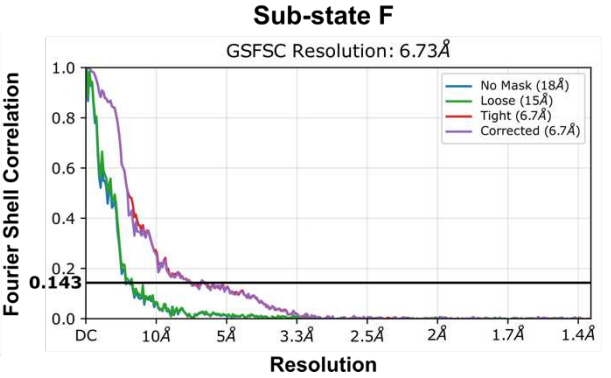
Sub-state F
GSFSC Resolution: 6.73Å
No Mask (18Å)
Loose (15Å)
Tight (6.7Å)
Corrected (6.7Å)
Fourier Shell Correlation
0.143
DC 10Å 5Å 3.3Å 2.5Å 2Å 1.7Å 1.4Å
Resolution

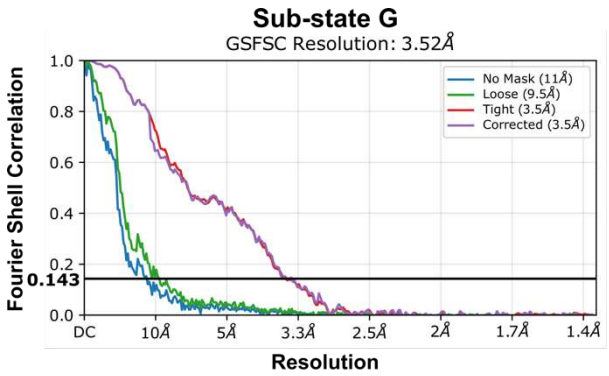
Sub-state G
GSFSC Resolution: 3.52Å
Fourier Shell Correlation
1.0
0.8
0.6
0.4
0.2
0.143
0.0
DC
10Å
5Å
3.3Å
2.5Å
2Å
1.7Å
1.4Å
Resolution
No Mask (11Å)
Loose (9.5Å)
Tight (3.5Å)
Corrected (3.5Å)

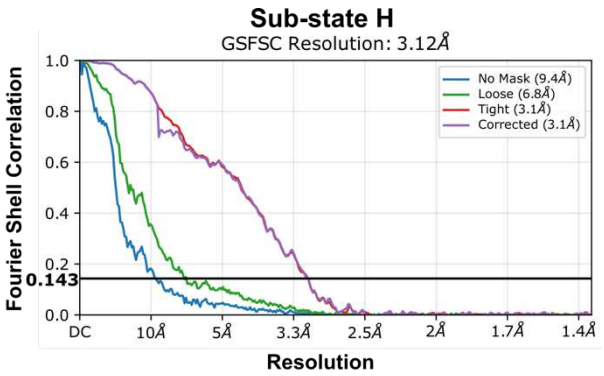
Sub-state H
GSFSC Resolution: 3.12Å
Fourier Shell Correlation
1.0
0.8
0.6
0.4
0.2
0.143
0.0
DC
10Å
5Å
3.3Å
2.5Å
2Å
1.7Å
1.4Å
Resolution
No Mask (9.4Å)
Loose (6.8Å)
Tight (3.1Å)
Corrected (3.1Å)

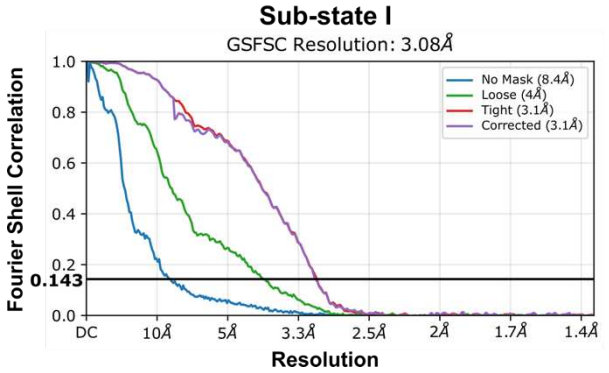
Sub-state I
GSFSC Resolution: 3.08Å
Fourier Shell Correlation
1.0
0.8
0.6
0.4
0.2
0.143
0.0
DC
10Å
5Å
3.3Å
2.5Å
2Å
1.7Å
1.4Å
Resolution
No Mask (8.4Å)
Loose (4Å)
Tight (3.1Å)
Corrected (3.1Å)

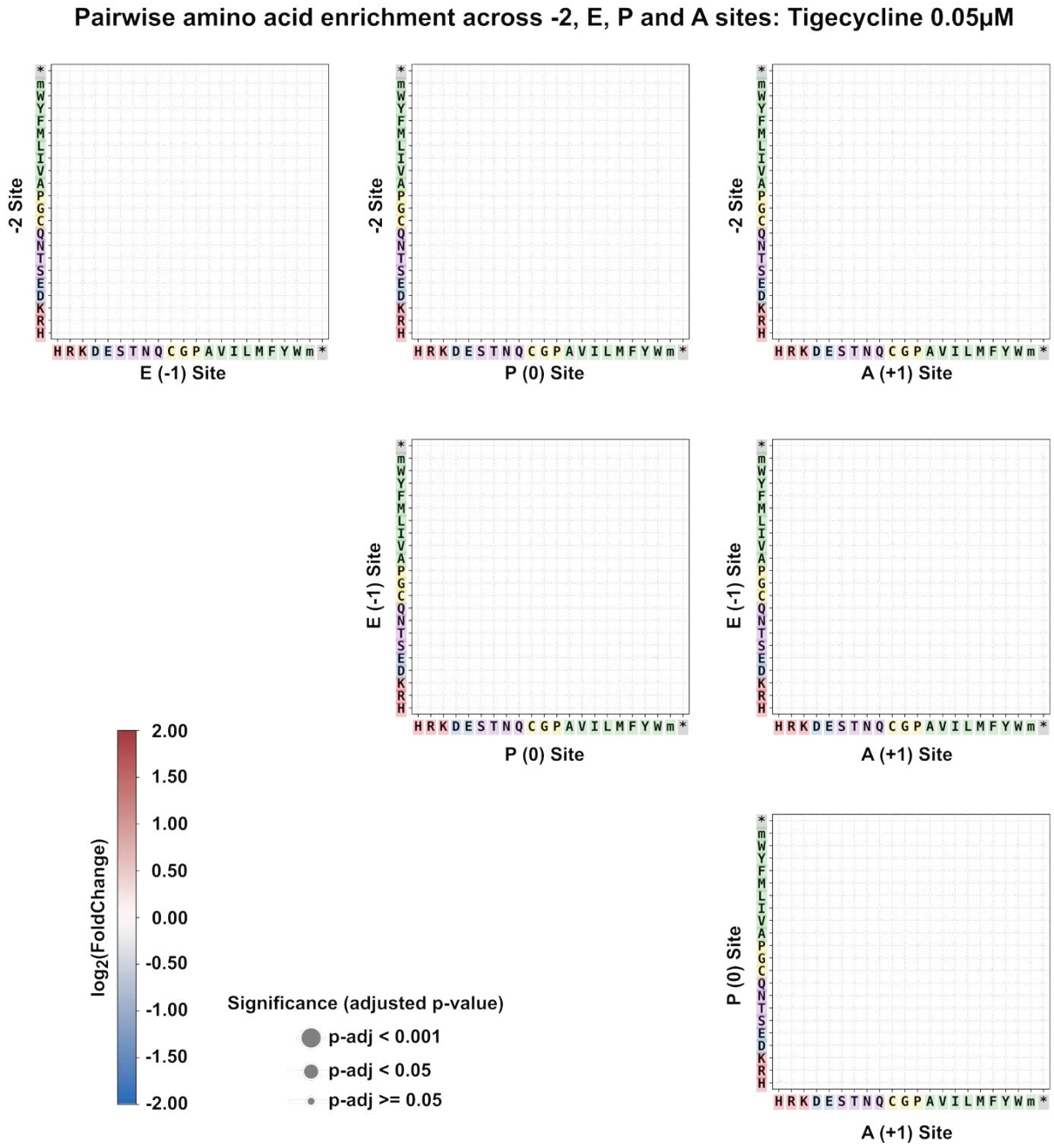

Supplementary Figure 59: Heatmap grid representing the di-amino acid motifs enriched across -2, E, P and A-sites in the presence of 0.05µM of tigecycline. Amino acid labels on the two axes are colored as follows: red – positively charged, blue – negatively charged, purple – polar, yellow – specific amino acids like Cys, Gly and Pro, and green – hydrophobic. Formyl methionine or fMet is denoted as m, while a stop codon is represented as an asterisk (*) symbol shaded in grey.

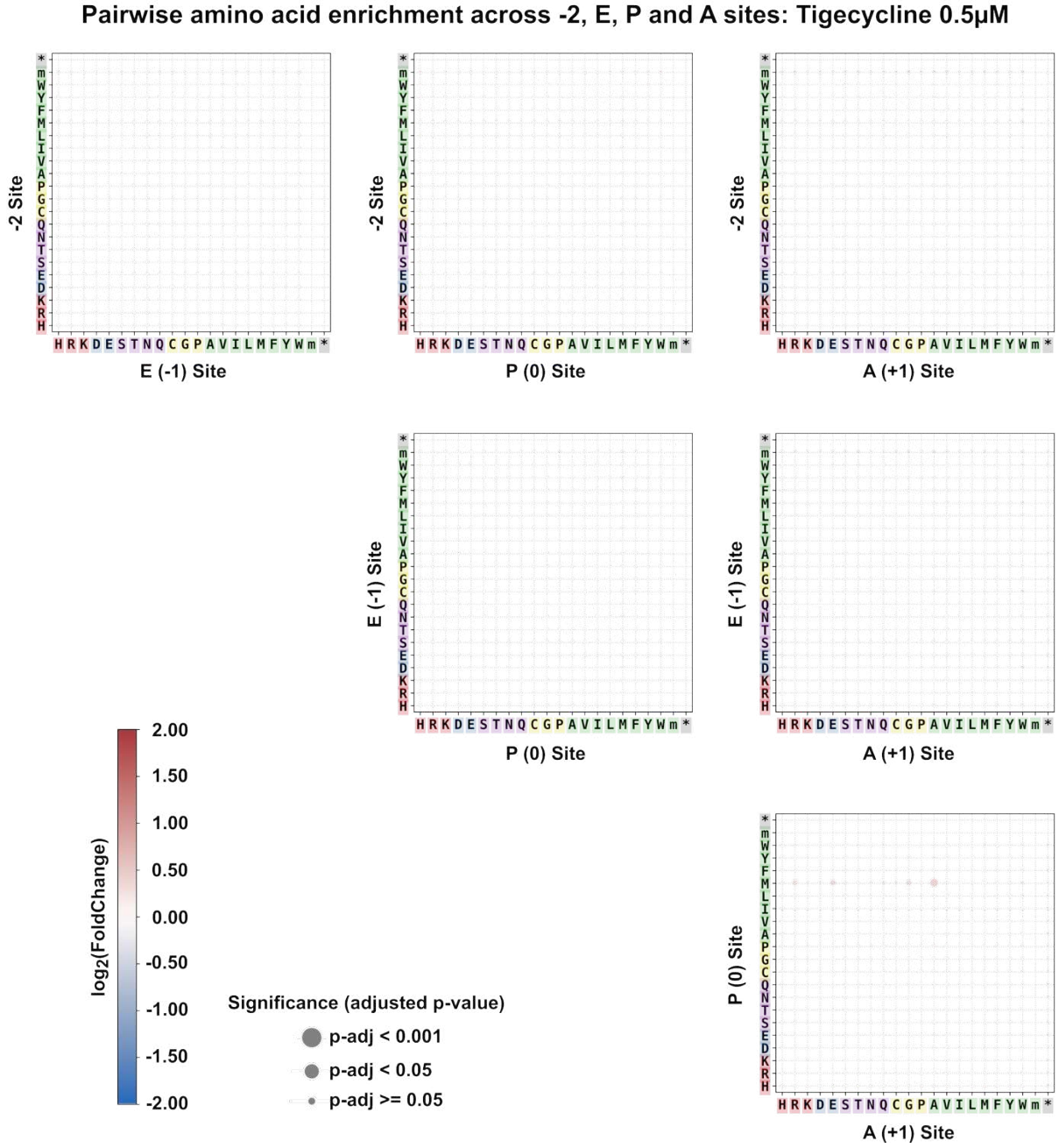

Supplementary Figure 60: Heatmap grid representing the di-amino acid motifs enriched across -2, E, P and A-sites in the presence of 0.5µM of tigecycline. Amino acid labels on the two axes are colored as follows: red – positively charged, blue – negatively charged, purple – polar, yellow – specific amino acids like Cys, Gly and Pro, and green – hydrophobic. Formyl methionine or fMet is denoted as m, while a stop codon is represented as an asterisk (*) symbol shaded in grey.

The following tables list the oligonucleotide and plasmid sequences used in this work. Oligonucleotides were bought from Eurogentec, and the plasmid was sequenced at Plasmidsaurus Inc. These oligonucleotides have also been used in previous studies such as Leroy et al. 2023; Gillard et al. 2026.

Supplementary Table 7: List of oligonucleotides used for iTP-Seq and toeprinting

Oligonucleotide name	Nucleic acid sequence
iTP_NNN15 (N represents equal proportions of each deoxynucleotide)	GGAGGAAAAAATATGNNNNNNNNNNNNNNNNNNNNNNNNNNNNNNNNNNNNNNNNNNNNNNNGCGATCTCGGTGTGA
Frag1_T7_RBS_ATG_ f	CGATCGAATTCTAATACGACTCACTATAGGGCTTAAGTATAAGGAGGAAAAAATATG
Stop_EcoRV_r	TATATGGATCCTTTTTGATATTGATATCTCATCACACCGAGATCG
Frag1_T7_f	CGATCGAATTCTAATACGACTCACTATAG
EcoRV_r	TATATGGATCCTTTTTGATATTGATA
cDNA_Fwd	GTATAAGGAGGAAAAAATATG
Linker_r	ATTGATGGTGCCTACAG
iTP_Biotin_standard	/5'Biosg/AAAAAAAAAAAAAATTAACTCCATCTAA
3'_linker_ApoI	/5rAPP/GGTATCTCGGTGTGACTGACTGAAAATTTCTGTAGGCACCATCAAT/ddC
NGS_f	AATGATACGGCGACCACCG
NGS_r	CAAGCAGAAGACGGCATACGAG
NGS_adapter_f	AATGATACGGCGACCACCGAGATCTACACTCTTTCCCTACACGACGCTCTTCCGATCTGTATAAGGAGGAAAAAATATG
NGS_adapter_index_r (the n6 stretch denotes the index sequence)	CAAGCAGAAGACGGCATACGAGATnnnnnnGTGACTGGAGTTCAGACGTGTGCTCTTCCGATCGATTGATGGTGCCTACAG
T7_TP	ATTAATACGACTCACTATAGG

TP_Rev_short	GGTTATAATGAATTTTGCTT
NV_YY	GGTTATAATGAATTTTGCTTATTAAC

Supplementary Table 8: List of TruSeq index sequences used in iTP-Seq for each replicate

TruSeq index number	Index sequence	Sample Name
i28	CTTTTG	No Antibiotics Rep1
i27	GAATCT	No Antibiotics Rep2
i37	ATTCCG	No Antibiotics Rep3
i12+3	TACAAG	No Antibiotics Rep4
i31	ATCGTG	TIG 0.05µM Rep1
i3+2	GCCTAA	TIG 0.05µM Rep2
i47+1	TCGCAT	TIG 0.05µM Rep3
i30	CCGGTG	TIG 0.5µM Rep1
i21+1	CGAAAC	TIG 0.5µM Rep2
i5	CACTGT	TIG 0.5µM Rep3
i48+2	ACGTCT	TIG 0.5µM Rep4
i2+1	ACATCG	TIG 5µM Rep1
i19+3	TTTCAC	TIG 5µM Rep2
i38	AGCTAG	TIG 5µM Rep3
i49+2	GCTCCA	TIG 5µM Rep4
i4+3	TGGTCA	TIG 50µM Rep1
i32	TGAGTG	TIG 50µM Rep2
i7+2	GATCTG	TIG 50µM Rep3
i50+2	CATCTA	TIG 50µM Rep4
i6+1	ATTGGC	TIG 500µM Rep1
i11+2	GTAGCC	TIG 500µM Rep2
i9	CTGATC	TIG 500µM Rep3
i51+3	TTGTTA	TIG 500µM Rep4
i8+3	TCAAGT	N502 0.4µM Rep1
i23+3	CCACTC	N502 0.4µM Rep2
i1	CGTGAT	N502 0.4µM Rep3
i52+3	ATACGG	N502 0.4µM Rep4
i10+1	AAGCTA	N502 40µM Rep1
i36	TGTTGG	N502 40µM Rep2
i40	TCTGAG	N502 40µM Rep3
i53+3	CCTTCG	N502 40µM Rep4

i14+1	GGAACT	N96624 0.3µM Rep1
i22+2	CGTACG	N96624 0.3µM Rep2
i41	GTCGTC	N96624 0.3µM Rep3
i54+3	CTACGC	N96624 0.3µM Rep4
i18+2	GCGGAC	N96624 40µM Rep1
i39	GTATAG	N96624 40µM Rep2
i42	CGATTA	N96624 40µM Rep3
i44	ATTATA	N96624 40µM Rep4

Key: TIG: Tigecycline; N502: NOSO-502; N96624: NOSO-96624; Rep: Replicate

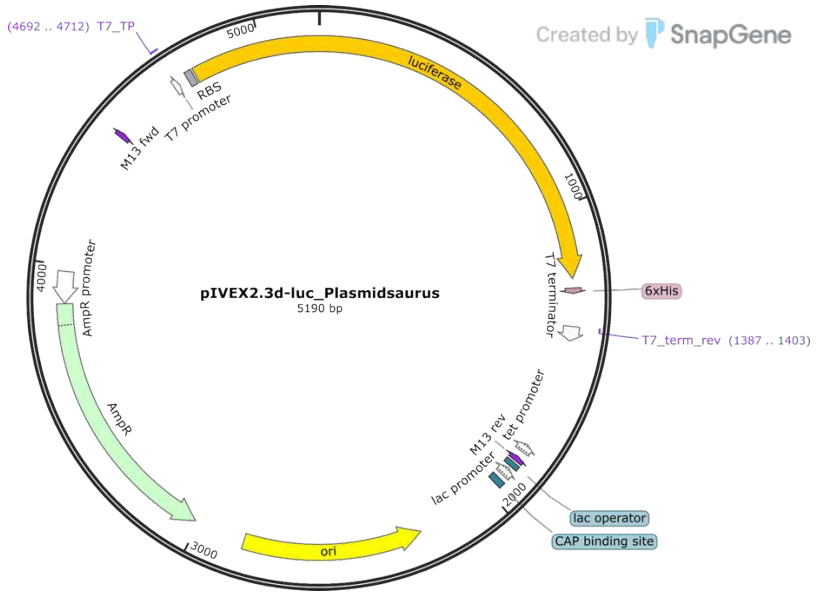

Supplementary Figure 61: Plasmid map of pIVEX2.3d-luc. The sequence corresponding to the luciferase gene was isolated from this plasmid stored in the lab by PCR using oligonucleotides T7_TP and T7_term_rev complementary to the T7 promoter and terminator regions, respectively (Figure created using Snapgene v8.2.3). The sequence of the isolated region is the following, where the two oligonucleotide sequences are underlined, and the translated luciferase region is indicated in gold:
ATTAATACGACTCACTATAGGGAGACCACAACGGTTTCCCTCTAGAAATAATTTTGTTTAACTTTAAGAAGGAGAT
ATACCATGGAAGACGCCAAAAACATAAAGAAAGGCCCGGCGCCATTCTATCCTCTAGAGGATGGAACCGCTGGA
GAGCAACTGCATAAGGCTATGAAGAGATACGCCCTGGTTCCTGGAACAATTGCTTTTACAGATGCACATATCGAG
GTGAACATCACGTACGCGGAATACTTCGAAATGTCCGTTCGGTTGGCAGAAGCTATGAAACGATATGGGCTGAAT
ACAAATCACAGAATCGTCGTATGCAGTGAAAACTCTCTTCAATTCTTTATGCCGGTGTTGGGCGCGTTATTTATCG
GAGTTGCAGTTGCGCCCGCGAACGACATTTATAATGAACGTGAATTGCTCAACAGTATGAACATTTCGCAGCCTA
CCGTAGTGTTTGTTTCCAAAAAGGGGTTGCAAAAAATTTTGAACGTGCAAAAAAAATTACCAATAATCCAGAAA
ATTATTATCATGGATTCTAAAACGGATTACCAGGGATTTCAGTCGATGTACACGTTCGTCACATCTCATCTACCTCC
CGGTTTTAATGAATACGATTTTGTACCAGAGTCCTTTGATCGTGACAAAACAATTGCACTGATAATGAATTCCTCT
GGATCTACTGGGTTACCTAAGGGTGTGGCCCTTCCGCATAGAACTGCCTGCGTCAGATTCTCGCATGCCAGAGAT
CCTATTTTTGGCAATCAAATCATTCCGGATACTGCGATTTTAAGTGTTGTTCCATTCCATCACGGTTTTGGAATGTT

TACTACACTCGGATATTTGATATGTGGATTTCGAGTCGTCTTAATGTATAGATTTGAAGAAGAGCTGTTTTTACGAT
CCCTTCAGGATTACAAAATTCAAAGTGCGTTGCTAGTACCAACCCTATTTTCATTCTTCGCCAAAAGCACTCTGAT
TGACAAATACGATTTATCTAATTTACACGAAATTGCTTCTGGGGGCGCACCTCTTTCGAAAGAAGTCGGGGAAGC
GGTTGCAAAACGCTTCCATCTTCCAGGGATACGACAAGGATATGGGCTCACTGAGACTACATCAGCTATTCTGAT
TACACCCGAGGGGGATGATAAACCGGGCGCGGTCGGTAAAGTTGTTCCATTTTTTGAAGCGAAGGTTGTGGATC
TGGATACCGGGAAAACGCTGGGCGTTAATCAGAGAGGCGAATTATGTGTCAGAGGACCTATGATTATGTCCGGT
TATGTAAACAATCCGGAAGCGACCAACGCCTTGATTGACAAGGATGGATGGCTACATTCTGGAGACATAGCTTAC
TGGGACGAAGACGAACACTTCTTCATAGTTGACCGCTTGAAGTCTTTAATTAAATACAAAGGATATCAGGTGGCC
CCCGCTGAATTGGAATCGATATTGTTACAACACCCCAACATCTTCGACGCGGGCGTGGCAGGTCTTCCCGACGAT
GACGCCGGTGAACTTCCCGCCGCCGTTGTTGTTTTGGAGCACGGAAAGACGATGACGGAAAAAGAGATCGTG
GATTACGTCGCCAGTCAAGTAACAACCGCGAAAAAGTTGCGCGGAGGAGTTGTGTTTGTGGACGAAGTACCGA
AAGGTCTTACCGGAAAACTCGACGCAAGAAAAATCAGAGAGATCCTCATAAAGGCCAAGAAGGGCGGAAAGT
CCAAATTGTAATAACTCGAGCGAGCTCCCGGGGGGGGTTCTCATCATCATCATCATTAATAAAAGGGCGAAT
TCCAGCACACTGGCGGCCGTTACTAGTGGATCCGGCTGCTAACAAAGCCCGAAAGGAAGCTGAGTTGGCTGCT
GCCACCGCTGAGCAATAACTAGCATAACCCC

Appendix A: Presentations at conferences (2022-2026)

During my PhD, I had the opportunity to present the work presented in this thesis at the following national and international conferences:

Oral Presentations:

- Conformational landscape of translation inhibition by the odilorhabdin class of context-dependent peptide antibiotics
  - 14th SifrARN, 30 June- 2 July 2026, Rennes, France
  - 13th Bordeaux RNA Club Symposium, 23-24 June 2026, Bordeaux, France

- Mechanism of translational miscoding and inhibition by the odilorhabdin class of context-dependent peptide antibiotics
  - 12th Bordeaux RNA Club Symposium, 17-18 June 2025, Bordeaux, France

Poster Presentations:

- **Bhattacharya, A.,** Gayral, D., Renault, T.T., Boissier, F., Gillard, M., Aleksandrova, E., Polikanov, Y.S., Gualtieri, M., & Innis, C.A. (2025). Mechanism of translational miscoding and inhibition by the odilorhabdin class of context-dependent peptide antibiotics.
  - 4th edition of the Integrative Structural Biology Meeting (BSI4), 15-19 December 2025, Bordeaux, France
  - Ribosomes 2025, 22-27 June 2025, Pacific Grove, California, USA

I shall also present a poster on this work at the upcoming 30th tRNA Conference, 20-24 September 2026, Heraklion, Crete, Greece.

During my PhD, I was also involved in the development of a novel high-throughput method using the principle of iTP-Seq to study co-translational protein folding, called FP-iTP-Seq. I also presented that work as a poster at the following conferences.

- **Bhattacharya, A.,** Metola, A., Westerfield, J.M., Gillard, M., Renault, T.T., von Heijne, G., & Innis, C.A. (2024). FP-iTP-Seq: a novel high-throughput method to study co-translational protein folding.
  - 13th Young Scientists' Symposium, 16 May 2025, Bordeaux, France
  - Protein Folding on the Ribosome or Nascent Chains Berlin, 15-18 December 2024, Berlin, Germany
  - 26th EMBL PhD Symposium, 4-6 December 2024, Heidelberg, Germany

Appendix B: Review article

Bhattacharya, Arunima, Thibaud T. Renault, and C. Axel Innis. 2024. 'The Ribosome as a Small-Molecule Sensor'. *Current Opinion in Microbiology* 77 (February): 102418. https://doi.org/10.1016/j.mib.2023.102418.

Available online at www.sciencedirect.com

ScienceDirect

Current Opinion in Microbiology

The ribosome as a small-molecule sensor

Arunima Bhattacharya, Thibaud T Renault and C Axel Innis

Sensing small molecules is crucial for microorganisms to adapt their genetic programs to changes in their environment. Arrest peptides encoded by short regulatory open reading frames program the ribosomes that translate them to undergo translational arrest in response to specific metabolites. Ribosome stalling in turn controls the expression of downstream genes on the same messenger RNA by translational or transcriptional means. In this review, we present our current understanding of the mechanisms by which ribosomes translating arrest peptides sense different metabolites, such as antibiotics or amino acids, to control gene expression.

Address
Univ. Bordeaux, Centre National de la Recherche Scientifique, Institut National de la Santé et de la Recherche Médicale, ARNA, UMR 5320, U1212, Institut Européen de Chimie et Biologie, F-33600 Pessac, France

Corresponding author: Innis, C. Axel (axel.innis@inserm.fr)

Current Opinion in Microbiology 2024, **77**:102418

This review comes from a themed issue on **Cell Regulation**

Edited by **Natalia Tschowri** and **Jürgen Lassak**

For complete overview of the section, please refer to the article collection, "Cell Regulation 2024"

Available online 29 December 2023

https://doi.org/10.1016/j.mib.2023.102418

1369–5274/© 2023 The Author(s). Published by Elsevier Ltd. This is an open access article under the CC BY license (http://creativecommons.org/licenses/by/4.0/).

Introduction

Microorganisms have evolved multiple strategies for detecting and responding to changes in their environment. Foremost among these is the ability to tune their gene expression according to the myriad of small molecules they encounter, such as nutrients, antibiotics, or other metabolites. Although much has been written about how these molecular cues are detected via allosteric transcription factors, two-component systems, protein kinases, or riboswitches [1], it is only in recent years that detailed mechanisms for a different class of sensors have come to light: metabolite-dependent arrest peptides [2–7]. Encoded by short open reading frames (ORFs) located upstream of the gene(s) to be regulated, arrest peptides feature conserved amino acid motifs that cause ribosomes that translate them to stall in response to specific metabolites, effectively programming these ribosomes to function as small-molecule sensors (Figure 1a). This review highlights recent advances in our understanding of the mechanisms by which arrest peptides detect fluctuating metabolite levels to control microbial gene expression.

Gene regulation by metabolite-dependent arrest peptides

Antibiotic-sensing arrest peptides

Arrest peptides were first reported in the 1980s as regulators of antibiotic resistance gene expression. The first arrest peptide discovered, ErmCL, is encoded upstream of *ermC*, an inducible gene in staphylococci that confers resistance to macrolide antibiotics such as erythromycin (Figure 1b) [8]. When erythromycin is absent or present at a low concentration, the ribosome-binding sequence (RBS) of *ermC* remains sequestered inside a short stem loop, thus hindering *ermC* expression [8,9]. A ribosome synthesizing ErmCL undergoes translational arrest when the concentration of erythromycin exceeds a certain threshold [10], causing it to stall on the mRNA. This changes the conformation of the transcript and unmasks the RBS of *ermC*, enabling translation of the resistance gene [8,9]. Since this initial discovery, arrest peptides that sense other classes of antibiotics (phenicols [11,12], lincosamides [13]) have been identified (Table 1). Such systems ensure that expression of the resistance gene, which entails a fitness cost for the bacterial host, only occurs upon exposure to the drug.

Amino acid-sensing arrest peptides

Microbial arrest peptides are also known to regulate amino acid metabolism (Table 1). In bacteria, the arrest peptide TnaC activates expression of the *tnaA/tnaB* operon in response to increased L-tryptophan levels, resulting in the biosynthesis of indole, an intercellular signaling molecule controlling biofilm formation and quorum sensing (Figure 1c) [14–16]. Similarly, the arrest peptide SpeFL/ORF34 controls expression of the polyamine biosynthesis operon *speF/potE* in response to the non-proteinogenic amino acid L-ornithine in γ-proteobacteria [17,18]. In both cases, ribosome stalling controls downstream gene expression by preventing premature transcription termination (Figure 1c) [15,17,18]. When the concentration of the cognate amino acid is present below a certain threshold, binding of the Rho termination factor to a *rho utilization* (*rut*) signal overlapping the regulatory upstream ORF (uORF) causes transcription to terminate before RNA polymerase has a chance to reach the downstream genes. Binding of the metabolite

Figure 1

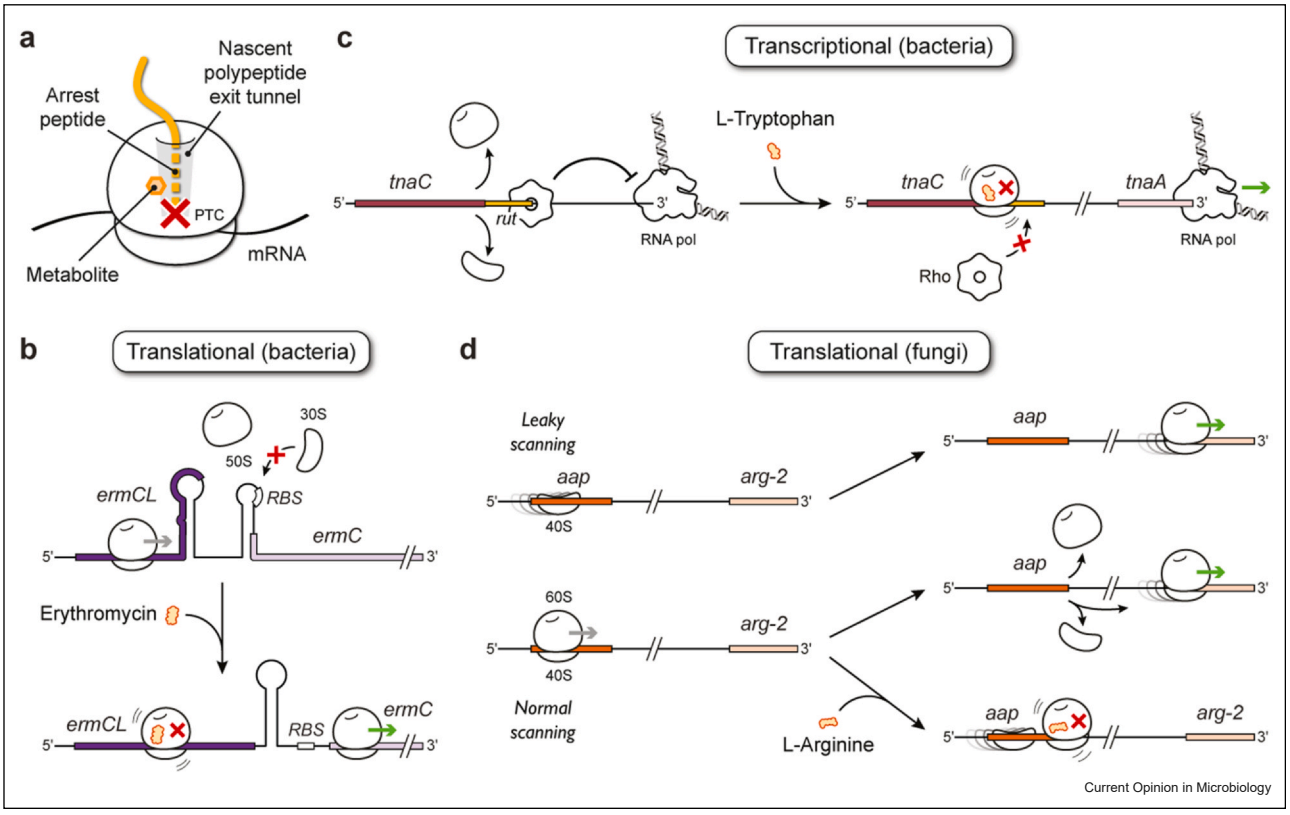

Gene regulation by metabolite-dependent arrest peptides. **(a)** Binding of a metabolite to a ribosome synthesizing an arrest peptide impairs the function of the ribosomal PTC. **(b)** Translational control of *ermC* expression by the ErmCL arrest peptide. When *ermCL* (purple) is translated in the absence of drug, an mRNA hairpin in the *ermCL_ermC* intergenic region sequesters the RBS of *ermC* (light purple), preventing its translation. Translation of *ermCL* in the presence of erythromycin causes the ribosome to stall, resulting in a structural rearrangement of the mRNA that exposes the RBS of *ermC*, enabling its translation. **(c)** Transcriptional control of tryptophanase (*tnaA*) (pink) and tryptophan permease (*tnaB*) expression by the TnaC arrest peptide. When L-tryptophan levels are low, binding of Rho to a *rut* site (yellow) immediately downstream of *tnaC* (maroon) results in premature transcription termination of the *tnaAB* operon. When L-tryptophan levels are high, the ribosome translating *tnaC* stalls, masking the *rut* site and preventing Rho binding. Transcription of the *tnaAB* operon by RNA polymerase can thus be completed. **(d)** In fungi, expression of the *arg-2* gene (light orange) is dependent on the leaky scanning of 40S subunits past the weak initiation site of *aap* (orange). When L-arginine levels are low, scanning ribosomes are able to reach *arg-2* and translate it. However, when L-arginine levels are high, a ribosome that has initiated translation of *aap* stalls, preventing scanning ribosomes from reaching and translating the *arg-2* gene.

to the ribosome during translation of the arrest peptide stalls the former on the mRNA so that it overlaps the *rut* site, preventing Rho from binding and allowing transcription to proceed. In contrast to the translational coupling observed for Erm peptides, regulation at the transcriptional level grants the possibility to control the expression of multiple genes.

Amino acid sensing by arrest peptides has also been observed outside the bacterial kingdom. In fungi, such as *Neurospora crassa* or *Saccharomyces cerevisiae*, the first step of arginine biosynthesis from glutamine is catalyzed by the small glutaminase subunit of the arginine-specific carbamoyl phosphate synthetase, encoded by the *arg-2* and CPA1 genes, respectively, in these two organisms. Expression of these genes is negatively regulated in response to L-arginine by an uORF encoding an arginine attenuator peptide (AAP) [2,19–21]. Unlike bacterial mRNA, which can be polycistronic, eukaryotic mRNA is monocistronic. This means that if a ribosome initiates protein synthesis on one ORF, there is no intrinsic mechanism to proceed to the next one, even if it is present in the same mRNA. In the case of the AAP, signal transduction takes advantage of the scanning process inherent in eukaryotic translation initiation (Figure 1d). The start codon of the regulatory uORF encoding the AAP is in a weak initiation context [22], resulting in low translation of the AAP when L-arginine levels are low, which in turn allows translation of the CPA1 or *arg-2* gene downstream via leaky scanning; in the presence of high levels of L-arginine, translation termination arrest occurs when the stop codon of the AAP is in the ribosomal A site and nascent AAP hinders the peptide-releasing activity of the ribosomal peptidyl

Table 1

Representative metabolite-dependent arrest peptides.

Metabolite	Metabolite-dependent arrest peptide	Arrest peptide (P-site residue underlined; residues in bold have been incorporated into the nascent peptide at the point of stalling)	References
Macrolide (e.g. erythromycin) 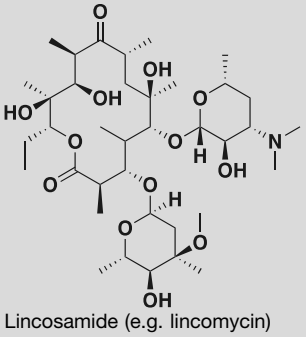	ErmAL1	**MCTSIAVV**EITLSHS	[31–34,42,50]
	Erm36L	**MGSPSIAVT**RFRRF	
	ErmBL	**MLVFQMRNVD**KTSTILKQTKNSDYADK	
	ErmCL	**MGIFSIFVI**STVHYQPNKK	
	ErmDL	**MTHSMRL**RFPTLNQ	
	MefAL	**MTASMRL**R	
	MsrDL	**MYLIFM**	
Lincosamide (e.g. lincomycin) 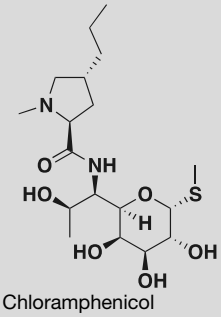	$Vga(A)_{LC}$ leader	MIN	[13]
Chloramphenicol 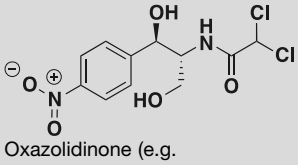	CmlA (cat-86 leader)	**MSTSKNAD**K	[11,12,51]
	Crb (CAT leader)	**MVKTD**K	
Oxazolidinone (e.g. linezolid) 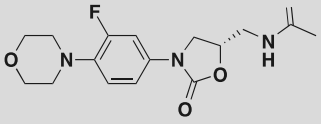	*Artificial sequence*	**MFKAF**K	[47,52]
L-arginine 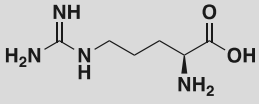	AAP, *Neurospora crassa*	**MNGRPSVFTSQDYLSDHLWRALNA**	[2,20]
	AAP, *Saccharomyces* sp.	**MFSLSNSQYTCQDYISDHIWKTSSH**	
L-ornithine 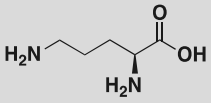	SpeFL	**MENNSRTMPHIRRTTHIMKFAHRNSFDFHFFNAR**	[18]
L-tryptophan 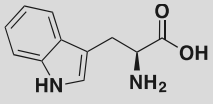	TnaC	**MNILHICVTSKWFNIDNKIVDHRP**	[37]

transferase center (PTC) [23,24]. This also blocks the preinitiation complexes that scan the 5′-cap region of the mRNA, preventing them from reaching the start codon of the downstream metabolic gene and translating it [19,24,25].

Arrest peptides capable of sensing other types of metabolites are likely to be widespread in nature, but comprehensive searches to identify them are lacking to date [3,25].

Mechanisms of small-molecule sensing by the ribosome

Although most of the arrest peptides listed above and the mechanisms by which they activate or repress gene expression through ribosome stalling have been known for years, it is only recently that we have begun to understand how arrest peptides can turn the ribosome into a small-molecule sensor. During translation, nascent polypeptides must travel through a long exit tunnel spanning the large ribosomal subunit before they are released into the cytoplasm or delivered to the membrane (Figure 1a) [26]. While most proteins complete this journey with ease, arrest peptides make stable interactions with the exit tunnel that ultimately cause the PTC to shut down, resulting in ribosome stalling. A striking example is the force-sensing *Vibrio* export monitoring polypeptide (VemP), which helps *Vibrio alginolyticus* adapt its protein-targeting machinery to changes in salinity [27]. Nascent VemP forms a highly compact structure within the exit tunnel that forces structural rearrangements within the PTC [28] and is but one of a diverse group of metabolite-independent arrest peptides, such as SecM or MifM [2,29], that detect pulling forces induced by the membrane translocation machinery. In contrast, metabolite-dependent arrest peptides only stall the ribosome when a sufficient concentration of a small-molecule co-inducer is present. A series of recent studies [18,30–39] suggest that the mechanisms by which they do so differ according to the intrinsic affinity of the small molecule for the ribosome.

High-affinity ligands

Macrolide antibiotics such as erythromycin bind to the nascent polypeptide exit tunnel with high affinity, even in the absence of translation [30]. Throughout evolution, the exit tunnel has undergone selective pressure to maintain a shape that allows the majority of nascent polypeptides to transit through it without impeding translation. However, macrolide binding partially obstructs the tunnel (Figure 2a), altering its shape and causing normally harmless amino acid sequences to form stable contacts with the ribosomal interior, ultimately preventing further translation [30].

Arrest peptides controlling the expression of resistance genes function according to this principle (Figure 2b) [4,40–42]. The simplest macrolide-dependent arrest motif is +X+, where + represents a positively charged amino acid such as arginine (R) or lysine (K), and X represents any amino acid [41,43]. This motif is found in arrest peptides such as ErmDL or MefAL, and the mechanism by which it causes ribosome stalling in the presence of the antibiotic has been extensively characterized, both biochemically and structurally [31,32,44]. In brief, the side chain of the first positively charged residue of the +X+ motif (often an arginine) is forced to occupy the A-site crevice of the PTC by the ribosome-bound drug, thus preventing an incoming positively charged amino acid from properly accommodating into the ribosomal A site [31]. Interestingly, the mechanisms by which erythromycin and telithromycin stall ribosomes at the RLR motif of ErmDL differ. While erythromycin engages with the N-terminal region of the arrest peptide to maximize ribosome stalling, telithromycin-induced stalling is exclusively dependent on the +X+ motif [31].

Another well-characterized example is the MsrDL peptide controlling the expression of antibiotic resistance ABC-Fs (ARE ABC-Fs) in streptococci, whose short hydrophobic sequence is unable to bypass the tunnel-bound drug, instead making contacts at the PTC that disrupt release factor action [32]. ErmBL, a macrolide-sensing peptide controlling the expression of the *ermB* methyltransferase in *Streptococcus sanguinis*, is forced to interact with the ribosomal exit tunnel by the drug, preventing proper accommodation of Lys-tRNA^{Lys} in the A site [33]. Similarly, the ErmCL peptide of *Staphylococcus aureus* induces perturbations of the PTC that also prevent stable binding of the aminoacyl-tRNA at the A site [34]. Other antibiotics that bind to the nascent polypeptide exit tunnel also show sequence-dependent effects, such as the recently discovered antibiotic tetracenomycin X [35], which preferentially stalls ribosomes at Gln–Lys (QK) motifs [36]. However, no such motifs have been shown to control the expression of resistance genes to tetracenomycins to date.

Low-affinity ligands

In contrast with ribosome-targeting antibiotics, amino acids such as L-ornithine, L-tryptophan, or L-arginine are not known to bind the ribosome with high affinity, meaning that their detection by an arrest peptide must occur via a different mechanism. *E. coli* ribosomes translating *speFL* undergo translational arrest in response to millimolar concentrations of L-ornithine, with a conserved HIRRXXH(I/L)M motif within the SpeFL N-terminus playing a critical functional role [18]. In the presence of 10 mM L-ornithine, nascent SpeFL adopts a complex structure within the exit tunnel, comprising an N-terminal sensor domain that sandwiches an L-ornithine molecule against the ribosome, and a compacted

Figure 2

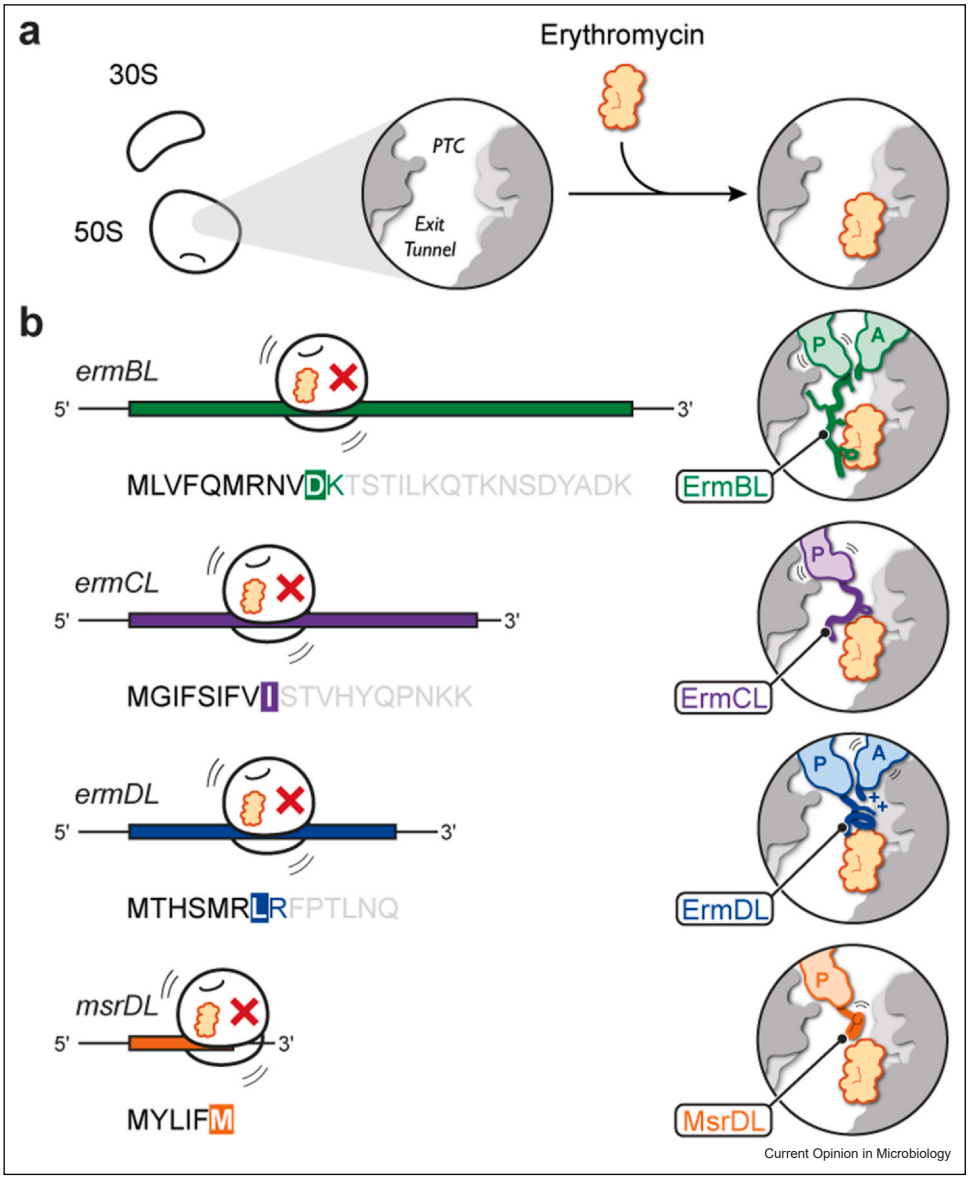

Macrolide-sensing arrest peptides. **(a)** The nascent polypeptide exit tunnel of the large ribosomal subunit has evolved to limit its interaction with nascent peptides. However, binding of erythromycin or other macrolide antibiotics near the PTC partially occludes the tunnel, promoting interactions with nascent amino acid motifs. **(b)** Examples of macrolide-sensing arrest peptides interacting with the tunnel-bound drug and inactivating the PTC via different mechanisms: ErmBL (green), ErmCL (purple), ErmDL (blue), and MsrDL (orange). P-site and A-site tRNAs are labeled P and A, respectively. C-terminal residues of peptidyl-tRNAs in the stalled complexes are boxed, important A-site residues for ErmBL and ErmDL are colored, and side chains for key peptide residues are shown. Motion lines are used to indicate tRNAs whose positioning is perturbed or, in the case of MsrDL, to depict interference of the nascent peptide with the action of release factor. Plus signs (+) are used to indicate positive charges for the RLR motif of ErmDL.

C-terminal effector domain that fills the upper tunnel (Figure 3a) [18]. L-ornithine engages with the ribosome and the sensor domain of nascent SpeFL through every available hydrogen bond donor and acceptor, accounting for a highly specific interaction. Once contacts with L-ornithine have been established — most likely after approximately two-thirds of SpeFL have been synthesized by the ribosome — synthesis of the effector domain continues until its mainly hydrophobic residues form a compact core, thus altering the conformation of the PTC to prevent release factor-1 action. Unable to undergo termination, the SpeFL-ribosome complex stalls. Throughout this highly dynamic process, a fine balance between the competing kinetics of ligand binding and SpeFL synthesis is needed to achieve the desired outcome. Indeed, there is likely a narrow

Figure 3

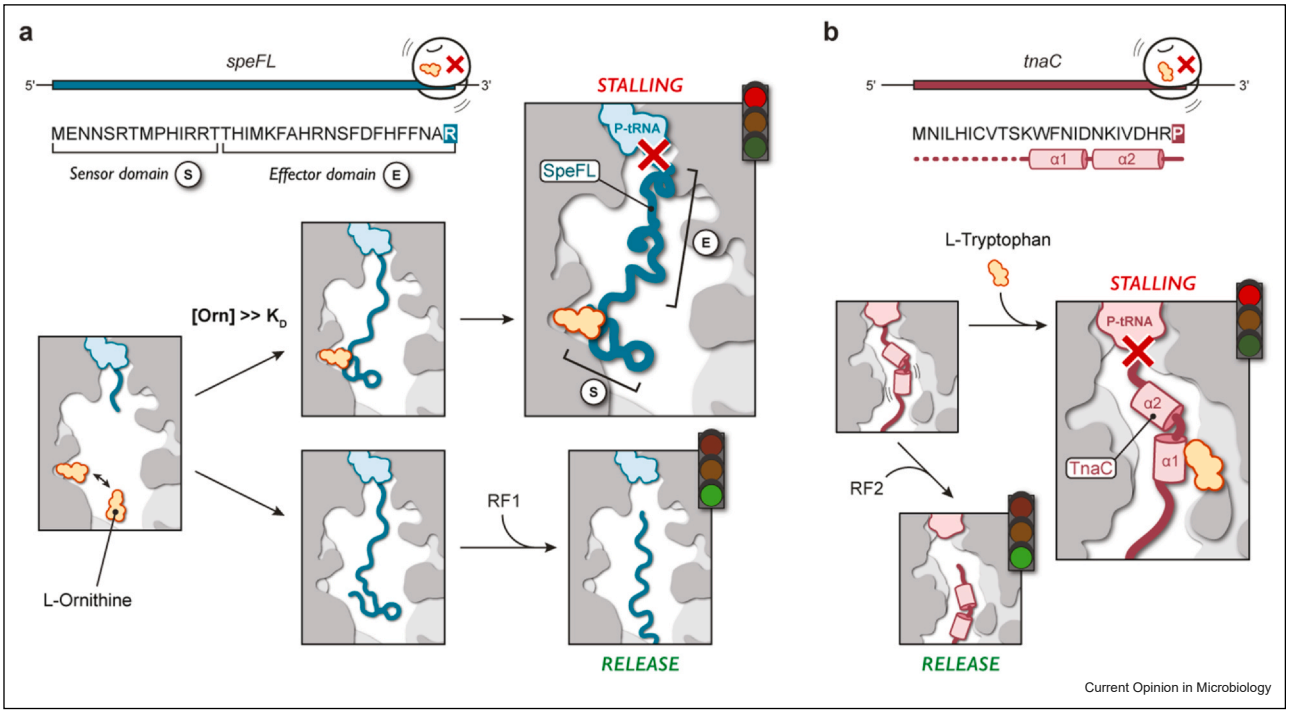

Amino acid-sensing arrest peptides. **(a)** Mechanism of L-ornithine sensing by a ribosome translating *speFL*. Binding of L-ornithine to the ribosome is stabilized by the sensor domain of SpeFL (S), ultimately leading to the inactivation of the peptide release activity of the PTC by the SpeFL effector domain (E). Since the binding affinity of L-ornithine for the empty ribosome is low, a concentration of ligand well above the K_D of the interaction is needed to ensure the timely capture of a single L-ornithine molecule by the ribosome–SpeFL complex. Orn denotes L-ornithine and the C-terminal residue of peptidyl-tRNA is boxed. **(b)** Mechanism of L-tryptophan sensing by a ribosome-translating *tnaC*. Binding of a single L-tryptophan molecule stabilizes the compact α-helical fold of the TnaC C-terminal region, impairing RF2-mediated translation termination. The C-terminal residue of peptidyl-tRNA is boxed. Alpha helices α1 and α2 of TnaC are shown as cylinders.

window of opportunity for the sensor domain of SpeFL to fold and engage the ribosome and L-ornithine. If the latter is not readily available for binding at the opportune moment, translation of *speFL* will ensue and the ribosome will not stall. L-ornithine capture by SpeFL is therefore thought to be a kinetically controlled process, as is often seen for riboswitches [45]. This means that the L-ornithine concentration must be well above its K_D for the ribosome–SpeFL complex to ensure the timely binding of the ligand when it is needed [18].

A corollary of this model is that the concentration of ligand required to achieve stalling — in other words, the sensitivity of the system — must be proportional to the rate of translation. Recent studies performed on the TnaC arrest peptide lend support to this notion. Ribosomes translating *tnaC* in the presence of millimolar concentrations of L-tryptophan stall upon reaching the stop codon. Cryo-EM structures show that the C-terminal half of TnaC adopts a compact α-helical fold, which is stabilized by the binding of a single molecule of L-tryptophan. TnaC thus perturbs the conformation of the PTC, interfering with release factor-2 (RF2) accommodation and causing termination arrest (Figure 3b) [37,38]. Interestingly, a TnaC variant featuring a C-terminal R23F mutation located near the PTC displays dramatically increased sensitivity to L-tryptophan despite having a ligand-binding site some ~20 Å away from the mutation that is identical to that of wild-type TnaC [37]. Thus, it appears that the different L-tryptophan sensitivities of wild-type and R23F TnaC are not the result of altered ligand binding, but rather depend on the competing rates of L-tryptophan binding and RF2-catalyzed peptide release. Like SpeFL, TnaC is thought to operate under a kinetic regime. If L-tryptophan binds before RF2, ribosomes stall. If RF2 binds first, TnaC is released, and ribosomes detach from the mRNA. Rather than affecting the ability of L-tryptophan to bind to the ribosome nascent chain complex, the R23F mutation is thought to slow down RF2-catalyzed TnaC release. The longer the ribosome remains paused at the stop codon due to slower release, the lesser the concentration of L-tryptophan needed to stall the complex and the greater the sensitivity [37,38].

It is possible that the high- and low-affinity scenarios described here represent extreme cases along a

continuum. Although chloramphenicol-specific arrest peptides such as CmlA or Cat-86 [11,12] have not yet been characterized structurally, recent studies have shown that chloramphenicol [39,46] or oxazolidinone antibiotics [46,47] stall the ribosome when certain amino acids are found at the penultimate position of the nascent peptide. Cases such as these, in which particular nascent peptide residues are needed to stabilize the binding of a drug to the ribosome, are also likely to operate under kinetic control.

Outlook

Unlike allosteric transcription factors or riboswitches, in which metabolite sensing and transduction of the signal to control gene expression are intertwined, metabolite-dependent arrest peptides are modular by nature, making them ideally suited for the development of novel biological sensors for *in vivo* applications, such as microbial-living therapeutics [48]. For example, unrelated arrest peptides have successfully been fused to the *ermCL_ermC* intergenic region to activate the expression of *lacZα* [36,49]. Since arrest peptides can be combined with expression platforms in a plug-and-play fashion to control the expression of any gene either co- or posttranscriptionally, realizing the potential of arrest peptides as biological sensors will require new arrest peptides capable of sensing different types of molecules to be identified, either from natural sources using bioinformatics or genomic approaches, or *de novo* using a combination of directed evolution and/or computational protein design. Although it remains to be seen whether ligand-sensing mechanisms similar to the ones described here will be observed for the AAP, other metabolite-dependent arrest peptides in mammals or plants not covered in this review [2,3,25], or yet-to-be-discovered microbial arrest peptides, developing a deep understanding of such mechanisms will be key to making arrest peptides come of age.

CRediT authorship contribution statement

Arunima Bhattacharya: Writing – original draft, Writing – review & editing, Visualization. **Thibaud T Renault:** Writing – original draft, Writing – review & editing, Visualization. **C Axel Innis:** Writing – original draft, Writing – review & editing, Visualization, Supervision, Funding acquisition.

Data Availability

No data were used for the research described in the article.

Declaration of Competing Interest

The authors declare that they have no known competing financial interests or personal relationships that could have appeared to influence the work reported in this paper.

Acknowledgements

We thank Pauline Cossard for providing chemical diagrams of metabolites. C.A.I. is a European Molecular Biology Organization (EMBO) Young Investigator (Project number 3869) and has received funding from the European Research Council (ERC) under the European Union's Horizon 2020 research and innovation program (Grant Agreement no. 724040). A.B. has received funding from the Agence Nationale de la Recherche, France (ANR-22-CE11-0012-01).

References and recommended reading

Papers of particular interest, published within the period of review, have been highlighted as:

- • of special interest
- •• of outstanding interest

1. Ledezma-Tejeida D, Schastnaya E, Sauer U: **Metabolism as a signal generator in bacteria**. *Curr Opin Syst Biol* 2021, **28**:100404.
2. Ito K, Chiba S: **Arrest peptides: cis-acting modulators of translation**. *Annu Rev Biochem* 2013, **82**:171-202.
3. Seip B, Innis CA: **How widespread is metabolite sensing by ribosome-arresting nascent peptides?** *J Mol Biol* 2016, **428**:2217-2227.
4. Ramu H, Mankin A, Vazquez-Laslop N: **Programmed drug-dependent ribosome stalling**. *Mol Microbiol* 2009, **71**:811-824.
5. Wilson DN, Arenz S, Beckmann R: **Translation regulation via nascent polypeptide-mediated ribosome stalling**. *Curr Opin Struct Biol* 2016, **37**:123-133.
6. Dever TE, Ivanov IP, Sachs MS: **Conserved upstream open reading frame nascent peptides that control translation**. *Annu Rev Genet* 2020, **54**:237-264.
7. Chiba S, Fujiwara K, Chadani Y, Taguchi H: **Nascent chain-mediated translation regulation in bacteria: translation arrest and intrinsic ribosome destabilization**. *J Biochem* 2023, **173**:227-236.
8. Horinouchi S, Weisblum B: **Posttranscriptional modification of mRNA conformation: mechanism that regulates erythromycin-induced resistance**. *Proc Natl Acad Sci USA* 1980, **77**:7079-7083.
9. Gryczan TJ, Grandi G, Hahn J, Grandi R, Dubnau D: **Conformational alteration of mRNA structure and the posttranscriptional regulation of erythromycin-induced drug resistance**. *Nucleic Acids Res* 1980, **8**:6081-6097.
10. Vazquez-Laslop N, Thum C, Mankin AS: **Molecular mechanism of drug-dependent ribosome stalling**. *Mol Cell* 2008, **30**:190-202.
11. Alexieva Z, Duvall EJ, Ambulos NP, Kim UJ, Lovett PS: **Chloramphenicol induction of cat-86 requires ribosome stalling at a specific site in the leader**. *Proc Natl Acad Sci USA* 1988, **85**:3057-3061.
12. Gu Z, Rogers EJ, Lovett PS: **Peptidyl transferase inhibition by the nascent leader peptide of an inducible cat gene**. *J Bacteriol* 1993, **175**:5309-5313.
13. Vimberg V, Cavanagh JP, Novotna M, Lenart J, Nguyen Thi Ngoc B, Vesela J, Pain M, Koberska M, Balikova Novotna G: **Ribosome-mediated attenuation of vga(A) expression is shaped by the antibiotic resistance specificity of Vga(A) protein variants**. *Antimicrob Agents Chemother* 2020, **64**:e00666-20.
14. Stewart V, Yanofsky C: **Evidence for transcription antitermination control of tryptophanase operon expression in *Escherichia coli* K-12**. *J Bacteriol* 1985, **164**:731-740.
15. Konan KV, Yanofsky C: **Rho-dependent transcription termination in the tna operon of *Escherichia coli*: roles of the boxA sequence and the rut site**. *J Bacteriol* 2000, **182**:3981-3988.

16. Gong F, Yanofsky C: **Reproducing tna operon regulation in vitro in an S-30 system. Tryptophan induction inhibits cleavage of TnaC peptidyl-tRNA**. *J Biol Chem* 2001, **276**:1974-1983.

17. Ben-Zvi T, Pushkarev A, Seri H, Elgrably-Weiss M, Papenfort K, Altuvia S: **mRNA dynamics and alternative conformations adopted under low and high arginine concentrations control polyamine biosynthesis in Salmonella**. *PLoS Genet* 2019, **15**:e1007646.

18. •• Herrero del Valle A, Seip B, Cervera-Marzal I, Sacheau G, Seefeldt AC, Innis CA: **Ornithine capture by a translating ribosome controls bacterial polyamine synthesis**. *Nat Microbiol* 2020, **5**:554-561.
In this study, a ribosome synthesizing the arrest peptide SpeFL is shown to capture a single L-ornithine molecule to activate the expression of polyamine biosynthetic genes in γ-proteobacteria. L-ornithine sensing is proposed to be kinetically controlled, with L-ornithine binding and translation elongation competing to determine ribosomal fate.

19. Luo Z, Sachs MS: **Role of an upstream open reading frame in mediating arginine-specific translational control in *Neurospora crassa***. *J Bacteriol* 1996, **178**:2172-2177.

20. Delbecq P, Calvo O, Filipkowski RK, Piérard A, Messenguy F: **Functional analysis of the leader peptide of the yeast gene CPA1 and heterologous regulation by other fungal peptides**. *Curr Genet* 2000, **38**:105-112.

21. Spevak CC, Ivanov IP, Sachs MS: **Sequence requirements for ribosome stalling by the arginine attenuator peptide**. *J Biol Chem* 2010, **285**:40933-40942.

22. Werner M, Feller A, Messenguy F, Piérard A: **The leader peptide of yeast gene CPA1 is essential for the translational repression of its expression**. *Cell* 1987, **49**:805-813.

23. Wei J, Wu C, Sachs MS: **The arginine attenuator peptide interferes with the ribosome peptidyl transferase center**. *Mol Cell Biol* 2012, **32**:2396-2406.

24. Wu C, Wei J, Lin P-J, Tu L, Deutsch C, Johnson AE, Sachs MS: **Arginine changes the conformation of the arginine attenuator peptide relative to the ribosome tunnel**. *J Mol Biol* 2012, **416**:518-533.

25. Zhang H, Wang Y, Lu J: **Function and evolution of upstream ORFs in eukaryotes**. *Trends Biochem Sci* 2019, **44**:782-794.

26. Nissen P, Hansen J, Ban N, Moore PB, Steitz TA: **The structural basis of ribosome activity in peptide bond synthesis**. *Science* 2000, **289**:920-930.

27. Ishii E, Chiba S, Hashimoto N, Kojima S, Homma M, Ito K, Akiyama Y, Mori H: **Nascent chain-monitored remodeling of the Sec machinery for salinity adaptation of marine bacteria**. *Proc Natl Acad Sci USA* 2015, **112**:E5513-E5522.

28. Su T, Cheng J, Sohmen D, Hedman R, Berninghausen O, Von Heijne G, Wilson DN, Beckmann R: **The force-sensing peptide VemP employs extreme compaction and secondary structure formation to induce ribosomal stalling**. *eLife* 2017, **6**:e25642.

29. Sakiyama K, Shimokawa-Chiba N, Fujiwara K, Chiba S: **Search for translation arrest peptides encoded upstream of genes for components of protein localization pathways**. *Nucleic Acids Res* 2021, **49**:1550-1566.

30. Tu D, Blaha G, Moore PB, Steitz TA: **Structures of MLSBK antibiotics bound to mutated large ribosomal subunits provide a structural explanation for resistance**. *Cell* 2005, **121**:257-270.

31. •• Beckert B, Leroy EC, Sothiselvam S, Bock LV, Svetlov MS, Graf M, Arenz S, Abdelshahid M, Seip B, Grubmüller H, *et al.*: **Structural and mechanistic basis for translation inhibition by macrolide and ketolide antibiotics**. *Nat Commun* 2021, **12**:4466.
Using structural, biochemical, and molecular simulation data, the authors dissect the mechanism for the main mode of translation inhibition by macrolide and ketolide antibiotics at +X + motifs. In addition, they show that although these related classes of antibiotics share a similar backbone, they trigger ribosome stalling on *ermDL* through different mechanisms.

32. • Fostier CR, Ousalem F, Leroy EC, Ngo S, Soufari H, Innis CA, Hashem Y, Boël G: **Regulation of the macrolide resistance ABC-F translation factor MsrD**. *Nat Commun* 2023, **14**:3891.
In this work, the authors characterize the mechanism by which expression of the ARE ABC-F protein MsrD is controlled by the macrolide-sensing arrest peptide MsrDL, evidencing a coupling between transcription and translation mediated by the presence of a NusG-dependent RNA-polymerase pause site in *msrDL*.

33. Arenz S, Bock LV, Graf M, Innis CA, Beckmann R, Grubmüller H, Vaiana AC, Wilson DN: **A combined cryo-EM and molecular dynamics approach reveals the mechanism of ErmBL-mediated translation arrest**. *Nat Commun* 2016, **7**:12026.

34. Arenz S, Meydan S, Starosta AL, Berninghausen O, Beckmann R, Vázquez-Laslop N, Wilson DN: **Drug sensing by the ribosome induces translational arrest via active site perturbation**. *Mol Cell* 2014, **56**:446-452.

35. Osterman IA, Wieland M, Maviza TP, Lashkevich KA, Lukianov DA, Komarova ES, Zakalyukina YV, Buschauer R, Shiriaev DI, Leyn SA, *et al.*: **Tetracenomycin X inhibits translation by binding within the ribosomal exit tunnel**. *Nat Chem Biol* 2020, **16**:1071-1077.

36. Leroy EC, Perry TN, Renault TT, Innis CA: **Tetracenomycin X sequesters peptidyl-tRNA during translation of QK motifs**. *Nat Chem Biol* 2023, **19**:1091-1096.

37. •• van der Stel A-X, Gordon ER, Sengupta A, Martínez AK, Klepacki D, Perry TN, Herrero del Valle A, Vázquez-Laslop N, Sachs MS, Cruz-Vera LR, *et al.*: **Structural basis for the tryptophan sensitivity of TnaC-mediated ribosome stalling**. *Nat Commun* 2021, **12**:5340.
Using a combined biochemical and structural approach, the authors characterize the L-tryptophan-sensing arrest peptide TnaC and a variant with greatly enhanced sensitivity for this amino acid. Ribosomes translating wild-type or hypersensitive *tnaC* form identical L-tryptophan-binding sites, suggesting that the ligand sensitivity of each variant is determined by the relative rates of L-tryptophan binding and peptidyl-tRNA cleavage.

38. • Su T, Kudva R, Becker T, Buschauer R, Komar T, Berninghausen O, von Heijne G, Cheng J, Beckmann R: **Structural basis of l-tryptophan-dependent inhibition of release factor 2 by the TnaC arrest peptide**. *Nucleic Acids Res* 2021, **49**:9539-9547.
Here, the authors determine the structures of ribosomes stalled during translation of *tnaC* in the presence of L-tryptophan, revealing the mechanism by which RF2-mediated translation termination is inhibited to control the expression of the *tnaAB* operon.

39. •• Syroegin EA, Flemmich L, Klepacki D, Vazquez-Laslop N, Micura R, Polikanov YS: **Structural basis for the context-specific action of the classic peptidyl transferase inhibitor chloramphenicol**. *Nat Struct Mol Biol* 2022, **29**:152-161.
This structural study examines the context dependence of ribosomal arrest induced by the antibiotic chloramphenicol. The penultimate residue of the nascent polypeptide is shown to be essential for high-affinity binding of the drug to the ribosome, hinting at the mechanism by which chloramphenicol-sensing arrest peptides activate the expression of resistance genes.

40. Dubnau D: **Induction of ermC requires translation of the leader peptide**. *EMBO J* 1985, **4**:533-537.

41. Kannan K, Kanabar P, Schryer D, Florin T, Oh E, Bahroos N, Tenson T, Weissman JS, Mankin AS: **The general mode of translation inhibition by macrolide antibiotics**. *Proc Natl Acad Sci USA* 2014, **111**:15958-15963.

42. Sothiselvam S, Liu B, Han W, Ramu H, Klepacki D, Atkinson GC, Brauer A, Remm M, Tenson T, Schulten K, *et al.*: **Macrolide antibiotics allosterically predispose the ribosome for translation arrest**. *Proc Natl Acad Sci USA* 2014, **111**:9804-9809.

43. Davis AR, Gohara DW, Yap M-NF: **Sequence selectivity of macrolide-induced translational attenuation**. *Proc Natl Acad Sci USA* 2014, **111**:15379-15384.

44. Chancey ST, Bai X, Kumar N, Drabek EF, Daugherty SC, Colon T, Ott S, Sengamalay N, Sadzewicz L, Tallon LJ, *et al.*: **Transcriptional attenuation controls macrolide inducible efflux and resistance in *Streptococcus pneumoniae* and in other gram-positive bacteria containing mef/mel(msr(D)) elements**. *PLoS One* 2015, **10**:e0116254.

45. Wayment-Steele H, Wu M, Gotrik M, Das R: **Evaluating riboswitch optimality**. *Methods Enzym* 2019, **623**:417-450.

46. Marks J, Kannan K, Roncase EJ, Klepacki D, Kefi A, Orelle C, Vázquez-Laslop N, Mankin AS: **Context-specific inhibition of translation by ribosomal antibiotics targeting the peptidyl transferase center**. *Proc Natl Acad Sci USA* 2016, **113**:12150-12155.

47. Tsai K, Stojković V, Lee DJ, Young ID, Szal T, Klepacki D, Vázquez-Laslop N, Mankin AS, Fraser JS, Fujimori DG: **Structural basis for context-specific inhibition of translation by oxazolidinone antibiotics**. *Nat Struct Mol Biol* 2022, **29**:162-171.

48. Inda ME, Lu TK: **Microbes as biosensors**. *Annu Rev Microbiol* 2020, **74**:337-359.

49. Bailey M, Chettiath T, Mankin AS: **Induction of *erm* (C) expression by noninducing antibiotics**. *Antimicrob Agents Chemother* 2008, **52**:866-874.

50. Vázquez-Laslop N, Ramu H, Mankin A: **Nascent peptide-mediated ribosome stalling promoted by antibiotics**. In *Ribosomes*. Edited by Rodnina MV, Wintermeyer W, Green R. Springer Vienna; 2011:377-392.

51. Rogers EJ, Kim UJ, Ambulos NP, Lovett PS: **Four codons in the cat-86 leader define a chloramphenicol-sensitive ribosome stall sequence**. *J Bacteriol* 1990, **172**:110-115.

52. Choi J, Marks J, Zhang J, Chen D-H, Wang J, Vázquez-Laslop N, Mankin AS, Puglisi JD: **Dynamics of the context-specific translation arrest by chloramphenicol and linezolid**. *Nat Chem Biol* 2020, **16**:310-317.

References

Abraham, E. P., and E. Chain. 1940. 'An Enzyme from Bacteria Able to Destroy Penicillin'. *Nature* 146 (3713): 837–837. https://doi.org/10.1038/146837a0.

Adamczyk, Andrew J., and Arieh Warshel. 2011. 'Converting Structural Information into an Allosteric-Energy-Based Picture for Elongation Factor Tu Activation by the Ribosome'. *Proceedings of the National Academy of Sciences* 108 (24): 9827–32. https://doi.org/10.1073/pnas.1105714108.

Adams, Jerry M. 1968. 'On the Release of the Formyl Group from Nascent Protein'. *Journal of Molecular Biology* 33 (3): 571–89. https://doi.org/10.1016/0022-2836(68)90307-0.

Adio, Sarah, Tamara Senyushkina, Frank Peske, Niels Fischer, Wolfgang Wintermeyer, and Marina V. Rodnina. 2015. 'Fluctuations between Multiple EF-G-Induced Chimeric tRNA States during Translocation on the Ribosome'. *Nature Communications* 6 (1): 7442. https://doi.org/10.1038/ncomms8442.

Adio, Sarah, Heena Sharma, Tamara Senyushkina, et al. 2018. 'Dynamics of Ribosomes and Release Factors during Translation Termination in E. Coli'. *eLife* 7 (June): e34252. https://doi.org/10.7554/eLife.34252.

Agirrezabala, Xabier, Jianlin Lei, Julie L. Brunelle, Rodrigo F. Ortiz-Meoz, Rachel Green, and Joachim Frank. 2008. 'Visualization of the Hybrid State of tRNA Binding Promoted by Spontaneous Ratcheting of the Ribosome'. *Molecular Cell* 32 (2): 190–97. https://doi.org/10.1016/j.molcel.2008.10.001.

Agris, Paul F. 2004. 'Decoding the Genome: A Modified View'. *Nucleic Acids Research* 32 (1): 223–38. https://doi.org/10.1093/nar/gkh185.

Akhurst, R. J. 1982. 'Antibiotic Activity of Xenorhabdus Spp., Bacteria Symbiotically Associated with Insect Pathogenic Nematodes of the Families Heterorhabditidae and Steinernematidae'. *Microbiology* 128 (12): 3061–65. https://doi.org/10.1099/00221287-128-12-3061.

Alejo, Jose L., and Scott C. Blanchard. 2017. 'Miscoding-Induced Stalling of Substrate Translocation on the Bacterial Ribosome'. *Proceedings of the National Academy of Sciences* 114 (41). https://doi.org/10.1073/pnas.1707539114.

Ambrogelly, Alexandre, Sotiria Palioura, and Dieter Söll. 2007. 'Natural Expansion of the Genetic Code'. *Nature Chemical Biology* 3 (1): 29–35. https://doi.org/10.1038/nchembio847.

Antoun, Ayman, Michael Y. Pavlov, Martin Lovmar, and Måns Ehrenberg. 2006a. 'How Initiation Factors Maximize the Accuracy of tRNA Selection in Initiation of Bacterial

Protein Synthesis'. *Molecular Cell* 23 (2): 183–93. https://doi.org/10.1016/j.molcel.2006.05.030.

Antoun, Ayman, Michael Y. Pavlov, Martin Lovmar, and Måns Ehrenberg. 2006b. 'How Initiation Factors Tune the Rate of Initiation of Protein Synthesis in Bacteria'. *The EMBO Journal* 25 (11): 2539–50. https://doi.org/10.1038/sj.emboj.7601140.

Årdal, Christine, Manica Balasegaram, Ramanan Laxminarayan, et al. 2020. 'Antibiotic Development — Economic, Regulatory and Societal Challenges'. *Nature Reviews Microbiology* 18 (5): 267–74. https://doi.org/10.1038/s41579-019-0293-3.

Årdal, Christine, Enrico Baraldi, Ursula Theuretzbacher, et al. 2018. 'Insights into Early Stage of Antibiotic Development in Small- and Medium-Sized Enterprises: A Survey of Targets, Costs, and Durations'. *Journal of Pharmaceutical Policy and Practice* 11 (1): 8. https://doi.org/10.1186/s40545-018-0135-0.

Asahara, Haruichi, Hyouta Himeno, Koji Tamura, Tsunemi Hasegawa, Kimitsuna Watanabe, and Mikio Shimizu. 1993. 'Recognition Nucleotides of Escherichia Coli tRNALeu and Its Elements Facilitating Discrimination from tRNASer and tRNATyr'. *Journal of Molecular Biology* 231 (2): 219–29. https://doi.org/10.1006/jmbi.1993.1277.

Attwood, Marie L. G., Alan Noel, Pippa Griffin, Emilie Racine, Maxime Gualtieri, and Alasdair MacGowan. 2025. '*In Vitro* Activity of NOSO-502, a Novel-Action Antimicrobial, against Clinical Strains of Enterobacterales Including MDR Strains'. *Journal of Antimicrobial Chemotherapy*, May 16, dkaf152. https://doi.org/10.1093/jac/dkaf152.

Ban, Nenad, Roland Beckmann, Jamie Hd Cate, et al. 2014. 'A New System for Naming Ribosomal Proteins'. *Current Opinion in Structural Biology* 24 (February): 165–69. https://doi.org/10.1016/j.sbi.2014.01.002.

Ban, Nenad, Poul Nissen, Jeffrey Hansen, Peter B. Moore, and Thomas A. Steitz. 2000. 'The Complete Atomic Structure of the Large Ribosomal Subunit at 2.4 Å Resolution'. *Science* 289 (5481): 905–20. https://doi.org/10.1126/science.289.5481.905.

Barden, Timothy C., Brian L. Buckwalter, Raymond T. Testa, Peter J. Petersen, and Ving J. Lee. 1994. '"Glycylcyclines". 3. 9-Aminodoxycyclinecarboxamides'. *Journal of Medicinal Chemistry* 37 (20): 3205–11. https://doi.org/10.1021/jm00046a003.

Barlam, Tamar F., Sara E. Cosgrove, Lilian M. Abbo, et al. 2016. 'Implementing an Antibiotic Stewardship Program: Guidelines by the Infectious Diseases Society of America and the Society for Healthcare Epidemiology of America'. *Clinical Infectious Diseases* 62 (10): e51–77. https://doi.org/10.1093/cid/ciw118.

Barraud, Pierre, Emmanuelle Schmitt, Yves Mechulam, Frédéric Dardel, and Carine Tisné. 2008. 'A Unique Conformation of the Anticodon Stem-Loop Is Associated with the

Capacity of tRNAfMet to Initiate Protein Synthesis'. *Nucleic Acids Research* 36 (15): 4894–901. https://doi.org/10.1093/nar/gkn462.

Barrell, B. G., A. T. Bankier, and J. Drouin. 1979. 'A Different Genetic Code in Human Mitochondria'. *Nature* 282 (5735): 189–94. https://doi.org/10.1038/282189a0.

Barrenechea, Victor, Maryhory Vargas-Reyes, Miguel Quiliano, and Pohl Milón. 2021. 'A Complementary Mechanism of Bacterial mRNA Translation Inhibition by Tetracyclines'. *Frontiers in Microbiology* 12 (June): 682682. https://doi.org/10.3389/fmicb.2021.682682.

Beckert, Bertrand, Elodie C. Leroy, Shanmugapriya Sothiselvam, et al. 2021. 'Structural and Mechanistic Basis for Translation Inhibition by Macrolide and Ketolide Antibiotics'. *Nature Communications* 12 (1): 4466. https://doi.org/10.1038/s41467-021-24674-9.

Belardinelli, Riccardo, Heena Sharma, Neva Caliskan, et al. 2016. 'Choreography of Molecular Movements during Ribosome Progression along mRNA'. *Nature Structural & Molecular Biology* 23 (4): 342–48. https://doi.org/10.1038/nsmb.3193.

Benjamini, Yoav, and Yosef Hochberg. 1995. 'Controlling the False Discovery Rate: A Practical and Powerful Approach to Multiple Testing'. *Journal of the Royal Statistical Society Series B: Statistical Methodology* 57 (1): 289–300. https://doi.org/10.1111/j.2517-6161.1995.tb02031.x.

Beringer, Malte, and Marina V. Rodnina. 2007. 'The Ribosomal Peptidyl Transferase'. *Molecular Cell* 26 (3): 311–21. https://doi.org/10.1016/j.molcel.2007.03.015.

Bernabeu, C., and J. A. Lake. 1982. 'Nascent Polypeptide Chains Emerge from the Exit Domain of the Large Ribosomal Subunit: Immune Mapping of the Nascent Chain'. *Proceedings of the National Academy of Sciences of the United States of America* 79 (10): 3111–15. https://doi.org/10.1073/pnas.79.10.3111.

Bertagnolio, Silvia, Zlatina Dobreva, Chad M. Centner, et al. 2024. 'WHO Global Research Priorities for Antimicrobial Resistance in Human Health'. *The Lancet Microbe* 5 (11): 100902. https://doi.org/10.1016/S2666-5247(24)00134-4.

Bhattacharya, Arunima, Thibaud T. Renault, and C. Axel Innis. 2024. 'The Ribosome as a Small-Molecule Sensor'. *Current Opinion in Microbiology* 77 (February): 102418. https://doi.org/10.1016/j.mib.2023.102418.

Biophysical Society., and Richard B. Roberts. 1958. *Microsomal Particles and Protein Synthesis; Papers Presented at the First Symposium of the Biophysical Society, at the Massachusetts Institute of Technology, Cambridge, February 5, 6, and 8, 1958*. Published on behalf of the Washington Academy of Sciences, Washington, D.C., by Pergamon Press. https://doi.org/10.5962/bhl.title.6261.

Biou, Valérie, Anna Yaremchuk, Michael Tukalo, and Stephen Cusack. 1994. 'The 2.9 Å Crystal Structure of *T. Thermophilus* Seryl-tRNA Synthetase Complexed with $tRNA^{Ser}$'. *Science* 263 (5152): 1404–10. https://doi.org/10.1126/science.8128220.

Björk, Glenn R. .., Johanna U. Ericson, Claes E. D. Gustafsson, Tord G. Hagervall, Yvonne H. Jönsson, and P. Mikael Wikström. 1987. 'TRANSFER RNA MODIFICATION'. *Annual Review of Biochemistry* 56 (1): 263–85. https://doi.org/10.1146/annurev.bi.56.070187.001403.

Blanchard, Scott C., Ruben L. Gonzalez, Harold D. Kim, Steven Chu, and Joseph D. Puglisi. 2004. 'tRNA Selection and Kinetic Proofreading in Translation'. *Nature Structural & Molecular Biology* 11 (10): 1008–14. https://doi.org/10.1038/nsmb831.

Blanchard, Scott C., Harold D. Kim, Ruben L. Gonzalez, Joseph D. Puglisi, and Steven Chu. 2004. 'tRNA Dynamics on the Ribosome during Translation'. *Proceedings of the National Academy of Sciences* 101 (35): 12893–98. https://doi.org/10.1073/pnas.0403884101.

Blin, Kai, Simon Shaw, Lisa Vader, et al. 2025. 'antiSMASH 8.0: Extended Gene Cluster Detection Capabilities and Analyses of Chemistry, Enzymology, and Regulation'. *Nucleic Acids Research* 53 (W1): W32–38. https://doi.org/10.1093/nar/gkaf334.

Bloudoff, Kristjan, and T. Martin Schmeing. 2017. 'Structural and Functional Aspects of the Nonribosomal Peptide Synthetase Condensation Domain Superfamily: Discovery, Dissection and Diversity'. *Biochimica et Biophysica Acta (BBA) - Proteins and Proteomics* 1865 (11): 1587–604. https://doi.org/10.1016/j.bbapap.2017.05.010.

Bock, Lars V., Christian Blau, Gunnar F. Schröder, et al. 2013. 'Energy Barriers and Driving Forces in tRNA Translocation through the Ribosome'. *Nature Structural & Molecular Biology* 20 (12): 1390–96. https://doi.org/10.1038/nsmb.2690.

Bode, Helge B. 2009. 'Entomopathogenic Bacteria as a Source of Secondary Metabolites'. *Current Opinion in Chemical Biology* 13 (2): 224–30. https://doi.org/10.1016/j.cbpa.2009.02.037.

Bohman, K., T. Ruusala, P. C. Jelenc, and C. G. Kurland. 1984. 'Kinetic Impairment of Restrictive Streptomycin-Resistant Ribosomes'. *Molecular and General Genetics MGG* 198 (1): 90–99. https://doi.org/10.1007/BF00328706.

Borg, Anneli, Michael Pavlov, and Måns Ehrenberg. 2016. 'Mechanism of Fusidic Acid Inhibition of RRF- and EF-G-Dependent Splitting of the Bacterial Post-Termination Ribosome'. *Nucleic Acids Research* 44 (7): 3264–75. https://doi.org/10.1093/nar/gkw178.

Borovinskaya, Maria A., Shinichiro Shoji, Kurt Fredrick, and Jamie H. D. Cate. 2008. 'Structural Basis for Hygromycin B Inhibition of Protein Biosynthesis'. *RNA (New York, N.Y.)* 14 (8): 1590–99. https://doi.org/10.1261/rna.1076908.

Borovinskaya, Maria A., Shinichiro Shoji, James M. Holton, Kurt Fredrick, and Jamie H. D. Cate. 2007. 'A Steric Block in Translation Caused by the Antibiotic Spectinomycin'. *ACS Chemical Biology* 2 (8): 545–52. https://doi.org/10.1021/cb700100n.

Brandi, Letizia, Attilio Fabbretti, Michele Di Stefano, Ameriga Lazzarini, Monica Abbondi, and Claudio O. Gualerzi. 2006. 'Characterization of GE82832, a Peptide Inhibitor of Translocation Interacting with Bacterial 30S Ribosomal Subunits'. *RNA (New York, N.Y.)* 12 (7): 1262–70. https://doi.org/10.1261/rna.61206.

Brandi, Letizia, Sonia Maffioli, Stefano Donadio, et al. 2012. 'Structural and Functional Characterization of the Bacterial Translocation Inhibitor GE82832'. *FEBS Letters* 586 (19): 3373–78. https://doi.org/10.1016/j.febslet.2012.07.040.

Bremer, Hans, and Patrick P. Dennis. 2008. 'Modulation of Chemical Composition and Other Parameters of the Cell at Different Exponential Growth Rates'. *EcoSal Plus* 3 (1): 10.1128/ecosal.5.2.3. https://doi.org/10.1128/ecosal.5.2.3.

Brenner, S., L. Barnett, E. R. Katz, and F. H. C. Crick. 1967. 'UGA: A Third Nonsense Triplet in the Genetic Code'. *Nature* 213 (5075): 449–50. https://doi.org/10.1038/213449a0.

Brenner, S., A. O. W. Stretton, and S. Kaplan. 1965. 'Genetic Code: The "Nonsense" Triplets for Chain Termination and Their Suppression'. *Nature* 206 (4988): 994–98. https://doi.org/10.1038/206994a0.

Brilot, Axel F., Andrei A. Korostelev, Dmitri N. Ermolenko, and Nikolaus Grigorieff. 2013. 'Structure of the Ribosome with Elongation Factor G Trapped in the Pretranslocation State'. *Proceedings of the National Academy of Sciences* 110 (52): 20994–99. https://doi.org/10.1073/pnas.1311423110.

Brodersen, D. E., W. M. Clemons Jr., A. P. Carter, R. J. Morgan-Warren, B. T. Wimberly, and V. Ramakrishnan. 2000. 'The Structural Basis for the Action of the Antibiotics Tetracycline, Pactamycin, and Hygromycin B, on the 30S Ribosomal Subunit'. *Cell* 103 (7): 1143–54. Scopus. https://doi.org/10.1016/S0092-8674(00)00216-6.

Brosius, J., T. J. Dull, and H. F. Noller. 1980. 'Complete Nucleotide Sequence of a 23S Ribosomal RNA Gene from Escherichia Coli.' *Proceedings of the National Academy of Sciences* 77 (1): 201–4. https://doi.org/10.1073/pnas.77.1.201.

Brosius, J., M. L. Palmer, P. J. Kennedy, and H. F. Noller. 1978. 'Complete Nucleotide Sequence of a 16S Ribosomal RNA Gene from Escherichia Coli.' *Proceedings of the National Academy of Sciences* 75 (10): 4801–5. https://doi.org/10.1073/pnas.75.10.4801.

Bulatov, Timur, Sebastian Gensel, Andi Mainz, et al. 2022. 'Total Synthesis and Biological Evaluation of Paenilamicins from the Honey Bee Pathogen *Paenibacillus Larvae*'. *Journal of the American Chemical Society* 144 (1): 288–96. https://doi.org/10.1021/jacs.1c09616.

Bulkley, David, Letizia Brandi, Yury S. Polikanov, et al. 2014. 'The Antibiotics Dityromycin and GE82832 Bind Protein S12 and Block EF-G-Catalyzed Translocation'. *Cell Reports* 6 (2): 357–65. https://doi.org/10.1016/j.celrep.2013.12.024.

Bulkley, David, Francis Johnson, and Thomas A. Steitz. 2012. 'The Antibiotic Thermorubin Inhibits Protein Synthesis by Binding to Inter-Subunit Bridge B2a of the Ribosome'. *Journal of Molecular Biology* 416 (4): 571–78. https://doi.org/10.1016/j.jmb.2011.12.055.

Byrgazov, Konstantin, Irina Grishkovskaya, Stefan Arenz, et al. 2015. 'Structural Basis for the Interaction of Protein S1 with the Escherichia Coli Ribosome'. *Nucleic Acids Research* 43 (1): 661–73. https://doi.org/10.1093/nar/gku1314.

Capecchi, M. R. 1967. 'Polypeptide Chain Termination in Vitro: Isolation of a Release Factor.' *Proceedings of the National Academy of Sciences* 58 (3): 1144–51. https://doi.org/10.1073/pnas.58.3.1144.

Carbone, Christine E., Anna B. Loveland, Howard B. Gamper, Ya-Ming Hou, Gabriel Demo, and Andrei A. Korostelev. 2021. 'Time-Resolved Cryo-EM Visualizes Ribosomal Translocation with EF-G and GTP'. *Nature Communications* 12 (1): 7236. https://doi.org/10.1038/s41467-021-27415-0.

Carter, A. P., W. M. Clemons, D. E. Brodersen, et al. 2001. 'Crystal Structure of an Initiation Factor Bound to the 30S Ribosomal Subunit'. *Science* (New York, N.Y.) 291 (5503): 498–501. https://doi.org/10.1126/science.1057766.

Carter, Andrew P., William M. Clemons, Ditlev E. Brodersen, Robert J. Morgan-Warren, Brian T. Wimberly, and V. Ramakrishnan. 2000. 'Functional Insights from the Structure of the 30S Ribosomal Subunit and Its Interactions with Antibiotics'. *Nature* 407 (6802): 340–48. https://doi.org/10.1038/35030019.

Chang, Bill, Saman Halgamuge, and Sen-Lin Tang. 2006. 'Analysis of SD Sequences in Completed Microbial Genomes: Non-SD-Led Genes Are as Common as SD-Led Genes'. *Gene* 373 (May): 90–99. https://doi.org/10.1016/j.gene.2006.01.033.

Chen, Bo, Sandip Kaledhonkar, Ming Sun, et al. 2015. 'Structural Dynamics of Ribosome Subunit Association Studied by Mixing-Spraying Time-Resolved Cryogenic Electron Microscopy'. *Structure* 23 (6): 1097–105. https://doi.org/10.1016/j.str.2015.04.007.

Chen, Chunlai, Xiaonan Cui, John F. Beausang, et al. 2016. 'Elongation Factor G Initiates Translocation through a Power Stroke'. *Proceedings of the National Academy of Sciences* 113 (27): 7515–20. https://doi.org/10.1073/pnas.1602668113.

Chen, Chunlai, Benjamin Stevens, Jaskarin Kaur, et al. 2011. 'Single-Molecule Fluorescence Measurements of Ribosomal Translocation Dynamics'. *Molecular Cell* 42 (3): 367–77. https://doi.org/10.1016/j.molcel.2011.03.024.

Cheng, Yifan. 2015. ‘Single-Particle Cryo-EM at Crystallographic Resolution’. *Cell* 161 (3): 450–57. https://doi.org/10.1016/j.cell.2015.03.049.

Choi, Junhong, James Marks, Jingji Zhang, et al. 2020. ‘Dynamics of the Context-Specific Translation Arrest by Chloramphenicol and Linezolid’. *Nature Chemical Biology* 16 (3): 310–17. https://doi.org/10.1038/s41589-019-0423-2.

Clark, B. F. C., and K. A. Marcker. 1966. ‘The Role of N-Formyl-Methionyl-sRNA in Protein Biosynthesis’. *Journal of Molecular Biology* 17 (2): 394-IN7. https://doi.org/10.1016/S0022-2836(66)80150-X.

Cone, J. E., R. M. Del Río, J. N. Davis, and T. C. Stadtman. 1976. ‘Chemical Characterization of the Selenoprotein Component of Clostridial Glycine Reductase: Identification of Selenocysteine as the Organoselenium Moiety’. *Proceedings of the National Academy of Sciences of the United States of America* 73 (8): 2659–63. https://doi.org/10.1073/pnas.73.8.2659.

Conover, L. H., W. T. Moreland, A. R. English, C. R. Stephens, and F. J. Pilgrim. 1953. ‘TERRAMYCIN. XI. TETRACYCLINE’. *Journal of the American Chemical Society* 75 (18): 4622–23. https://doi.org/10.1021/ja01114a537.

Cornish, Peter V., Dmitri N. Ermolenko, Harry F. Noller, and Taekjip Ha. 2008. ‘Spontaneous Intersubunit Rotation in Single Ribosomes’. *Molecular Cell* 30 (5): 578–88. https://doi.org/10.1016/j.molcel.2008.05.004.

Cornish, Peter V., Dmitri N. Ermolenko, David W. Staple, et al. 2009. ‘Following Movement of the L1 Stalk between Three Functional States in Single Ribosomes’. *Proceedings of the National Academy of Sciences* 106 (8): 2571–76. https://doi.org/10.1073/pnas.0813180106.

Cox, Georgina, and Gerard D. Wright. 2013. ‘Intrinsic Antibiotic Resistance: Mechanisms, Origins, Challenges and Solutions’. *International Journal of Medical Microbiology* 303 (6–7): 287–92. https://doi.org/10.1016/j.ijmm.2013.02.009.

Crick, F. H. 1958. ‘On Protein Synthesis’. *Symposia of the Society for Experimental Biology* 12: 138–63.

Crick, F. H. C. 1966. ‘Codon—Anticodon Pairing: The Wobble Hypothesis’. *Journal of Molecular Biology* 19 (2): 548–55. https://doi.org/10.1016/S0022-2836(66)80022-0.

Crick, F. H. C., Leslie Barnett, S. Brenner, and R. J. Watts-Tobin. 1961. ‘General Nature of the Genetic Code for Proteins’. *Nature* 192 (4809): 1227–32. https://doi.org/10.1038/1921227a0.

Crofton, J., and D. A. Mitchison. 1948. ‘Streptomycin Resistance in Pulmonary Tuberculosis’. *BMJ* 2 (4588): 1009–15. https://doi.org/10.1136/bmj.2.4588.1009.

Croll, Tristan Ian. 2018. 'ISOLDE: A Physically Realistic Environment for Model Building into Low-Resolution Electron-Density Maps'. *Acta Crystallographica. Section D, Structural Biology* 74 (Pt 6): 519–30. https://doi.org/10.1107/S2059798318002425.

Cunha, Carlos E., Riccardo Belardinelli, Frank Peske, Wolf Holtkamp, Wolfgang Wintermeyer, and Marina V. Rodnina. 2013. 'Dual Use of GTP Hydrolysis by Elongation Factor G on the Ribosome'. *Translation* 1 (1): e24315. https://doi.org/10.4161/trla.24315.

Cusack, S., A. Yaremchuk, and M. Tukalo. 2000. 'The 2 A Crystal Structure of Leucyl-tRNA Synthetase and Its Complex with a Leucyl-Adenylate Analogue'. *The EMBO Journal* 19 (10): 2351–61. https://doi.org/10.1093/emboj/19.10.2351.

Davidovich, Chen, Anat Bashan, Tamar Auerbach-Nevo, Rachel D. Yaggie, Richard R. Gontarek, and Ada Yonath. 2007. 'Induced-Fit Tightens Pleuromutilins Binding to Ribosomes and Remote Interactions Enable Their Selectivity'. *Proceedings of the National Academy of Sciences* 104 (11): 4291–96. https://doi.org/10.1073/pnas.0700041104.

Davies, Julian, and Dorothy Davies. 2010. 'Origins and Evolution of Antibiotic Resistance'. *Microbiology and Molecular Biology Reviews* 74 (3): 417–33. https://doi.org/10.1128/MMBR.00016-10.

Davis, B. D. 1987. 'Mechanism of Bactericidal Action of Aminoglycosides'. *Microbiological Reviews* 51 (3): 341–50. https://doi.org/10.1128/mr.51.3.341-350.1987.

Davis, B. D., L. L. Chen, and P. C. Tai. 1986. 'Misread Protein Creates Membrane Channels: An Essential Step in the Bactericidal Action of Aminoglycosides.' *Proceedings of the National Academy of Sciences* 83 (16): 6164–68. https://doi.org/10.1073/pnas.83.16.6164.

Daviter, Tina, Hans-Joachim Wieden, and Marina V. Rodnina. 2003. 'Essential Role of Histidine 84 in Elongation Factor Tu for the Chemical Step of GTP Hydrolysis on the Ribosome'. *Journal of Molecular Biology* 332 (3): 689–99. https://doi.org/10.1016/S0022-2836(03)00947-1.

Deeks, Emma D. 2019. 'Sarecycline: First Global Approval'. *Drugs* 79 (3): 325–29. https://doi.org/10.1007/s40265-019-1053-4.

Demeshkina, Natalia, Lasse Jenner, Eric Westhof, Marat Yusupov, and Gulnara Yusupova. 2012. 'A New Understanding of the Decoding Principle on the Ribosome'. *Nature* 484 (7393): 256–59. https://doi.org/10.1038/nature10913.

Diaconu, Mihaela, Ute Kothe, Frank Schlünzen, et al. 2005. 'Structural Basis for the Function of the Ribosomal L7/12 Stalk in Factor Binding and GTPase Activation'. *Cell* 121 (7): 991–1004. https://doi.org/10.1016/j.cell.2005.04.015.

Doctor, B. P., Jean Apgar, and Robert W. Holley. 1961. 'Fractionation of Yeast Amino Acid-Acceptor Ribonucleic Acids by Countercurrent Distribution'. *Journal of Biological Chemistry* 236 (4): 1117–20. https://doi.org/10.1016/S0021-9258(18)64251-6.

Domagk, Gerhard. 1935. 'Ein Beitrag zur Chemotherapie der bakteriellen Infektionen'. *DMW - Deutsche Medizinische Wochenschrift* 61 (07): 250–53. https://doi.org/10.1055/s-0028-1129486.

Duggar, B. M. 1948. 'AUREOMYCIN: A PRODUCT OF THE CONTINUING SEARCH FOR NEW ANTIBIOTICS'. *Annals of the New York Academy of Sciences* 51 (2): 177–81. https://doi.org/10.1111/j.1749-6632.1948.tb27262.x.

Dunin-Horkawicz, S. 2006. 'MODOMICS: A Database of RNA Modification Pathways'. *Nucleic Acids Research* 34 (90001): D145–49. https://doi.org/10.1093/nar/gkj084.

Dunkle, Jack A., Leyi Wang, Michael B. Feldman, et al. 2011. 'Structures of the Bacterial Ribosome in Classical and Hybrid States of tRNA Binding'. *Science* (New York, N.Y.) 332 (6032): 981–84. https://doi.org/10.1126/science.1202692.

Duval, Mélodie, Alexey Korepanov, Olivier Fuchsbauer, et al. 2013. 'Escherichia Coli Ribosomal Protein S1 Unfolds Structured mRNAs Onto the Ribosome for Active Translation Initiation'. *PLoS Biology* 11 (12): e1001731. https://doi.org/10.1371/journal.pbio.1001731.

Duval, Mélodie, Angelita Simonetti, Isabelle Caldelari, and Stefano Marzi. 2015. 'Multiple Ways to Regulate Translation Initiation in Bacteria: Mechanisms, Regulatory Circuits, Dynamics'. *Biochimie* 114 (July): 18–29. https://doi.org/10.1016/j.biochi.2015.03.007.

Ehrlich, P. 1913. 'Address in Pathology, ON CHEMIOTHERAPY: Delivered before the Seventeenth International Congress of Medicine'. *British Medical Journal* 2 (2746): 353–59. https://doi.org/10.1136/bmj.2.2746.353.

Erlacher, Matthias D., Kathrin Lang, Nisha Shankaran, et al. 2005. 'Chemical Engineering of the Peptidyl Transferase Center Reveals an Important Role of the 2'-Hydroxyl Group of A2451'. *Nucleic Acids Research* 33 (5): 1618–27. https://doi.org/10.1093/nar/gki308.

Erlacher, Matthias D., Kathrin Lang, Brigitte Wotzel, Renate Rieder, Ronald Micura, and Norbert Polacek. 2006. 'Efficient Ribosomal Peptidyl Transfer Critically Relies on the Presence of the Ribose 2'-OH at A2451 of 23S rRNA'. *Journal of the American Chemical Society* 128 (13): 4453–59. https://doi.org/10.1021/ja0588454.

Ermolenko, Dmitri N., Zigurts K. Majumdar, Robyn P. Hickerson, P. Clint Spiegel, Robert M. Clegg, and Harry F. Noller. 2007. 'Observation of Intersubunit Movement of the Ribosome in Solution Using FRET'. *Journal of Molecular Biology* 370 (3): 530–40. https://doi.org/10.1016/j.jmb.2007.04.042.

Ermolenko, Dmitri N., and Harry F. Noller. 2011. ‘mRNA Translocation Occurs during the Second Step of Ribosomal Intersubunit Rotation’. *Nature Structural & Molecular Biology* 18 (4): 457–62. https://doi.org/10.1038/nsmb.2011.

Ermolenko, Dmitri N., P. Clint Spiegel, Zigurts K. Majumdar, Robyn P. Hickerson, Robert M. Clegg, and Harry F. Noller. 2007. ‘The Antibiotic Viomycin Traps the Ribosome in an Intermediate State of Translocation’. *Nature Structural & Molecular Biology* 14 (6): 493–97. https://doi.org/10.1038/nsmb1243.

Ewing, B., L. Hillier, M. C. Wendl, and P. Green. 1998. ‘Base-Calling of Automated Sequencer Traces Using Phred. I. Accuracy Assessment’. *Genome Research* 8 (3): 175–85. https://doi.org/10.1101/gr.8.3.175.

Ewing, Brent, and Phil Green. 1998. ‘Base-Calling of Automated Sequencer Traces Using *Phred.* II. Error Probabilities’. *Genome Research* 8 (3): 186–94. https://doi.org/10.1101/gr.8.3.186.

Fabbretti, Attilio, Cynthia L. Pon, Scott P. Hennelly, Walter E. Hill, J. Stephen Lodmell, and Claudio O. Gualerzi. 2007. ‘The Real-Time Path of Translation Factor IF3 onto and off the Ribosome’. *Molecular Cell* 25 (2): 285–96. https://doi.org/10.1016/j.molcel.2006.12.011.

Fei, Jingyi, Jonathan E. Bronson, Jake M. Hofman, Rathi L. Srinivas, Chris H. Wiggins, and Ruben L. Gonzalez. 2009. ‘Allosteric Collaboration between Elongation Factor G and the Ribosomal L1 Stalk Directs tRNA Movements during Translation’. *Proceedings of the National Academy of Sciences* 106 (37): 15702–7. https://doi.org/10.1073/pnas.0908077106.

Fei, Jingyi, Pallav Kosuri, Daniel D. MacDougall, and Ruben L. Gonzalez. 2008. ‘Coupling of Ribosomal L1 Stalk and tRNA Dynamics during Translation Elongation’. *Molecular Cell* 30 (3): 348–59. https://doi.org/10.1016/j.molcel.2008.03.012.

Feldman, Michael B., Daniel S. Terry, Roger B. Altman, and Scott C. Blanchard. 2010. ‘Aminoglycoside Activity Observed on Single Pre-Translocation Ribosome Complexes’. *Nature Chemical Biology* 6 (1): 54–62. https://doi.org/10.1038/nchembio.274.

Fischer, Niels, Andrey L. Konevega, Wolfgang Wintermeyer, Marina V. Rodnina, and Holger Stark. 2010. ‘Ribosome Dynamics and tRNA Movement by Time-Resolved Electron Cryomicroscopy’. *Nature* 466 (7304): 329–33. https://doi.org/10.1038/nature09206.

Fleming, Alexander. 1929. ‘On the Antibacterial Action of Cultures of a Penicillium, with Special Reference to Their Use in the Isolation of B. Influenzae’. *The British Journal of Experimental Pathology* 10 (3): 226–36.

Forst, Steven, Barbara Dowds, Noël Boemare, and Erko Stackebrandt. 1997. '*XENORHABDUS* AND *PHOTORHABDUS* SPP.: Bugs That Kill Bugs'. *Annual Review of Microbiology* 51 (1): 47–72. https://doi.org/10.1146/annurev.micro.51.1.47.

Fourmy, D., M. I. Recht, S. C. Blanchard, and J. D. Puglisi. 1996. 'Structure of the A Site of Escherichia Coli 16S Ribosomal RNA Complexed with an Aminoglycoside Antibiotic'. *Science* (New York, N.Y.) 274 (5291): 1367–71. https://doi.org/10.1126/science.274.5291.1367.

Frank, Joachim. 2016. 'Generalized Single-Particle Cryo-EM--a Historical Perspective'. *Microscopy* (Oxford, England) 65 (1): 3–8. https://doi.org/10.1093/jmicro/dfv358.

Frank, Joachim, and Rajendra Kumar Agrawal. 2000. 'A Ratchet-like Inter-Subunit Reorganization of the Ribosome during Translocation'. *Nature* 406 (6793): 318–22. https://doi.org/10.1038/35018597.

Frank, Joachim, Haixiao Gao, Jayati Sengupta, Ning Gao, and Derek J. Taylor. 2007. 'The Process of mRNA–tRNA Translocation'. *Proceedings of the National Academy of Sciences* 104 (50): 19671–78. https://doi.org/10.1073/pnas.0708517104.

Frank, Joachim, Jun Zhu, Pawel Penczek, et al. 1995. 'A Model of Protein Synthesis Based on Cryo-Electron Microscopy of the E. Coli Ribosome'. *Nature* 376 (6539): 441–44. https://doi.org/10.1038/376441a0.

Freistroffer, David V., Michael Yu. Pavlov, Jane MacDougall, Richard H. Buckingham, and Måns Ehrenberg. 1997. 'Release Factor RF3 in E.Coli Accelerates the Dissociation of Release Factors RF1 and RF2 from the Ribosome in a GTP-Dependent Manner'. *The EMBO Journal* 16 (13): 4126–33. https://doi.org/10.1093/emboj/16.13.4126.

Fromm, Simon A., Kate M. O'Connor, Michael Purdy, et al. 2023. 'The Translating Bacterial Ribosome at 1.55 Å Resolution Generated by Cryo-EM Imaging Services'. *Nature Communications* 14 (1): 1095. https://doi.org/10.1038/s41467-023-36742-3.

Fu, Ziao, Gabriele Indrisiunaite, Sandip Kaledhonkar, et al. 2019. 'The Structural Basis for Release-Factor Activation during Translation Termination Revealed by Time-Resolved Cryogenic Electron Microscopy'. *Nature Communications* 10 (1): 2579. https://doi.org/10.1038/s41467-019-10608-z.

Fu, Ziao, Sandip Kaledhonkar, Anneli Borg, et al. 2016. 'Key Intermediates in Ribosome Recycling Visualized by Time-Resolved Cryoelectron Microscopy'. *Structure* (London, England : 1993) 24 (12): 2092–101. https://doi.org/10.1016/j.str.2016.09.014.

Gao, Haixiao, Zhihong Zhou, Urmila Rawat, et al. 2007. 'RF3 Induces Ribosomal Conformational Changes Responsible for Dissociation of Class I Release Factors'. *Cell* 129 (5): 929–41. https://doi.org/10.1016/j.cell.2007.03.050.

Gao, Ning, Andrey V. Zavialov, Wen Li, et al. 2005. 'Mechanism for the Disassembly of the Posttermination Complex Inferred from Cryo-EM Studies'. *Molecular Cell* 18 (6): 663–74. https://doi.org/10.1016/j.molcel.2005.05.005.

Gao, Yong-Gui, Maria Selmer, Christine M. Dunham, Albert Weixlbaumer, Ann C. Kelley, and V. Ramakrishnan. 2009. 'The Structure of the Ribosome with Elongation Factor G Trapped in the Posttranslocational State'. *Science* 326 (5953): 694–99. https://doi.org/10.1126/science.1179709.

Garofalo, Raffaella, Ingo Wohlgemuth, Michael Pearson, Christof Lenz, Henning Urlaub, and Marina V. Rodnina. 2019. 'Broad Range of Missense Error Frequencies in Cellular Proteins'. *Nucleic Acids Research* 47 (6): 2932–45. https://doi.org/10.1093/nar/gky1319.

Gavrilova, L. P., and A. S. Spirin. 1971. 'Stimulation of "Non-Enzymic" Translocation in Ribosomes by p-Chloromercuribenzoate'. *FEBS Letters* 17 (2): 324–26. https://doi.org/10.1016/0014-5793(71)80177-1.

Geggier, Peter, Richa Dave, Michael B. Feldman, et al. 2010. 'Conformational Sampling of Aminoacyl-tRNA during Selection on the Bacterial Ribosome'. *Journal of Molecular Biology* 399 (4): 576–95. https://doi.org/10.1016/j.jmb.2010.04.038.

Giege, R., M. Sissler, and C. Florentz. 1998. 'Universal Rules and Idiosyncratic Features in tRNA Identity'. *Nucleic Acids Research* 26 (22): 5017–35. https://doi.org/10.1093/nar/26.22.5017.

Gilchrist, Cameron L. M., and Yit-Heng Chooi. 2021. 'Clinker & Clustermap.Js: Automatic Generation of Gene Cluster Comparison Figures'. *Bioinformatics* 37 (16): 2473–75. https://doi.org/10.1093/bioinformatics/btab007.

Gillard, Mélanie, Thibaud T. Renault, and C. Axel Innis. 2026. 'iTP-Seq: A Scalable Profiling Workflow to Characterize Bacterial Translation Landscapes in Vitro'. *Nature Protocols*, ahead of print, January 15. https://doi.org/10.1038/s41596-025-01294-x.

Girodat, Dylan, Hans-Joachim Wieden, Scott C. Blanchard, and Karissa Y. Sanbonmatsu. 2023. 'Geometric Alignment of Aminoacyl-tRNA Relative to Catalytic Centers of the Ribosome Underpins Accurate mRNA Decoding'. *Nature Communications* 14 (1): 5582. https://doi.org/10.1038/s41467-023-40404-9.

Glaub, Alina, Christopher Huptas, Klaus Neuhaus, and Zachary Ardern. 2020. 'Recommendations for Bacterial Ribosome Profiling Experiments Based on Bioinformatic Evaluation of Published Data'. *Journal of Biological Chemistry* 295 (27): 8999–9011. https://doi.org/10.1074/jbc.RA119.012161.

Goddard, Thomas D., Conrad C. Huang, Elaine C. Meng, et al. 2018. 'UCSF ChimeraX: Meeting Modern Challenges in Visualization and Analysis'. *Protein Science: A Publication of the Protein Society* 27 (1): 14–25. https://doi.org/10.1002/pro.3235.

Gorini, L., G. A. Jacoby, and L. Breckenridge. 1966. 'Ribosomal Ambiguity'. *Cold Spring Harbor Symposia on Quantitative Biology* 31 (0): 657–64. https://doi.org/10.1101/SQB.1966.031.01.084.

Goyal, Akanksha, Riccardo Belardinelli, Cristina Maracci, Pohl Milón, and Marina V. Rodnina. 2015. 'Directional Transition from Initiation to Elongation in Bacterial Translation'. *Nucleic Acids Research* 43 (22): 10700–10712. https://doi.org/10.1093/nar/gkv869.

Goyal, Akanksha, Riccardo Belardinelli, and Marina V. Rodnina. 2017. 'Non-Canonical Binding Site for Bacterial Initiation Factor 3 on the Large Ribosomal Subunit'. *Cell Reports* 20 (13): 3113–22. https://doi.org/10.1016/j.celrep.2017.09.012.

Grentzmann, Guido, Dominique Brechemier-Baey, Valerie Heurgué-Hamard, and Richard H. Buckingham. 1995. 'Function of Polypeptide Chain Release Factor RF-3 in Escherichia Coli'. *Journal of Biological Chemistry* 270 (18): 10595–600. https://doi.org/10.1074/jbc.270.18.10595.

Grigoriadou, Christina, Stefano Marzi, Dongli Pan, Claudio O. Gualerzi, and Barry S. Cooperman. 2007. 'The Translational Fidelity Function of IF3 during Transition from the 30 S Initiation Complex to the 70 S Initiation Complex'. *Journal of Molecular Biology* 373 (3): 551–61. https://doi.org/10.1016/j.jmb.2007.07.031.

Grill, S., C. O. Gualerzi, P. Londei, and U. Bläsi. 2000. 'Selective Stimulation of Translation of Leaderless mRNA by Initiation Factor 2: Evolutionary Implications for Translation'. *The EMBO Journal* 19 (15): 4101–10. https://doi.org/10.1093/emboj/19.15.4101.

Gromadski, Kirill B., and Marina V. Rodnina. 2004. 'Kinetic Determinants of High-Fidelity tRNA Discrimination on the Ribosome'. *Molecular Cell* 13 (2): 191–200. https://doi.org/10.1016/s1097-2765(04)00005-x.

Grossman, Trudy H. 2016. 'Tetracycline Antibiotics and Resistance'. *Cold Spring Harbor Perspectives in Medicine* 6 (4): a025387. https://doi.org/10.1101/cshperspect.a025387.

Grunberg-Manago, M., P. Dessen, D. Pantaloni, T. Godefroy-Colburn, A. D. Wolfe, and J. Dondon. 1975. 'Light-Scattering Studies Showing the Effect of Initiation Factors on the Reversible Dissociation of Escherichia Coli Ribosomes'. *Journal of Molecular Biology* 94 (3): 461–78. https://doi.org/10.1016/0022-2836(75)90215-6.

Gualtieri, Maxime, André Aumelas, and Jacques-Olivier Thaler. 2009. 'Identification of a New Antimicrobial Lysine-Rich Cyclolipopeptide Family from Xenorhabdus Nematophila'. *The Journal of Antibiotics* 62 (6): 295–302. https://doi.org/10.1038/ja.2009.31.

GUALTIERI, Maxime, RACINE, Emilie, VILLAIN-GUILLOT, Philippe, et al. 2024. NEW ODILORHABDINS ANALOGUES AS ANTIBIOTICS AGAINST MULTI-RESISTANT BACTERIA. Patent WO/2024/200838, filed 29 March 2024, and issued 10 March 2024. https://patentscope.wipo.int/search/en/detail.jsf?docId=WO2024200838.

Gualtieri, Maxime, Philippe Villain-Guillot, Alan Givaudan, and Sylvie Pages. 2016. Peptide derivatives as antibiotics. U.S. Patent and Trademark Office (USPTO) Patent US 9,260,481 B2, filed 28 September 2012, and issued 16 February 2016.

Guo, Zhuojun, and Harry F. Noller. 2012. 'Rotation of the Head of the 30S Ribosomal Subunit during mRNA Translocation'. *Proceedings of the National Academy of Sciences of the United States of America* 109 (50): 20391–94. https://doi.org/10.1073/pnas.1218999109.

Haas, L. F. 1999. 'Papyrus of Ebers and Smith'. *Journal of Neurology, Neurosurgery & Psychiatry* 67 (5): 578–578. https://doi.org/10.1136/jnnp.67.5.578.

Hao, Bing, Weimin Gong, Tsuneo K. Ferguson, Carey M. James, Joseph A. Krzycki, and Michael K. Chan. 2002. 'A New UAG-Encoded Residue in the Structure of a Methanogen Methyltransferase'. *Science* (New York, N.Y.) 296 (5572): 1462–66. https://doi.org/10.1126/science.1069556.

Hartz, Dieter, David S. McPheeters, Robert Traut, and Larry Gold. 1988. '[27] Extension Inhibition Analysis of Translation Initiation Complexes'. In *Methods in Enzymology*, vol. 164. Elsevier. https://doi.org/10.1016/S0076-6879(88)64058-4.

Hassan, Asem, Sandra Byju, Frederico Campos Freitas, et al. 2023. 'Ratchet, Swivel, Tilt and Roll: A Complete Description of Subunit Rotation in the Ribosome'. *Nucleic Acids Research* 51 (2): 919–34. https://doi.org/10.1093/nar/gkac1211.

Hausner, Thomas-Peter, Johannes Atmadja, and Knud H. Nierhaus. 1987. 'Evidence That the G2661 Region of 23S rRNA Is Located at the Ribosomal Binding Sites of Both Elongation Factors'. *Biochimie* 69 (9): 911–23. https://doi.org/10.1016/0300-9084(87)90225-2.

Herrero del Valle, Alba, and C. Axel Innis. 2020. 'Prospects for Antimicrobial Development in the Cryo-EM Era – a Focus on the Ribosome'. *FEMS Microbiology Reviews* 44 (6): 793–803. https://doi.org/10.1093/femsre/fuaa032.

Hirashima, Akikazu, and Akira Kaji. 1970. 'Factor Dependent Breakdown of Polysomes'. *Biochemical and Biophysical Research Communications* 41 (4): 877–83. https://doi.org/10.1016/0006-291X(70)90165-8.

Hirashima, Akikazu, and Akira Kaji. 1972. 'Factor-Dependent Release of Ribosomes from Messenger RNA'. *Journal of Molecular Biology* 65 (1): 43–58. https://doi.org/10.1016/0022-2836(72)90490-1.

Hirashima, Akikazu, and Akira Kaji. 1973. 'Role of Elongation Factor G and a Protein Factor on the Release of Ribosomes from Messenger Ribonucleic Acid'. *Journal of Biological Chemistry* 248 (21): 7580–87. https://doi.org/10.1016/S0021-9258(19)43330-9.

Hoagland, M. B., M. L. Stephenson, J. F. Scott, L. I. Hecht, and P. C. Zamecnik. 1958. 'A Soluble Ribonucleic Acid Intermediate in Protein Synthesis'. *The Journal of Biological Chemistry* 231 (1): 241–57.

Holley, Robert W., Jean Apgar, George A. Everett, et al. 1965. 'Structure of a Ribonucleic Acid'. *Science* 147 (3664): 1462–65. https://doi.org/10.1126/science.147.3664.1462.

Holm, Mikael, Anneli Borg, Måns Ehrenberg, and Suparna Sanyal. 2016. 'Molecular Mechanism of Viomycin Inhibition of Peptide Elongation in Bacteria'. *Proceedings of the National Academy of Sciences of the United States of America* 113 (4): 978–83. https://doi.org/10.1073/pnas.1517541113.

Holm, Mikael, Chandra Sekhar Mandava, Måns Ehrenberg, and Suparna Sanyal. 2019. 'The Mechanism of Error Induction by the Antibiotic Viomycin Provides Insight into the Fidelity Mechanism of Translation'. *eLife* 8 (June): e46124. https://doi.org/10.7554/eLife.46124.

Holtkamp, Wolf, Wolfgang Wintermeyer, and Marina V. Rodnina. 2014. 'Synchronous tRNA Movements during Translocation on the Ribosome Are Orchestrated by Elongation Factor G and GTP Hydrolysis'. *BioEssays* 36 (10): 908–18. https://doi.org/10.1002/bies.201400076.

Honeyman, Laura, Mohamed Ismail, Mark L. Nelson, et al. 2015. 'Structure-Activity Relationship of the Aminomethylcyclines and the Discovery of Omadacycline'. *Antimicrobial Agents and Chemotherapy* 59 (11): 7044–53. https://doi.org/10.1128/AAC.01536-15.

Hopfield, J. J. 1974. 'Kinetic Proofreading: A New Mechanism for Reducing Errors in Biosynthetic Processes Requiring High Specificity'. *Proceedings of the National Academy of Sciences* 71 (10): 4135–39. https://doi.org/10.1073/pnas.71.10.4135.

Hopfield, J. J., T. Yamane, V. Yue, and S. M. Coutts. 1976. 'Direct Experimental Evidence for Kinetic Proofreading in Amino Acylation of tRNAIle'. *Proceedings of the National Academy of Sciences of the United States of America* 73 (4): 1164–68. https://doi.org/10.1073/pnas.73.4.1164.

Horan, Lucas H., and Harry F. Noller. 2007. 'Intersubunit Movement Is Required for Ribosomal Translocation'. *Proceedings of the National Academy of Sciences* 104 (12): 4881–85. https://doi.org/10.1073/pnas.0700762104.

Hussain, Tanweer, Jose L. Llácer, Brian T. Wimberly, Jeffrey S. Kieft, and V. Ramakrishnan. 2016. 'Large-Scale Movements of IF3 and tRNA during Bacterial Translation Initiation'. *Cell* 167 (1): 133-144.e13. https://doi.org/10.1016/j.cell.2016.08.074.

Hutchings, Matthew I., Andrew W. Truman, and Barrie Wilkinson. 2019. 'Antibiotics: Past, Present and Future'. *Current Opinion in Microbiology* 51 (October): 72–80. https://doi.org/10.1016/j.mib.2019.10.008.

Ibba, Michael, and Dieter Söll. 2000. 'Aminoacyl-tRNA Synthesis'. *Annual Review of Biochemistry* 69 (1): 617–50. https://doi.org/10.1146/annurev.biochem.69.1.617.

Ingolia, Nicholas T., Sina Ghaemmaghami, John R. S. Newman, and Jonathan S. Weissman. 2009. 'Genome-Wide Analysis in Vivo of Translation with Nucleotide Resolution Using Ribosome Profiling'. *Science* (New York, N.Y.) 324 (5924): 218–23. https://doi.org/10.1126/science.1168978.

Ingolia, Nicholas T., Jeffrey A. Hussmann, and Jonathan S. Weissman. 2019. 'Ribosome Profiling: Global Views of Translation'. *Cold Spring Harbor Perspectives in Biology* 11 (5): a032698. https://doi.org/10.1101/cshperspect.a032698.

Ito, K., M. Uno, and Y. Nakamura. 2000. 'A Tripeptide "anticodon" Deciphers Stop Codons in Messenger RNA'. *Nature* 403 (6770): 680–84. https://doi.org/10.1038/35001115.

Ito, Koreaki, and Shinobu Chiba. 2013. 'Arrest Peptides: *Cis* -Acting Modulators of Translation'. *Annual Review of Biochemistry* 82 (1): 171–202. https://doi.org/10.1146/annurev-biochem-080211-105026.

Jangra, Manoj, Dmitrii Y. Travin, Elena V. Aleksandrova, et al. 2025. 'A Broad-Spectrum Lasso Peptide Antibiotic Targeting the Bacterial Ribosome'. *Nature* 640 (8060): 1022–30. https://doi.org/10.1038/s41586-025-08723-7.

Janosi, L. 1998. 'Evidence for Invivo Ribosome Recycling, the Fourth Step in Protein Biosynthesis'. *The EMBO Journal* 17 (4): 1141–51. https://doi.org/10.1093/emboj/17.4.1141.

Jenner, Lasse, Agata L. Starosta, Daniel S. Terry, et al. 2013. 'Structural Basis for Potent Inhibitory Activity of the Antibiotic Tigecycline during Protein Synthesis'. *Proceedings of the National Academy of Sciences* 110 (10): 3812–16. https://doi.org/10.1073/pnas.1216691110.

Jesús Cabañas, María, David Vázquez, and Juan Modolell. 1978. 'Inhibition of Ribosomal Translocation by Aminoglycoside Antibiotics'. *Biochemical and Biophysical Research Communications* 83 (3): 991–97. https://doi.org/10.1016/0006-291X(78)91493-6.

Jevons, M. Patricia. 1961. '"Celbenin" - Resistant Staphylococci'. *British Medical Journal* 1 (5219): 124–25.

Jin, Hong, Ann C. Kelley, David Loakes, and V. Ramakrishnan. 2010. 'Structure of the 70S Ribosome Bound to Release Factor 2 and a Substrate Analog Provides Insights into Catalysis of Peptide Release'. *Proceedings of the National Academy of Sciences* 107 (19): 8593–98. https://doi.org/10.1073/pnas.1003995107.

Johansson, Magnus, Martin Lovmar, and Måns Ehrenberg. 2008. 'Rate and Accuracy of Bacterial Protein Synthesis Revisited'. *Current Opinion in Microbiology* 11 (2): 141–47. https://doi.org/10.1016/j.mib.2008.02.015.

Johansson, Magnus, Jingji Zhang, and Måns Ehrenberg. 2012. 'Genetic Code Translation Displays a Linear Trade-off between Efficiency and Accuracy of tRNA Selection'. *Proceedings of the National Academy of Sciences* 109 (1): 131–36. https://doi.org/10.1073/pnas.1116480109.

Julián, Patricia, Andrey L. Konevega, Sjors H. W. Scheres, et al. 2008. 'Structure of Ratcheted Ribosomes with tRNAs in Hybrid States'. *Proceedings of the National Academy of Sciences* 105 (44): 16924–27. https://doi.org/10.1073/pnas.0809587105.

Julián, Patricia, Pohl Milon, Xabier Agirrezabala, et al. 2011. 'The Cryo-EM Structure of a Complete 30S Translation Initiation Complex from Escherichia Coli'. *PLoS Biology* 9 (7): e1001095. https://doi.org/10.1371/journal.pbio.1001095.

Kaji, Hideko, and Akira Kaji. 1964. 'SPECIFIC BINDING OF sRNA WITH THE TEMPLATE-RIBOSOME COMPLEX'. *Proceedings of the National Academy of Sciences* 52 (6): 1541–47. https://doi.org/10.1073/pnas.52.6.1541.

Kaledhonkar, Sandip, Ziao Fu, Kelvin Caban, et al. 2019. 'Late Steps in Bacterial Translation Initiation Visualized Using Time-Resolved Cryo-EM'. *Nature* 570 (7761): 400–404. https://doi.org/10.1038/s41586-019-1249-5.

Kannan, Krishna, Pinal Kanabar, David Schryer, et al. 2014. 'The General Mode of Translation Inhibition by Macrolide Antibiotics'. *Proceedings of the National Academy of Sciences* 111 (45): 15958–63. https://doi.org/10.1073/pnas.1417334111.

Kannan, Krishna, Nora Vázquez-Laslop, and Alexander S. Mankin. 2012. 'Selective Protein Synthesis by Ribosomes with a Drug-Obstructed Exit Tunnel'. *Cell* 151 (3): 508–20. https://doi.org/10.1016/j.cell.2012.09.018.

Karimi, Reza, and Måns Ehrenberg. 1994. 'Dissociation Rate of Cognate Peptidyl-tRNA from the A-Site of Hyper-Accurate and Error-Prone Ribosomes'. *European Journal of Biochemistry* 226 (2): 355–60. https://doi.org/10.1111/j.1432-1033.1994.tb20059.x.

Karimi, Reza, Michael Y. Pavlov, Richard H. Buckingham, and Måns Ehrenberg. 1999. 'Novel Roles for Classical Factors at the Interface between Translation Termination and Initiation'. *Molecular Cell* 3 (5): 601–9. https://doi.org/10.1016/S1097-2765(00)80353-6.

Kaur, Manpreet, Dmitrii Y. Travin, Max J. Berger, et al. 2026. 'A Natural Depsipeptide Antibiotic Binds the E-Site of the Bacterial Ribosome'. *Nature* 655 (8123): 737–46. https://doi.org/10.1038/s41586-026-10589-2.

Khaitovich, Philipp, Alexander S. Mankin, Rachel Green, Laura Lancaster, and Harry F. Noller. 1999. 'Characterization of Functionally Active Subribosomal Particles from *Thermus Aquaticus*'. *Proceedings of the National Academy of Sciences* 96 (1): 85–90. https://doi.org/10.1073/pnas.96.1.85.

Kim, S. H., G. J. Quigley, F. L. Suddath, et al. 1973. 'Three-Dimensional Structure of Yeast Phenylalanine Transfer RNA: Folding of the Polynucleotide Chain'. *Science* 179 (4070): 285–88. https://doi.org/10.1126/science.179.4070.285.

Kim, S. H., J. L. Sussman, F. L. Suddath, et al. 1974. 'The General Structure of Transfer RNA Molecules'. *Proceedings of the National Academy of Sciences* 71 (12): 4970–74. https://doi.org/10.1073/pnas.71.12.4970.

Kirchner, Sebastian, Zhiwei Cai, Robert Rauscher, et al. 2017. 'Alteration of Protein Function by a Silent Polymorphism Linked to tRNA Abundance'. *PLOS Biology* 15 (5): e2000779. https://doi.org/10.1371/journal.pbio.2000779.

Kirchner, Sebastian, Robert Rauscher, Andreas Czech, and Zoya Ignatova. 2017. 'Microarray-Based Quantification of Cellular tRNAs V1'. Preprint, March 24. https://doi.org/10.17504/protocols.io.hfcb3iw.

Kohanski, Michael A., Daniel J. Dwyer, Jamey Wierzbowski, Guillaume Cottarel, and James J. Collins. 2008. 'Mistranslation of Membrane Proteins and Two-Component System Activation Trigger Antibiotic-Mediated Cell Death'. *Cell* 135 (4): 679–90. https://doi.org/10.1016/j.cell.2008.09.038.

Koller, Timm O., Max J. Berger, Martino Morici, et al. 2024. 'Paenilamicins Are Context-Specific Translocation Inhibitors of Protein Synthesis'. *Nature Chemical Biology* 20 (12): 1691–700. https://doi.org/10.1038/s41589-024-01752-9.

Korczak, Lukasz, Piotr Majewski, Dominika Iwaniuk, et al. 2024. 'Molecular Mechanisms of Tigecycline-Resistance among Enterobacterales'. *Frontiers in Cellular and Infection Microbiology* 14 (April): 1289396. https://doi.org/10.3389/fcimb.2024.1289396.

Korostelev, Andrei A. 2022. 'The Structural Dynamics of Translation'. *Annual Review of Biochemistry* 91 (June): 245–67. https://doi.org/10.1146/annurev-biochem-071921-122857.

Korostelev, Andrei, Haruichi Asahara, Laura Lancaster, et al. 2008. 'Crystal Structure of a Translation Termination Complex Formed with Release Factor RF2'. *Proceedings of the National Academy of Sciences* 105 (50): 19684–89. https://doi.org/10.1073/pnas.0810953105.

Korostelev, Andrei, Sergei Trakhanov, Martin Laurberg, and Harry F. Noller. 2006. 'Crystal Structure of a 70S Ribosome-tRNA Complex Reveals Functional Interactions and Rearrangements'. *Cell* 126 (6): 1065–77. https://doi.org/10.1016/j.cell.2006.08.032.

Korostelev, Andrei, Jianyu Zhu, Haruichi Asahara, and Harry F. Noller. 2010. 'Recognition of the Amber UAG Stop Codon by Release Factor RF1'. *The EMBO Journal* 29 (15): 2577–85. https://doi.org/10.1038/emboj.2010.139.

Kothe, Ute, and Marina V. Rodnina. 2006. 'Delayed Release of Inorganic Phosphate from Elongation Factor Tu Following GTP Hydrolysis on the Ribosome'. *Biochemistry* 45 (42): 12767–74. https://doi.org/10.1021/bi061192z.

Kothe, Ute, Hans-Joachim Wieden, Dagmar Mohr, and Marina V. Rodnina. 2004. 'Interaction of Helix D of Elongation Factor Tu with Helices 4 and 5 of Protein L7/12 on the Ribosome'. *Journal of Molecular Biology* 336 (5): 1011–21. https://doi.org/10.1016/j.jmb.2003.12.080.

Koutmou, Kristin S., Megan E. McDonald, Julie L. Brunelle, and Rachel Green. 2014. 'RF3:GTP Promotes Rapid Dissociation of the Class 1 Termination Factor'. *RNA* 20 (5): 609–20. https://doi.org/10.1261/rna.042523.113.

Krause, Kevin M., Alisa W. Serio, Timothy R. Kane, and Lynn E. Connolly. 2016. 'Aminoglycosides: An Overview'. *Cold Spring Harbor Perspectives in Medicine* 6 (6): a027029. https://doi.org/10.1101/cshperspect.a027029.

Krishnan, Karthik M., William J. Van Etten, and Gary R. Janssen. 2010. 'Proximity of the Start Codon to a Leaderless mRNA's 5' Terminus Is a Strong Positive Determinant of Ribosome Binding and Expression in Escherichia Coli'. *Journal of Bacteriology* 192 (24): 6482–85. https://doi.org/10.1128/JB.00756-10.

Kuhlenkoetter, Stephan, Wolfgang Wintermeyer, and Marina V. Rodnina. 2011. 'Different Substrate-Dependent Transition States in the Active Site of the Ribosome'. *Nature* 476 (7360): 351–54. https://doi.org/10.1038/nature10247.

Kurland, C. G. 1960. 'Molecular Characterization of Ribonucleic Acid from Escherichia Coli Ribosomes'. *Journal of Molecular Biology* 2 (2): 83–91. https://doi.org/10.1016/S0022-2836(60)80029-0.

Kurland, C. G. 1992. 'Translational Accuracy and the Fitness of Bacteria'. *Annual Review of Genetics* 26: 29–50. https://doi.org/10.1146/annurev.ge.26.120192.000333.

Lancaster, Laura, and Harry F. Noller. 2005. 'Involvement of 16S rRNA Nucleotides G1338 and A1339 in Discrimination of Initiator tRNA'. *Molecular Cell* 20 (4): 623–32. https://doi.org/10.1016/j.molcel.2005.10.006.

Lang, Kathrin, Matthias Erlacher, Daniel N. Wilson, Ronald Micura, and Norbert Polacek. 2008. 'The Role of 23S Ribosomal RNA Residue A2451 in Peptide Bond Synthesis Revealed by Atomic Mutagenesis'. *Chemistry & Biology* 15 (5): 485–92. https://doi.org/10.1016/j.chembiol.2008.03.014.

Lanois-Nouri, Anne, Lucile Pantel, Jun Fu, et al. 2022. 'The Odilorhabdin Antibiotic Biosynthetic Cluster and Acetyltransferase Self-Resistance Locus Are Niche and Species Specific'. *mBio* 13 (1): e02826-21. https://doi.org/10.1128/mbio.02826-21.

Laxminarayan, Ramanan. 2022. 'The Overlooked Pandemic of Antimicrobial Resistance'. *The Lancet* 399 (10325): 606–7. https://doi.org/10.1016/S0140-6736(22)00087-3.

Leclercq, Roland, Eliane Derlot, Jean Duval, and Patrice Courvalin. 1988. 'Plasmid-Mediated Resistance to Vancomycin and Teicoplanin in Enterococcus Faecium'. *New England Journal of Medicine* 319 (3): 157–61. https://doi.org/10.1056/NEJM198807213190307.

Leder, P., and M. M. Nau. 1967. 'Initiation of Protein Synthesis. 3. Factor-GTP-Codon-Dependent Binding of F-Met-tRNA to Ribosomes.' *Proceedings of the National Academy of Sciences* 58 (2): 774–81. https://doi.org/10.1073/pnas.58.2.774.

Lee, C. P., B. L. Seong, and U. L. RajBhandary. 1991. 'Structural and Sequence Elements Important for Recognition of Escherichia Coli Formylmethionine tRNA by Methionyl-tRNA Transformylase Are Clustered in the Acceptor Stem'. *The Journal of Biological Chemistry* 266 (27): 18012–17.

Leroy, Elodie C., Thomas N. Perry, Thibaud T. Renault, and C. Axel Innis. 2023. 'Tetracenomycin X Sequesters Peptidyl-tRNA during Translation of QK Motifs'. *Nature Chemical Biology* 19 (9): 1091–96. https://doi.org/10.1038/s41589-023-01343-0.

Lewis, Kim. 2013. 'Platforms for Antibiotic Discovery'. *Nature Reviews Drug Discovery* 12 (5): 371–87. https://doi.org/10.1038/nrd3975.

Li, Xiang, Mengjiao Wang, Timo Denk, et al. 2024. 'Structural Basis for Differential Inhibition of Eukaryotic Ribosomes by Tigecycline'. *Nature Communications* 15 (1): 5481. https://doi.org/10.1038/s41467-024-49797-7.

Liebschner, Dorothee, Pavel V. Afonine, Matthew L. Baker, et al. 2019. 'Macromolecular Structure Determination Using X-Rays, Neutrons and Electrons: Recent Developments in Phenix'. *Acta Crystallographica. Section D, Structural Biology* 75 (Pt 10): 861–77. https://doi.org/10.1107/S2059798319011471.

Lin, Jinzhong, Matthieu G. Gagnon, David Bulkley, and Thomas A. Steitz. 2015. 'Conformational Changes of Elongation Factor G on the Ribosome during tRNA Translocation'. *Cell* 160 (1–2): 219–27. https://doi.org/10.1016/j.cell.2014.11.049.

Lin, Jinzhong, Dejian Zhou, Thomas A. Steitz, Yury S. Polikanov, and Matthieu G. Gagnon. 2018. 'Ribosome-Targeting Antibiotics: Modes of Action, Mechanisms of Resistance, and Implications for Drug Design'. *Annual Review of Biochemistry* 87 (1): 451–78. https://doi.org/10.1146/annurev-biochem-062917-011942.

Ling, Clarence, and Dmitri N. Ermolenko. 2015. 'Initiation Factor 2 Stabilizes the Ribosome in a Semirotated Conformation'. *Proceedings of the National Academy of Sciences* 112 (52): 15874–79. https://doi.org/10.1073/pnas.1520337112.

Liu, Qi, and Kurt Fredrick. 2015. 'Roles of Helix H69 of 23S rRNA in Translation Initiation'. *Proceedings of the National Academy of Sciences of the United States of America* 112 (37): 11559–64. https://doi.org/10.1073/pnas.1507703112.

Liu, Yuan, Shuangyang Ding, Jianzhong Shen, and Kui Zhu. 2019. 'Nonribosomal Antibacterial Peptides That Target Multidrug-Resistant Bacteria'. *Natural Product Reports* 36 (4): 573–92. https://doi.org/10.1039/C8NP00031J.

Loftfield, R. B. 1963. 'THE FREQUENCY OF ERRORS IN PROTEIN BIOSYNTHESIS'. *The Biochemical Journal* 89 (1): 82–92. https://doi.org/10.1042/bj0890082.

Loftfield, R. B., and D. Vanderjagt. 1972. 'The Frequency of Errors in Protein Biosynthesis'. *The Biochemical Journal* 128 (5): 1353–56. https://doi.org/10.1042/bj1281353.

Lomakin, Ivan B., Swapnil C. Devarkar, Shivali Patel, Ayman Grada, and Christopher G. Bunick. 2023. 'Sarecycline Inhibits Protein Translation in *Cutibacterium Acnes* 70S Ribosome Using a Two-Site Mechanism'. *Nucleic Acids Research*, March 2, gkad103. https://doi.org/10.1093/nar/gkad103.

López-Alonso, Jorge P., Attilio Fabbretti, Tatsuya Kaminishi, et al. 2016. 'Structure of a 30S Pre-Initiation Complex Stalled by GE81112 Reveals Structural Parallels in Bacterial and Eukaryotic Protein Synthesis Initiation Pathways'. *Nucleic Acids Research*, December 15, gkw1251. https://doi.org/10.1093/nar/gkw1251.

Love, Michael I., Wolfgang Huber, and Simon Anders. 2014. 'Moderated Estimation of Fold Change and Dispersion for RNA-Seq Data with DESeq2'. *Genome Biology* 15 (12): 550. https://doi.org/10.1186/s13059-014-0550-8.

Loveland, Anna B., Gabriel Demo, Nikolaus Grigorieff, and Andrei A. Korostelev. 2017. 'Ensemble Cryo-EM Elucidates the Mechanism of Translation Fidelity'. *Nature* 546 (7656): 113–17. https://doi.org/10.1038/nature22397.

Loveland, Anna B., Gabriel Demo, and Andrei A. Korostelev. 2020. 'Cryo-EM of Elongating Ribosome with EF-Tu•GTP Elucidates tRNA Proofreading'. *Nature* 584 (7822): 640–45. https://doi.org/10.1038/s41586-020-2447-x.

Ly, Cindy T., Mediha E. Altuntop, and Yuhong Wang. 2010. 'Single-Molecule Study of Viomycin's Inhibition Mechanism on Ribosome Translocation'. *Biochemistry* 49 (45): 9732–38. https://doi.org/10.1021/bi101029g.

Ma, Jiong, Allan Campbell, and Samuel Karlin. 2002. 'Correlations between Shine-Dalgarno Sequences and Gene Features Such as Predicted Expression Levels and Operon Structures'. *Journal of Bacteriology* 184 (20): 5733–45. https://doi.org/10.1128/JB.184.20.5733-5745.2002.

MacDougall, Daniel D., and Ruben L. Gonzalez. 2015. 'Translation Initiation Factor 3 Regulates Switching between Different Modes of Ribosomal Subunit Joining'. *Journal of Molecular Biology* 427 (9): 1801–18. https://doi.org/10.1016/j.jmb.2014.09.024.

MacNair, Craig R., Steven T. Rutherford, and Man-Wah Tan. 2024. 'Alternative Therapeutic Strategies to Treat Antibiotic-Resistant Pathogens'. *Nature Reviews Microbiology* 22 (5): 262–75. https://doi.org/10.1038/s41579-023-00993-0.

Maden, B. E. H., R. R. Traut, and R. E. Monro. 1968. 'Ribosome-Catalysed Peptidyl Transfer: The Polyphenylalanine System'. *Journal of Molecular Biology* 35 (2): 333–45. https://doi.org/10.1016/S0022-2836(68)80028-2.

Magnet, Sophie, and John S. Blanchard. 2005. 'Molecular Insights into Aminoglycoside Action and Resistance'. *Chemical Reviews* 105 (2): 477–98. https://doi.org/10.1021/cr0301088.

Maisnier-Patin, Sophie, Otto G. Berg, Lars Liljas, and Dan I. Andersson. 2002. 'Compensatory Adaptation to the Deleterious Effect of Antibiotic Resistance in Salmonella Typhimurium'. *Molecular Microbiology* 46 (2): 355–66. https://doi.org/10.1046/j.1365-2958.2002.03173.x.

Mandal, N., D. Mangroo, J. J. Dalluge, J. A. McCloskey, and U. L. Rajbhandary. 1996. 'Role of the Three Consecutive G:C Base Pairs Conserved in the Anticodon Stem of Initiator tRNAs in Initiation of Protein Synthesis in Escherichia Coli'. *RNA* (New York, N.Y.) 2 (5): 473–82.

Mangano, Kyle, James Marks, Dorota Klepacki, et al. 2022. 'Context-Based Sensing of Orthosomycin Antibiotics by the Translating Ribosome'. *Nature Chemical Biology* 18 (11): 1277–86. https://doi.org/10.1038/s41589-022-01138-9.

Maracci, Cristina, and Marina V. Rodnina. 2016. 'Review: Translational GTPases'. *Biopolymers* 105 (8): 463–75. https://doi.org/10.1002/bip.22832.

Maracci, Cristina, Ingo Wohlgemuth, and Marina V. Rodnina. 2015. 'Activities of the Peptidyl Transferase Center of Ribosomes Lacking Protein L27'. *RNA* (New York, N.Y.) 21 (12): 2047–52. https://doi.org/10.1261/rna.053330.115.

Marcker, K., and F. Sanger. 1964. 'N-Formyl-Methionyl-S-RNA'. *Journal of Molecular Biology* 8 (6): 835-IN8. https://doi.org/10.1016/S0022-2836(64)80164-9.

Marks, James, Krishna Kannan, Emily J. Roncase, et al. 2016. 'Context-Specific Inhibition of Translation by Ribosomal Antibiotics Targeting the Peptidyl Transferase Center'. *Proceedings of the National Academy of Sciences* 113 (43): 12150–55. https://doi.org/10.1073/pnas.1613055113.

Marshall, R. Andrew, Colin Echeverría Aitken, and Joseph D. Puglisi. 2009. 'GTP Hydrolysis by IF2 Guides Progression of the Ribosome into Elongation'. *Molecular Cell* 35 (1): 37–47. https://doi.org/10.1016/j.molcel.2009.06.008.

Marshall, R. Andrew, Magdalena Dorywalska, and Joseph D. Puglisi. 2008. 'Irreversible Chemical Steps Control Intersubunit Dynamics during Translation'. *Proceedings of the National Academy of Sciences* 105 (40): 15364–69. https://doi.org/10.1073/pnas.0805299105.

Martell, Michael J., and James H. Boothe. 1967. 'The 6-Deoxytetracyclines. VII. Alkylated Aminotetracyclines Possessing Unique Antibacterial Activity'. *Journal of Medicinal Chemistry* 10 (1): 44–46. https://doi.org/10.1021/jm00313a009.

Mayer, C., A. Stortchevoi, C. Kohrer, U. Varshney, and U. L. Rajbhandary. 2001. 'Initiator tRNA and Its Role in Initiation of Protein Synthesis'. *Cold Spring Harbor Symposia on Quantitative Biology* 66 (0): 195–206. https://doi.org/10.1101/sqb.2001.66.195.

McCormick, J. R. D., Newell O. Sjolander, Ursula Hirsch, Elmer R. Jensen, and Albert P. Doerschuk. 1957. 'A NEW FAMILY OF ANTIBIOTICS: THE DEMETHYLTETRACYCLINES'. *Journal of the American Chemical Society* 79 (16): 4561–63. https://doi.org/10.1021/ja01573a089.

McCormick, J.R.D, Jensen, Elmer R, Miller, Philip A., and Doerschuk, Albert P. 1960. 'The 6-Deoxytetracyclines. 1 Further Studies on the Relationship between Structure and Antibacterial Activity in the Tetracycline Series'. *Journal of the American Chemical Society* 82 (13): 3381–86.

McGlincy, Nicholas J., and Nicholas T. Ingolia. 2017. 'Transcriptome-Wide Measurement of Translation by Ribosome Profiling'. *Methods* 126 (August): 112–29. https://doi.org/10.1016/j.ymeth.2017.05.028.

Meng, Elaine C., Thomas D. Goddard, Eric F. Pettersen, et al. 2023. 'UCSF ChimeraX : Tools for Structure Building and Analysis'. *Protein Science* 32 (11): e4792. https://doi.org/10.1002/pro.4792.

Mikuni, O., K. Ito, J. Moffat, et al. 1994. 'Identification of the prfC Gene, Which Encodes Peptide-Chain-Release Factor 3 of Escherichia Coli'. *Proceedings of the National*

Academy of Sciences of the United States of America 91 (13): 5798–802. https://doi.org/10.1073/pnas.91.13.5798.

Milón, Pohl, Cristina Maracci, Liudmila Filonava, Claudio O. Gualerzi, and Marina V. Rodnina. 2012. 'Real-Time Assembly Landscape of Bacterial 30S Translation Initiation Complex'. *Nature Structural & Molecular Biology* 19 (6): 609–15. https://doi.org/10.1038/nsmb.2285.

Mittelstaet, Joerg, Andrey L. Konevega, and Marina V. Rodnina. 2011. 'Distortion of tRNA upon Near-Cognate Codon Recognition on the Ribosome'. *Journal of Biological Chemistry* 286 (10): 8158–64. https://doi.org/10.1074/jbc.M110.210021.

Moazed, Danesh, and Harry F. Noller. 1989. 'Intermediate States in the Movement of Transfer RNA in the Ribosome'. *Nature* 342 (6246): 142–48. https://doi.org/10.1038/342142a0.

Moazed, Danesh, and Harry F. Noller. 1990. 'Binding of tRNA to the Ribosomal A and P Sites Protects Two Distinct Sets of Nucleotides in 16 S rRNA'. *Journal of Molecular Biology* 211 (1): 135–45. https://doi.org/10.1016/0022-2836(90)90016-F.

Moazed, Danesh, James M. Robertson, and Harry F. Noller. 1988. 'Interaction of Elongation Factors EF-G and EF-Tu with a Conserved Loop in 23S RNA'. *Nature* 334 (6180): 362–64. https://doi.org/10.1038/334362a0.

Modolfll, Juan, and David Vázquez. 1977. 'The Inhibition of Ribosomal Translocation by Viomycin'. *European Journal of Biochemistry* 81 (3): 491–97. https://doi.org/10.1111/j.1432-1033.1977.tb11974.x.

Mohammad, Fuad, and Allen Buskirk. 2019. 'Protocol for Ribosome Profiling in Bacteria'. *BIO-PROTOCOL* 9 (24). https://doi.org/10.21769/BioProtoc.3468.

Mohan, Srividya, John Paul Donohue, and Harry F. Noller. 2014. 'Molecular Mechanics of 30S Subunit Head Rotation'. *Proceedings of the National Academy of Sciences* 111 (37): 13325–30. https://doi.org/10.1073/pnas.1413731111.

Mohan, Srividya, and Harry F. Noller. 2017. 'Recurring RNA Structural Motifs Underlie the Mechanics of L1 Stalk Movement'. *Nature Communications* 8 (February): 14285. https://doi.org/10.1038/ncomms14285.

Monro, R. E. 1967. 'Catalysis of Peptide Bond Formation by 50 s Ribosomal Subunits from Escherichia Coli'. *Journal of Molecular Biology* 26 (1): 147–51. https://doi.org/10.1016/0022-2836(67)90271-9.

Mordret, Ernest, Orna Dahan, Omer Asraf, et al. 2019. 'Systematic Detection of Amino Acid Substitutions in Proteomes Reveals Mechanistic Basis of Ribosome Errors and Selection for Translation Fidelity'. *Molecular Cell* 75 (3): 427-441.e5. https://doi.org/10.1016/j.molcel.2019.06.041.

Morse, Justin C., Dylan Girodat, Benjamin J. Burnett, et al. 2020. 'Elongation Factor-Tu Can Repetitively Engage Aminoacyl-tRNA within the Ribosome during the Proofreading Stage of tRNA Selection'. *Proceedings of the National Academy of Sciences* 117 (7): 3610–20. https://doi.org/10.1073/pnas.1904469117.

Müller, Sebastian, Eva Garcia-Gonzalez, Andi Mainz, et al. 2014. 'Paenilamicin: Structure and Biosynthesis of a Hybrid Nonribosomal Peptide/Polyketide Antibiotic from the Bee Pathogen *Paenibacillus Larvae*'. *Angewandte Chemie International Edition* 53 (40): 10821–25. https://doi.org/10.1002/anie.201404572.

Munro, James B., Roger B. Altman, Nathan O'Connor, and Scott C. Blanchard. 2007. 'Identification of Two Distinct Hybrid State Intermediates on the Ribosome'. *Molecular Cell* 25 (4): 505–17. https://doi.org/10.1016/j.molcel.2007.01.022.

Munro, James B., Roger B. Altman, Chang-Shung Tung, Jamie H. D. Cate, Kevin Y. Sanbonmatsu, and Scott C. Blanchard. 2010. 'Spontaneous Formation of the Unlocked State of the Ribosome Is a Multistep Process'. *Proceedings of the National Academy of Sciences* 107 (2): 709–14. https://doi.org/10.1073/pnas.0908597107.

Murphy, Frank V., Venki Ramakrishnan, Andrzej Malkiewicz, and Paul F. Agris. 2004. 'The Role of Modifications in Codon Discrimination by tRNALysUUU'. *Nature Structural & Molecular Biology* 11 (12): 1186–91. https://doi.org/10.1038/nsmb861.

Murray, James B., Samy O. Meroueh, Rupert J. M. Russell, Georg Lentzen, Jalal Haddad, and Shahriar Mobashery. 2006. 'Interactions of Designer Antibiotics and the Bacterial Ribosomal Aminoacyl-tRNA Site'. *Chemistry & Biology* 13 (2): 129–38. https://doi.org/10.1016/j.chembiol.2005.11.004.

Muzellec, Boris, Maria Teleńczuk, Vincent Cabeli, and Mathieu Andreux. 2023. 'PyDESeq2: A Python Package for Bulk RNA-Seq Differential Expression Analysis'. *Bioinformatics* 39 (9): btad547. https://doi.org/10.1093/bioinformatics/btad547.

Naghavi, Mohsen, Stein Emil Vollset, Kevin S. Ikuta, et al. 2024. 'Global Burden of Bacterial Antimicrobial Resistance 1990–2021: A Systematic Analysis with Forecasts to 2050'. *The Lancet* 404 (10459): 1199–226. https://doi.org/10.1016/S0140-6736(24)01867-1.

Nakahigashi, Kenji, Yuki Takai, Michiko Kimura, et al. 2016. 'Comprehensive Identification of Translation Start Sites by Tetracycline-Inhibited Ribosome Profiling'. *DNA Research* 23 (3): 193–201. https://doi.org/10.1093/dnares/dsw008.

Nakahigashi, Kenji, Yuki Takai, Yuh Shiwa, et al. 2014. 'Effect of Codon Adaptation on Codon-Level and Gene-Level Translation Efficiency in Vivo'. *BMC Genomics* 15 (1): 1115. https://doi.org/10.1186/1471-2164-15-1115.

Niblett, Dustin, Charlotte Nelson, Calvin S. Leung, et al. 2021. 'Mutations in Domain IV of Elongation Factor EF-G Confer -1 Frameshifting'. *RNA* (New York, N.Y.) 27 (1): 40–53. https://doi.org/10.1261/rna.077339.120.

Nikolay, Rainer, David Van Den Bruck, John Achenbach, and Knud H. Nierhaus. 2015. 'Ribosomal Proteins: Role in Ribosomal Functions'. In *Encyclopedia of Life Sciences*, 1st edn, by Wiley. Wiley. https://doi.org/10.1002/9780470015902.a0000687.pub4.

Ninio, J. 1975. 'Kinetic Amplification of Enzyme Discrimination'. *Biochimie* 57 (5): 587–95. https://doi.org/10.1016/s0300-9084(75)80139-8.

Nirenberg, M. W., O. W. Jones, P. Leder, B. F. C. Clark, W. S. Sly, and S. Pestka. 1963. 'On the Coding of Genetic Information'. *Cold Spring Harbor Symposia on Quantitative Biology* 28 (0): 549–57. https://doi.org/10.1101/SQB.1963.028.01.074.

Nissen, Poul, Jeffrey Hansen, Nenad Ban, Peter B. Moore, and Thomas A. Steitz. 2000. 'The Structural Basis of Ribosome Activity in Peptide Bond Synthesis'. *Science* 289 (5481): 920–30. https://doi.org/10.1126/science.289.5481.920.

Noller, Harry F., and Jonathan B. Chaires. 1972. 'Functional Modification of 16S Ribosomal RNA by Kethoxal'. *Proceedings of the National Academy of Sciences* 69 (11): 3115–18. https://doi.org/10.1073/pnas.69.11.3115.

Noller, Harry F., Vernita Hoffarth, and Ludwika Zimniak. 1992. 'Unusual Resistance of Peptidyl Transferase to Protein Extraction Procedures'. *Science* 256 (5062): 1416–19. https://doi.org/10.1126/science.1604315.

Nomura, M., C. V. Lowry, and C. Guthrie. 1967. 'The Initiation of Protein Synthesis: Joining of the 50S Ribosomal Subunit to the Initiation Complex.' *Proceedings of the National Academy of Sciences* 58 (4): 1487–93. https://doi.org/10.1073/pnas.58.4.1487.

O'Connor, M., S. T. Gregory, U. L. Rajbhandary, and A. E. Dahlberg. 2001. 'Altered Discrimination of Start Codons and Initiator tRNAs by Mutant Initiation Factor 3'. *RNA* (New York, N.Y.) 7 (7): 969–78. https://doi.org/10.1017/s1355838201010184.

Ogawa, Koichi, and Akira Kaji. 1975. 'Requirement for Ribosome-Releasing Factor for the Release of Ribosomes at the Termination Codon'. *European Journal of Biochemistry* 58 (2): 411–19. https://doi.org/10.1111/j.1432-1033.1975.tb02388.x.

Ogle, James M., Ditlev E. Brodersen, William M. Clemons, Michael J. Tarry, Andrew P. Carter, and V. Ramakrishnan. 2001. 'Recognition of Cognate Transfer RNA by the 30 *S* Ribosomal Subunit'. *Science* 292 (5518): 897–902. https://doi.org/10.1126/science.1060612.

Ogle, James M., Andrew P. Carter, and V. Ramakrishnan. 2003. 'Insights into the Decoding Mechanism from Recent Ribosome Structures'. *Trends in Biochemical Sciences* 28 (5): 259–66. https://doi.org/10.1016/S0968-0004(03)00066-5.

Ogle, James M., Frank V. Murphy, Michael J. Tarry, and V. Ramakrishnan. 2002. 'Selection of tRNA by the Ribosome Requires a Transition from an Open to a Closed Form'. *Cell* 111 (5): 721–32. https://doi.org/10.1016/S0092-8674(02)01086-3.

Olson, Matthew W., Alexey Ruzin, Eric Feyfant, Thomas S. Rush, John O'Connell, and Patricia A. Bradford. 2006. 'Functional, Biophysical, and Structural Bases for Antibacterial Activity of Tigecycline'. *Antimicrobial Agents and Chemotherapy* 50 (6): 2156–66. https://doi.org/10.1128/AAC.01499-05.

Ōmura, Satoshi, Yuzuru Iwai, Atsushi Hirano, Juichi Awaya, Yoko Suzuki, and Katsumi Matsumoto. 1977. 'A New Antibiotic, AM-2504'. *Agricultural and Biological Chemistry* 41 (9): 1827–28. https://doi.org/10.1080/00021369.1977.10862771.

Orelle, Cédric, Skylar Carlson, Bindiya Kaushal, et al. 2013. 'Tools for Characterizing Bacterial Protein Synthesis Inhibitors'. *Antimicrobial Agents and Chemotherapy* 57 (12): 5994–6004. https://doi.org/10.1128/AAC.01673-13.

Orelle, Cédric, Teresa Szal, Dorota Klepacki, Karen J. Shaw, Nora Vázquez-Laslop, and Alexander S. Mankin. 2013. 'Identifying the Targets of Aminoacyl-tRNA Synthetase Inhibitors by Primer Extension Inhibition'. *Nucleic Acids Research* 41 (14): e144–e144. https://doi.org/10.1093/nar/gkt526.

Ortiz-Meoz, Rodrigo F., and Rachel Green. 2010. 'Functional Elucidation of a Key Contact between tRNA and the Large Ribosomal Subunit rRNA during Decoding'. *RNA* (New York, N.Y.) 16 (10): 2002–13. https://doi.org/10.1261/rna.2232710.

Osterman, Ilya A., Maximiliane Wieland, Tinashe P. Maviza, et al. 2020. 'Tetracenomycin X Inhibits Translation by Binding within the Ribosomal Exit Tunnel'. *Nature Chemical Biology* 16 (10): 1071–77. https://doi.org/10.1038/s41589-020-0578-x.

Palade, George E. 1955. 'A SMALL PARTICULATE COMPONENT OF THE CYTOPLASM'. *The Journal of Cell Biology* 1 (1): 59–68. https://doi.org/10.1083/jcb.1.1.59.

Pallesen, Jesper, Yaser Hashem, Gürkan Korkmaz, et al. 2013. 'Cryo-EM Visualization of the Ribosome in Termination Complex with Apo-RF3 and RF1'. *eLife* 2 (June): e00411. https://doi.org/10.7554/eLife.00411.

Pan, Dongli, Stanislav V. Kirillov, and Barry S. Cooperman. 2007. 'Kinetically Competent Intermediates in the Translocation Step of Protein Synthesis'. *Molecular Cell* 25 (4): 519–29. https://doi.org/10.1016/j.molcel.2007.01.014.

Pantel, Lucile, Tanja Florin, Malgorzata Dobosz-Bartoszek, et al. 2018. 'Odilorhabdins, Antibacterial Agents That Cause Miscoding by Binding at a New Ribosomal Site'. *Molecular Cell* 70 (1): 83-94.e7. https://doi.org/10.1016/j.molcel.2018.03.001.

Pantel, Lucile, François Guérin, Marine Serri, et al. 2022. 'Exploring Cluster-Dependent Antibacterial Activities and Resistance Pathways of NOSO-502 and Colistin against Enterobacter Cloacae Complex Species'. *Antimicrobial Agents and Chemotherapy* 0 (0): e00776-22. https://doi.org/10.1128/aac.00776-22.

Pantel, Lucile, Paulo Juarez, Marine Serri, et al. 2021. 'Missense Mutations in the CrrB Protein Mediate Odilorhabdin Derivative Resistance in Klebsiella Pneumoniae'. *Antimicrobial Agents and Chemotherapy* 65 (5): e00139-21. https://doi.org/10.1128/AAC.00139-21.

Pape, T., W. Wintermeyer, and M. Rodnina. 1999. 'Induced Fit in Initial Selection and Proofreading of Aminoacyl-tRNA on the Ribosome'. *The EMBO Journal* 18 (13): 3800–3807. https://doi.org/10.1093/emboj/18.13.3800.

Pape, T., W. Wintermeyer, and M. V. Rodnina. 1998. 'Complete Kinetic Mechanism of Elongation Factor Tu-Dependent Binding of Aminoacyl-tRNA to the A Site of the E. Coli Ribosome'. *The EMBO Journal* 17 (24): 7490–97. https://doi.org/10.1093/emboj/17.24.7490.

Parajuli, Narayan Prasad, Andrew Emmerich, Chandra Sekhar Mandava, Michael Y. Pavlov, and Suparna Sanyal. 2023. 'Antibiotic Thermorubin Tethers Ribosomal Subunits and Impedes A-Site Interactions to Perturb Protein Synthesis in Bacteria'. *Nature Communications* 14 (1): 918. https://doi.org/10.1038/s41467-023-36528-7.

Peske, Frank, Stephan Kuhlenkoetter, Marina V. Rodnina, and Wolfgang Wintermeyer. 2014. 'Timing of GTP Binding and Hydrolysis by Translation Termination Factor RF3'. *Nucleic Acids Research* 42 (3): 1812–20. https://doi.org/10.1093/nar/gkt1095.

Peske, Frank, Marina V. Rodnina, and Wolfgang Wintermeyer. 2005. 'Sequence of Steps in Ribosome Recycling as Defined by Kinetic Analysis'. *Molecular Cell* 18 (4): 403–12. https://doi.org/10.1016/j.molcel.2005.04.009.

Peske, Frank, Andreas Savelsbergh, Vladimir I. Katunin, Marina V. Rodnina, and Wolfgang Wintermeyer. 2004. 'Conformational Changes of the Small Ribosomal Subunit During Elongation Factor G-Dependent tRNA–mRNA Translocation'. *Journal of Molecular Biology* 343 (5): 1183–94. https://doi.org/10.1016/j.jmb.2004.08.097.

Pestka, S. 1969. 'Studies on the Formation of Transfer Ribonucleic Acid-Ribosome Complexes'. *Journal of Biological Chemistry* 244 (6): 1533–39. https://doi.org/10.1016/S0021-9258(18)91792-8.

Petersen, P. J., N. V. Jacobus, W. J. Weiss, P. E. Sum, and R. T. Testa. 1999. 'In Vitro and In Vivo Antibacterial Activities of a Novel Glycylcycline, the 9- *t* -Butylglycylamido

Derivative of Minocycline (GAR-936)'. *Antimicrobial Agents and Chemotherapy* 43 (4): 738–44. https://doi.org/10.1128/aac.43.4.738.

Petrychenko, Valentyn, Bee-Zen Peng, Ana C. De A. P. Schwarzer, Frank Peske, Marina V. Rodnina, and Niels Fischer. 2021. 'Structural Mechanism of GTPase-Powered Ribosome-tRNA Movement'. *Nature Communications* 12 (1): 5933. https://doi.org/10.1038/s41467-021-26133-x.

Piepersberg, W., A. Böck, and H. G. Wittmann. 1975. 'Effect of Different Mutations in Ribosomal Protein S5 of Escherichia Coli on Translational Fidelity'. *Molecular & General Genetics: MGG* 140 (2): 91–100. https://doi.org/10.1007/BF00329777.

Pioletti, M. 2001. 'Crystal Structures of Complexes of the Small Ribosomal Subunit with Tetracycline, Edeine and IF3'. *The EMBO Journal* 20 (8): 1829–39. https://doi.org/10.1093/emboj/20.8.1829.

Polikanov, Yury S., Thomas A. Steitz, and C. Axel Innis. 2014. 'A Proton Wire to Couple Aminoacyl-tRNA Accommodation and Peptide-Bond Formation on the Ribosome'. *Nature Structural & Molecular Biology* 21 (9): 787–93. https://doi.org/10.1038/nsmb.2871.

Poulis, Panagiotis, Frank Peske, and Marina V. Rodnina. 2023. 'The Many Faces of Ribosome Translocation along the mRNA: Reading Frame Maintenance, Ribosome Frameshifting and Translational Bypassing'. *Biological Chemistry* 404 (8–9): 755–67. https://doi.org/10.1515/hsz-2023-0142.

Powers, T., and H. F. Noller. 1994. 'Selective Perturbation of G530 of 16 S rRNA by Translational Miscoding Agents and a Streptomycin-Dependence Mutation in Protein S12'. *Journal of Molecular Biology* 235 (1): 156–72. https://doi.org/10.1016/s0022-2836(05)80023-3.

Prabhakar, Arjun, Mark C. Capece, Alexey Petrov, Junhong Choi, and Joseph D. Puglisi. 2017. 'Post-Termination Ribosome Intermediate Acts as the Gateway to Ribosome Recycling'. *Cell Reports* 20 (1): 161–72. https://doi.org/10.1016/j.celrep.2017.06.028.

Präve, Leonard, Carsten E. Seyfert, Kenan A. J. Bozhüyük, Emilie Racine, Rolf Müller, and Helge B. Bode. 2024. 'Investigation of the Odilorhabdin Biosynthetic Gene Cluster Using NRPS Engineering'. *Angewandte Chemie International Edition*, May 27, e202406389. https://doi.org/10.1002/anie.202406389.

Punjani, Ali, John L. Rubinstein, David J. Fleet, and Marcus A. Brubaker. 2017. 'cryoSPARC: Algorithms for Rapid Unsupervised Cryo-EM Structure Determination'. *Nature Methods* 14 (3): 290–96. https://doi.org/10.1038/nmeth.4169.

Quan, Selwyn, Ole Skovgaard, Robert E. McLaughlin, Ed T. Buurman, and Catherine L. Squires. 2015. 'Markerless Escherichia Coli Rrn Deletion Strains for Genetic Determination of

Ribosomal Binding Sites'. *G3* (Bethesda, Md.) 5 (12): 2555–57. https://doi.org/10.1534/g3.115.022301.

Quirk, Mary. 2002. 'First VRSA Isolate Identified in USA'. *The Lancet Infectious Diseases* 2 (9): 510. https://doi.org/10.1016/S1473-3099(02)00380-8.

Racine, Emilie, and Maxime Gualtieri. 2019. 'From Worms to Drug Candidate: The Story of Odilorhabdins, a New Class of Antimicrobial Agents'. *Frontiers in Microbiology* 10 (December): 2893. https://doi.org/10.3389/fmicb.2019.02893.

Racine, Emilie, Patrice Nordmann, Lucile Pantel, et al. 2018. '*In Vitro* and *In Vivo* Characterization of NOSO-502, a Novel Inhibitor of Bacterial Translation'. *Antimicrobial Agents and Chemotherapy* 62 (9): e01016-18. https://doi.org/10.1128/AAC.01016-18.

RajBhandary, U. L. 1994. 'Initiator Transfer RNAs'. *Journal of Bacteriology* 176 (3): 547–52. https://doi.org/10.1128/jb.176.3.547-552.1994.

Ramrath, David J. F., Laura Lancaster, Thiemo Sprink, et al. 2013. 'Visualization of Two Transfer RNAs Trapped in Transit during Elongation Factor G-Mediated Translocation'. *Proceedings of the National Academy of Sciences* 110 (52): 20964–69. https://doi.org/10.1073/pnas.1320387110.

Ramu, Haripriya, Alexander Mankin, and Nora Vazquez-Laslop. 2009. 'Programmed Drug-Dependent Ribosome Stalling'. *Molecular Microbiology* 71 (4): 811–24. https://doi.org/10.1111/j.1365-2958.2008.06576.x.

Ratje, Andreas H., Justus Loerke, Aleksandra Mikolajka, et al. 2010. 'Head Swivel on the Ribosome Facilitates Translocation by Means of Intra-Subunit tRNA Hybrid Sites'. *Nature* 468 (7324): 713–16. https://doi.org/10.1038/nature09547.

Rawat, Urmila B. S., Andrey V. Zavialov, Jayati Sengupta, et al. 2003. 'A Cryo-Electron Microscopic Study of Ribosome-Bound Termination Factor RF2'. *Nature* 421 (6918): 87–90. https://doi.org/10.1038/nature01224.

Rawat, Urmila, Haixiao Gao, Andrey Zavialov, Richard Gursky, Måns Ehrenberg, and Joachim Frank. 2006. 'Interactions of the Release Factor RF1 with the Ribosome as Revealed by Cryo-EM'. *Journal of Molecular Biology* 357 (4): 1144–53. https://doi.org/10.1016/j.jmb.2006.01.038.

Ringquist, S., T. Jones, E. E. Snyder, T. Gibson, I. Boni, and L. Gold. 1995. 'High-Affinity RNA Ligands to Escherichia Coli Ribosomes and Ribosomal Protein S1: Comparison of Natural and Unnatural Binding Sites'. *Biochemistry* 34 (11): 3640–48. https://doi.org/10.1021/bi00011a019.

Ringquist, Steven, Sidney Shinedling, Doug Barrick, et al. 1992. 'Translation Initiation in *Escherichia Coli* : Sequences within the Ribosome-binding Site'. *Molecular Microbiology* 6 (9): 1219–29. https://doi.org/10.1111/j.1365-2958.1992.tb01561.x.

Risuleo, Gianfranco, Claudio Gualerzi, and Cynthia Pon. 1976. 'Specificity and Properties of the Destabilization, Induced by Initiation Factor IF-3, of Ternary Complexes of the 30-S Ribosomal Subunit, Aminoacyl-tRNA and Polynucleotides'. *European Journal of Biochemistry* 67 (2): 603–13. https://doi.org/10.1111/j.1432-1033.1976.tb10726.x.

Robertus, J. D., J. E. Ladner, J. T. Finch, et al. 1974. 'Structure of Yeast Phenylalanine tRNA at 3 A Resolution'. *Nature* 250 (467): 546–51. https://doi.org/10.1038/250546a0.

Rodnina, Marina V. 2012. 'Quality Control of mRNA Decoding on the Bacterial Ribosome'. In *Advances in Protein Chemistry and Structural Biology*, vol. 86. Elsevier. https://doi.org/10.1016/B978-0-12-386497-0.00003-7.

Rodnina, Marina V. 2023. 'Decoding and Recoding of mRNA Sequences by the Ribosome'. *Annual Review of Biophysics* 52 (1): 161–82. https://doi.org/10.1146/annurev-biophys-101922-072452.

Rodnina, Marina V., Kirill B. Gromadski, Ute Kothe, and Hans-Joachim Wieden. 2005. 'Recognition and Selection of tRNA in Translation'. *FEBS Letters* 579 (4): 938–42. https://doi.org/10.1016/j.febslet.2004.11.048.

Rodnina, Marina V., Tillmann Pape, Rainer Fricke, Lothar Kuhn, and Wolfgang Wintermeyer. 1996. 'Initial Binding of the Elongation Factor Tu·GTP·Aminoacyl-tRNA Complex Preceding Codon Recognition on the Ribosome'. *Journal of Biological Chemistry* 271 (2): 646–52. https://doi.org/10.1074/jbc.271.2.646.

Rodnina, Marina V., Andreas Savelsbergh, Vladimir I. Katunin, and Wolfgang Wintermeyer. 1997. 'Hydrolysis of GTP by Elongation Factor G Drives tRNA Movement on the Ribosome'. *Nature* 385 (6611): 37–41. https://doi.org/10.1038/385037a0.

Rodnina, Marina V, and Wolfgang Wintermeyer. 2001. 'Ribosome Fidelity: tRNA Discrimination, Proofreading and Induced Fit'. *Trends in Biochemical Sciences* 26 (2): 124–30. https://doi.org/10.1016/S0968-0004(00)01737-0.

Rodnina, M.V., R. Fricke, L. Kuhn, and W. Wintermeyer. 1995. 'Codon-dependent Conformational Change of Elongation Factor Tu Preceding GTP Hydrolysis on the Ribosome.' *The EMBO Journal* 14 (11): 2613–19. https://doi.org/10.1002/j.1460-2075.1995.tb07259.x.

Ronn, Magnus, Zhijian Zhu, Philip C. Hogan, et al. 2013. 'Process R&D of Eravacycline: The First Fully Synthetic Fluorocycline in Clinical Development'. *Organic Process Research & Development* 17 (5): 838–45. https://doi.org/10.1021/op4000219.

Rosset, R., and L. Gorini. 1969. 'A Ribosomal Ambiguity Mutation'. *Journal of Molecular Biology* 39 (1): 95–112. https://doi.org/10.1016/0022-2836(69)90336-2.

Rould, M. A., J. J. Perona, D. Söll, and T. A. Steitz. 1989. 'Structure of E. Coli Glutaminyl-tRNA Synthetase Complexed with tRNA(Gln) and ATP at 2.8 A Resolution'. *Science* (New York, N.Y.) 246 (4934): 1135–42. https://doi.org/10.1126/science.2479982.

Rundlet, Emily J., Mikael Holm, Magdalena Schacherl, et al. 2021. 'Structural Basis of Early Translocation Events on the Ribosome'. *Nature* 595 (7869): 741–45. https://doi.org/10.1038/s41586-021-03713-x.

Safdari, Haaris A., Martino Morici, Ana Sanchez-Castro, et al. 2025. 'The Translation Inhibitors Kasugamycin, Edeine and GE81112 Target Distinct Steps during 30S Initiation Complex Formation'. *Nature Communications* 16 (1): 2470. https://doi.org/10.1038/s41467-025-57731-8.

Salsi, Enea, Elie Farah, Jillian Dann, and Dmitri N. Ermolenko. 2014. 'Following Movement of Domain IV of Elongation Factor G during Ribosomal Translocation'. *Proceedings of the National Academy of Sciences* 111 (42): 15060–65. https://doi.org/10.1073/pnas.1410873111.

Salsi, Enea, Elie Farah, Zoe Netter, Jillian Dann, and Dmitri N. Ermolenko. 2015. 'Movement of Elongation Factor G between Compact and Extended Conformations'. *Journal of Molecular Biology* 427 (2): 454–67. https://doi.org/10.1016/j.jmb.2014.11.010.

Samaha, Raymond R., Rachel Green, and Harry F. Noller. 1995. 'A Base Pair between tRNA and 23S rRNA in the Peptidyl Transferase Centre of the Ribosome'. *Nature* 377 (6547): 309–14. https://doi.org/10.1038/377309a0.

Sander, G., R. C. Marsh, and A. Parmeggiani. 1972. 'Isolation and Characterization of Two Acidic Proteins from the 50S Subunit Required for GTPase Activities of Both EF G and EF T'. *Biochemical and Biophysical Research Communications* 47 (4): 866–73. https://doi.org/10.1016/0006-291X(72)90573-6.

Sanderson, Lee E., and Olke C. Uhlenbeck. 2007. 'Exploring the Specificity of Bacterial Elongation Factor Tu for Different tRNAs'. *Biochemistry* 46 (21): 6194–200. https://doi.org/10.1021/bi602548v.

Sarciaux, Matthieu, Lucile Pantel, Camille Midrier, et al. 2018. 'Total Synthesis and Structure–Activity Relationships Study of Odilorhabdins, a New Class of Peptides Showing Potent Antibacterial Activity'. *Journal of Medicinal Chemistry* 61 (17): 7814–26. https://doi.org/10.1021/acs.jmedchem.8b00790.

Savelsbergh, Andreas, Marina V. Rodnina, and Wolfgang Wintermeyer. 2009. 'Distinct Functions of Elongation Factor G in Ribosome Recycling and Translocation'. *RNA* (New York, N.Y.) 15 (5): 772–80. https://doi.org/10.1261/rna.1592509.

Scharff, Lars B., Liam Childs, Dirk Walther, and Ralph Bock. 2011. 'Local Absence of Secondary Structure Permits Translation of mRNAs That Lack Ribosome-Binding Sites'. *PLoS Genetics* 7 (6): e1002155. https://doi.org/10.1371/journal.pgen.1002155.

Schedlbauer, Andreas, Tatsuya Kaminishi, Borja Ochoa-Lizarralde, et al. 2015. 'Structural Characterization of an Alternative Mode of Tigecycline Binding to the Bacterial Ribosome'. *Antimicrobial Agents and Chemotherapy* 59 (5): 2849–54. https://doi.org/10.1128/AAC.04895-14.

Schimmel, P. R., and D. Söll. 1979. 'Aminoacyl-tRNA Synthetases: General Features and Recognition of Transfer RNAs'. *Annual Review of Biochemistry* 48: 601–48. https://doi.org/10.1146/annurev.bi.48.070179.003125.

Schlünzen, Frank, Erez Pyetan, Paola Fucini, Ada Yonath, and Jörg M. Harms. 2004. 'Inhibition of Peptide Bond Formation by Pleuromutilins: The Structure of the 50S Ribosomal Subunit from Deinococcus Radiodurans in Complex with Tiamulin'. *Molecular Microbiology* 54 (5): 1287–94. https://doi.org/10.1111/j.1365-2958.2004.04346.x.

Schmeing, T. Martin, Kevin S. Huang, David E. Kitchen, Scott A. Strobel, and Thomas A. Steitz. 2005. 'Structural Insights into the Roles of Water and the 2' Hydroxyl of the P Site tRNA in the Peptidyl Transferase Reaction'. *Molecular Cell* 20 (3): 437–48. https://doi.org/10.1016/j.molcel.2005.09.006.

Schmeing, T. Martin, and V. Ramakrishnan. 2009. 'What Recent Ribosome Structures Have Revealed about the Mechanism of Translation'. *Nature* 461 (7268): 1234–42. https://doi.org/10.1038/nature08403.

Schmeing, T. Martin, Rebecca M. Voorhees, Ann C. Kelley, et al. 2009. 'The Crystal Structure of the Ribosome Bound to EF-Tu and Aminoacyl-tRNA'. *Science* 326 (5953): 688–94. https://doi.org/10.1126/science.1179700.

Schmitt, Emmanuelle, Michel Panvert, Sylvain Blanquet, and Yves Mechulam. 1998. 'Crystal Structure of Methionyl-tRNAfMet Transformylase Complexed with the Initiator Formyl-Methionyl-tRNAfMet'. *The EMBO Journal* 17 (23): 6819–26. https://doi.org/10.1093/emboj/17.23.6819.

Schuwirth, Barbara S., Maria A. Borovinskaya, Cathy W. Hau, et al. 2005. 'Structures of the Bacterial Ribosome at 3.5 A Resolution'. *Science* (New York, N.Y.) 310 (5749): 827–34. https://doi.org/10.1126/science.1117230.

Scolnick, E., R. Tompkins, T. Caskey, and M. Nirenberg. 1968. 'Release Factors Differing in Specificity for Terminator Codons.' *Proceedings of the National Academy of Sciences* 61 (2): 768–74. https://doi.org/10.1073/pnas.61.2.768.

Seip, Britta, and C. Axel Innis. 2016. 'How Widespread Is Metabolite Sensing by Ribosome-Arresting Nascent Peptides?' *Journal of Molecular Biology* 428 (10): 2217–27. https://doi.org/10.1016/j.jmb.2016.04.019.

Seip, Britta, Guénaël Sacheau, Denis Dupuy, and C. Axel Innis. 2018. 'Ribosomal Stalling Landscapes Revealed by High-Throughput Inverse Toeprinting of mRNA Libraries'. *Life Science Alliance* 1 (5): e201800148. https://doi.org/10.26508/lsa.201800148.

Selmer, Maria, Christine M. Dunham, Frank V. Murphy, et al. 2006. 'Structure of the 70 *S* Ribosome Complexed with mRNA and tRNA'. *Science* 313 (5795): 1935–42. https://doi.org/10.1126/science.1131127.

Senior, Kathryn. 2005. 'New Antibiotic Approved for MRSA'. *The Lancet Infectious Diseases* 5 (8): 474. https://doi.org/10.1016/S1473-3099(05)70179-1.

Seo, Hyuk-Soo, Michael Kiel, Dongli Pan, V. Samuel Raj, Akira Kaji, and Barry S. Cooperman. 2004. 'Kinetics and Thermodynamics of RRF, EF-G, and Thiostrepton Interaction on the Escherichia Coli Ribosome'. *Biochemistry* 43 (40): 12728–40. https://doi.org/10.1021/bi048927p.

Seong, B. L., and U. L. RajBhandary. 1987. 'Escherichia Coli Formylmethionine tRNA: Mutations in GGGCCC Sequence Conserved in Anticodon Stem of Initiator tRNAs Affect Initiation of Protein Synthesis and Conformation of Anticodon Loop'. *Proceedings of the National Academy of Sciences of the United States of America* 84 (2): 334–38. https://doi.org/10.1073/pnas.84.2.334.

Shao, Qiuya, Anas Khawaja, Minh Duc Nguyen, et al. 2025. 'T Cell Toxicity Induced by Tigecycline Binding to the Mitochondrial Ribosome'. *Nature Communications* 16 (1): 4080. https://doi.org/10.1038/s41467-025-59388-9.

Sharma, Divya, Anthony R. Cukras, Elizabeth J. Rogers, Daniel R. Southworth, and Rachel Green. 2007. 'Mutational Analysis of S12 Protein and Implications for the Accuracy of Decoding by the Ribosome'. *Journal of Molecular Biology* 374 (4): 1065–76. https://doi.org/10.1016/j.jmb.2007.10.003.

Sharma, Pankaz K., Yun Xiang, Mitsunori Kato, and Arieh Warshel. 2005. 'What Are the Roles of Substrate-Assisted Catalysis and Proximity Effects in Peptide Bond Formation by the Ribosome?' *Biochemistry* 44 (34): 11307–14. https://doi.org/10.1021/bi0509806.

Sherman, Fred, John W. Stewart, and Susumu Tsunasawa. 1985. 'Methionine or Not Methionine at the Beginning of a Protein'. *BioEssays* 3 (1): 27–31. https://doi.org/10.1002/bies.950030108.

Shetty, Sunil, Souvik Bhattacharyya, and Umesh Varshney. 2015. 'Is the Cellular Initiation of Translation an Exclusive Property of the Initiator tRNAs?' *RNA Biology* 12 (7): 675–80. https://doi.org/10.1080/15476286.2015.1043507.

Shimizu, Yoshihiro, Akio Inoue, Yukihide Tomari, et al. 2001. 'Cell-Free Translation Reconstituted with Purified Components'. *Nature Biotechnology* 19 (8): 751–55. https://doi.org/10.1038/90802.

Shine, J., and L. Dalgarno. 1974. 'The 3'-Terminal Sequence of *Escherichia Coli* 16S Ribosomal RNA: Complementarity to Nonsense Triplets and Ribosome Binding Sites'. *Proceedings of the National Academy of Sciences* 71 (4): 1342–46. https://doi.org/10.1073/pnas.71.4.1342.

Shoji, Shinichiro, Sarah E. Walker, and Kurt Fredrick. 2006. 'Reverse Translocation of tRNA in the Ribosome'. *Molecular Cell* 24 (6): 931–42. https://doi.org/10.1016/j.molcel.2006.11.025.

Sievers, Annette, Malte Beringer, Marina V. Rodnina, and Richard Wolfenden. 2004. 'The Ribosome as an Entropy Trap'. *Proceedings of the National Academy of Sciences* 101 (21): 7897–901. https://doi.org/10.1073/pnas.0402488101.

Simonetti, Angelita, Stefano Marzi, Alexander G. Myasnikov, et al. 2008. 'Structure of the 30S Translation Initiation Complex'. *Nature* 455 (7211): 416–20. https://doi.org/10.1038/nature07192.

Söll, Dieter. 1971. 'Enzymatic Modification of Transfer RNA: Modified Nucleosides Form at the Polynucleotide Level, but Their Function Is Not Established.' *Science* 173 (3994): 293–99. https://doi.org/10.1126/science.173.3994.293.

Sordyl, Dominik, Etienne Boileau, Agata Bernat, et al. 2026. 'MODOMICS: A Database of RNA Modifications and Related Information. 2025 Update and 20th Anniversary'. *Nucleic Acids Research* 54 (D1): D219–25. https://doi.org/10.1093/nar/gkaf1284.

Spirin, A. S., O. E. Kostiashkina, and J. Jonák. 1976. 'Contribution of the Elongation Factors to Resistance of Ribosomes against Inhibitors: Comparison of the Inhibitor Effects on the Factor-Dependent and Factor-Free Translation Systems'. *Journal of Molecular Biology* 101 (4): 553–62. https://doi.org/10.1016/0022-2836(76)90244-8.

Srinivasan, Gayathri, Carey M. James, and Joseph A. Krzycki. 2002. 'Pyrrolysine Encoded by UAG in Archaea: Charging of a UAG-Decoding Specialized tRNA'. *Science* (New York, N.Y.) 296 (5572): 1459–62. https://doi.org/10.1126/science.1069588.

Stanley, Robin E., Gregor Blaha, Robert L. Grodzicki, Michael D. Strickler, and Thomas A. Steitz. 2010. 'The Structures of the Anti-Tuberculosis Antibiotics Viomycin and Capreomycin Bound to the 70S Ribosome'. *Nature Structural & Molecular Biology* 17 (3): 289–93. https://doi.org/10.1038/nsmb.1755.

Stark, Holger, Marina V. Rodnina, Hans-Joachim Wieden, Marin Van Heel, and Wolfgang Wintermeyer. 2000. 'Large-Scale Movement of Elongation Factor G and Extensive

Conformational Change of the Ribosome during Translocation'. *Cell* 100 (3): 301–9. https://doi.org/10.1016/S0092-8674(00)80666-2.

Steitz, J. A., and K. Jakes. 1975. 'How Ribosomes Select Initiator Regions in mRNA: Base Pair Formation between the 3' Terminus of 16S rRNA and the mRNA during Initiation of Protein Synthesis in Escherichia Coli'. *Proceedings of the National Academy of Sciences of the United States of America* 72 (12): 4734–38. https://doi.org/10.1073/pnas.72.12.4734.

Stephens, C. R., L. H. Conover, F. A. Hochstein, et al. 1952. 'TERRAMYCIN. VIII. STRUCTURE OF AUREOMYCIN AND TERRAMYCIN'. *Journal of the American Chemical Society* 74 (19): 4976–77. https://doi.org/10.1021/ja01139a533.

Sum, P. E., Ving J. Lee, Raymond T. Testa, et al. 1994. 'Glycylcyclines. 1. A New Generation of Potent Antibacterial Agents through Modification of 9-Aminotetracyclines'. *Journal of Medicinal Chemistry* 37 (1): 184–88. https://doi.org/10.1021/jm00027a023.

Süssmuth, Roderich D., and Andi Mainz. 2017. 'Nonribosomal Peptide Synthesis—Principles and Prospects'. *Angewandte Chemie International Edition* 56 (14): 3770–821. https://doi.org/10.1002/anie.201609079.

Svidritskiy, Egor, Gabriel Demo, Anna B. Loveland, Chen Xu, and Andrei A. Korostelev. 2019. 'Extensive Ribosome and RF2 Rearrangements during Translation Termination'. *eLife* 8 (September): e46850. https://doi.org/10.7554/eLife.46850.

Sylvers, L. A., K. C. Rogers, M. Shimizu, E. Ohtsuka, and D. Söll. 1993. 'A 2-Thiouridine Derivative in tRNAGlu Is a Positive Determinant for Aminoacylation by Escherichia Coli Glutamyl-tRNA Synthetase'. *Biochemistry* 32 (15): 3836–41. https://doi.org/10.1021/bi00066a002.

Syroegin, Egor A., Laurin Flemmich, Dorota Klepacki, Nora Vazquez-Laslop, Ronald Micura, and Yury S. Polikanov. 2022. 'Structural Basis for the Context-Specific Action of the Classic Peptidyl Transferase Inhibitor Chloramphenicol'. *Nature Structural & Molecular Biology* 29 (2): 152–61. https://doi.org/10.1038/s41594-022-00720-y.

Thompson, R. C., and P. J. Stone. 1977. 'Proofreading of the Codon-Anticodon Interaction on Ribosomes.' *Proceedings of the National Academy of Sciences* 74 (1): 198–202. https://doi.org/10.1073/pnas.74.1.198.

Tissières, A., and J. D. Watson. 1958. 'Ribonucleoprotein Particles from Escherichia Coli'. *Nature* 182 (4638): 778–80. https://doi.org/10.1038/182778b0.

Tissières, A., J. D. Watson, D. Schlessinger, and B. R. Hollingworth. 1959. 'Ribonucleoprotein Particles from Escherichia Coli'. *Journal of Molecular Biology* 1 (3): 221–33. https://doi.org/10.1016/S0022-2836(59)80029-2.

Tobias, Nicholas J., Hendrik Wolff, Bardya Djahanschiri, et al. 2017. 'Natural Product Diversity Associated with the Nematode Symbionts Photorhabdus and Xenorhabdus'. *Nature Microbiology* 2 (12): 1676–85. https://doi.org/10.1038/s41564-017-0039-9.

Traut, R. R., and R. E. Monro. 1964. 'The Puromycin Reaction and Its Relation to Protein Synthesis'. *Journal of Molecular Biology* 10 (1): 63–72. https://doi.org/10.1016/S0022-2836(64)80028-0.

Trobro, Stefan, and Johan Åqvist. 2009. 'Mechanism of the Translation Termination Reaction on the Ribosome'. *Biochemistry* 48 (47): 11296–303. https://doi.org/10.1021/bi9017297.

Tsai, Albert, Sotaro Uemura, Magnus Johansson, et al. 2013. 'The Impact of Aminoglycosides on the Dynamics of Translation Elongation'. *Cell Reports* 3 (2): 497–508. https://doi.org/10.1016/j.celrep.2013.01.027.

Tsai, Kaitlyn, Vanja Stojković, D. John Lee, et al. 2022. 'Structural Basis for Context-Specific Inhibition of Translation by Oxazolidinone Antibiotics'. *Nature Structural & Molecular Biology* 29 (2): 162–71. https://doi.org/10.1038/s41594-022-00723-9.

Tsegaye, Solomon, Gobena Dedefo, and Mohammed Mehdi. 2021. 'Biophysical Applications in Structural and Molecular Biology'. *Biological Chemistry* 402 (10): 1155–77. https://doi.org/10.1515/hsz-2021-0232.

Urbonavicius, J., Q. Qian, J. M. Durand, T. G. Hagervall, and G. R. Björk. 2001. 'Improvement of Reading Frame Maintenance Is a Common Function for Several tRNA Modifications'. *The EMBO Journal* 20 (17): 4863–73. https://doi.org/10.1093/emboj/20.17.4863.

Valle, Mikel, Andrey Zavialov, Wen Li, et al. 2003. 'Incorporation of Aminoacyl-tRNA into the Ribosome as Seen by Cryo-Electron Microscopy'. *Nature Structural & Molecular Biology* 10 (11): 899–906. https://doi.org/10.1038/nsb1003.

Van Acken, Ute. 1975. 'Proteinchemical Studies on Ribosomal Proteins S4 and S12 from Ram (Ribosomal Ambiguity) Mutants of Escherichia Coli'. *Molecular and General Genetics MGG* 140 (1): 61–68. https://doi.org/10.1007/BF00268989.

Varshney, U., C. P. Lee, and U. L. RajBhandary. 1993. 'From Elongator tRNA to Initiator tRNA.' *Proceedings of the National Academy of Sciences* 90 (6): 2305–9. https://doi.org/10.1073/pnas.90.6.2305.

Varshney, U., C. P. Lee, B. L. Seong, and U. L. RajBhandary. 1991. 'Mutants of Initiator tRNA That Function Both as Initiators and Elongators'. *The Journal of Biological Chemistry* 266 (27): 18018–24.

Varshney, U., and U. L. RajBhandary. 1992. 'Role of Methionine and Formylation of Initiator tRNA in Initiation of Protein Synthesis in Escherichia Coli'. *Journal of Bacteriology* 174 (23): 7819–26. https://doi.org/10.1128/jb.174.23.7819-7826.1992.

Vázquez-Laslop, Nora, and Alexander S. Mankin. 2014. 'Triggering Peptide-Dependent Translation Arrest by Small Molecules: Ribosome Stalling Modulated by Antibiotics'. In *Regulatory Nascent Polypeptides*, edited by Koreaki Ito. Springer Japan. https://doi.org/10.1007/978-4-431-55052-5_10.

Vázquez-Laslop, Nora, and Alexander S. Mankin. 2018. 'Context-Specific Action of Ribosomal Antibiotics'. *Annual Review of Microbiology* 72 (1): 185–207. https://doi.org/10.1146/annurev-micro-090817-062329.

Vazquez-Laslop, Nora, Celine Thum, and Alexander S. Mankin. 2008. 'Molecular Mechanism of Drug-Dependent Ribosome Stalling'. *Molecular Cell* 30 (2): 190–202. https://doi.org/10.1016/j.molcel.2008.02.026.

Vesper, Oliver, Shahar Amitai, Maria Belitsky, et al. 2011. 'Selective Translation of Leaderless mRNAs by Specialized Ribosomes Generated by MazF in Escherichia Coli'. *Cell* 147 (1): 147–57. https://doi.org/10.1016/j.cell.2011.07.047.

Voorhees, Rebecca M., T. Martin Schmeing, Ann C. Kelley, and V. Ramakrishnan. 2010. 'The Mechanism for Activation of GTP Hydrolysis on the Ribosome'. *Science* 330 (6005): 835–38. https://doi.org/10.1126/science.1194460.

Voorhees, Rebecca M., Albert Weixlbaumer, David Loakes, Ann C. Kelley, and V. Ramakrishnan. 2009. 'Insights into Substrate Stabilization from Snapshots of the Peptidyl Transferase Center of the Intact 70S Ribosome'. *Nature Structural & Molecular Biology* 16 (5): 528–33. https://doi.org/10.1038/nsmb.1577.

Waksman, S. A., and H. B. Woodruff. 1940. 'Bacteriostatic and Bactericidal Substances Produced by a Soil Actinomyces.' *Experimental Biology and Medicine* 45 (2): 609–14. https://doi.org/10.3181/00379727-45-11768.

Waksman, Selman A., and Albert Schatz. 1945. 'Streptomycin–Origin, Nature, and Properties*††Journal Series Paper of the Department of Microbiology of the New Jersey Agricultural Experiment Station, Rutgers University.' *Journal of the American Pharmaceutical Association (Scientific Ed.)* 34 (11): 273–91. https://doi.org/10.1002/jps.3030341102.

Waksman, Selman A., and H. Boyd Woodruff. 1941. '*Actinomyces Antibioticus* , a New Soil Organism Antagonistic to Pathogenic and Non-Pathogenic Bacteria'. *Journal of Bacteriology* 42 (2): 231–49. https://doi.org/10.1128/jb.42.2.231-249.1941.

Wald, Abraham. 1943. 'Tests of Statistical Hypotheses Concerning Several Parameters When the Number of Observations Is Large'. *Transactions of the American Mathematical Society* 54 (3): 426–82. https://doi.org/10.1090/S0002-9947-1943-0012401-3.

Wallin, Göran, and Johan Åqvist. 2010. 'The Transition State for Peptide Bond Formation Reveals the Ribosome as a Water Trap'. *Proceedings of the National Academy of Sciences* 107 (5): 1888–93. https://doi.org/10.1073/pnas.0914192107.

Walsh, Christopher T. 2008. 'The Chemical Versatility of Natural-Product Assembly Lines'. *Accounts of Chemical Research* 41 (1): 4–10. https://doi.org/10.1021/ar7000414.

Wang, Leyi, Arto Pulk, Michael R. Wasserman, et al. 2012. 'Allosteric Control of the Ribosome by Small-Molecule Antibiotics'. *Nature Structural & Molecular Biology* 19 (9): 957–63. https://doi.org/10.1038/nsmb.2360.

Wasserman, Michael R., Jose L. Alejo, Roger B. Altman, and Scott C. Blanchard. 2016. 'Multiperspective smFRET Reveals Rate-Determining Late Intermediates of Ribosomal Translocation'. *Nature Structural & Molecular Biology* 23 (4): 333–41. https://doi.org/10.1038/nsmb.3177.

Weissbach, Herbert, David Lee Miller, and John Hachmann. 1970. 'Studies on the Role of Factor Ts in Polypeptide Synthesis'. *Archives of Biochemistry and Biophysics* 137 (1): 262–69. https://doi.org/10.1016/0003-9861(70)90433-9.

Weixlbaumer, Albert, Hong Jin, Cajetan Neubauer, et al. 2008. 'Insights into Translational Termination from the Structure of RF2 Bound to the Ribosome'. *Science* (New York, N.Y.) 322 (5903): 953–56. https://doi.org/10.1126/science.1164840.

Wen, Jin-Der, Laura Lancaster, Courtney Hodges, et al. 2008. 'Following Translation by Single Ribosomes One Codon at a Time'. *Nature* 452 (7187): 598–603. https://doi.org/10.1038/nature06716.

Wieden, Hans-Joachim, Kirill Gromadski, Dmytro Rodnin, and Marina V. Rodnina. 2002. 'Mechanism of Elongation Factor (EF)-Ts-Catalyzed Nucleotide Exchange in EF-Tu'. *Journal of Biological Chemistry* 277 (8): 6032–36. https://doi.org/10.1074/jbc.M110888200.

Wilson, Daniel N. 2014. 'Ribosome-Targeting Antibiotics and Mechanisms of Bacterial Resistance'. *Nature Reviews Microbiology* 12 (1): 35–48. https://doi.org/10.1038/nrmicro3155.

Wimberly, Brian T., Ditlev E. Brodersen, William M. Clemons, et al. 2000. 'Structure of the 30S Ribosomal Subunit'. *Nature* 407 (6802): 327–39. https://doi.org/10.1038/35030006.

Wohlgemuth, Ingo, Raffaella Garofalo, Ekaterina Samatova, et al. 2021. 'Translation Error Clusters Induced by Aminoglycoside Antibiotics'. *Nature Communications* 12 (1). https://doi.org/10.1038/s41467-021-21942-6.

Wohlgemuth, Ingo, Corinna Pohl, Joerg Mittelstaet, Andrey L. Konevega, and Marina V. Rodnina. 2011. 'Evolutionary Optimization of Speed and Accuracy of Decoding on the Ribosome'. *Philosophical Transactions of the Royal Society B: Biological Sciences* 366 (1580): 2979–86. https://doi.org/10.1098/rstb.2011.0138.

World Health Organization. 2024. *WHO Bacterial Priority Pathogens List 2024: Bacterial Pathogens of Public Health Importance, to Guide Research, Development, and Strategies to Prevent and Control Antimicrobial Resistance*. 1st ed. World Health Organization.

World Health Organization. 2025. *Analysis of Antibacterial Agents in Clinical and Preclinical Development: Overview and Analysis 2025.*

Wright, Gerard, Michael Cook, Min Xu, et al. 2025. 'Saskemycin, a Potent and Selective Antimycobacterial Agent Targeting a Unique Site on the Ribosome'. Preprint, In Review, November 7. https://doi.org/10.21203/rs.3.rs-7820265/v1.

Wu, X. Q., and U. L. RajBhandary. 1997. 'Effect of the Amino Acid Attached to Escherichia Coli Initiator tRNA on Its Affinity for the Initiation Factor IF2 and on the IF2 Dependence of Its Binding to the Ribosome'. *The Journal of Biological Chemistry* 272 (3): 1891–95. https://doi.org/10.1074/jbc.272.3.1891.

Yaghoubi, Sajad, Angelina Olegovna Zekiy, Marcela Krutova, et al. 2022. 'Tigecycline Antibacterial Activity, Clinical Effectiveness, and Mechanisms and Epidemiology of Resistance: Narrative Review'. *European Journal of Clinical Microbiology & Infectious Diseases: Official Publication of the European Society of Clinical Microbiology* 41 (7): 1003–22. https://doi.org/10.1007/s10096-020-04121-1.

Yamamoto, Hiroshi, Daniela Wittek, Romi Gupta, et al. 2016. '70S-Scanning Initiation Is a Novel and Frequent Initiation Mode of Ribosomal Translation in Bacteria'. *Proceedings of the National Academy of Sciences of the United States of America* 113 (9): E1180-1189. https://doi.org/10.1073/pnas.1524554113.

Yang, W. K., and G. D. Novelli. 1968. 'Multiple Isoaccepting Transfer RNA's in a Muouse Plasma Cell Tumor'. *Proceedings of the National Academy of Sciences of the United States of America* 59 (1): 208–15. https://doi.org/10.1073/pnas.59.1.208.

Yao, Li, Yue Li, Te-Wie Tsai, Shoujun Xu, and Yuhong Wang. 2013. 'Noninvasive Measurement of the Mechanical Force Generated by Motor Protein EF-G during Ribosome Translocation'. *Angewandte Chemie* (International ed. in English) 52 (52): 14041–44. https://doi.org/10.1002/anie.201307419.

Yarahmadi, Aref, Hamide Najafiyan, Mohammad Hasan Yousefi, et al. 2025. 'Beyond Antibiotics: Exploring Multifaceted Approaches to Combat Bacterial Resistance in the Modern Era: A Comprehensive Review'. *Frontiers in Cellular and Infection Microbiology* 15 (March): 1493915. https://doi.org/10.3389/fcimb.2025.1493915.

Young, R., and H. Bremer. 1976. 'Polypeptide-Chain-Elongation Rate in Escherichia Coli B/r as a Function of Growth Rate'. *The Biochemical Journal* 160 (2): 185–94. https://doi.org/10.1042/bj1600185.

Zaher, Hani S., and Rachel Green. 2009a. 'Fidelity at the Molecular Level: Lessons from Protein Synthesis'. *Cell* 136 (4): 746–62. https://doi.org/10.1016/j.cell.2009.01.036.

Zaher, Hani S., and Rachel Green. 2009b. 'Quality Control by the Ribosome Following Peptide Bond Formation'. *Nature* 457 (7226): 161–66. https://doi.org/10.1038/nature07582.

Zaher, Hani S., Jeffrey J. Shaw, Scott A. Strobel, and Rachel Green. 2011. 'The 2'-OH Group of the Peptidyl-tRNA Stabilizes an Active Conformation of the Ribosomal PTC'. *The EMBO Journal* 30 (12): 2445–53. https://doi.org/10.1038/emboj.2011.142.

Zavialov, A. V., R. H. Buckingham, and M. Ehrenberg. 2001. 'A Posttermination Ribosomal Complex Is the Guanine Nucleotide Exchange Factor for Peptide Release Factor RF3'. *Cell* 107 (1): 115–24. https://doi.org/10.1016/s0092-8674(01)00508-6.

Zavialov, Andrei V, Liliana Mora, Richard H. Buckingham, and Måns Ehrenberg. 2002. 'Release of Peptide Promoted by the GGQ Motif of Class 1 Release Factors Regulates the GTPase Activity of RF3'. *Molecular Cell* 10 (4): 789–98. https://doi.org/10.1016/S1097-2765(02)00691-3.

Zhang, Jiajie, Kassian Kobert, Tomáš Flouri, and Alexandros Stamatakis. 2014. 'PEAR: A Fast and Accurate Illumina Paired-End reAd mergeR'. *Bioinformatics* (Oxford, England) 30 (5): 614–20. https://doi.org/10.1093/bioinformatics/btt593.

Zhang, Jingji, Michael Y. Pavlov, and Måns Ehrenberg. 2018. 'Accuracy of Genetic Code Translation and Its Orthogonal Corruption by Aminoglycosides and Mg2+ Ions'. *Nucleic Acids Research* 46 (3): 1362–74. https://doi.org/10.1093/nar/gkx1256.

Zhang, Ling, Ying-Hui Wang, Xing Zhang, Laura Lancaster, Jie Zhou, and Harry F. Noller. 2020. 'The Structural Basis for Inhibition of Ribosomal Translocation by Viomycin'. *Proceedings of the National Academy of Sciences* 117 (19): 10271–77. https://doi.org/10.1073/pnas.2002888117.

Zhang, Yan, Nikolay A. Aleksashin, Dorota Klepacki, et al. 2022. 'The Context of the Ribosome Binding Site in mRNAs Defines Specificity of Action of Kasugamycin, an Inhibitor of Translation Initiation'. *Proceedings of the National Academy of Sciences* 119 (4): e2118553119. https://doi.org/10.1073/pnas.2118553119.

Zhao, Miao, Alexander J. Lepak, Karen Marchillo, Jamie VanHecker, and David R. Andes. 2018. 'In Vivo Pharmacodynamic Characterization of a Novel Odilorhabdin Antibiotic, NOSO-502, against Escherichia Coli and Klebsiella Pneumoniae in a Murine Thigh Infection Model'. *Antimicrobial Agents and Chemotherapy* 62 (9): e01067-18. https://doi.org/10.1128/AAC.01067-18.

Zhou, Jie, Laura Lancaster, John Paul Donohue, and Harry F. Noller. 2013. 'Crystal Structures of EF-G–Ribosome Complexes Trapped in Intermediate States of Translocation'. *Science* 340 (6140): 1236086. https://doi.org/10.1126/science.1236086.

Zhou, Jie, Laura Lancaster, John Paul Donohue, and Harry F. Noller. 2014. 'How the Ribosome Hands the A-Site tRNA to the P Site during EF-G–Catalyzed Translocation'. *Science* 345 (6201): 1188–91. https://doi.org/10.1126/science.1255030.

Zinoni, F., A. Birkmann, T. C. Stadtman, and A. Böck. 1986. 'Nucleotide Sequence and Expression of the Selenocysteine-Containing Polypeptide of Formate Dehydrogenase (Formate-Hydrogen-Lyase-Linked) from Escherichia Coli'. *Proceedings of the National Academy of Sciences of the United States of America* 83 (13): 4650–54. https://doi.org/10.1073/pnas.83.13.4650.